

THE IMPACT OF STAR FORMATION ON THE INTERSTELLAR MEDIUM
IN DWARF GALAXIES

by
Crystal Linn Martin

A Dissertation Submitted to the Faculty of the
DEPARTMENT OF ASTRONOMY
In Partial Fulfillment of the Requirements
For the Degree of
DOCTOR OF PHILOSOPHY
In the Graduate College
THE UNIVERSITY OF ARIZONA

1 9 9 6

INFORMATION TO USERS

This manuscript has been reproduced from the microfilm master. UMI films the text directly from the original or copy submitted. Thus, some thesis and dissertation copies are in typewriter face, while others may be from any type of computer printer.

The quality of this reproduction is dependent upon the quality of the copy submitted. Broken or indistinct print, colored or poor quality illustrations and photographs, print bleedthrough, substandard margins, and improper alignment can adversely affect reproduction.

In the unlikely event that the author did not send UMI a complete manuscript and there are missing pages, these will be noted. Also, if unauthorized copyright material had to be removed, a note will indicate the deletion.

Oversize materials (e.g., maps, drawings, charts) are reproduced by sectioning the original, beginning at the upper left-hand corner and continuing from left to right in equal sections with small overlaps. Each original is also photographed in one exposure and is included in reduced form at the back of the book.

Photographs included in the original manuscript have been reproduced xerographically in this copy. Higher quality 6" x 9" black and white photographic prints are available for any photographs or illustrations appearing in this copy for an additional charge. Contact UMI directly to order.

UMI

A Bell & Howell Information Company
300 North Zeeb Road, Ann Arbor MI 48106-1346 USA
313/761-4700 800/521-0600

THE IMPACT OF STAR FORMATION ON THE INTERSTELLAR MEDIUM
IN DWARF GALAXIES

by
Crystal Linn Martin

A Dissertation Submitted to the Faculty of the
DEPARTMENT OF ASTRONOMY
In Partial Fulfillment of the Requirements
For the Degree of
DOCTOR OF PHILOSOPHY
In the Graduate College
THE UNIVERSITY OF ARIZONA

1 9 9 6

UMI Number: 9713414

UMI Microform 9713414
Copyright 1997, by UMI Company. All rights reserved.

**This microform edition is protected against unauthorized
copying under Title 17, United States Code.**


UMI
300 North Zeeb Road
Ann Arbor, MI 48103

THE UNIVERSITY OF ARIZONA ®
GRADUATE COLLEGE

As members of the Final Examination Committee, we certify that we have read the dissertation prepared by Crystal Linn Martin

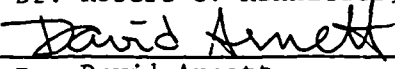
entitled The Impact of Star Formation on the Interstellar
Medium in Dwarf Galaxies

and recommend that it be accepted as fulfilling the dissertation requirement for the Degree of Doctor of Philosophy




Dr. Robert C. Kennicutt, Jr.

August 21, 1996
Date



Dr. David Arnett

August 21, 1996
Date



Dr. Hans-Walter Rix

August 21, 1996
Date

Date

Date

Date

Date

Final approval and acceptance of this dissertation is contingent upon the candidate's submission of the final copy of the dissertation to the Graduate College.

I hereby certify that I have read this dissertation prepared under my direction and recommend that it be accepted as fulfilling the dissertation requirement.



Dissertation Director

August 26, 1996
Date

Dr. Robert C. Kennicutt, Jr.

STATEMENT BY AUTHOR

This dissertation has been submitted in partial fulfillment of requirements for an advanced degree at The University of Arizona and is deposited in the University Library to be made available to borrowers under rules of the Library.

Brief quotations from this dissertation are allowable without special permission, provided that accurate acknowledgment of source is made. Requests for permission for extended quotation from or reproduction of this manuscript in whole or in part may be granted by the head of the major department or the Dean of the Graduate College when in his or her judgment the proposed use of the material is in the interests of scholarship. In all other instances, however, permission must be obtained from the author.

SIGNED: Cynthia Martin

ACKNOWLEDGMENTS

I feel very fortunate to have had the opportunity to complete my graduate studies at Steward Observatory, and I thank the faculty, staff, and grad students here for creating a productive environment. One of my best decisions along the way was choosing Rob Kennicutt as my thesis advisor. I thank him heartily for showing me the ropes at the telescope and providing excellent scientific guidance at many critical points in my dissertation research. By example, he has taught me a great deal about quality research and writing. I am also grateful to Dave Arnett for advice and many discussions about stellar and galactic evolution. My theoretical excursions have certainly added to the quality of my graduate education. Support from an NSF Graduate Fellowship and an AZ Space Grant Fellowship has been appreciated, and I thank Rob and Dave for additional funding when it was needed.

Many others have contributed directly or indirectly to this dissertation. The gas dynamical study would not have been possible without the support of Kitt Peak National Observatory. The contributions of Gary Schmidt, Mike Lesser, and Craig Foltz to the Blue Channel Spectrograph at the MMT made the spectroscopic study of the DIG feasible. The general enthusiasm of professors Bechtold, Benz, Burrows, Liebert, Olszewski, Pinto, G. Rieke, and Rix toward my questions has been appreciated. Chapters 2 and 3 have benefitted from discussions with Joe Shields. Discussions with Julio Navarro, Grant Bazan, and Margaret Hanson have also been helpful. I thank my officemates, especially Chris Fryer and Paul Harding, for enlightening debates following colloquia and Sally Oey for more rigorous discussions about the dynamics of bubbles.

My graduate career would certainly have been less productive had the minutes outside Steward not been so enjoyable. Though I have never been fond of hot weather, I have certainly developed a deep affection for the Sonoran desert and its sky islands. Thanks much to Craig, Jason, Andy, Laird, and Peter for exploring some of it on foot. Thanks also to my tennis partners over the last few years for giving me something else to concentrate on for a few hours every week. Finally, I would like to extend an enormous thank-you to my parents for their continuing support and understanding.

DEDICATION

Dedicated to my grandparents – Geneva, Stan, and Blaine – for being the wonderful people that they are.

TABLE OF CONTENTS

LIST OF FIGURES	10
LIST OF TABLES	12
ABSTRACT	13
1 INTRODUCTION	15
1.1 An Observational Strategy	16
1.2 Objectives	17
1.3 Organization of Presentation	18
2 THE EXCITATION OF DIFFUSE, WARM IONIZED GAS	20
2.1 Introduction	20
2.2 Spectrophotometry	22
2.2.1 The Sample of Galaxies	22
2.2.2 Observations	26
2.2.3 Analysis of Spectra	30
2.3 The HII Region Excitation Sequence	33
2.3.1 O/H Abundances Ratios	38
2.3.2 Photoionization Models	39
2.3.3 Physical Properties Underlying the Excitation Sequence	39
2.4 The HII Region - DIG Spectral Transition	42
2.4.1 The Empirical Spectral Transition	42
2.4.2 Photoionization of the DIG by Dilute Stellar Radiation	50
2.4.3 Additional Excitation Mechanisms	54
2.5 Summary	57
3 He I λ 5876 RECOMBINATION LINE RADIATION FROM THE DIG	77

3.1	Introduction	77
3.2	Measurements of He I $\lambda 5876$ Line Emission	79
3.2.1	The Galaxies	79
3.2.2	Observations and Reductions	79
3.2.3	Results	81
3.3	Discussion: The Source of Ionizing Photons	85
3.3.1	Constraints on the Stellar Mass Function	85
3.3.2	The Morphology Problem	87
3.3.3	The Contribution of Shock-Excited Gas to He I $\lambda 5876$ Emission	90
3.4	Summary	91
4	KINEMATIC EVIDENCE FOR SUPERBUBBLES IN I ZW 18	92
4.1	Introduction	92
4.2	Observations and Analysis	94
4.2.1	Optical Imaging	94
4.2.2	High-Resolution Spectroscopy	99
4.2.3	X-Ray Detection	103
4.3	Modeling the Gas Dynamics	104
4.3.1	The Superbubble Model	105
4.3.2	Application to I Zw 18	107
4.3.3	The Star Formation History	109
4.3.4	Results	113
4.4	Discussion	113
4.4.1	A Starburst-Driven Galactic Wind	114
4.4.2	Chemical Enrichment of the ISM	118
4.4.3	The O/H Abundance Ratio in the Ionized Gas	119
4.5	Summary	127

5	THE FORMATION OF GALACTIC WINDS IN DWARF GALAXIES . .	130
5.1	Introduction	130
5.2	Observations and Analysis	133
5.3	The Kinematic Atlas and Catalog	134
5.3.1	Navigating the Echellograms	136
5.3.2	Highlights of the Tour	138
5.3.3	Summary: A Catalog of Superbubbles	143
5.4	Dynamical Interpretation	145
5.4.1	Timescales and Energies	145
5.4.2	Implications for the Star Formation History	148
5.4.3	The Fate of the ISM	150
5.5	Summary: Some Comments on the Role of Gas Dynamical Feedback in the Evolution of Dwarf Galaxies	154
6	SUMMARY	170
6.1	Main Results	170
A	SOFT X-RAY EMISSION FROM NGC 5253	175
7.1	Introduction	178
7.2	X-Ray Observations and Results	179
7.2.1	Spatial Analysis	179
7.2.2	Spectral Analysis	180
7.3	The Physical Nature of the X-Ray Emission	182
7.3.1	X-Rays from Normal Stars and XRBs	182
7.3.2	Spherical Accretion	182
7.3.3	Supernova Remnants	183
7.3.4	Standard Superbubble	184
7.3.5	Superbubble in a Cloudy Medium	185
7.4	Structure of the WIM	186

7.4.1	Optical Imaging	187
7.4.2	Kinematic Structure of the WIM	188
7.5	Summary and Discussion	189
7.5.1	Comparison with Other Starburst Regions	189
7.5.2	Energetics and Dynamics of the Ionized ISM in NGC 5253 . .	189
7.6	References	190
REFERENCES		193

LIST OF FIGURES

2.1	Red continuum images of the galaxies.	26
2.2	HII region excitation sequence projected into [NII] $\lambda 6583$ / $H\alpha$ vs [OII] $\lambda\lambda 3727$ / [OIII] $\lambda 5007$ plane	35
2.3	HII region excitation sequence projected into [OIII] $\lambda 5007$ / $H\beta$ vs [SII] $\lambda\lambda 6717, 31$ / $H\alpha$ plane.	36
2.4	HII-region excitation sequence projected into [OI] $\lambda 6300$ / $H\alpha$ vs [OII] $\lambda\lambda 3727$ / [OIII] $\lambda 5007$ plane.	37
2.5	Gradients in Emission-Line Ratios.	44
2.6	The HII-DIG transition sequence projected onto the [NII] $\lambda 6583$ / $H\alpha$ ha vs [OII] $\lambda\lambda 3727$ / [OIII] $\lambda 5007$ plane.	59
2.7	The HII-DIG transition sequence projected onto the [OIII] $\lambda 5007$ / $H\beta$ vs [OII] $\lambda\lambda 3727$ / [OIII] $\lambda 5007$ plane.	62
2.8	The HII-DIG transition sequence projected onto the [OI] $\lambda 6300$ / $H\alpha$ vs [OII] $\lambda\lambda 3727$ / [OIII] $\lambda 5007$ plane.	66
2.9	Excitation sequence produced by radial structure of model nebulae. .	69
2.10	Transition sequence from photoionized gas clouds to shock-excited clouds	70
2.11	Turbulent mixing layers.	71
2.11	Turbulent mixing layers.	76
3.1	He I $\lambda 5876$ / $H\alpha$ intensity ratio	83
3.2	Gradients in Emission-Line Ratios	84
3.3	Theoretical He I $\lambda 5876$ / $H\alpha$ intensity ratio	86
4.1	$H\alpha$ image of I Zw 18	96
4.2	Echelle spectrum of $H\alpha$ emission	100
4.3	$H\alpha$ position-velocity diagrams	102
4.4	Sketch of possible bipolar bubble geometry	106

4.5	Longslit spectrum of $H\alpha$ emission	121
4.6	Abundance variations along slit A	126
5.1	$H\alpha$ echellograms	157
5.2	Location of Kinematic Shells	161
5.3	Distribution of shell sizes and radial velocities.	166
5.4	Bubble ages and power requirements.	167
5.5	Constraints on the average ambient H density.	168
5.6	The Fate of the Superbubbles.	169
7.1	Red continuum image of NGC 5253	191
7.2	Surface brightness contours of hard X-rays	177
7.3	Spatial Extent of X-ray Source	180
7.4	Pulse-height spectrum of NGC 5253	181
7.5	Chi-squared grid for spectral fit	181
7.6	Image of equivalent width of $H\alpha + [NII]$	185
7.7	Radial profile of rms electron density	185
7.8	Kinematic Structure of the WIM	187
7.9	Position-velocity diagrams	187
7.10	Emission-line profiles in core	188

LIST OF TABLES

2.1	The Sample of Galaxies	24
2.2	Slit Positions	27
2.3	Optical Spectroscopy	45
2.4	Reddening Estimates	46
2.5	O/H Abundance Ratios	47
2.6	Gradients in Ionization Parameter	53
3.1	Properties of the Galaxies	80
3.2	The DIG in Different Types of Galaxies	88
4.1	Properties of I Zw 18	98
4.2	Starburst Models	121
4.3	Gravitational Potential Model	122
4.4	MMT Spectra and Derived Emission Line Ratios	124
5.1	Slit Positions	135
5.2	Properties of Supershells	144
5.3	Superbubble Environment	151
7.1	Measured Properties of the X-ray Emitting Gas	182

ABSTRACT

This thesis is an observational study of the impact of star formation on the interstellar medium. Emission from the ionized component of the interstellar gas is used to measure both the kinematics and the physical properties of the gas in 14 dwarf galaxies.

The galaxies examined contain $H\alpha + [NII]$ emission from ionized gas outside the HII regions. This warm ionized medium has a substantial power requirement and often shows arcs and filaments on scales exceeding 100 pc. To determine the mix of physical processes exciting the gas, I examine optical emission-line ratios measured from ~ 1000 apertures with dimensions $\sim 30 - 150$ pc. I find that, relative to HII regions, the spectrum of the DIG is characterized by high $[O I] / H\alpha$ in addition to high $[O II] / [O III]$, $[S II] / H\alpha$, $[N II] / H\alpha$ and low $[O III] / H\beta$. The HII - DIG spectral transition defines a narrow sequence in diagnostic line-ratio diagrams which is distinct from the HII-region excitation sequence. Photoionization modeling demonstrates that the HII-DIG sequence is driven primarily by a decrease in the relative density of ionizing photons to atoms - consistent with ionization by distant stellar clusters. The strength of the He I $\lambda 5876$ emission relative to that in $H\alpha$ implies stars of mass greater than $35 M_{\odot}$ contribute to the ionizing continuum. A second excitation process, shocks with speeds from $60 - 100 \text{ km s}^{-1}$, is shown to contribute up to 50% of the emission from the lowest surface brightness gas.

High-resolution, longslit spectra reveal organized gas flows on scales ranging from the resolution limit, about $20 - 100 \text{ km s}^{-1}$, to galactic-scale dimensions, roughly 1 kpc. Many of the expanding shells detected kinematically are coincident

with arcs or filaments in the galaxy images, and the geometry of the larger bubbles is often polar rather than spherical. The simplest dynamical models for their growth imply ages from 1 – 20 Myr and require energies from 1 to more than 6000 supernovae. The extent, mass, and rotation of the neutral gas are compiled from the literature and used to argue that many of these bubbles breakthrough the HI disk and form galactic winds. A detailed study of I Zw 18 suggests such winds could have a strong influence on the chemical evolution of dwarfs. The total mass of gas escaping the galaxies is, however, not yet well-constrained and may be quite small.

CHAPTER 1

INTRODUCTION

The feedback between star formation and the interstellar medium (ISM) plays a critical role in the formation and evolution of galaxies. It has been recognized on theoretical grounds for some time that the shock waves generated by supernovae explosions create a substantial turbulent pressure (e.g. McCray & Snow 1979), play a fundamental role in the thermal balance and phase structure of the ISM (Field, Goldsmith, & Habing 1969), and sometimes trigger additional star formation (McCray & Kafatos 1987). Although this feedback may typically be self-regulating (Dopita 1985), the potential disruption of the feedback cycle via the expulsion of the ISM following a major star formation episode has generated much interest. Such galactic winds, driven by an ensemble of supernovae and stellar winds, have been proposed as the process underlying the mass – metallicity relation among galaxies, the metallicity – radius relation within galaxies, the enrichment of the IGM, the disappearance of the faint-blue galaxies, and the formation of structure in the universe (Ostriker & Cowie 1981). Hence, a solid understanding of both the dynamical impact of massive stars on the gas and the repercussions for the physical properties of the ISM is clearly of fundamental importance to a large number of

issues in contemporary astronomy.

The ionized component of the ISM is an essential link in the transfer of mass, energy, and momentum from stars to the bulk mass of the interstellar gas, which is typically neutral hydrogen (HI). The ionized component dominates the volume of the ISM in galaxies with hot stars and is found in two phases – warm ionized gas ($T \approx 10^4$ K) and hot ionized gas ($T \approx 10^6$ K) – which are in rough pressure equilibrium. Emission from the latter occurs in the X-ray regime, although absorption by the highly ionized atoms produces numerous lines in the satellite ultraviolet. The warm ionized medium (WIM), however, is readily observed in the optical and will serve as the primary “window” into the feedback process in this work.

1.1. An Observational Strategy

This thesis presents an observational study of the ISM in nearby dwarf galaxies with current star formation activity. Such galaxies provide a favorable environment for the growth of superbubbles because of their lack of differential rotation and their low metallicity. Since the gravitational potential well is relatively shallow in these galaxies, the shell velocities might even exceed the galaxy’s escape velocity. It has even been suggested that the entire ISM is permanently driven out of dwarf galaxies early in their evolution (Larson 1974; Dekel & Silk 1986).

The dynamics and physical properties of the ionized medium in a sample of 14 low-luminosity galaxies are described in this thesis. The criteria on which the galaxies were selected is explained most extensively in § 2.2.1 of Chapter 2. The morphology, kinematics, and physical properties of the warm ionized gas are investigated using new emission-line images, high-resolution spectra of the

H α emission, and moderate-resolution optical spectra, respectively. The emission-line and continuum images were also used to measure galactic star formation rates, compare the morphology of the gas and stars, and select slit positions for the spectroscopic observations.

New and archival ROSAT observations were examined for about 1/2 of the galaxies; however their resolution and/or sensitivity was typically inadequate for detections of the hot ionized phase of the ISM. Critical properties of the neutral hydrogen gas were compiled from the literature for most of the galaxies.

1.2. Objectives

Several key questions are addressed by this thesis. In a classic paper, Dekel & Silk (1986) described how starburst-driven mass loss could straightforwardly explain the general structural properties of dwarf galaxies. If this scenario is correct, we should “see” examples of these galactic winds in nearby galaxies. Although expanding shells of gas are often found, it remains unclear whether a “wind-phase” in which mass is ejected from the galaxy occurs. If winds do develop, how much material is actually ejected? DeYoung & Heckman (1994) have argued that mass-ejection is more difficult than originally proposed (e.g. Larson 1974; Dekel & Silk 1986). Even a small amount of mass-loss could, however, be extremely important for the chemical evolution of these galaxies (Marconi et al. 1994; DeYoung & Gallagher 1990). Another critical issue is the source of the energy that keeps the WIM ionized. Although stars seem to be the only source capable of supplying the required power, the physical mechanisms involved in the transfer of the energy are poorly constrained. Is photoionization sufficient? Or do shocks contribute? Are the regions of ionized gas which extend well beyond the centers of star formation

activity ionized by nearby stars? Or does the ionizing radiation manage to travel many times its average mean free path? What are the implications for the relative topology of the phases of interstellar gas?

1.3. Organization of Presentation

Chapters 2 and 5 focus on the differences in the physical and dynamical properties of the DIG (diffuse ionized gas) among and within the galaxies. The analysis aims to present the major results and provide an extensive database and direction for further investigation. The case studies in Chapter 3, Chapter 4, and Appendix A examine a particular galaxy or question in detail as described below. Chapter 6 provides a concise summary of the most important results from the thesis.

The ISM must be relatively porous as seen from a hot star if the extended low surface brightness gas visible in optical emission-line images is ionized by stars in the young, centrally-located stellar associations. Chapter 2 examines this “photoionization from afar” hypothesis using estimates of the relative density of photons to atoms, and the analysis is continued in Chapter 4 which looks for spatial variations in the spectral energy distribution of the Lyman continuum radiation ionizing the DIG. This discussion was separated from Chapter 2 because of the timeliness of the results. Two recent studies of the DIG in the Milky Way indicate the ionizing spectrum there is softer than expected (Reynolds & Tufte 1995; Heiles et al. 1996).

Chapter 4 presents a case-study of one of the most metal-poor galaxies known – I Zw 18. Spectra of this galaxy have played an important role in measurements of the primordial He/H abundance ratio – a quantity of great interest for constraining the mean baryon density of the universe in the context of standard Big-Bang

nucleosynthesis theory (e.g. Pagel et al. 1992). Since I Zw 18 may be experiencing its first episode of star formation (Sargent & Searle 1970; Lequeux & Viallefond 1980; Kunth et al. 1994), it provides a unique opportunity to examine feedback in a young galaxy.

New observations of NGC 5253 were obtained with the ROSAT (Röntgensatellit), an X-ray astronomy satellite launched by Germany, the United States, and Great Britain. One of the most controversial issues underlying our understanding of the ISM today is the volume filling factor of the hot ionized phase of interstellar gas (McKee 1990; Slavin & Cox 1993; Shelton & Cox 1994; Burrows & Mendenhall 1994). Such hot gas emits thermal Bremsstrahlung and line-emission in the soft X-ray region of the electromagnetic spectrum, where the instruments on ROSAT are much more sensitive than previous X-ray satellites. The observations were made in collaboration with the director of this thesis, Dr. Robert Kennicutt; and our analysis and results are presented in Appendix A.

CHAPTER 2

THE EXCITATION OF DIFFUSE, WARM IONIZED GAS

2.1. Introduction

The interplay between star formation and the interstellar medium (ISM) is a fundamental aspect of galaxy formation and evolution. The rate and distribution of star formation appear to directly influence conditions in the warm ionized component of the interstellar medium (hereafter, WIM or DIG for diffuse ionized gas). In the Milky Way, the power requirements of the warm ionized medium (WIM) or DIG (diffuse ionized gas) are substantial; Reynolds (1984) estimates 100% of the Galactic supernova energy or about 20% of the ionizing photons from O stars are required to keep it ionized. The DIG fills at least 20% of the interstellar volume and contains about 1/5 of the atomic gas by mass if conditions within 2-3 kpc of the sun are typical (Reynolds 1991; Kulkarni & Heiles 1987). Observations of other galaxies demonstrate a close relationship between the presence and morphology of a WIM (or DIG) and the rate and distribution

of star formation (Dettmar 1992). Among edge-on galaxies, for example, those with the highest infrared luminosities and surface brightnesses have a prominent layer of ionized gas (e.g. NGC 891, Rand et al. 1992; Dettmar et al. 1992); but the extraplanar DIG in typical spirals is restricted to a few patches in radius (Rand 1996). Similarly, the DIG in M 31 is strongly concentrated near regions of star formation (Walterbos & Braun 1994). Among normal galaxies, the largest star forming complexes and the largest number of young associations (per unit luminosity) are found in Magellanic irregulars (Kennicutt 1988). Extra-HII region $H\alpha$ emission contributes as much as $\sim 50\%$ of the $H\alpha$ flux from some of these galaxies (e.g. NGC 4449 and NGC 4214; Kennicutt et al. 1989). Much of this emission comes from relatively high surface brightness (~ 100 rayleighs) shells and filaments, referred to as “interstellar froth” (Hunter & Gallagher 1990). The relatively high surface-brightness emission-line filaments extending along the minor axis of many infrared-selected galaxies are dynamically associated with galactic winds (Heckman, Armus, & Miley 1990; Lehnert & Heckman 1996); and the unusually high amount of star formation in these galaxies is often concentrated in the nucleus (Armus, Heckman, & Miley 1989, 1990).

The spectrum and kinematics of the DIG reflect many of the relevant physical processes transporting energy, mass, and momentum between stars and the ISM. The spectrum of the DIG in Magellanic irregulars as well as the Milky Way is characterized by high ratios of low ionization lines (e.g. [SII], [NII], and [OII]) relative to $H\alpha$ but low $[OIII]\lambda 5007 / H\beta$ (Hunter & Gallagher 1990; Reynolds 1985a; Reynolds 1985b; Reynolds 1985c). However, the low surface brightness of the DIG has made spectroscopic studies of its spatial variations and low intensity lines challenging. In this paper, I present longslit spectra across 15 galaxies and an analysis of the emission-line ratios including the $[OI]\lambda 6300 / H\alpha$ intensity.

The galaxies have B band luminosities ranging from $0.002L^*$ to $0.2L^*$ and O/H abundance ratios between 2% $(\text{O}/\text{H})_{\odot}$ and approximately solar; I will refer to them as “dwarfs.” Using over ~ 1000 spectra extracted from these observations, I examine the spectral gradient from HII regions to the DIG and discuss variations in the excitation mechanism within these environments. A companion paper will discuss the gas kinematics of the same sample.

This paper is organized as follows. The sample, the spectrophotometric observations, and the data analysis are outlined in § 2.2. In § 2.3, spectra of the HII regions are used to establish a baseline excitation sequence. I derive O/H abundance ratios and introduce photoionization models to constrain other nebular properties. Section 2.4 illustrates the empirical spectral transition from the HII regions to the DIG, distinguishes this “transition sequence” from the classical HII region excitation sequence, and discusses the underlying physical changes in the DIG. The results are summarized in § 2.5 and related to work on other galaxies.

2.2. Spectrophotometry

2.2.1. The Sample of Galaxies

Table 2.1 summarizes the properties of the sample. The luminosities of these galaxies range from roughly $0.002L^*$ to $0.2L^*$ (Schechter 1976), and I will refer to them collectively as “dwarfs.” They were selected on the basis of recent star formation activity and drawn from samples of Wolf-Rayet galaxies (Conti 1991), blue compact dwarfs (Thuan & Martin 1981 ; Sargent & Searle 1970), and Magellanic irregulars (Hunter & Gallagher 1990; Hunter 1982). To ensure the data would be spatially resolved on scales $\lesssim 100$ pc, only galaxies closer than ~ 10 Mpc were considered for the sample. The quintessential starburst galaxy, M 82, was

added as a more luminous comparison object in which the starburst is having a particularly strong impact on the ISM. Most of the galaxies are isolated systems, although II Zw 40 is a recent merger product (Brinks & Klein 1988) and NGC 3077 is involved in a tidal interaction with M 81 (e.g. Appelton et al. 1981).

The apparent isophotal diameters listed in col. 4 of Table 2.1 are typically only a few arcminutes, so two observations with a longslit ($3'$) are often adequate to sample the emission-line spectrum across an entire galaxy. Observations of the larger galaxies were made at more positions. Table 2.2 identifies the position of each observation and assigns it a label for future reference. The offset stars are identified in Figure 2.1 where the slit positions are superposed on sketches of the red continuum emission.

The $H\alpha$ morphology of the galaxies (Martin 1996) strongly influenced my selection of slit positions. The striking contrast between the continuum and emission-line morphology creates the illusion in Figure 2.1 that the entire slit misses the galaxy in a few cases. The strategy was to center the slit on the brightest HII region and to orient the slit along the major/minor axis of the extended $H\alpha$ emission in the first/second observations respectively. In practice, the irregular morphology of the galaxies made this procedure ambiguous. The desire to keep the component of differential atmospheric refraction along the slit less than $0''.5$ tightly constrained the allowable deviation from the parallactic angle for all but the galaxies transiting near the zenith.

Table 2.1 The Sample of Galaxies

Galaxy	d (ref)	M_B	D	M(HI)	Type	ref.
	(Mpc)	(mag)	(')	(M_\odot)	(RC3)	
NGC 1569	2.2	-17.26	3.1	8.4e7	IBm	1, 9
NGC 1800	8.1	-16.67	2.2	1.6e8	IB(s)m	2, 10
II Zw 40	10.1	-14.54	1.3	4.5e8	cI(pec)	3, 11
NGC 2363	3.6	-16.75	8.0	9.9e8	IB(s)m	4, 11
NGC 2537	7.5	-17.36	1.7	2.8e8	SB(s)m(pec)	2, 11
IZw18	10.0	-13.84	0.5	7.0e7	...	5, 12
M82	3.6	-18.95	11.7	8.8e8	I0	4, 13
NGC 3077	3.6	-17.37	5.4	1.2e9	I0	4, 13
Sex A	1.31	-13.84	4.4	1.1e8	IB(s)m	6, 14
VII Zw 403	3.6	-13.68		4.9e7	Pec	4, 15
NGC 3738	4.0	-16.0	3.3	1.6e8	Im	7, 7
NGC 4214	3.6	-17.65	9.6	1.1e8	IAB(s)m	2, 7
NGC 4449	3.6	-17.86	5.6	2.4e9	IBm	2, 16
NGC 4861	7.5	-17.6	4.2	5.0e8	SB(s)m	2, 11
NGC 5253	4.1 ± 0.2	-17.62	4.5	1.4e8	Im(pec) ?	8, 17

TABLE NOTES:

col. 3 – Blue magnitude from RC3.

col. 4 – Angular diameter at the 25 B-mag $''^{-2}$ isophote. Tully, R. B. 1988, *Nearby Galaxies Catalog*, Cambridge University Press, Cambridge.

col. 5 – Mass of HI scaled to the distance adopted in column 2.

TABLE REFERENCES (for distances):

- (1) Israel, F. P., & DeBruyn, A. G. 1988, A&A, 198, 109.
- (2) Calzetti, D., Bohlin, R. C., Kinney, A. L., Storchi-Bergmann, T., & Heckman, T. M. 1995, ApJ, 443, 136. (They used $H_0 = 50$, and I scale their distances to $H_0 = 75$. The heliocentric velocity from the RSA is reduced to the centroid of the local group in the RSA-way.)
- (3) Brinks, E. & Klein, U. 1988, MNRAS, 231, 63P. ($V_{\text{sun}} = 795 \text{ km s}^{-1}$ and $H_0 = 75$).
- (4) Adopt distance to M81 – NGC 2403 group. Estimate from Cepheids as reported in Madore, B. F., Freedman, W. L., & Lee, M. G. 1993, ApJ, 106, 2243.
- (5) Dufour, R. J., & Hester, J. J. 1990, ApJ, 350, 149 (They use $v_{\text{sun}} = 795 \text{ km s}^{-1}$ of LV81 and $H_0 = 75$.)
- (6) Madore, B. F. & Freedman, W. L. 1991, PASP, 103, 933.
- (7) Hunter, D., Gallagher, J., & Rautenkranz, D. 1982, ApJS, 49, 53 (HGR). (Adopt systemic galactocentric velocity = 301 and $H_0 = 75$.)
- (8) Saha, A., Sandage, A., Labhardt, L., Schwengeler, H., Tammann, G. A., Panagia, N., & Macchetto, F. D. 1995, ApJ, 438, 8.

TABLE REFERENCES (for HI masses):

- (9) Reakes, M. 1980, MNRAS, 192, 297. (30% vs. Roberts and HGR)
- (10) Gallagher, J. S., Knapp, G. R., & Hunter, D. A. 1981, AJ, 86, 344.
- (11) Thuan, T. X., & Martin, G. E. 1981, ApJ, 247, 823 (TM).
- (12) Lequeux, J., & Viallefond, F. 1980, A&A, 91, 269.
- (13) Appelton et al. 1981, MNRAS, 195, 327 (A81).
- (14) Huchtmeier, W. K., Seiradakis, J. H., Materne, J. 1981, A&A102, 134.
- (15) Tully, R. B., Boesgaard, A. M., Dyck, H. M., & Schempp, W. V. 1981, ApJ, 246, 38.
- (16) Hunter, D. A., & Gallagher, J. S., III 1986, PASP, 98, 5. (...from FT81 or FT75 ?)
- (17) Reif, K., Mobold, U., Goss, W. M., vanWoerden, H., & Siegman, B. 1982, A&AS, 40, 451.

2.2.2. Observations

Longslit spectra were obtained between 1993 December and 1995 March at the MMT using the Blue Channel Spectrograph and a Loral $3k \times 1k$ CCD detector (see Table 2.3). The instrument was configured with a 500 gpm grating blazed at 5410 \AA in 1st order and a UV-36 blocking filter. This setup provided spectral coverage from approximately 3700 \AA to 6800 \AA . Most of the data were obtained with a $1'' \times 180''$ slit which yielded a spectral resolution $\Delta\lambda \sim 3.5 - 5.0 \text{ \AA FWHM}$.

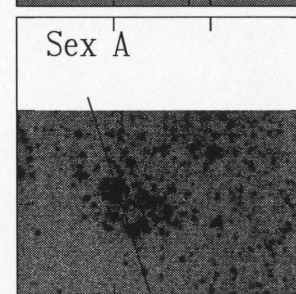
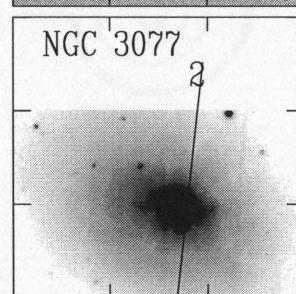
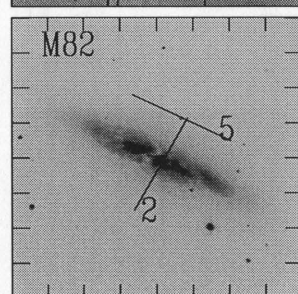
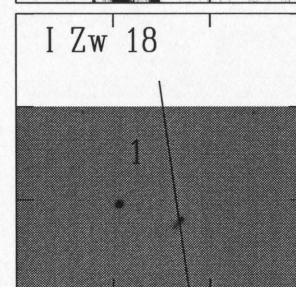
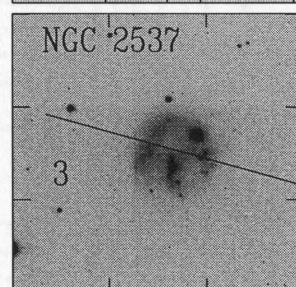
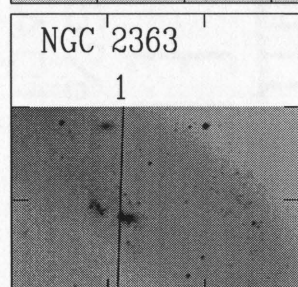
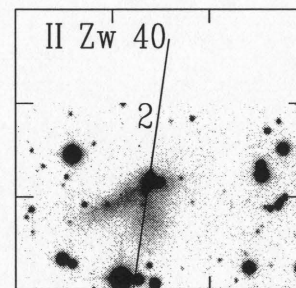
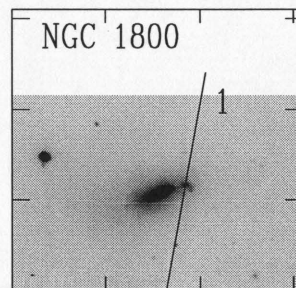
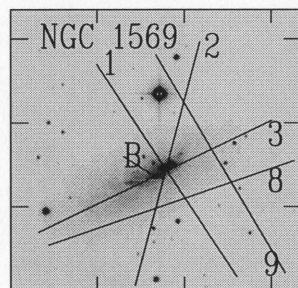
The program started during the commissioning phase of the instrument and several improvements were made to the instrument/detector combination between runs that affect the quality of the data. New camera optics introduced to flatten the curved focal plane prior to the December run produced asymmetric line profiles. This defect was gradually eliminated between subsequent runs, but the amount of distortion (i.e. curvature of the spectrum in the spatial direction) increased from negligible to several pixels. The middle third of the original Loral chip was littered with bad columns, so prior to each run I meticulously calculated the grating tilt that would minimize the damage to the data. A cosmetically clean chip was introduced for the November run and used henceforth. Both Loral chips were blue sensitive with a quantum efficiency of ~ 0.6 at $\lambda 3700 \text{ \AA}$.

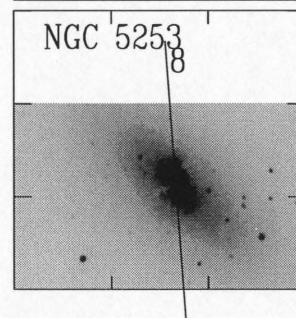
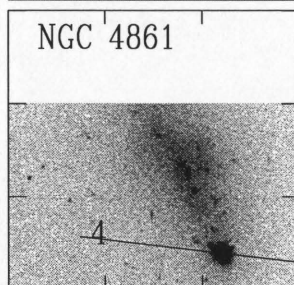
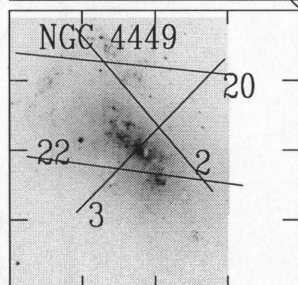
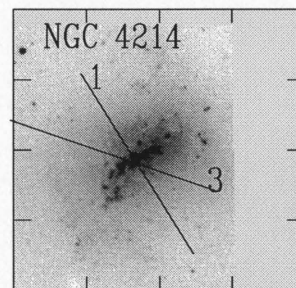
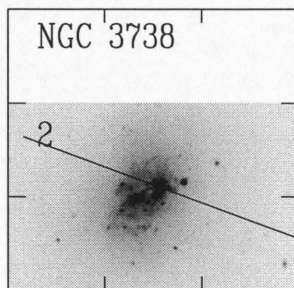
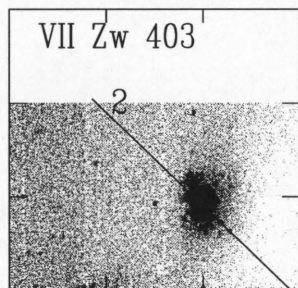
The data reduction followed standard procedures (e.g. ASP Conf. Series 1992). Zero-second exposures, quartz lamp exposures, and long dark exposures were used to correct for pixel-to-pixel voltage offsets and gain variations and to check for

Figure 2.1 Red continuum images of the galaxies taken with Steward Observatory 90-in telescope. Slit positions of spectra discussed in this paper are identified. See Table 2 for the position angle and offset from the reference star or cluster indicated.

Table 2.2 Slit Positions

Galaxy	Slit	Run	PA	Offset	Comments
NGC1569	1.	Nov 27	32.4	8.4W, 3.9N	
	2.	Feb 5	-14.34	8.4W, 8.7N (B)	
	3.	Feb 5	116.4	Knot B	CR Problem
	8.	Mar 25	109.7	11.4W, 19.2S	
	9.	Jan 30	29.7	45.3W, 8.7N	
NGC1800	2.	Nov 27	-2.9	78.3W, 20.4S	Big apertures.
IIZw40	2.	Jan 30	172.	Cont. center	HeI5876 on n.s. line; CR Problem
NGC2363	1.	Feb 4	178.	53.1E, 65.1S	
NGC2537	1.	Feb 3	-172.6	Cont. knot	
	3.	Jan 30	73.8	6.9E, 11.6S	
I Zw 18	1	Feb 5	7.6	1.2E, 0.3N	from NW cont. knot
NGC3034	2.	Mar 26	151.	48.8E, 44.6N	
	5.	Jan 30	64.	14.9E, 124.1N	
NGC3077	2.	Mar 26	174.1	25.3E, 56.8S	
SexA	3.	Mar 25	17.	7.7E, 5.8S	
7ZW403	2.	Jun 8	45.	Cont. center	$d_{\perp} < 0.76''$. Big apertures.
NGC3738	2.	Mar 25	69.	15.2E, 0.50S	
	4.	Jan 30	145.5	8.1E, 3.7S	
NGC4214	1.	Jan 30	31.	24.9E, 23.6S	
	3.	Mar 26	70.3	24.9E, 23.6S	
	4.	Jan 30	106.6	16.8E, 20.7S	CR Problem
NGC4449	2.	Mar 25	38.8	52.8W, 26.1N	
	3.	Jun 8	137.2	Cont. center	
	20.	Mar 25	84.	36.3W, 65.7N	
	22.	Mar 26	82.	44.7W, 26.4S	
NGC4861	6.	Mar 26	21.1	Knot center	
	4.	Jun 8	83.1	Cont. center	CR Problem
NGC5253	8.	Mar 25	4.	57.3W, 50.6N	Big apertures.





dark current. Exposures of the twilight sky were used to model the illumination pattern along the slit and then flatten the data along the spatial dimension. Strong vignetting was discovered near the ends of the slit, and up to 15" of the data was discarded in some cases. Between 4000 Å and 6800 Å the sky flattened to better than 1%, and 4–6% variations were noted beyond this region. A two-dimensional wavelength calibration was made from exposures of a HeNeAr lamp. The transformation was generally determined separately for each slit position and accurate to ~ 0.5 Å although calibrations were obtained less frequently during the February run. A second transformation designed to correct for geometrical distortion was derived from either multiple exposures of a star offset along the slit or an exposure of the quartz lamp through an aperture plate containing ten holes of known separation.

The data were flux calibrated using observations of several sub-dwarf standard stars (Massey et al. 1988) taken periodically throughout each run. The standards were observed at the parallactic angle with a 5" slit, and the sensitivity functions show good agreement after a zeropoint offset. The observing conditions, which are summarized Table 2.3, varied from photometric to snowstorms; and only a relative flux calibration will be used for this paper. As shown in Table 2.3, the residuals in the flux calibration for most of the data are about 0.02 mag. The seeing measured from the standard star observations was typically about 1"8 FWHM but was as large as 5" at the beginning of a couple nights.

2.2.3. Analysis of Spectra

The spectra were sky subtracted and continuum subtracted in their two-dimensional formats. A template of the night sky spectrum was constructed from either a region of the slit beyond the galaxy or a series of offset sky exposures taken between galaxy frames. The sky frame was subtracted from the data, and the line-free

region of the continuum was then fit by a low order polynomial in 4 or 5 segments and subtracted. The intensity profiles of the emission lines along the slit were easy to examine in these “cleaned” frames.

An initial concern was whether a given row of the spectrum at widely separated wavelengths represented emission from the same location on the sky. Comparison of the [OIII] $\lambda 5007$ and [OII] $\lambda 3727$ profiles along the slit, as well as the $H\alpha$ and $H\beta$ profiles, demonstrated that any offsets from differential atmospheric refraction along the slit and/or instrument flexure were less than 3 pixels ($1''.8$). However, the slight variation in focus with wavelength mentioned earlier was sometimes revealed in this comparison and does introduce a small systematic error in the ratios of widely separated lines.

Several sets of extraction apertures were introduced for each two-dimensional spectrogram to maximize the return of physical measurements. The data are deep enough that the spatial variations of the bright spectral lines can be measured on angular scales comparable to the seeing. In practice, however, wavelength-sensitive focus variations along the slit and differential atmospheric refraction along the slit limit the scale on which several diagnostic line ratios can be measured to $\geq 3''.0$. An IRAF script was used to automatically extract spectra on this minimum scale and measure the brightest lines – [OII] $\lambda\lambda$ 3726,29, $H\beta$, [OIII] $\lambda 4959$, [OIII] $\lambda 5007$, $H\alpha$, [NII] $\lambda 6584$, and [SII] $\lambda\lambda$ 6717,31. The spatial limits were generally determined by the S/N of the unresolved [OII] doublet. To achieve comparable S/N, the weaker lines [OI] $\lambda 6300$ and HeI $\lambda 5876$ had to be measured in larger spatial bins. These measurements were made using the *splot* task in IRAF so the residuals from the sky subtraction (telluric [OI] and NaI) could be checked by eye. The results from this maximum sampling analysis are described in § 2.4. A third set of apertures defined by the extent of the detected [OIII] $\lambda 4363$ emission was used to derive

the O/H abundance ratios reported in § 2.3. The apertures for the HII region measurements discussed in § 2.3 were selected based on the surface brightness profile of the H α emission along the slit and the morphology of the H α image.

Emission-line fluxes were measured by integrating over the line profile in the cleaned frame, and the continuum was measured in three 100 Å bandpasses centered at $\lambda 4250$ Å, $\lambda 5150$ Å, and $\lambda 6450$ Å. The statistical errors introduced by counting electrons, sky subtraction, continuum subtraction, CCD calibration, and readnoise were estimated from the 1σ fluctuations in the “cleaned” frame and the width of the line. This error was combined in quadrature with the systematic uncertainty in the flux calibration to yield the fractional uncertainty in the line flux

$$\frac{\delta F}{F} = ((\delta c_\lambda)^2 N_\lambda + (\sigma_F)^2)^{(1/2)}.$$

The uncertainty was dominated by systematic errors in the bright regions while read noise and counting statistics limit the lowest surface brightness measured.

The reddening was estimated two ways. First, the logarithmic extinction at H β , $c(\text{H}\beta)$, was derived as a function of slit position from the H α / H β ratios measured in the small apertures. I assumed a Balmer absorption equivalent width of $2 \text{ Å} \pm 2 \text{ Å}$ to correct for underlying stellar absorption (McCall, Rybski, & Shields 1985), an electron density of 100 cm^{-3} , an electron temperature of $1.5 \times 10^4 \text{ K}$, and the interstellar extinction curve of Miller & Mathews (1972). The resultant reddening was remarkably uniform across most of the galaxies with several exceptions. A rapid rise is observed toward the starburst region in M 82 and to a lesser degree in NGC 3077 and NGC 5253. A shallow gradient, corresponding to change in $c(\text{H}\beta) \sim 1.0 \text{ mag}$, was observed across the minor axis outflows in NGC 1569 and M 82 and is consistent with the southern side of the outflow being on the near side of the galactic disk in both cases.

This method has two limitations. The errors become large where the H β emission

equivalent width is small relative to the $H\beta$ absorption equivalent width, and the true absorption equivalent width may be larger than 2 \AA for some galaxies. For example, the spectral synthesis calculations of Olofsson (1995) predict $ew(abs) \sim 1.5 - 6.5 \text{ \AA}$ and those of Diaz (1988) have $ew(abs) \sim 7 - 15 \text{ \AA}$. Since the absorption equivalent widths of $H\gamma$, $H\beta$, and $H\alpha$ are typically within 1 \AA of each other in these calculations, the values of both $c(H\beta)$ and $ew(abs)$ can, in principle, be derived from the $H\gamma / H\beta$ and $H\alpha / H\beta$ ratios. I applied this second method to the higher S/N spectra from the HII region apertures. The uncertainties from this method are difficult to quantify. Systematic errors from the focus variations, the subtraction of the night sky line Hg I $\lambda 4358$ from the broad absorption wings of $H\gamma$, or a contribution from collisional excitation could lead to spurious results. Table 2.4 shows that the reddening derived this way is generally consistent with the average value derived from the smaller apertures. When a slit position crossed a prominent HII region, I generally adopted the solution for $c(H\beta)$ in the HII region to correct the line ratios all along that slit for reddening. The variation in $c(H\beta)$ along the slit was taken into account, however, in M 82 and NGC 1569. At the remaining positions, I used the average $c(H\beta)$ along the slit to correct all the extracted spectra. The uncertainty in the reddening, $\delta c(H\beta)$, was set equal to the magnitude of the variations in $c(H\beta)$ along the slit or the uncertainty in $c(H\beta)$ at a typical position, whichever was larger.

2.3. The HII Region Excitation Sequence

Since the physical boundary between the HII regions and the DIG is not well-defined, the natural starting point for interpreting the spectral signature of the DIG are the spectra of the giant HII regions in the same sample of galaxies. Figures 2.2, 2.3, and 2.4 show the excitation sequence defined by

the HII-regions in my sample as projected into the $[\text{NII}] \lambda 6583 / \text{H}\alpha$ vs $[\text{OII}]\lambda\lambda 3727 / [\text{OIII}]\lambda 5007$, $[\text{OIII}]\lambda 5007 / \text{H}\beta$ vs $[\text{SII}]\lambda\lambda 6717, 31 / \text{H}\alpha$, and $[\text{OI}]\lambda 6300 / \text{H}\alpha$ vs $[\text{OII}]\lambda\lambda 3727 / [\text{OIII}]\lambda 5007$ planes. This section examines whether the physical properties of the HII regions in these dwarfs are any different from the well-studied HII regions residing in the disks of spiral galaxies. This analysis also serves to introduce the tools needed to discuss the physical properties of the DIG in § 2.4. Since the general HII-region sequence is understood in terms of an excitation sequence driven primarily by the oxygen abundance and its role in regulating the nebula's temperature (Aller 1942; Searle 1971; McCall, Rybski, & Shields 1985; Dopita & Evans 1985), I begin the section by deriving the O/H abundance ratio in my sample of HII regions. Calculations of the spectrum emerging from a photoionized nebula are then introduced as tools for deriving secondary properties of the ionized gas.

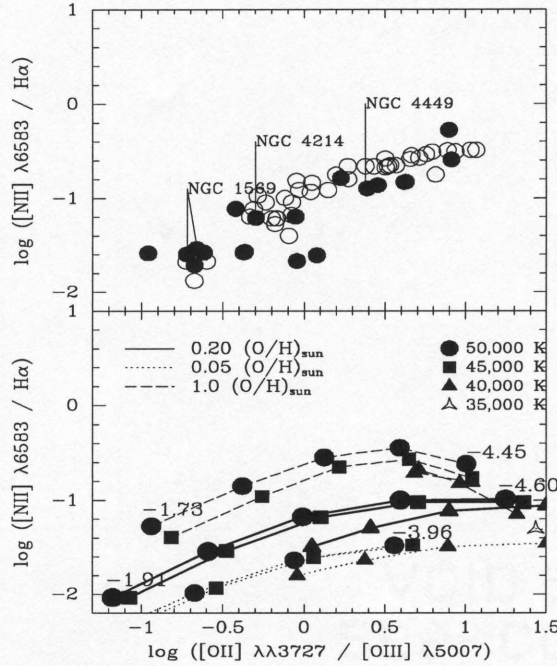


Figure 2.2 HII region excitation sequence projected into $[\text{NII}] \lambda 6583 / \text{H}\alpha$ vs $[\text{OII}] \lambda \lambda 3727 / [\text{OIII}] \lambda 5007$ plane. (a) Reddening-corrected data for the HII regions in the dwarf galaxy sample are represented by solid points, and measurements from Kennicutt & Garnett (1996) for HII regions in M 101 are shown by open symbols. (b) Results from photoionization models. Line ratios of model nebulae. Lines follow an ionization parameter sequence from left to right. The triangles mark multiplicative increments of 4.7 in $U(\text{sp})$ from $10^{-1.91}$ to $10^{-4.60}$. The shift between lines of the same style illustrate a softening of the ionizing radiation field. Nebulae ionized by Kurucz model atmospheres of $T_{\text{ion}} = 50,000, 45,000, 40,000$ K are shown; and the 35,000 K model lies beyond the empirical loci in all but the $[\text{OI}] \lambda 6300 / \text{H}\alpha$ vs $[\text{OII}] \lambda \lambda 3727 / [\text{OIII}] \lambda 5007$ diagram. Solid lines denote models with $\text{O}/\text{H} = 0.20 (\text{O}/\text{H})_{\odot}$; and the dotted and dashed tracks represent extremely metal poor ($\text{O}/\text{H} = 0.05 (\text{O}/\text{H})_{\odot}$) and metal rich ($\text{O}/\text{H} = (\text{O}/\text{H})_{\odot}$) HII regions, respectively.

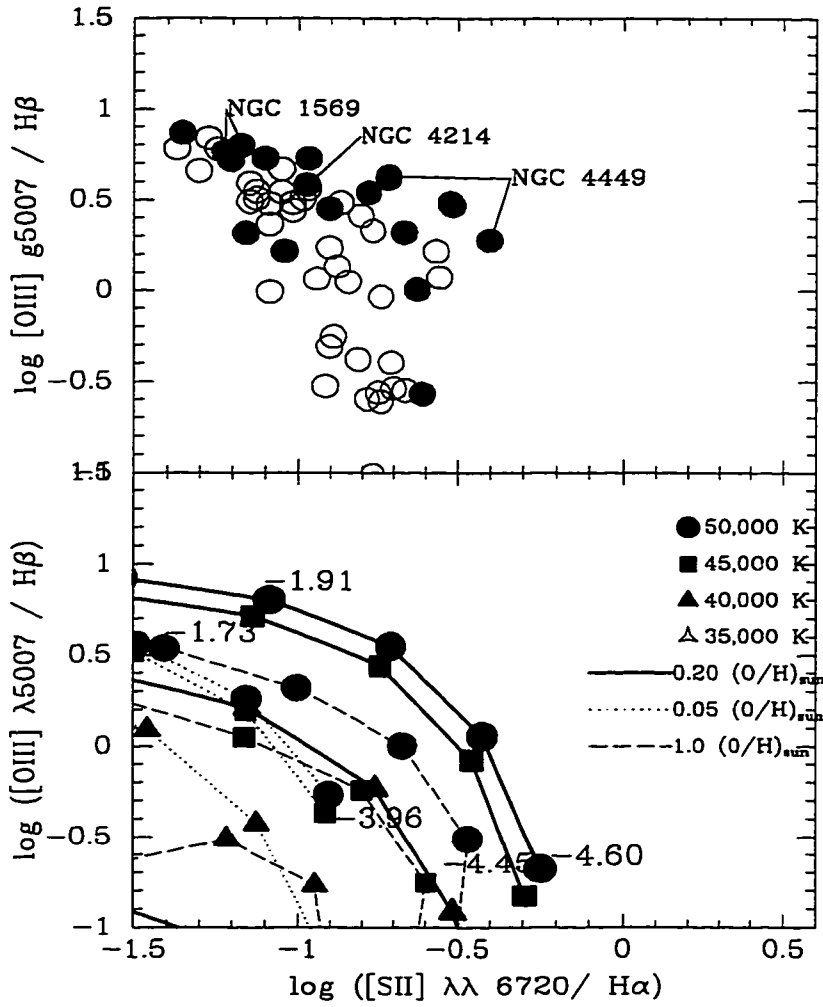


Figure 2.3 (a,b) HII region excitation sequence projected into $[\text{OIII}]\lambda 5007 / \text{H}\beta$ vs $[\text{SII}]\lambda\lambda 6717, 31 / \text{H}\alpha$ plane. Symbols have the same meaning as in Figure 2.2.

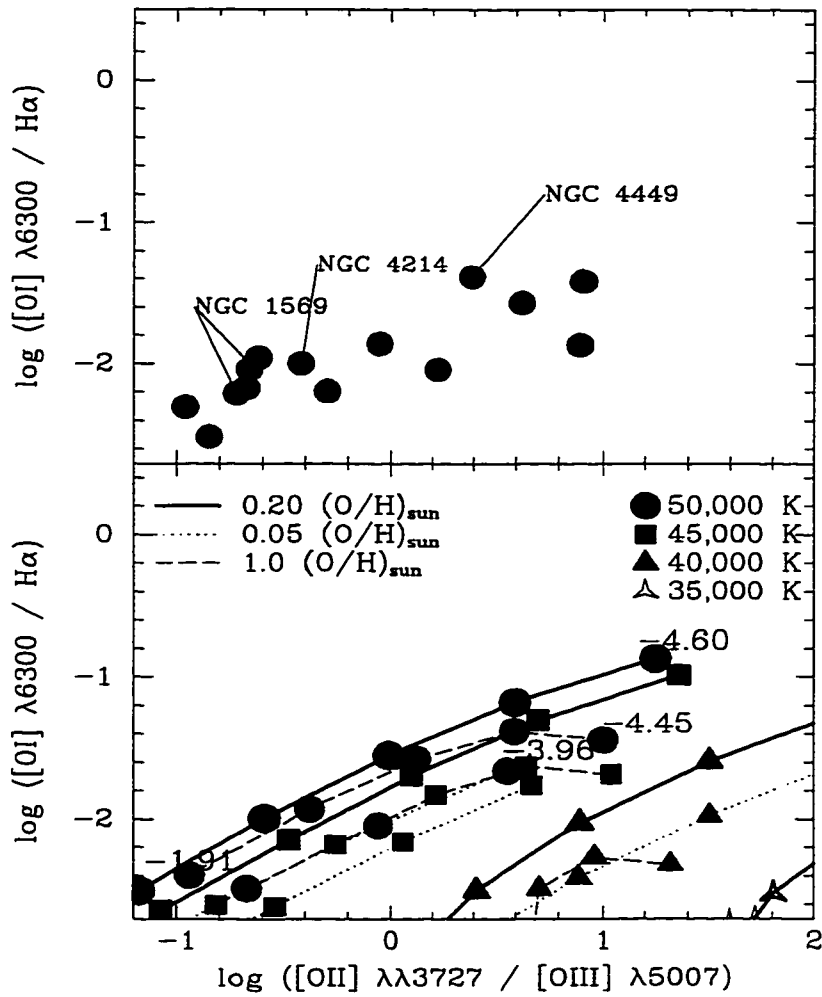


Figure 2.4 (a,b) HII-region excitation sequence projected into $[\text{OI}]\lambda 6300 / \text{H}\alpha$ vs $[\text{OII}]\lambda\lambda 3727 / [\text{OIII}]\lambda 5007$ plane. Symbols have the same meaning as in Figure 2.2.

2.3.1. O/H Abundances Ratios

Table 2.5 lists the O/H abundance ratio derived from each spectrum with an [OIII] $\lambda 4363$ detection. The electron temperature in the O^{++} zone was derived from the [OIII] $\lambda\lambda 4959 + 5007$ to $\lambda 4363$ ratio (Osterbrock 1989). For all galaxies except I Zw 18 (Martin 1996), the electron temperature in the O^+ zone was estimated from $T_e(O^{++})$ using a relationship defined by Campbell, Terlevich, and Melnick (1986) from the photoionization models of Stasinska (1982). Ionic abundances, O^+/H and O^{++}/H , were then calculated assuming an electron density of 100 cm^{-3} (De Robertis, Dufour, & Hunt 1987; Shaw & Dufour 1995). The average total O/H abundances for each galaxy in col. 2 of Table 2.5 show good agreement with the previously published measurements in col. 3. Most of the galaxies have gas-phase oxygen abundances between 10% and 25% solar. Three galaxies – I Zw 18, VII Zw 403, and Sex A – are notoriously more metal-poor. The four galaxies without an [OIII] $\lambda 4363$ detection are most likely more metal-rich based on the strength of [NII] $\lambda 6584$; empirical estimates of O/H allow values as high as solar (e.g. Pagel et al. 1979).

2.3.2. Photoionization Models

In addition to abundance, the shape of the Lyman continuum and the ionization parameter must be specified to describe the spectrum of an ionization-bounded HII region. I calculated three sets of model nebulae with CLOUDY (Ferland 1993) to provide a grid of spectra for estimating the physical properties of the HII regions. All models assume an isotropic, homogeneous distribution of clouds fills a fraction ϵ of the volume around a hot star of temperature T_{ion} . In terms of the Stromgren radius, $R_S = (3Q/4\pi\alpha_B n^2 \epsilon)^{1/3}$, the nebular ionization parameter is then defined by

$$U \equiv \frac{Q}{(4\pi R_S^2 n c)},$$

where n is the density of the clouds and Q represents the luminosity of hydrogen ionizing photons. The first set of models has solar composition (Grevesse & Anders 1989), while the second and third sets have abundance ratios appropriate for dwarfs. Specifically, the oxygen to hydrogen abundance was reduced to 20% $(\text{O}/\text{H})_{\odot}$ and 5% $(\text{O}/\text{H})_{\odot}$; the nitrogen to oxygen abundance ratio, $\log(N/\text{O}) = -1.5$ (Garnett 1990), reflects the secondary production of N; the carbon to oxygen ratio was set according to the empirical results of Garnett et al. (1995); and the other elements scale with the oxygen abundance. The line intensity ratios of the model nebulae are shown in Figures 2.2b, 2.3b, 2.4b.

2.3.3. Physical Properties Underlying the Excitation Sequence

Kennicutt & Garnett (1996, KG96) have shown that the HII region sequence in M 101 is indistinguishable from the general excitation sequence of HII regions in nearby galaxies (e.g. McCall, Rybski, & Shields (1985, MRS); Osterbrock, Tran, & Veilleux 1992). I compare my sample to the former in Figure 2.2 and Figure 2.3. My sample is indistinguishable from the M 101 HII regions in the $[\text{NII}] \lambda 6583 / \text{H}\alpha$ vs

$[\text{OII}]\lambda\lambda 3727 / [\text{OIII}]\lambda 5007$ plane. The differences in the $[\text{OIII}]\lambda 5007 / \text{H}\beta$ vs $[\text{SII}]\lambda\lambda 6717, 31 / \text{H}\alpha$ plane are at least partly a metallicity effect. Most of the HII regions in the dwarfs are 5% - 25% $(\text{O}/\text{H})_{\odot}$, but only 2 giant HII regions – accounting for 6 spectra – in KG96 have $\text{O}/\text{H} < 25\% (\text{O}/\text{H})_{\odot}$. The locus defined by the models curves over at high metallicity. The 4 galaxies (5 HII region spectra) without $\lambda 4363$ detections all lie to the right of $\log[\text{SII}]\lambda\lambda 6717, 31 / \text{H}\alpha = -0.70$ in Figure 2.3 placing them closer to the majority of the M 101 HII regions. The highest $[\text{SII}]\lambda\lambda 6717, 31 / \text{H}\alpha$ point, however, is from NGC 4449. Overall, the HII regions in M 101 cover a larger range in O/H and reach higher metallicity, $\max(\text{O}/\text{H}) = 1.66 - 3.7 (\text{O}/\text{H})_{\odot}$, where the range comes from the empirical calibrations of the bright-line method by Dopita & Evans or MRS (Figure 11 of KG96).

A second parameter in addition to O/H is required to explain the dwarf galaxy excitation sequence. In all 3 BPT diagrams, the wide separation of the nearly equal metallicity HII regions in the Magellanic irregulars NGC 1569, NGC 4214, and NGC 4449 illustrates this fact rather dramatically. Alternatively, comparison of the models at 5% $(\text{O}/\text{H})_{\odot}$ to those at solar having the identical U and T_{ion} reveals a shift in the BPT diagrams considerably less than the spread in the data.

Inspection of the models in Figure 2.2b shows that the two decade range of $[\text{OII}]\lambda\lambda 3727 / [\text{OIII}]\lambda 5007$ could be driven by either a decrease in ionization parameter from $U = 10^{-2.1}$ to $10^{-4.3}$ at $T_{\text{ion}} \gtrsim 45,000$ K or a decrease in T_{ion} from $\sim 45,000$ K to a temperature between 35,000 K and 40,000 K at constant $U \approx 10^{-2.1}$. Fortunately, the locus in the $[\text{OIII}]\lambda 5007 / \text{H}\beta$ vs $[\text{SII}]\lambda\lambda 6717, 31 / \text{H}\alpha$ plane can resolve this ambiguity since gradients in T_{ion} are nearly perpendicular to gradients in the ionization parameter (Figure 2.3b). In Figure 2.3a, the variation in $[\text{SII}]\lambda\lambda 6717, 31 / \text{H}\alpha$ exhibited by the data can be explained by a change in

ionization parameter from $10^{-2.4}$ to $10^{-3.7}$. The same change in U , $U = 10^{-2.4}$ to $U = 10^{-3.6}$, describes the HII region sequence in the $[\text{OI}]\lambda 6300 / \text{H}\alpha$ vs $[\text{OII}]\lambda\lambda 3727 / [\text{OIII}]\lambda 5007$ diagram well. Since this is slightly smaller than the range of U required to explain the large spread in $[\text{OII}]\lambda\lambda 3727 / [\text{OIII}]\lambda 5007$ in the $[\text{NII}]\lambda 6583 / \text{H}\alpha$ vs $[\text{OII}]\lambda\lambda 3727 / [\text{OIII}]\lambda 5007$ plane, the sequence must result at least partly from a variation in T_{ion} among the HII regions.

Some variation in ionization parameter among the HII regions in my sample is required. The minimum T_{ion} consistent with the high $[\text{OIII}]\lambda 5007 / \text{H}\beta$ values of the low-abundance HII regions in Figure 2.3 is $\approx 45,000$ K. For the three Im's mentioned above, Martin & Kennicutt (1996) reach similar conclusions based on the ionization state of He. One can see in Figure 2.2a, that reducing the stellar temperature of a model from 55,000 K to 45,000 K will only account for about half of the measured $[\text{OII}]\lambda\lambda 3727 / [\text{OIII}]\lambda 5007$ range. The necessary variation in U is about a factor of 16. If the high and low metallicity HII regions contain stars in the same mass range, then a decrease in $T_{\text{ion}} \lesssim 3000$ K is expected just from the increase in abundance (cf. Figure 1 of McGaugh 1991, which is based on Maeder 1990). This minimum temperature shift combined with an ionization parameter that varies over a factor of 16 is sufficient to account for the observed range of $[\text{OII}]\lambda\lambda 3727 / [\text{OIII}]\lambda 5007$.

Any correlation between U and O/H among the HII regions is evidently weak. For example, NGC 1569, NGC 4214, and NGC 4449 have a similar oxygen abundance; but the ionization parameter is $\sim 10^{-2.4}$ in NGC 1569, decreases to $10^{-3.6}$ in NGC 4449, and is intermediate to these values in the NGC 4214 HII regions. The low $[\text{OII}]\lambda\lambda 3727 / [\text{OIII}]\lambda 5007$ (and high U) in NGC 1569 is more "normal" in the sense that NGC 1569 fits the $[\text{OII}]\lambda\lambda 3727 / [\text{OIII}]\lambda 5007$ vs R_{23} relation defined by M 101 HII regions (which cover a larger metallicity range) (cf.

Figure 6a of Kennicutt & Garnett 1996).

The physical conditions in the HII regions residing in my sample of galaxies appear to be indistinguishable from those residing in M 101, aside from the larger range in oxygen abundance and T_{ion} in the latter. Among the 6 HII regions with $O/H \lesssim 0.25 (O/H)_{\odot}$ measured by KG96 in M 101 the variation in ionization parameter estimated from $[\text{SII}] / [\text{SIII}]$ is quite similar – $U = 10^{-1.8}$ to $10^{-3.1}$. KG96 use the radiation hardness parameter of Vilchez & Pagel to show T_{ion} varies from 35,000 K to 60,000 K across M 101; however, within NGC 5471 the variation is only 45,000 K to 60,000 K – equivalent to the giant HII regions in my sample. Hence, the O/H , U , and T_{ion} in the HII regions of the dwarfs are not unusual and provide a starting point for describing the physical properties of the DIG in the same systems.

2.4. The HII Region - DIG Spectral Transition

In this section the spatial variations in the emission-line spectrum are explored using the line intensities measured from the sequence of small aperture spectra. I discuss whether the line ratios can be produced by dilute photoionization models and whether the inferred parameters of such models are consistent with the morphology and stellar content of the galaxies. Where stellar photoionization proves inadequate, I investigate the contribution of other excitation mechanisms to the spectrum.

2.4.1. The Empirical Spectral Transition

The spectrum of the diffuse emission-line gas in all the dwarfs is characterized by strong lines of low ionization species of O, N, and S relative to the spectrum of giant HII regions in the same galaxy. The intensity ratios $[\text{SII}]\lambda\lambda 6717, 31 / \text{H}\alpha$ and $[\text{OII}]\lambda\lambda 3727 / [\text{OIII}]\lambda 5007$ typically reach values 1.0 dex higher than in the HII

regions while $[\text{NII}]\lambda 6583 / \text{H}\alpha$ increases by 0.5 dex and $[\text{OIII}]\lambda 5007 / \text{H}\beta$ decreases by 0.5 dex. The $[\text{OI}]\lambda 6300 / \text{H}\alpha$ ratio is also higher than measured in the HII regions. Since the galaxies sample a substantial range in metallicity (§ 2.3), it is not surprising that the absolute value of the line ratios of the DIG vary considerably.

Figure 2.5 demonstrates that the spectrum changes gradually from the HII complexes to the DIG. In galaxies with a single, dominant star-forming complex, this narrow spectral sequence corresponds directly to a gradient with respect to distance from the starburst region. However, in some of the galaxies, the large number of HII regions spread throughout the galaxy makes it difficult to identify which cluster dominates the ionization of a particular patch of DIG. It is perhaps surprising that within a single galaxy this general intervening medium is not characterized by a single emission-line spectrum. Rather the spectral signature across a galaxy correlates very strongly with the $\text{H}\alpha$ surface brightness regardless of whether the variations in surface brightness correspond to an HII region or a bright filament intersecting the slit. Hence the sequence of transition spectra is best correlated with $\text{H}\alpha$ surface brightness from an observational standpoint although distance from the ionizing cluster is probably the fundamental parameter for any physical interpretation.

The sequence of emission-line spectra for each galaxy forms a relatively narrow track in the line-ratio diagrams typically used to distinguish objects with different excitation mechanisms. The transition from HII regions (low $[\text{OII}]\lambda\lambda 3727 / [\text{OIII}]\lambda 5007$) to DIG (high $[\text{OII}]\lambda\lambda 3727 / [\text{OIII}]\lambda 5007$) is illustrated in the $[\text{NII}]\lambda 6583 / \text{H}\alpha$ vs $[\text{OII}]\lambda\lambda 3727 / [\text{OIII}]\lambda 5007$ plane in Figure 2.6. The tracks for many of the galaxies are almost indistinguishable from the HII region locus. The transition sequences across NGC 5253 and II Zw 40 are noticeably flatter than the HII-region sequence (cf. M101 sequence). NGC 2537

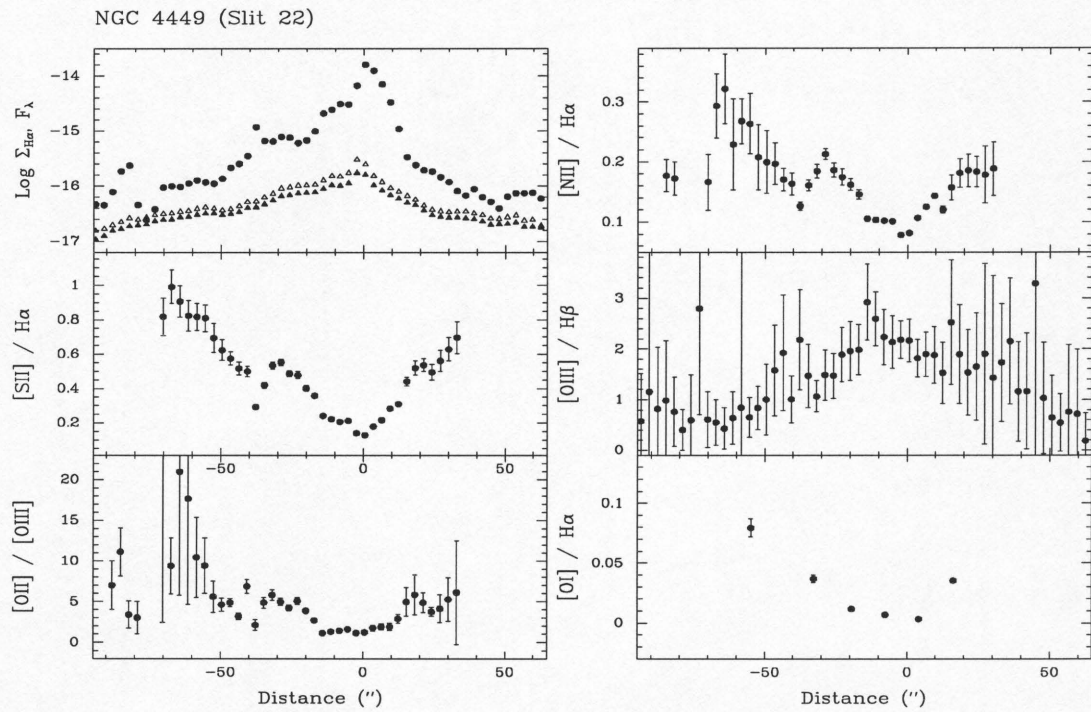


Figure 2.5 Dependence of line ratios on distance from the nearest HII complex. (a) Cut across NGC 4449 (position 22). (b) Cut along minor-axis of NGC 4861 (position 4).

Table 2.3 Optical Spectroscopy

Date	Photometric Conditions ?	Flux Calibration (mag)	Distortion Correction ?	Notes
Dec 17, 1993	Clouds	n/a	n	
Dec 18, 1993	Clouds	n/a	n	
Feb 3, 1994	Clouds	0.05	n	Wave cal. twice; Standards agree to 5%; 2 Stand.
Feb 4, 1994	PC	0.05	n	Wave cal. twice; Standards agree to 5%
Feb 5, 1994	n	0.03 (max)	n	Wave cal. twice; Re-reduced in Aug95
May 10, 1994	Snow	0.03	n	Wave cal. each
May 11, 1994	Rain	n/a	n	Wave cal. each
Jun 8, 1994	y	0.06 (rms)	n	Wave cal. each
Nov 26, 1994	Fog	n/a	y	
Nov 27, 1994	y	0.02 (max)	y	Wave cal. 4 times
Jan 30, 1995	n	0.01 (rms)	y	Wave cal. each
Mar 25, 1995	n	0.02 (rms)	y	Wave cal. each
Mar 26, 1995	y	0.02 (rms)	y	Wave cal. each

Note. — Observations obtained with the Multiple Mirror Telescope.

Figure 2.5 (b): NGC 4861 (Slit 4)

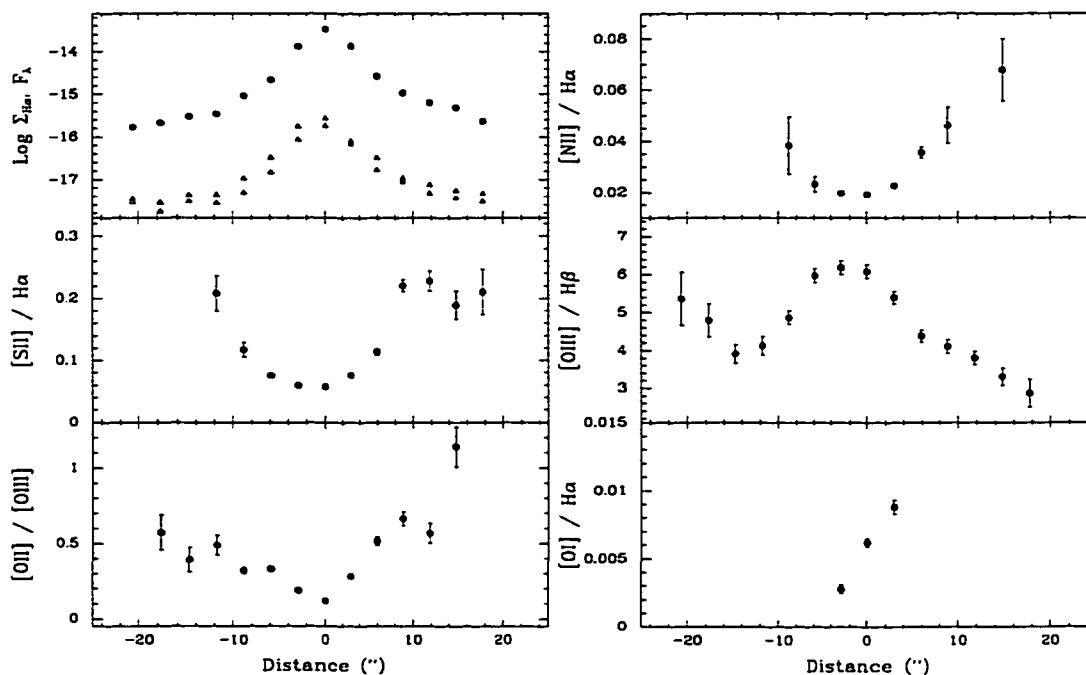


Table 2.4 Reddening Estimates

Galaxy	Position	$c(H\beta)$ Estimate along Slit	HII Aperture $c(H\beta)$ and $ew(abc)$	$c(H\beta)$ Adopted
NGC 1569	1		1.06, 2.0 Å	1.0(SW) to 1.4(NE)
	2	0.88 ± 0.04	0.83, 4.3 Å	0.4(SE) to 1.0(NW)
	3	0.90 ± 0.06	0.90, 2.1 Å	0.7(E) to 1.0(W)
	8	0.9 ± 0.1	...	0.9 ± 0.1
	9		...	0.6(S) to 1.0(N)
NGC 1800	2	0.98 ± 0.57	0.23, 6.5 Å	1 ± 1
II Zw 40	2	1.11 ± 0.05	1.17, -8.7 Å	1.1 ± 0.4
NGC 2363	1	-0.1 ± 0.04	-0.12, 15 Å	0.1 ± 0.1
NGC 2537	1	0.04 ± 0.10	0.40, 2.3 Å	0.3 ± 0.1
	3	0.3 ± 0.1	...	0.3 ± 0.1
I Zw 18	1	-0.1 ± 0.04	-0.09, 0.82 Å	0 ± 0.1
M82	2	2.0 ± 0.1	2.0, 1.78 Å	0.5 to 4.0
	5	0.4 ± 0.1	...	0.4 ± 0.1
NGC 3077	2	1.3 ± 0.4	0.74, 6.3 Å	0.8 ± 0.8
Sex A	3	0.0 ± 0.05	-0.02, 3.8 Å	0.0 ± 0.1
VII Zw 403	2	0.06 ± 0.04	0.06, 1.6 Å	0.1 ± 0.1
NGC 3738	4	0.20 ± 0.06	0.15, 4.2 Å	0.5 ± 0.5
	2	0.5 ± 0.5	...	0.5 ± 0.5
NGC 4214	3	0.09 ± 0.06	0.07, 2.7 Å	0.16 ± 0.1
	1	0.2 ± 0.2	...	0.2 ± 0.2
NGC 4449	20	0.05 ± 0.08	-0.06, 5.9 Å	0.05 ± 0.05
	22	0.3 ± 0.3	...	0.3 ± 0.3
	2	0.1 ± 0.1	...	0.1 ± 0.1
	3	0.8 ± 0.8	...	0.8 ± 0.8
NGC 4861	6	0.05 ± 0.04	0.044, 3.0 Å	-0.05 (SW) to 0.3 (NE)
	4	0.07 ± 0.07	...	0.07 ± 0.07
NGC 5253	8	0.23 ± 0.04	0.213, 4.6 Å	0.4 ± 0.4

Note - The symbol $c(H\beta)$ denotes the logarithmic extinction at $H\beta$. See text for details.

Table 2.5 O/H Abundance Ratios

Galaxy	Number of Observations	$\log(O/H)$	$\overline{\log(O/H)}$	References
NGC 1569	3	-3.78 (0.07)	-3.81 (0.10)	1, 3, 5, 10
NGC 1800	0	...		
II Zw 40	3	-3.88 (0.05)	-3.81 (0.07)	6, 7
NGC 2363	2	-4.06 (0.01)	-4.06 (0.04)	1, 5, 10
NGC 2537	0	...		
I Zw 18	1	-4.80 (0.1)	-4.80 (0.05)	3, 7
NGC 3034	0	...		
NGC 3077	0	...		
Sex A	1	-4.22 (0.10)	-4.51 (0.20)	5
VII Zw 403	1	-4.42 (0.06)	-4.21 (0.05)	2, 4
NGC 3738	2	-3.77 (0.01)		
NGC 4214	3	-3.78 (0.07)	-3.65 (0.08)	1, 5
NGC 4449	2	-3.69 (0.07)	-3.69 (0.05)	5
NGC 4861	3	-4.01 (0.02)	-3.95 (0.03)	8
NGC 5253	1	-3.77 (0.01)	-3.83 (0.11)	7, 9, 10

KEY TO REFERENCES - (1) Talent (1980); (2) Garnett (1990); (3) Skillman & Kennicutt (1993); (4) Tully et al. (1981); (5) Skillman et al. (1989); (6) Walsh & Roy (1993); (7) Pagel et al. (1992); (8) Dinerstein & Shields (1986); (9) Walsh & Roy (1989); (10) Hunter et al. (1982).

^aThis work.

^bMean of referenced sources. Uncertainty denotes the standard deviation of the mean of measurements included in columns 3 and 4.

and M82 (slit 5) show marked excursions toward the empirical LINER locus. (In NGC 4449 position 20, the two points at high $[\text{NII}] \lambda 6583 / \text{H}\alpha$ and low $[\text{OII}] \lambda \lambda 3727 / [\text{OIII}] \lambda 5007$ are coincident with a prominent supernova remnant.)

The HII-DIG transition sequences depart markedly from the HII region excitation sequence in the $[\text{OIII}] \lambda 5007 / \text{H}\beta$ vs $[\text{SII}] \lambda \lambda 6717, 31 / \text{H}\alpha$ diagrams (Figure 2.7). These tracks progress toward, and in many cases enter, the empirical LINER locus (Heckman 1980). This trend is particularly prominent in the higher abundance galaxies since the tracks start at HII regions with higher $[\text{SII}] \lambda \lambda 6717, 31 / \text{H}\alpha$. Notice that the track following the minor axis outflow of M 82 progresses “backwards” relative to the photoionization sequence (i.e. toward higher ionization parameter and/or lower metallicity). Only a few of the spectra from NGC 4449 lie within the HII locus, but the shape of the track does not appear to be unusual. The transition sequence just starts at high $[\text{SII}] \lambda \lambda 6717, 31 / \text{H}\alpha$ because the HII regions in NGC 4449 have a very low ionization parameter. With the exception of NGC 2363, the tracks in the low abundance galaxies with ionization parameters typical of disk HII regions (e.g. NGC 1569) have a slightly shallower slope than the HII region sequence.

The sequences for NGC 1569 stand out in the $[\text{OI}] \lambda 6300 / \text{H}\alpha$ vs $[\text{OII}] \lambda \lambda 3727 / [\text{OIII}] \lambda 5007$ plane. The tracks traverse the HII locus with a steep gradient in $[\text{OI}] \lambda 6300 / \text{H}\alpha$ relative to $[\text{OII}] \lambda \lambda 3727 / [\text{OIII}] \lambda 5007$ and would cut across a corner of the Seyfert 2 locus on their way toward the LINER locus if extrapolated. Just as was seen in the $[\text{OIII}] \lambda 5007 / \text{H}\beta$ vs $[\text{SII}] \lambda \lambda 6717, 31 / \text{H}\alpha$ plane, the spectral sequence across NGC 4449, NGC 4214, NGC 5253, and NGC 2537 traverses the HII locus straight toward the LINER locus. The sequence along the minor axis of M 82 exhibits the strongest move in this direction and actually reaches the LINER locus. Since all spectral sequences

depicted in Figure 2.8 represent a smaller spatial locus than the previous two figures, the endpoints should not be directly compared.

The only galaxy that stands out in all 3 BPT diagrams is M 82. The spectral progression along the minor axis is almost certainly a transition from stellar excitation near the nucleus to predominantly shocked-excited gas in the galactic wind (HAM). The tracks for M 82 provide an example of the changing spectral signature across the transition region from stellar photoionization to shock excitation of metal-rich gas clouds. The spectral signature of this transition in excitation mechanism is expected, however, to be sensitive to both the metallicity of the gas clouds and the shock velocity. In the next section, I introduce models of several excitation mechanisms to quantitatively address their contribution to the excitation of the DIG.

2.4.2. Photoionization of the DIG by Dilute Stellar Radiation

The Lyman continuum radiation from massive stars is the most obvious power source for the DIG for several reasons. First, the presence of emission and absorption features from Wolf-Rayet stars in the optical and UV spectra of many of these galaxies indicates massive stars have formed recently (Conti 1991). Second, the power requirements of the DIG inferred from the measured H recombination rate are quite large, and models of young stellar populations predict as much as 30% of the bolometric luminosity goes into ionizing radiation while the kinetic energy of supernovae and stellar winds totals only $\sim 3\%$ of L_{Bol} . Thirdly, the transition sequences in Figure 2.6, 2.7, and 2.8 remind one of the series of model nebulae in Figure 2.2, 2.3, 2.4 photoionized by hot stars with progressively lower cloud filling factors. Since massive stars are generally found in associations, the geometrical dilution of their radiation would naturally produce a decline in U with projected distance from the cluster. The aim of this section then is to determine if photoionization alone is sufficient to explain the observed spectral sequence.

Instead of computing the spectra of a sequence of models with different average ionization parameters over the nebula as in § 2.3, one can also calculate the emissivity of any model nebula as a function of projected radius. The average U along the line-of-sight will decrease outward toward the Stromgren radius. The two methods yield similar results for equivalent U . Since the former approach was introduced in § 2.3, I will employ the same set of models in most of the following discussion for consistency. However, since the second approach is conceptually akin to the geometry of the galaxies in this study I will draw attention to some of the subtle differences of the models in the diagnostic-line-ratio planes. For either type of model, the accuracy of the predictions probably declines for extremely low ionization parameter because of the thick transition layer and approximate

treatment of the radiative transport in CLOUDY.

Figure 2.9 shows spectral tracks as a function of projected radius for three spherical nebulae with high, moderate, and low ionization parameter in the $[\text{OIII}]\lambda 5007 / \text{H}\beta$ vs $[\text{SII}]\lambda\lambda 6717, 31 / \text{H}\alpha$ plane and illustrates two points characteristic of the other BPT diagrams. First, the ratios of low ionization lines (e.g. $[\text{SII}]$, $[\text{NII}]$, $[\text{OII}]$, and $[\text{OI}]$) relative to a hydrogen Balmer line saturate as the low ionization zone begins to fill the total nebular volume along the line-of-sight. The extreme values of the line ratios reached by these models are higher than those attained by the sequence of integrated models. Second, the curvature of the projected sequences differs from the integrated sequence. The effect is most apparent in the $[\text{OIII}]\lambda 5007 / \text{H}\beta$ vs $[\text{SII}]\lambda\lambda 6717, 31 / \text{H}\alpha$ plane. The tracks of the high U and low U projection models are flatter and steeper, respectively, than the integrated sequence. The change in slope reflects the changing thickness and structure of the transition from the high ionization zone (i.e. O^{++}) to the low ionization zone (e.g. O^+).

Estimating the Gradient in Ionization Parameter

I have estimated the gradient in U from the spectral change across several of the galaxies. Only slit positions crossing a first-ranked HII region were considered in the analysis. The change in ionization parameter, ΔU , was determined by comparing the observed range of $[\text{SII}]\lambda\lambda 6717, 31 / \text{H}\alpha$ and $[\text{OII}]\lambda\lambda 3727 / [\text{OIII}]\lambda 5007$ ratios (Figure 2.7) to the 20% $(\text{O}/\text{H})_{\odot}$ 45,000 K models in Figure 2.10. In NGC 1569, for example, I used the spectra extracted along slit positions 1 and 2 to estimate the ΔU between the main HII complex and the filaments extending along the minor axis (see $\text{H}\alpha$ images in Chapter 5). Either diagnostic leads me to suggest the ionization parameter varies from $\approx 10^{-2.24}$ to $\approx 10^{-3.24}$, or $\Delta(\log U) \approx 1.0 - 1.3$.

The projected spatial gradient is then, very roughly, $\frac{d \log(U/U_0)}{d \log(R/R_0)} \approx 0.91 - 1.22$, where R/R_0 is the ratio of the spatial region shown in Figure 2.6, 2.7 (~ 790 pc) to that of the aperture for the HII spectrum (~ 60 pc). Table 2.6 summarizes the results for the other galaxies; the estimated $\frac{d \log(U/U_0)}{d \log(R/R_0)}$ varies from 0.5 to 2.0.

These spectral estimates of the gradient in U are consistent with the simple, geometrical dilution of the stellar radiation. An estimate of the ionization parameter gradient based on a galaxy's morphology is necessarily crude because of uncertainties about the distribution hot stars, gas, and dust in the galaxy. Ignoring the attenuation of the ionizing radiation, the ionization parameter will drop as the inverse square of the distance from a point source source, $U = Q/(4\pi r^2 n(r)c)$, in a homogeneous medium. The average U along a line-of-sight. through the nebula will then fall inversely with the projected distance from the center, and it will be less steep if the density declines with distance from the cluster. This R^{-1} dependence is fortuitously close to the estimated gradient in NGC 1569.

Shortcomings of the Photoionization Models

The spectral transition along the major axis of NGC 1569 (slit 3) is also easily parameterized by a decrease in U , and this symmetry in the spectral gradient along the minor and major axes supports the idea that the spherical geometry dilutes the radiation from the starburst. However, the deeper spectra taken at positions S and SW of the main galaxy (positions 8 and 9) exhibit spectral tracks which extend all the way into the LINER locus. The emission along the major axis does not extend to such a low surface brightness, and these extreme line ratios are never reached. Hence, on spatial scales large enough to include the minor axis emission-line excess, I do find a significant difference in the spectral signature along the minor and major axes. Lehnert & Heckman (1996) reached a similar conclusion for a sample

Table 2.6 Gradients in Ionization Parameter

Galaxy Position	$\log(U_0/U)$	$\log(R/R_0)$	α
NGC 1569.1	1.0	1.097	0.91
NGC 1569.2	1.34	1.097	1.22
NGC 4449.3	0.76	1.114	0.68
NGC 4214.1	1.01	1.204	0.84
NGC 5253.8	1.34	0.866	1.55
NGC 4861.4	0.99	0.669	1.48
II Zw 40.2	1.17	0.536	2.18
NGC 2537.3	0.68	0.933	0.729
M82.2	0.7	1.374	0.509
NGC 3077.2	1.02	1.176	0.867

NOTES – Coefficient fit to $U = U_0(R/R_0)^{-\alpha}$, where R is the projected distance from the ionizing cluster.

of edge-on far-infrared galaxies. They demonstrated that spectra offset along the minor and major axes are statistically different, and that the former are more “LINER-like.”

The line-ratios produced by the photoionization models in Figure 2.10 do not cover the entire region spanned by the transition sequences. For example, the sequences for slits 8 and 9 of NGC 1569 have an excess of $[\text{OIII}]\lambda 5007 / \text{H}\beta$ at high $[\text{SII}]\lambda\lambda 6717, 31 / \text{H}\alpha$ compared to even the hottest, low U models. Inspection of Figure 2.7 shows that a similar discrepancy characterizes the transition sequence in NGC 4449, NGC 4214, NGC 5253, and NGC 2537 as well as NGC 3034. The tracks initially follow the series of models obtained by decreasing U but diverge beyond the HII regions. Abundance is not the second parameter because the strength of $[\text{OII}] + [\text{OIII}]$ relative to $\text{H}\beta$ reaches its highest value near $\text{O}/\text{H} \sim (\text{O}/\text{H})_{\odot}$. Hardening the Lyman continuum radiation of the models would move their locus closer to the DIG in the $[\text{OIII}]\lambda 5007 / \text{H}\beta$ vs $[\text{SII}]\lambda\lambda 6717, 31 / \text{H}\alpha$ diagram but is an unlikely solution. I estimate T_{ion} would have to be nearly 100,000 K to produce the extreme line ratios, so even the most massive normal stars are not hot enough. Absorption by diffuse atomic gas along the line-of-sight to the DIG is expected to increase the average energy of an ionizing photon. Using the results from Sokolowski’s (1994) model of the hardening, I estimate the increase in T_{ion} within DIG excited by a 50,000 K star would be less than 20,000 K. An excitation mechanism in addition to stellar photoionization is clearly required.

2.4.3. Additional Excitation Mechanisms

Evidence for Shocks

Shocks are likely the additional excitation mechanism in NGC 1569 since the kinematic evidence for a large-scale outflow is strong (Chapter 5; Heckman

et al. 1995). The second and third rows of Figure 2.10 show the positions of the 100 km s^{-1} and 60 km s^{-1} shock models of Shull & McKee (1979). The positions of the shock models are only approximate since the models are for a cosmic composition. (Unfortunately no set of shock models with abundance ratios appropriate to dwarfs was available.)

Mixing lines constructed from linear combinations of the shock models and HII region models illustrate the spectral transition accompanying an increasing contribution of shock excitation. To reproduce the NGC 1569 tracks in the $[\text{OIII}]\lambda 5007 / \text{H}\beta$ vs $[\text{SII}]\lambda\lambda 6717, 31 / \text{H}\alpha$ plane (and $[\text{NII}]\lambda 6583 / \text{H}\alpha$ vs $[\text{OII}]\lambda\lambda 3727 / [\text{OIII}]\lambda 5007$ and $[\text{OI}]\lambda 6300 / \text{H}\alpha$ vs $[\text{OII}]\lambda\lambda 3727 / [\text{OIII}]\lambda 5007$ planes), the shock speeds would need to lie in the $60\text{--}100 \text{ km s}^{-1}$ range. Shock speeds closer to 100 km s^{-1} are required to fit the sparse data in the $[\text{OI}]\lambda 6300 / \text{H}\alpha$ vs $[\text{OII}]\lambda\lambda 3727 / [\text{OIII}]\lambda 5007$ plane. From the mixing lines I estimate up to 30% of the emission comes from shock-excited gas in the lowest surface brightness regions of NGC 1569.

The evidence for shock excited gas is more dramatic in NGC 4449. This galaxy stands out as having a lot of low surface brightness filamentary emission – “a lot” both in terms of dominating the galaxy morphology and in terms of its contribution to the total $\text{H}\alpha$ luminosity (Kennicutt 1989). The line ratios of most of the DIG spectra fall outside the HII region locus in the $[\text{OIII}]\lambda 5007 / \text{H}\beta$ vs $[\text{SII}]\lambda\lambda 6717, 31 / \text{H}\alpha$ and $[\text{OI}]\lambda 6300 / \text{H}\alpha$ vs $[\text{OII}]\lambda\lambda 3727 / [\text{OIII}]\lambda 5007$ planes, but the mixing lines easily cover the observed locus. Along each slit position one can find a shock velocity between 60 km s^{-1} and 100 km s^{-1} for which the observed transition sequence corresponds directly to a steady increase in the fraction of emission from shock-excited gas. When considered alone, the tracks for NGC 4449 in the $[\text{NII}]\lambda 6583 / \text{H}\alpha$ vs $[\text{OII}]\lambda\lambda 3727 / [\text{OIII}]\lambda 5007$ plane do not require

shocks. However, shock-excitation cannot be ruled out because the mixing lines are contiguous with the HII sequence for some shock velocities between 60 km s^{-1} and 100 km s^{-1} . Also, the position of the shock models is expected to shift considerably in this diagram when a composition appropriate for dwarfs is used in the models – i.e. a low N/O abundance ratios in addition to low O/H. I estimate shock-excited gas clouds contribute as much as 50% of the emission in the lowest surface brightness regions.

The quintessential superwind, starburst galaxy - M82 - also shows unambiguous evidence for shock excitation. The strong contrast in track morphology reflects the roughly solar metallicity. Note the difference in direction for the fairly metal-rich neighbor, NGC 3077. Either the shocks in NGC 3077 are slower, the metallicity drops with R , or the spectrum hardens considerably.

The contribution in the other galaxies is smaller. Moderate velocity shocks and dilute photoionization cannot be distinguished by my data for low abundance, normal U galaxies.

Contributions from Turbulent Mixing Layers?

Radiation from turbulent mixing layers (TML; Begelman & Fabian 1990) is apparently not a prominent component of the optical spectrum of the DIG in these galaxies. The intensity of a single mixing layer is proportional to the gas pressure (Slavin, Shull, & Begelman 1993). Assuming the ISM is nearly isobaric, any surface brightness variations would simply reflect the number of mixing layers along the line-of-sight. and should not be correlated in any way with variations in the spectral signature. Since we observe a tight correlation between line ratios and surface brightness within any galaxy, the contribution of mixing layers to the spectrum is at most a secondary effect. Spectra of turbulent mixing layers

are difficult to distinguish from shock-excited gas – especially when neither set of models are tuned to the appropriate abundance. The two processes are best distinguished by their $[\text{OI}]\lambda 6300 / \text{H}\alpha$ ratios; Figure 6 of SSB shows that the $[\text{OI}]\lambda 6300 / \text{H}\alpha$ ratio of TML models is about a dex lower than shock models in the $30 \text{ km s}^{-1} - 100 \text{ km s}^{-1}$ range. In Figure 2.11, the data clearly exhibit $[\text{OI}]\lambda 6300 / \text{H}\alpha$ ratios higher than the TML models. The spectra of the TML models is most sensitive to the temperature of the intermediate temperature gas in the mixing layer. One can also see in Figure 2.11 that the sequence of TML models with $\log T \approx 5.5, 5.3, 5.0$ has a much shallower slope than the transition sequence in NGC 4449, NGC 1569, or NGC 3034. The TML models offer no advantage over shock models in the other two diagnostic planes discussed in this paper.

2.5. Summary

The formation and evolution of galaxies is strongly influenced by the impact of massive stars on the ISM. Much of the transfer of radiative and mechanical energy from stars to the ISM occurs through the warm and hot phases of the ISM. Our physical understanding of this important process is challenged by the complex topology of a multi-phase ISM. In this paper, I have presented new measurements of fundamental physical properties of the warm ionized gas derived from a large collection of optical spectra.

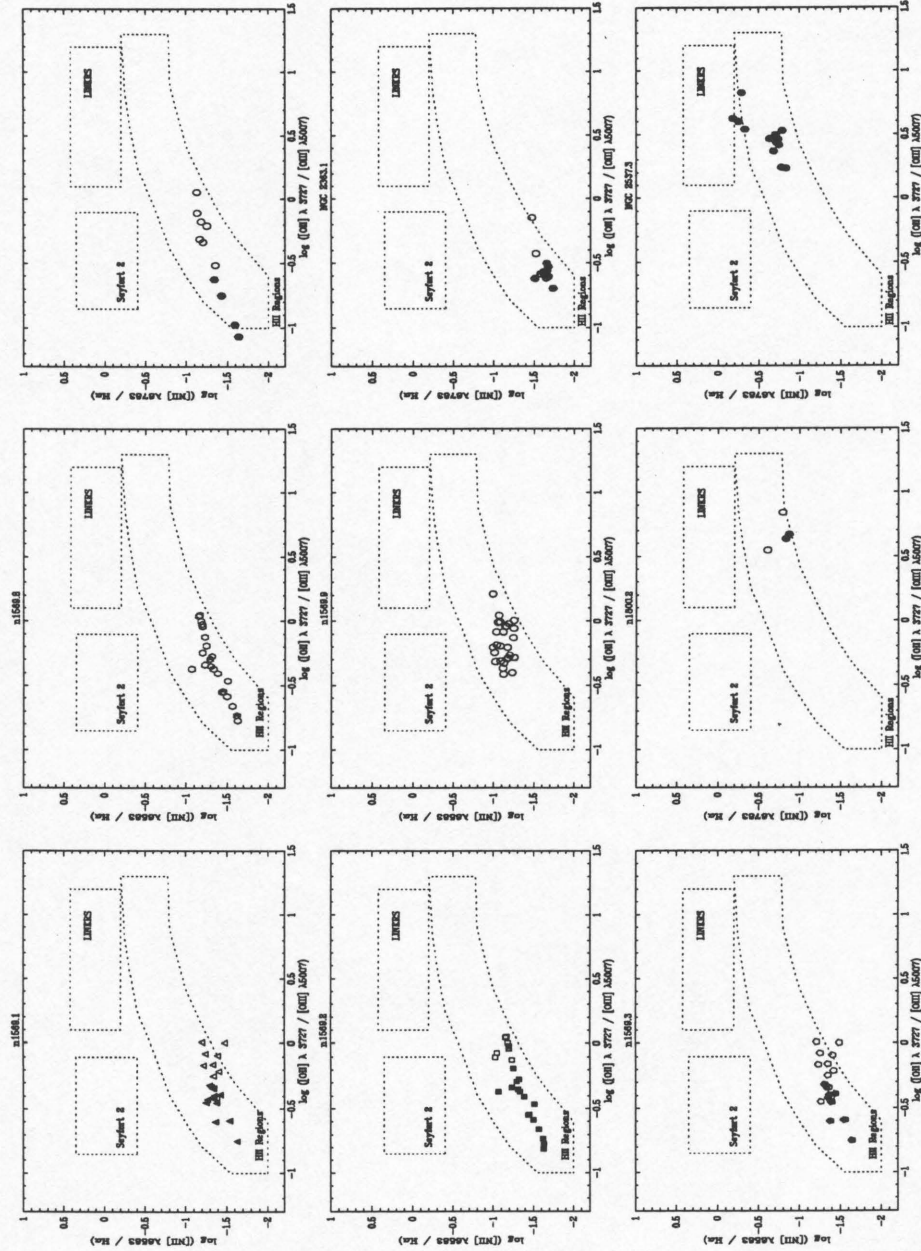
Previous spectroscopic studies of the DIG have emphasized the contrast of its spectral signature to that of HII regions and concluded photoionization was most likely the dominant excitation mechanism (Mathis 1986; Hunter & Gallagher 1990; Domgörgen & Mathis 1994; Golla, Dettmar, & Domgörgen 1996). This paper is among the first to demonstrate the gradual transition in the spectrum between HII regions and the DIG. The idea of a spectral “transition sequence” was

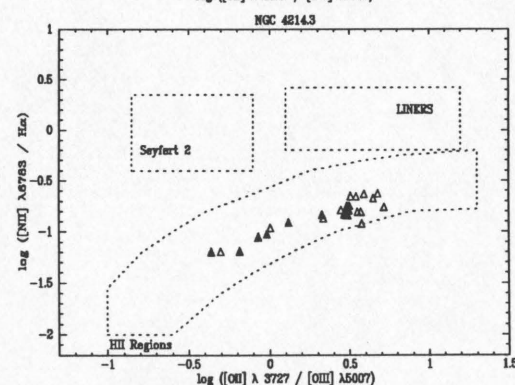
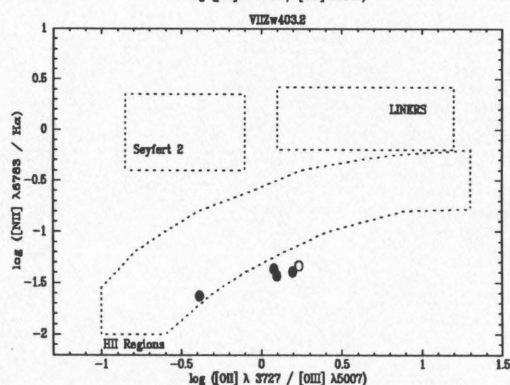
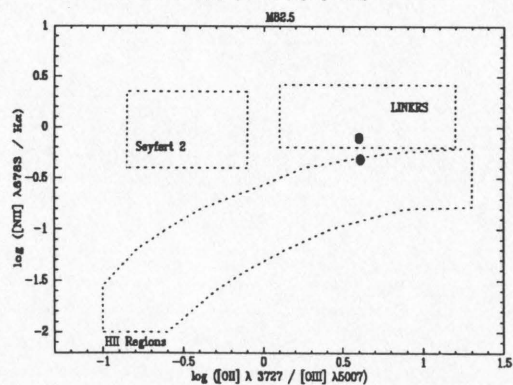
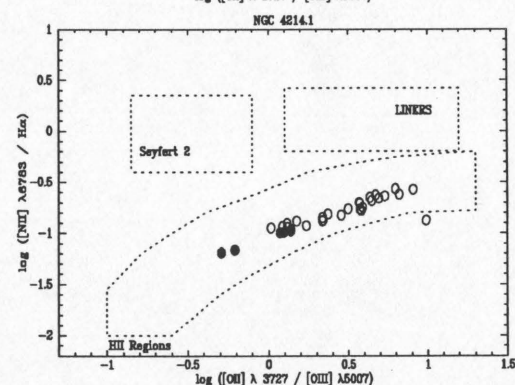
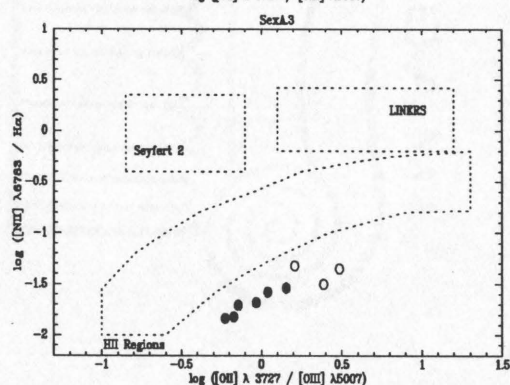
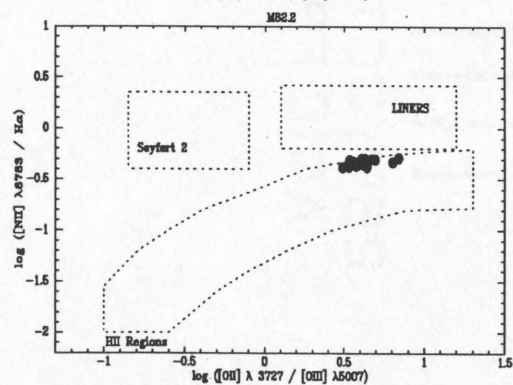
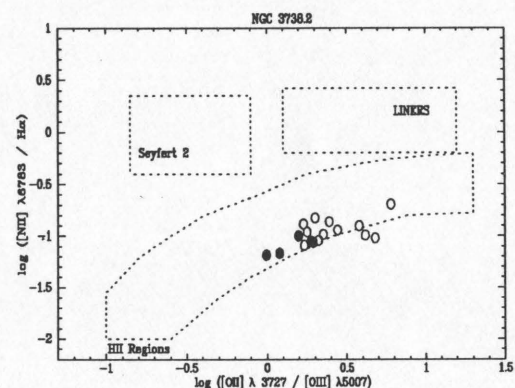
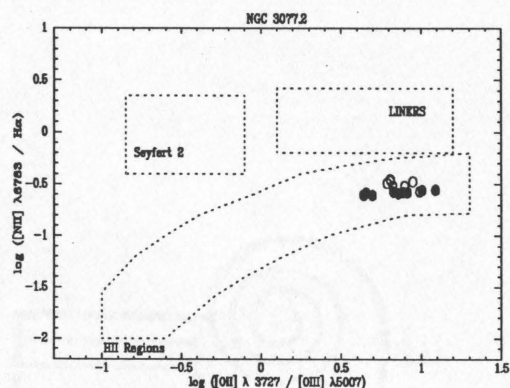
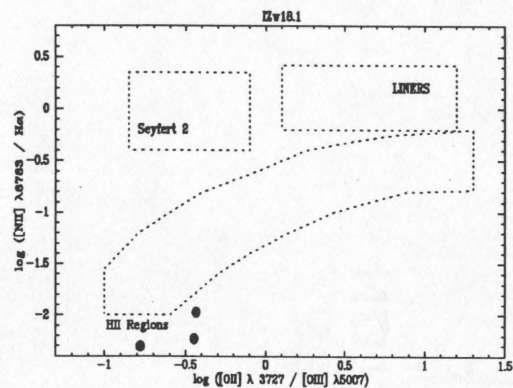
introduced to investigate the changing physical properties. I quantitatively showed how well simple geometrical dilution of the radiation from a star cluster produces the spectral change. In contrast to the HII region excitation sequence, ionization parameter rather than metallicity is the fundamental parameter. It was shown that the relatively high $[\text{OI}]\lambda 6300 / \text{H}\alpha$ and $[\text{OIII}]\lambda 5007 / \text{H}\beta$ from the lowest surface brightness regions provides the first unambiguous spectral evidence that shocks contribute to the excitation of the DIG. This is important since it confirms that the power requirements of the DIG tap the stars' kinetic as well as radiative energy.

In some extreme objects like NGC 4449, the emission from the shocked gas will have a noticeable influence on the integrated spectrum of the galaxy.

The homogeneous set of spectra for 14 star-forming galaxies sampling a factor ~ 50 in O/H abundance and a variety of morphological types provides an unprecedented opportunity to examine the variation of the DIG's spectral signature in different environments. Although the nature of the spectral transition is similar in each galaxy, the absolute values of the line ratios are sensitive to metallicity – as might be expected but not heretofore demonstrated. The spectral signature is also sensitive to the ionization parameter of the “parent” HII regions. This result indicates the physical properties in the DIG reflect the structure in the HII regions.

Figure 2.6 The HII-DIG transition sequence projected onto the $[\text{NII}] \lambda 6583 / \text{H}\alpha$ vs $[\text{OII}] \lambda \lambda 3727 / [\text{OIII}] \lambda 5007$ plane. The solid and open symbols in Figures 2.6, 2.7, and 2.8 denote regions within and outside HII regions respectively. Empirical loci for three classes of excitation mechanisms are from Shields & Filippenko (1990) and are based on data presented by Veilleux & Osterbrock (1987) and Baldwin, Phillips, & Terlevich (1981).





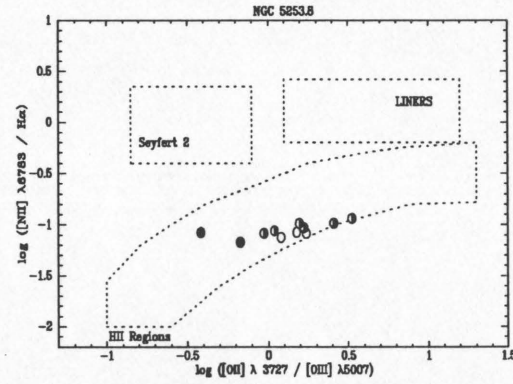
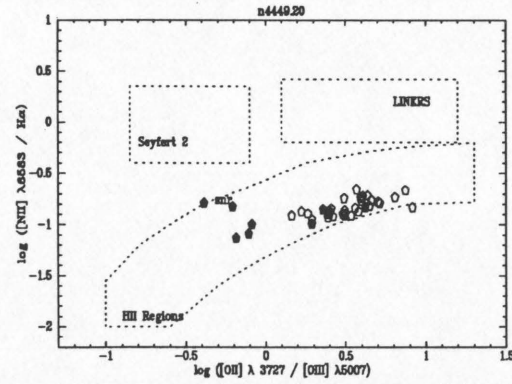
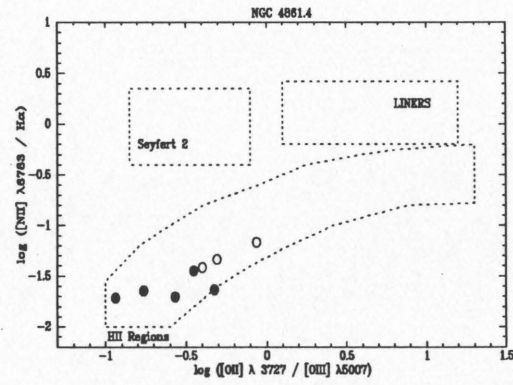
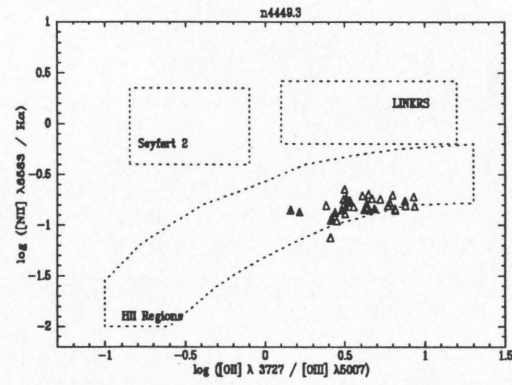
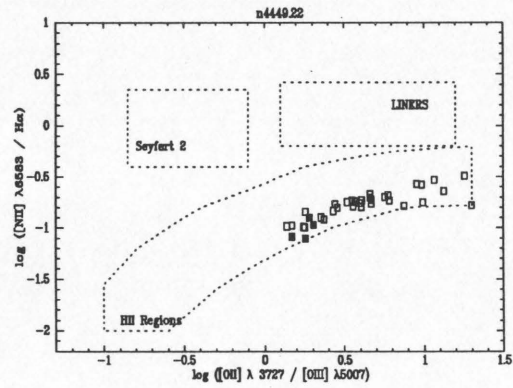
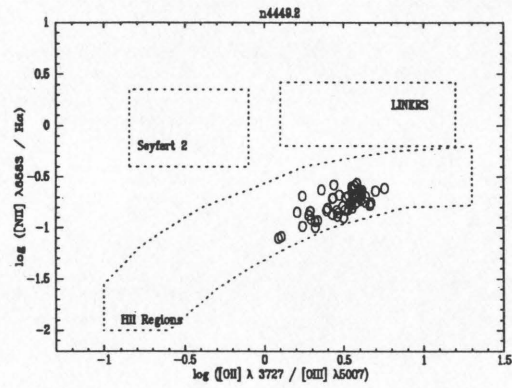
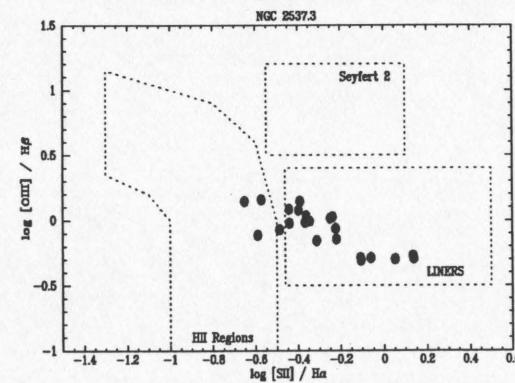
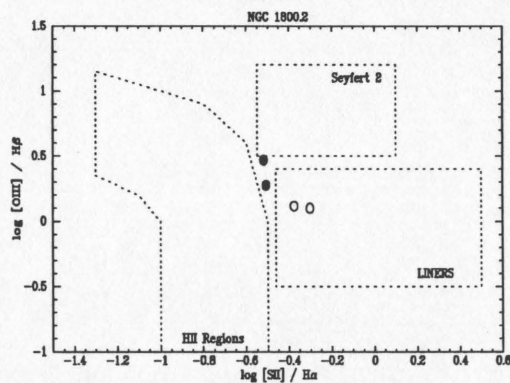
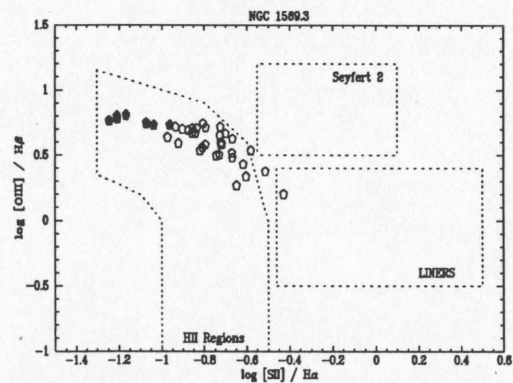
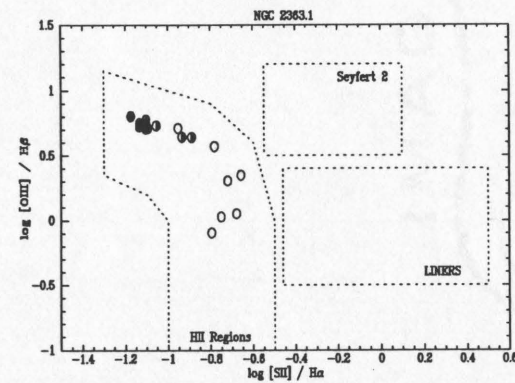
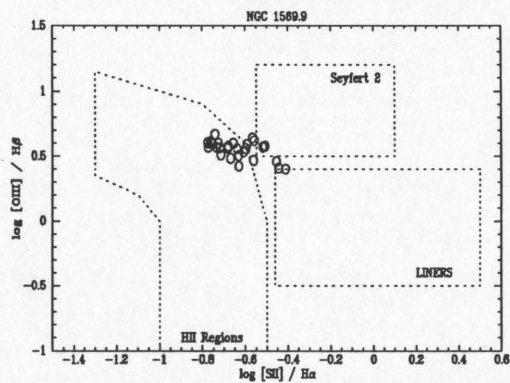
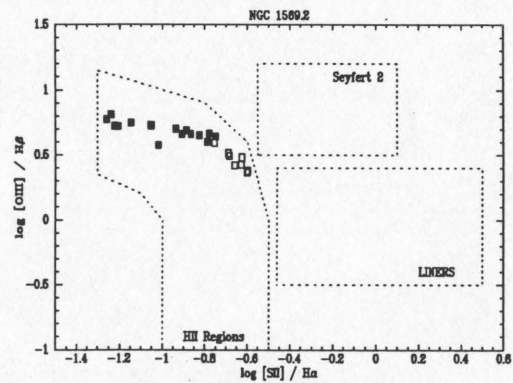
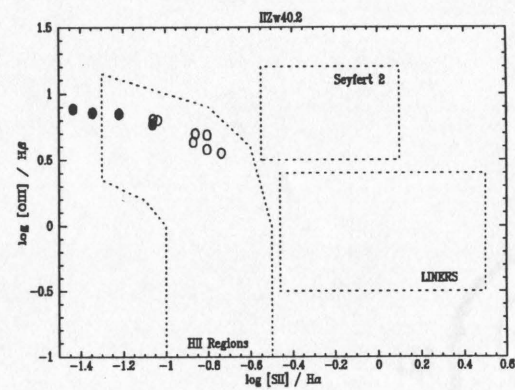
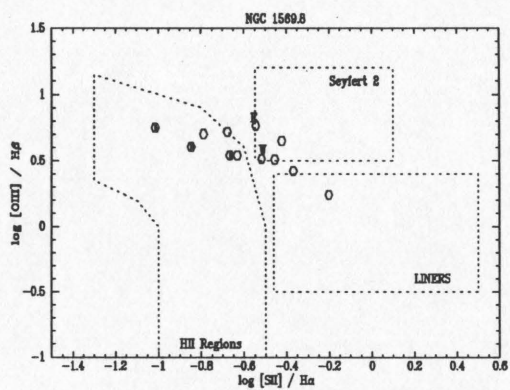
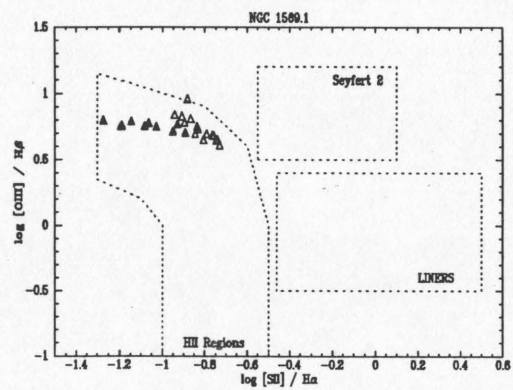
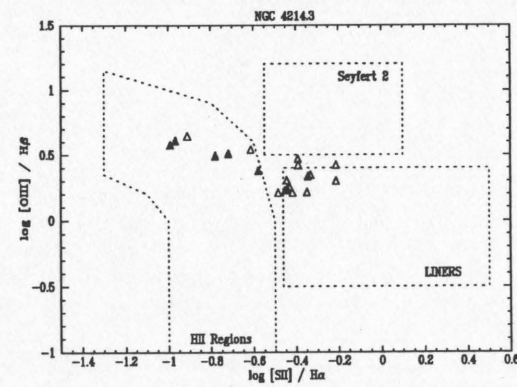
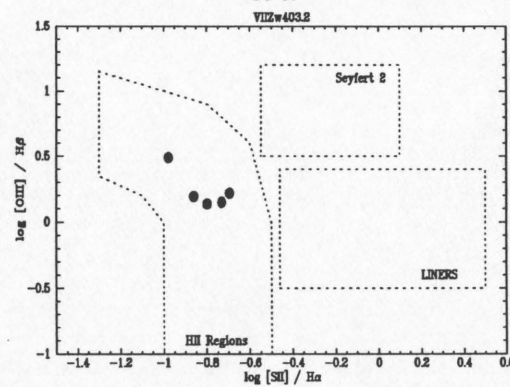
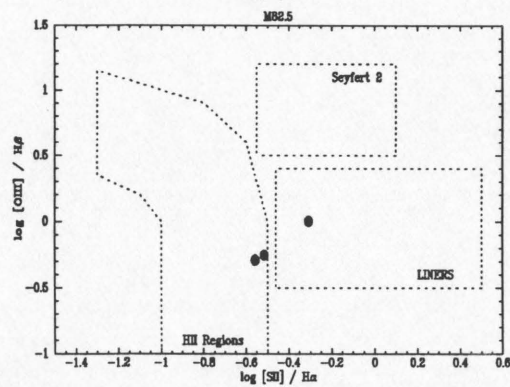
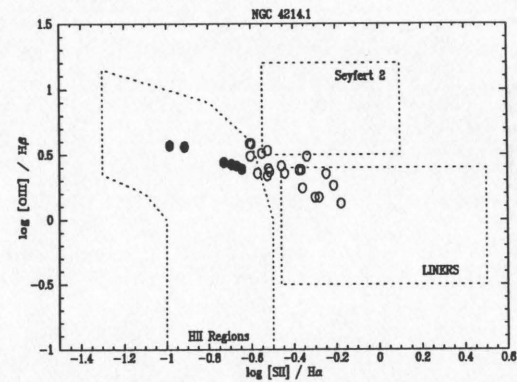
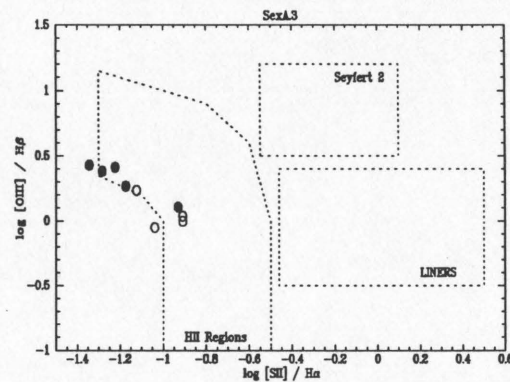
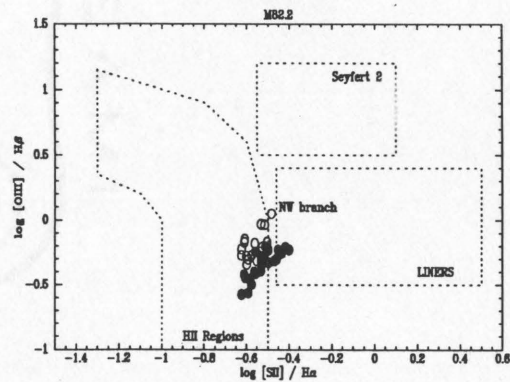
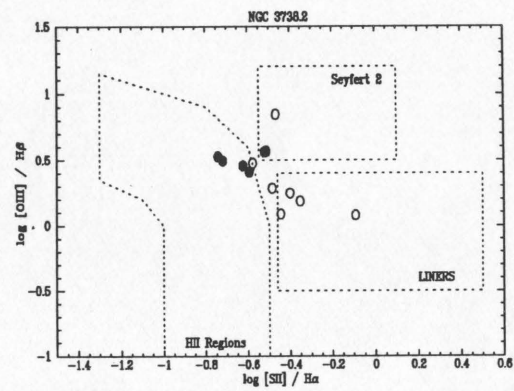
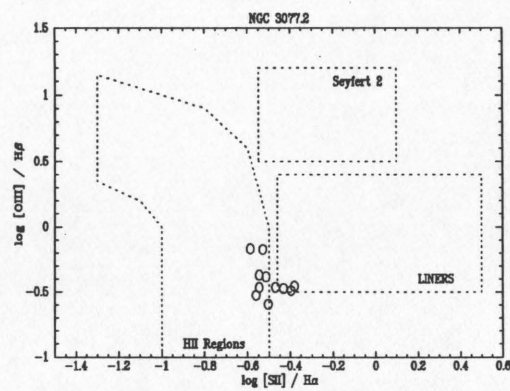
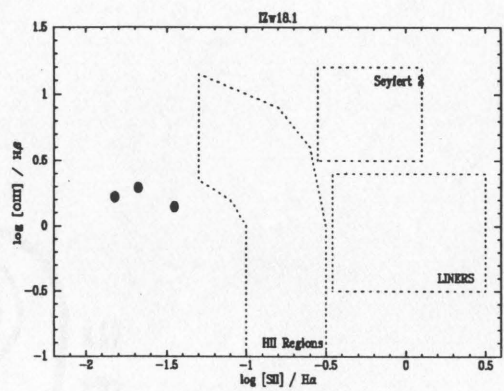


Figure 2.7 The HII-DIG transition sequence projected onto the $[\text{OIII}]\lambda 5007 / \text{H}\beta$ vs $[\text{SII}]\lambda\lambda 6717, 31 / \text{H}\alpha$ plane.





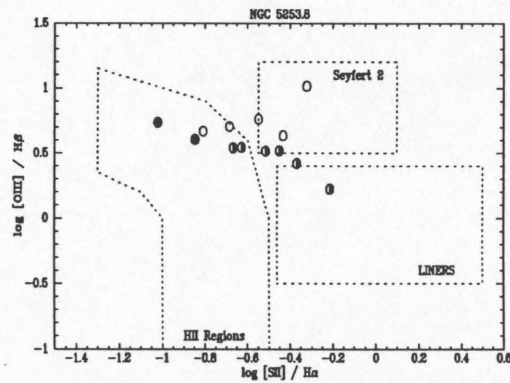
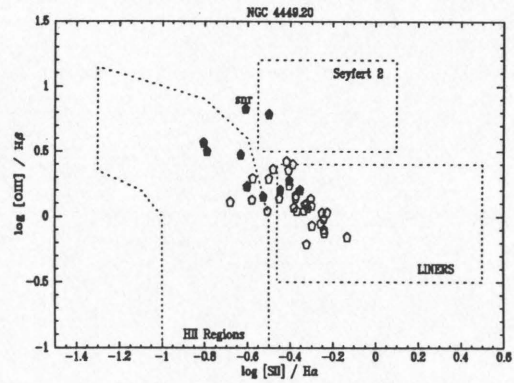
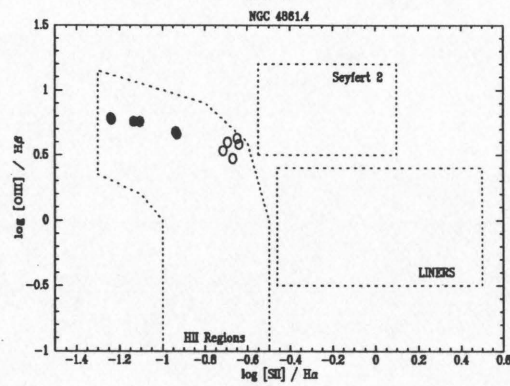
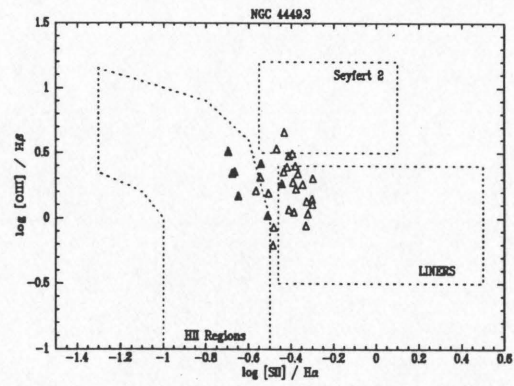
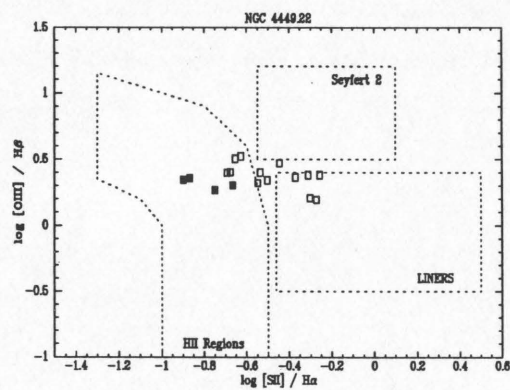
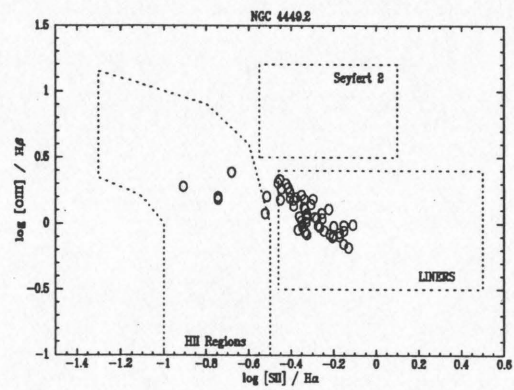
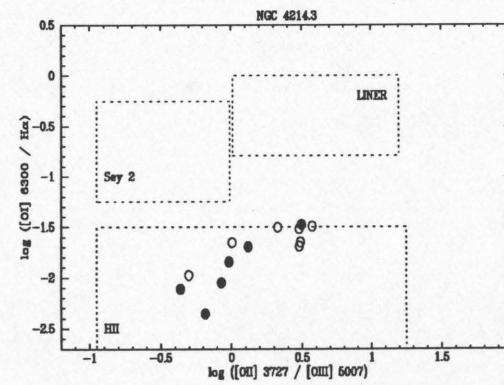
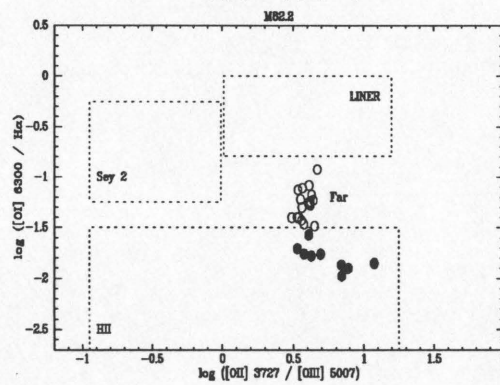
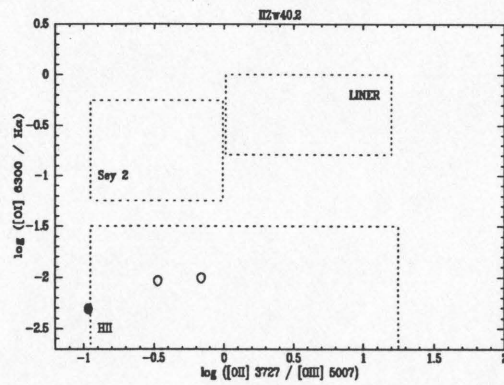
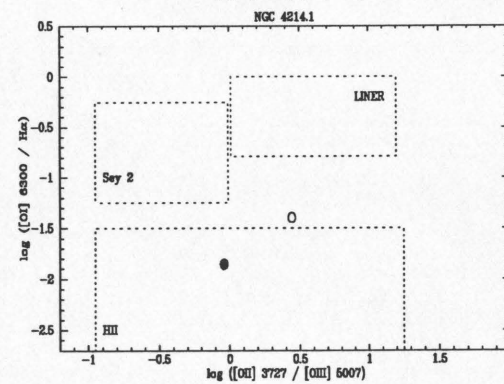
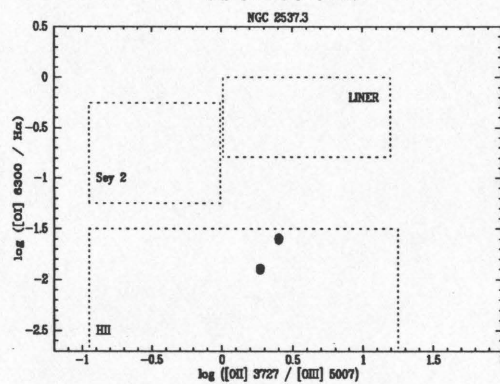
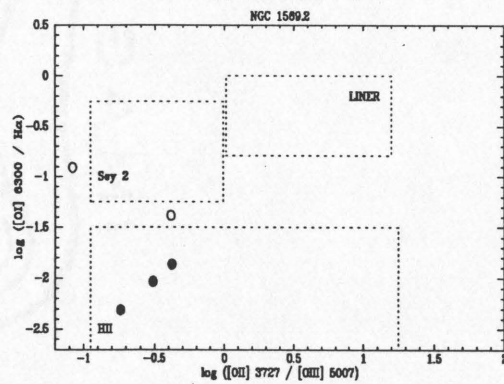
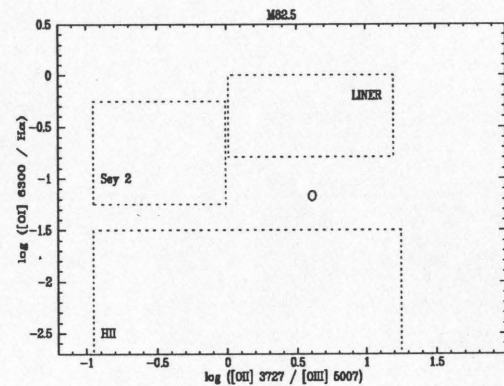
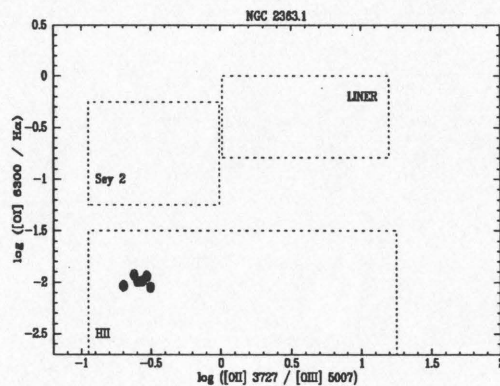
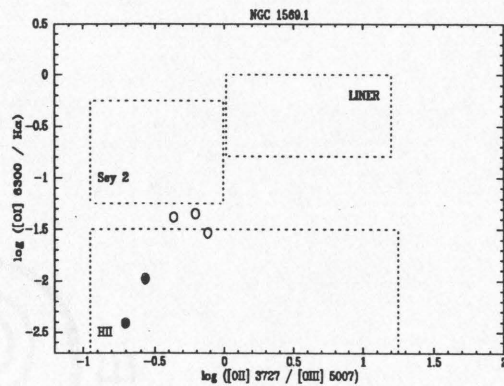
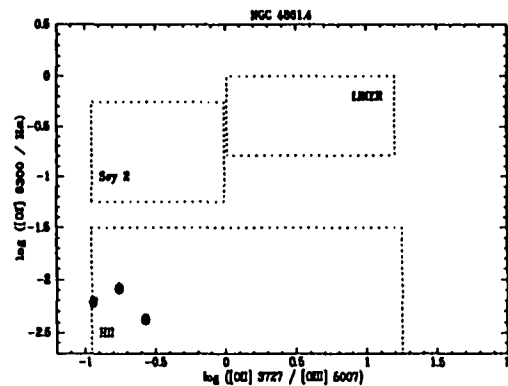
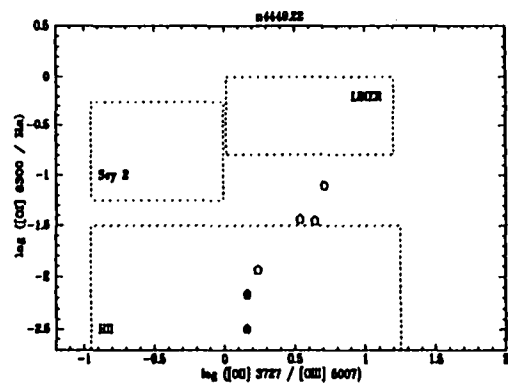
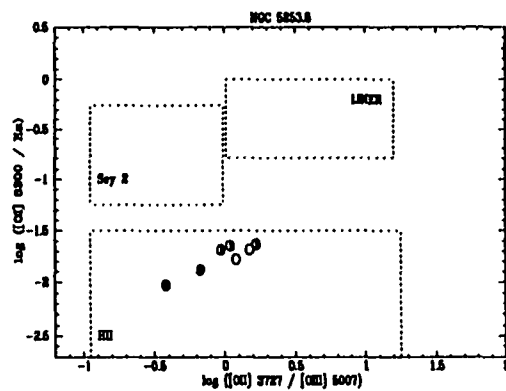
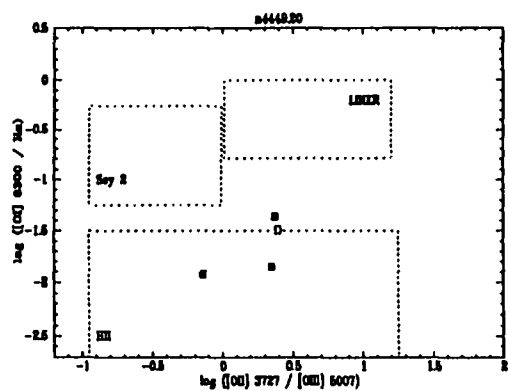


Figure 2.8 The HII-DIG transition sequence projected onto the $[\text{OI}]\lambda 6300 / \text{H}\alpha$ vs $[\text{OII}]\lambda\lambda 3727 / [\text{OIII}]\lambda 5007$ plane. Generally, larger apertures were used for the $[\text{OI}]\lambda 6300$ measurements to keep the error bars within a few tenths of a dex.





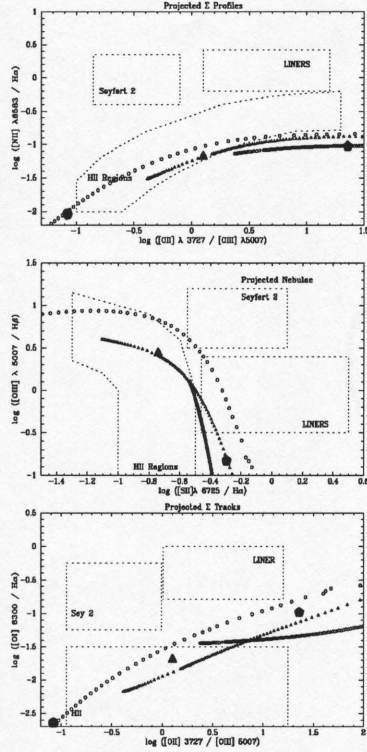


Figure 2.9 Excitation sequence produced by radial structure of model nebulae. The three models shown have volume averaged ionization parameters of $\log U(sp) = -1.90$, -3.23 , and -4.60 ; and their integrated line ratios are marked with a large circle, triangle, and pentagon respectively. The tracks (small symbols) follow a sequence of increasing projected radius from left to right and denote the surface brightness ratios. On the left, i.e. toward the central cluster, U_{los} is high; U decreases to the right toward the Stromgren radius. For all three models $T_{ion} = 45,000$ K and $O/H = 0.20(O/H)_{\odot}$.

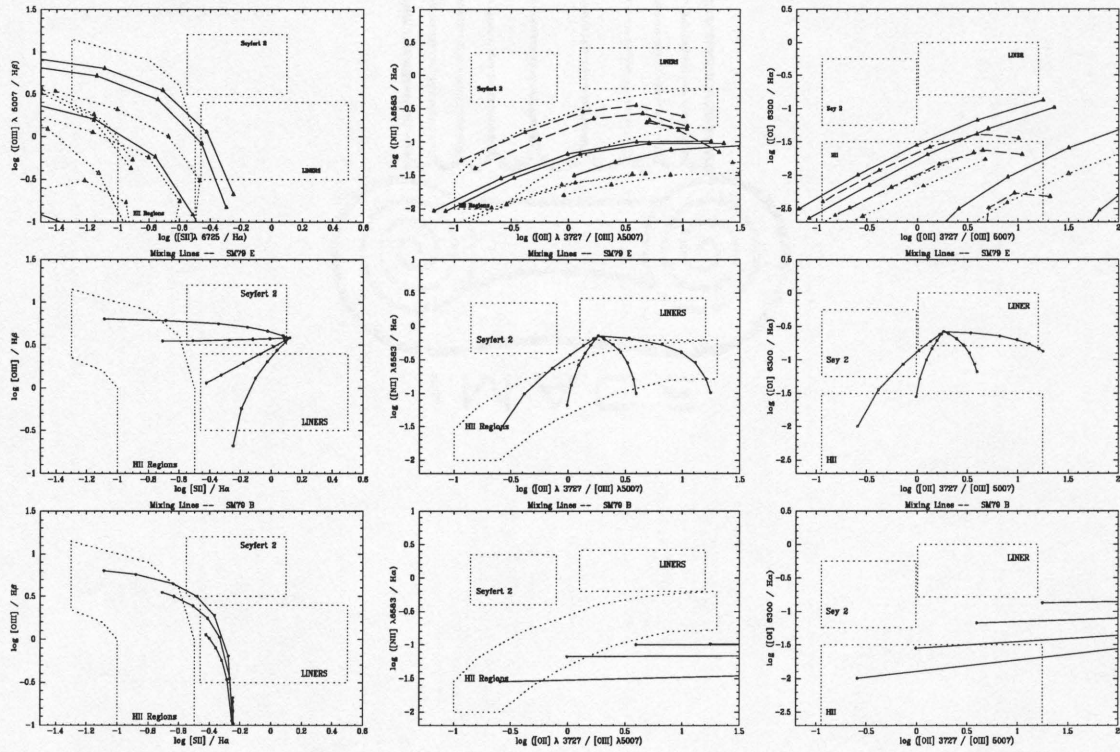


Figure 2.10 Theoretical emission-line sequence accompanying the transition from photoionized gas clouds to shock-excited clouds. (a) *Top Row*: Repeat of photoionization models for comparison. (b) *Middle Row*: The mixing lines depict linear combinations of four photoionized nebulae with the 100 km s⁻¹ shock model of Shull & McKee (1979) at cosmic abundance. From left to right the percentage contribution from shocks is is – 0%, 10%, 30%, 50%, 70%, 90%, 100% at successive tick marks. (c) *Bottom Row*: Same as (b) but the shock speed is 60 km s⁻¹.

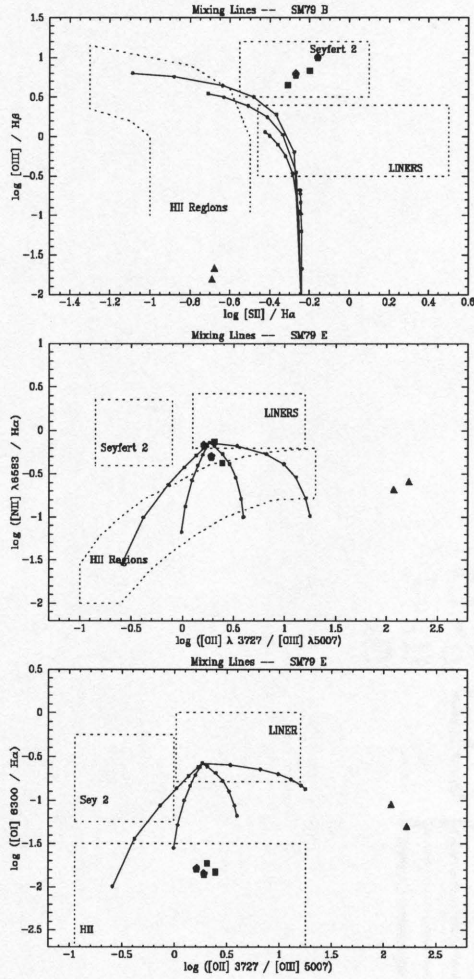


Figure 2.11 Turbulent mixing layers. Line ratios for turbulent mixing layers at mixing temperatures of $\bar{T} = 5.5, 5.3$, and 5.0 are represented by the pentagons, squares, and triangles, respectively (Slavin, Shull, & Begelman 1993). Models with shear velocities of 25 km s^{-1} and 100 km s^{-1} are shown at each temperature. The solid lines show a set of shock/photoionization models from Figure 2.10 for comparison.

PLEASE NOTE

**Page(s) not included with original material
and unavailable from author or university.
Filmed as received.**

UMI

CHAPTER 3

He I λ 5876 RECOMBINATION LINE RADIATION FROM THE DIG

3.1. Introduction

Diffuse, warm ionized gas comprises a significant fraction of the mass and volume of the interstellar medium in galaxies. We will refer to this component as the DIG, but it has also been called the diffuse ISM, Reynolds Layer, or warm ionized medium (WIM). In the Milky Way, it has been recognized for some time that Galactic O and B stars supply enough power to keep it ionized (Reynolds 1984). The close correlation between the presence of extended, diffuse ionized gas in other galaxies and various tracers of massive star formation has strengthened the OB-star photoionization hypothesis (Dettmar 1992; Rand 1996; Hunter & Gallagher 1990). The only conundrum has been how the Lyman continuum radiation from OB stars, scale height ~ 100 pc in the Milky Way, could reach the DIG which has a Galactic scale height ~ 1 kpc (Reynolds 1991).

The massive-star photoionization picture has been challenged, however, by new measurements of the He ionization fraction in the Galactic DIG. Reynolds & Tufte (1995) searched for the He I $\lambda 5876$ recombination line emission and set an upper limit of $\text{He I } \lambda 5876 / \text{H}\alpha \leq 0.011$ in the local DIG. Assuming a He/H abundance ratio of 1/10 by number in the DIG, the relative ionization fraction of He^+/He to H^+/H is $\chi(\text{He})/\chi(\text{H}) \lesssim 0.23$. Heiles et al. (1996) have observed H and He radio recombination lines at ~ 1.5 GHz at hundreds of positions toward the Galactic center and find $\chi(\text{He})/\chi(\text{H}) \lesssim 0.13$ in the diffuse ionized medium there. The high neutral fraction of He implies that the interstellar radiation field is softer than that expected from the Galactic O star population in the solar neighborhood (Reynolds & Tufte 1984) and is inconsistent with estimates of the global star formation rate in the Milky Way (Heiles et al. 1996). It remains unclear whether another excitation mechanism is involved, models of the ionizing luminosity from Galactic stars are inaccurate, or the radiative transport somehow softens the stellar Lyman continuum.

Nearby galaxies provide an opportunity to examine the relationship between the properties of the DIG and the stellar content of a galaxy. Among normal galaxies, Magellanic irregulars have the most intense star formation in terms of both the number of HII regions per unit luminosity and the ionizing luminosity of the brightest HII region (Kennicutt, Edgar, & Hodge 1989). To investigate the ionization state of He in the warm ionized phase of the ISM of such galaxies, we selected three Im's with copious amounts of diffuse and filamentary $\text{H}\alpha$ emission from a larger sample of dwarf galaxies (Martin 1996b). In this Letter, we report measurements of the He I $\lambda 5876$ line emission in the DIG from longslit spectra. A more detailed discussion of the emission-line spectra and their implications for the excitation the DIG can be found in Chapter 2 (Martin 1996a).

3.2. Measurements of He I $\lambda 5876$ Line Emission

3.2.1. The Galaxies

Table 1 compares some relevant properties of the observed galaxies to the Milky Way. They were selected for their star formation activity and proximity, which allows us to spectroscopically study regions less than 50 pc across. They are gas-rich and have absolute luminosities between those of the Small Magellanic Cloud and Large Magellanic Cloud. Gas is being turned into massive stars at the rate of 0.25 and $0.50 \text{ M}_{\odot} \text{ yr}^{-1}$ assuming the measured H recombination rates equal the stellar photoionization rates (Kennicutt & Kent 1983; Kennicutt, Tamblyn, & Congdon 1994). These current rates of star formation (SFR) are equal to or a few times larger than the past average rates of star formation in these galaxies (Kennicutt 1983; Kennicutt et al. 1994). However, both spatial and temporal fluctuations in the SFR have clearly occurred. For example, the northern region of NGC 4449 is younger than the main bar (e.g. Hill et al. 1994); and NGC 1569 is emerging from a major burst of star formation (Israel & de Bruyn 1988; Waller 1991; Heckman et al. 1995). The HII regions in all three galaxies have oxygen to hydrogen abundance ratios about $1/4 (\text{O}/\text{H})_{\odot}$ (Chapter 2 or Martin 1996a and references therein). Both NGC 4449 and NGC 1569 are classified as barred Magellanic irregulars, while NGC 4214 is described as a mixed family, S-shaped Im (de Vaucouleurs 1991). Many of the prominent filaments and shells seen in $\text{H}\alpha$ images are associated with large-scale gas flows apparently driven by the massive stars (Martin 1996c).

3.2.2. Observations and Reductions

We obtained longslit spectra at 11 positions across these galaxies at the Multiple Mirror Telescope during the period February 1994 to March 1995. The Blue Channel spectrograph was used with a 500 gpm grating, a Loral $3\text{k} \times 1\text{k}$ CCD

Table 3.1 Properties of the Galaxies

Galaxy	NGC 1569	NGC 4214	NGC 4449	Milky Way
d (Mpc) ^a	2.2	3.6	3.6	...
c(H β) ^b	0.85 ± 0.3	0.16 ± 0.1	0.29 ± 0.3	...
Γ (s ⁻¹) ^c	3.9e52	4.5e52	2.1e52	$\gtrsim 1.4e53$
b ^d	$\gtrsim 1$	$\gtrsim 1$	$\gtrsim 1$	≤ 1
log(O/H) ^e	-3.78 ± 0.07	-3.78 ± 0.07	-3.69 ± 0.07	...
M_{HI} (M $_{\odot}$) ^f	8.4e7	1.1e8	2.4e9	4.8e9

^aAdopted distance (Martin 1996b).

^bLogarithmic extinction at H β (see text).

^cRecombination rates calculated at 10⁴ K from the H α fluxes of Kennicutt & Kent (1983) and the extinction in row 2. The Galactic value is discussed by Heiles et al. (1996).

^dStellar birthrate parameter, the ratio of the current star formation rate to the past average rate (Kennicutt 1983; Kennicutt et al. 1994).

^eOxygen abundance (Martin 1996a).

^fMass of neutral hydrogen from Reakes (1980), Hunter, Gallagher, & Rautenkranz (1982), Hunter & Gallagher (1986), and Kulkarni & Heiles (1987).

detector, and a $1''$ by $3'$ slit. This setup produced a spectral resolution of $4 - 5 \text{ \AA}$ at $H\alpha$. Slit positions were chosen to sample both HII regions and extended, diffuse emission and were required to be close to the parallactic angle at the time of observation. Their exact locations are illustrated in Martin (1996a), where additional details about the observations and reductions can be found.

The He I $\lambda 5876$ line is clearly visible along a substantial length of the slit in the raw data. We divided this region into $3''$ apertures and extracted a series of one-dimensional spectra from the sky-subtracted and continuum-subtracted frames. The He I $\lambda 5876$, $H\alpha$, and $H\beta$ fluxes were measured from these spectra using the 'splot' task in IRAF. The logarithmic extinction at $H\beta$, $c(H\beta)$, was calculated from the relative intensities of the $H\alpha$ and $H\beta$ lines using the case B Balmer decrement at $T_e = 15,000 \text{ K}$ (Osterbrock 1989) and assuming a constant underlying stellar absorption equivalent width of $2 \text{ \AA} \pm 2 \text{ \AA}$. We found little variation of $c(H\beta)$ with position along the slit, so the mean value was adopted at each position angle. An uncertainty $\delta c(H\beta)$ was assigned based on the variation in $c(H\beta)$ along the slit or the formal error, whichever was larger. This term dominates the error estimates of the He I $\lambda 5876 / H\alpha$ intensity ratio. Only a portion of the data were obtained under photometric conditions, but the relative flux calibration for all observations is good to $\sim 2\%$ based on observations of multiple standard stars (Massey et al. 1988).

3.2.3. Results

Figure 1a shows the reddening-corrected ratio of the He I $\lambda 5876$ to $H\alpha$ emission-line intensity as a function of $H\alpha$ surface brightness along the 11 slit positions. The $H\alpha$ surface brightness is closely correlated with the angular distance from the nearest giant HII region along our slit positions and therefore provides a rough, relative measure of the distance to the ionizing cluster (cf. Figure 2). The average

He I $\lambda 5876$ / $H\alpha$ intensity ratio is 0.041, the lowest value is 0.028, and the highest value is 0.058. Comparison with panel b shows only NGC 1569 and position 3 in NGC 4449 ($PA = 137.2^\circ$) have large corrections for reddening. Across each galaxy, we find no systematic variation in He I $\lambda 5876$ / $H\alpha$ despite a decline in $H\alpha$ surface brightness by a factor of ~ 100 .

The gradients in other diagnostic line ratios measured from the same spectra emphasize the remarkable uniformity of He I $\lambda 5876$ / $H\alpha$. Figure 3.2 demonstrates the contrast along position 2 in NGC 1569. Across the region where He I $\lambda 5876$ / $H\alpha$ is measured, the $[SII]\lambda\lambda 6717, 31$ / $H\alpha$, $[NII] \lambda 6583$ / $H\alpha$, and $[OI]\lambda 6300$ / $H\alpha$ ratios increase by factors of a few, while $[OIII]\lambda 5007$ / $H\beta$ decreases by a similar factor. This behaviour is typical, and Figure 5 of Chapter 2 shows similar examples across NGC 4449 and NGC 4861.

Under normal conditions, the relative intensity of He I $\lambda 5876$ / $H\alpha$ can be predicted from the effective recombination coefficients of He and H. At $T = 10^4$ K and $n = 100 \text{ cm}^{-3}$, the recombination coefficients for He and H from Brocklehurst (1972) and Hummer & Storey (1987), respectively, yield an intensity ratio

$$\frac{F(5876)}{F(H\alpha)} = 0.470 \frac{\text{He}}{\text{H}} \frac{\chi(\text{He})}{\chi(\text{H})},$$

where He/H is the abundance ratio by number. (The revised emissivities of Smits (1996) would raise the coefficient in equation 1 by 0.004, while raising the temperature to 1.2×10^4 K would lower it by 0.004.) Assuming that the abundance ratio of He/H by number is $\lesssim 0.1$ and comparing the measured intensity ratios with equation 1, we see that $\chi(\text{He})/\chi(\text{H}) \approx 1$.

If we adopt $\chi(\text{He})/\chi(\text{H}) = 1$, then the mean ionic abundance of He^+ relative to H^+ is $\frac{\text{He}^+}{\text{H}^+} \equiv \bar{y}^+ = 0.085$. For this He abundance, the He vs O regression relation derived by Pagel et al. (1992) from 30 low-metallicity HII regions predicts $\log(O/H) = -3.69$, which is consistent with the O/H abundance measured in

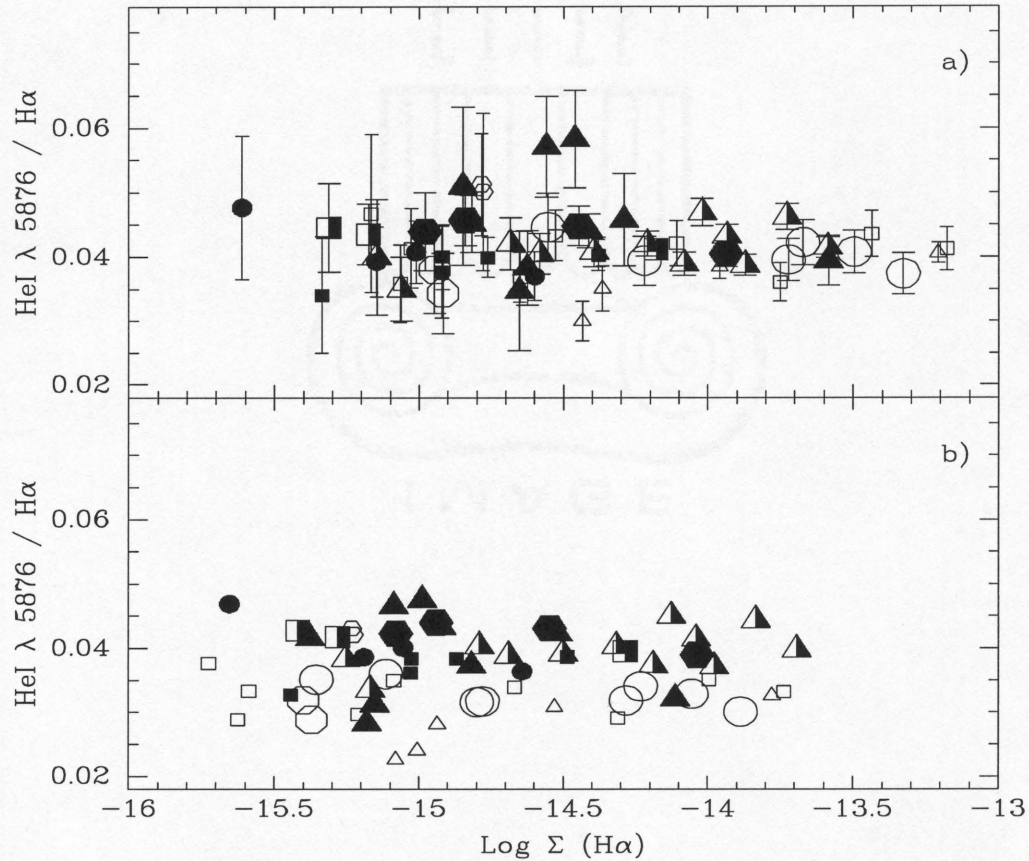


Figure 3.1 (a) Dependence of He I $\lambda 5876$ / $H\alpha$ intensity ratio on $H\alpha$ surface brightness. The surface brightness at the positions represented by large symbols is in units of $\text{ergs s}^{-1} \text{cm}^{-2} \text{arcsec}^{-2}$. The small symbols denote non-photometric data and could be misplaced by as much as ± 0.5 dex in surface brightness. Open symbols denote NGC 1569 – \bigcirc PA = 32.4° , \triangle PA = 116.4° , \square PA = -14.3° , “Hex” PA = 109.7° , and “Oct” PA = 29.7° . Closed symbols denote NGC 4449 – \bigcirc PA = 38.8° , \square PA = 84.0° , \triangle PA = 137.2° , “Hex” PA = 82.0° . Half-filled symbols denote NGC 4214 – \triangle PA = 70.3° , \square PA = 31.0° . (b) Emission-line ratio and surface brightness before application of reddening correction.

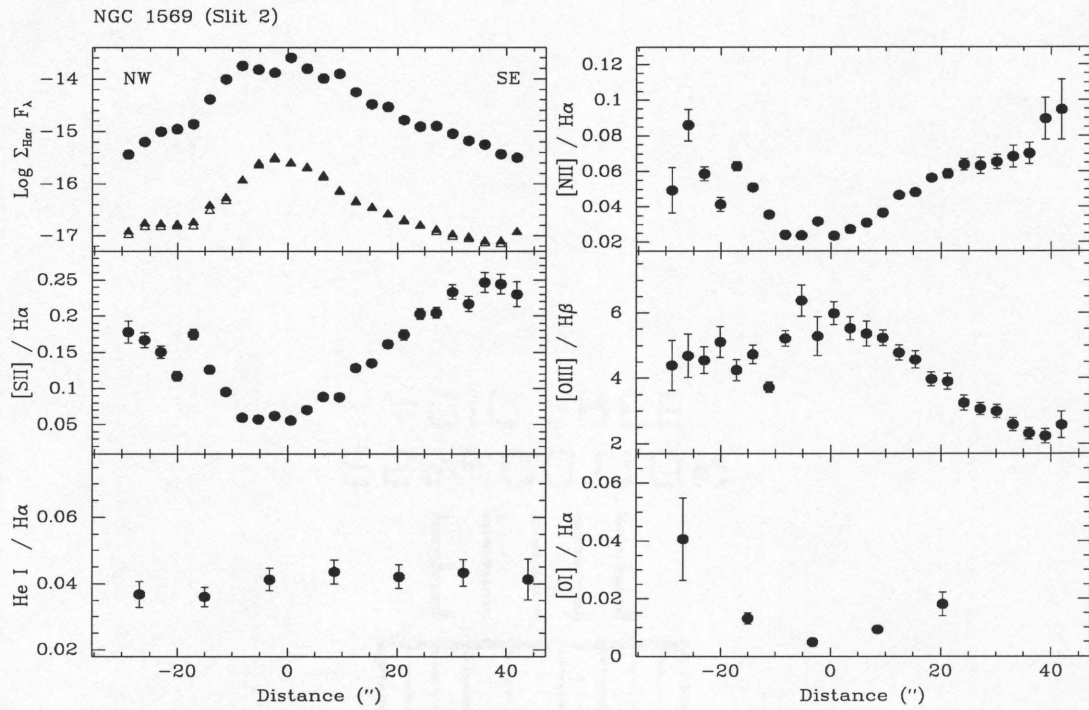


Figure 3.2 Emission-line ratios across NGC 1569, PA = 32.4°. Counterclockwise from top left, the ratios are: H α and continuum surface brightness, [SII] $\lambda\lambda$ 6717, 31 / H α ; He I λ 5876 / H α ; [NII] λ 6583 / H α ; [OIII] λ 5007 / H β ; and [OI] λ 6300 / H α .

NGC 4449. Across the O/H range of our three Ims, their Table 15 contains objects with y^+ varying from 0.081 to 0.090, so the inferred He/H abundance ratios of these Ims are typical of their O/H abundance. Variations in the He/H ratio among the HII regions within a single galaxy are probably less than a few percent (e.g. NGC 4214; Kobulnicky & Skillman 1996).

3.3. Discussion: The Source of Ionizing Photons

3.3.1. Constraints on the Stellar Mass Function

The high degree of He ionization places a constraint on the hardness of the Lyman continuum radiation ionizing the DIG. Figure 3.3 illustrates the response of a nebula's He I $\lambda 5876$ / $H\alpha$ ratio to the relative number of photons with $h\nu > 24.6$ eV, $Q(He)$, to $h\nu > 13.6$ eV, $Q(H)$, emerging from a Kurucz stellar atmosphere (1979). The ratio He I $\lambda 5876$ / $H\alpha$ increases linearly with $Q(He)/Q(H)$ until H begins to compete for $h\nu > 24.6$ eV photons and then saturates at a constant value when the volume-averaged $\chi(He) \approx \chi(H) \approx 1$ (Osterbrock 1989). Comparing the mean He I $\lambda 5876$ / $H\alpha \sim 0.041$ with Figure 3.3, we estimate $Q(He)/Q(H) \gtrsim 0.25$ for $He/H \approx 0.85$. This $Q(He)/Q(H)$ corresponds to an effective stellar temperature of $\gtrsim 45,000$ K and a mass $\gtrsim 40 M_\odot$ at solar metallicity. At $0.25 (O/H)_\odot$, stars with mass $\gtrsim 35 M_\odot$ have atmospheres this hot (cf. Figure 2. McGaugh 1991).

The integrated $Q(He)/Q(H)$ from a population of stars with upper mass limit m_u will be lower than the $Q(He)/Q(H)$ from a star of mass m_u . For example, continuous star formation with a Salpeter IMF and $m_u = 100 M_\odot$ produces $Q(He) / Q(H) = 0.23$, while lowering m_u to $30 M_\odot$ lowers $Q(He)/Q(H)$ to 0.07 (Leitherer & Heckman 1995). The ratio can be considerably higher, $Q(He) / Q(H) = 0.32$, if the duration of the burst is less than 10 Myr. Hence, $35 M_\odot$ is only a lower limit

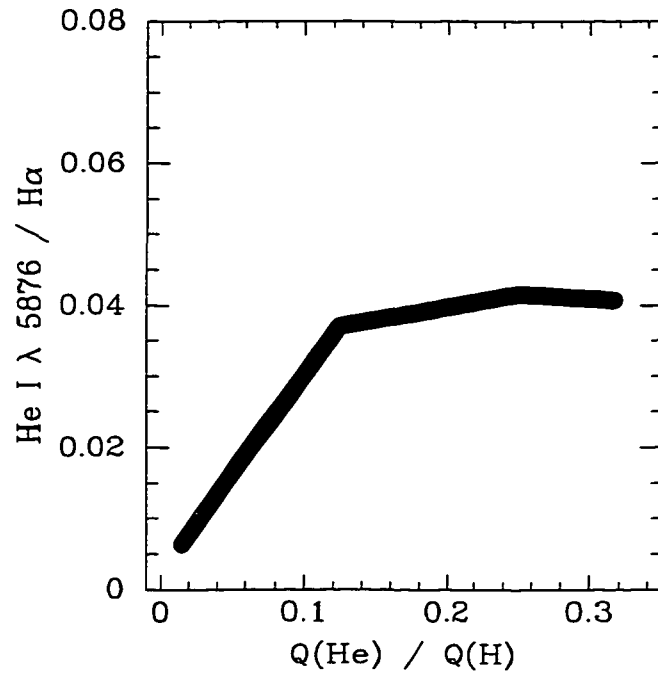


Figure 3.3 Theoretical dependence of $\text{He I } \lambda 5876 / \text{H}\alpha$ on the hardness of the stellar continuum. Photoionization models were computed with CLOUDY (version 84.09; Ferland 1993) and are described in detail in Martin (1996a). The models shown have $O/H = 0.20(O/H)_{\odot}$. The thick line corresponds to the estimated range of He abundance, $He/H = 0.08 - 0.09$.

on the upper mass cut-off of the ionizing population of stars, and the interstellar Lyman continuum in these irregulars is much harder than that which ionizes the WIM in the Milky Way.

Optical and ultraviolet spectra provide direct evidence for massive stars in all three galaxies. Several HII regions in NGC 4214 show strong, broad He II $\lambda 4686$ and C IV $\lambda\lambda 5808$ emission lines from WN and WC stars (Sargent & Filippenko 1991). Our spectra also reveal both of these features in several HII regions in NGC 4449 as well as broad $\lambda 4686$ in NGC 1569 (cf. Drissen, Roy, & Moffat 1991). These Wolf-Rayet stars are thought to be the short-lived descendants of the most massive O stars ($M \geq 35 M_{\odot}$) (Conti et al. 1983; Humphreys, Nichols, & Massey 1985). Spectral synthesis modeling of the Lyman continuum from the most prominent cluster in NGC 4214 suggests several hundred O stars are present in addition to the ~ 30 Wolf-Rayet stars (Leitherer et al. 1996). Since He I $\lambda 5876$ / $H\alpha$ is not sensitive to the ionizing continuum for $Q(He)/Q(H) > 0.12$, we cannot constrain any small changes in the shape of the ionizing continuum.

3.3.2. The Morphology Problem

Table 2 contrasts some critical properties of the DIG in Im's to the Galactic DIG. The high He ionization fraction of the DIG in the Im's is not the only difference. The surface brightness of the regions studied spectroscopically in the Im's is about 5 times brighter than even the DIG in the Galactic plane. In addition to diffuse (i.e. unresolved ?) emission, the DIG in the Im's contains a highly structured component of shells, arcs, and radial filaments, sometimes referred to as "interstellar froth" (Hunter & Gallagher 1990). Considering all these differences, is the extra-HII region $H\alpha$ emission in Magellanic irregulars a good analogy to the Reynolds Layer in the Milky Way ?

We believe the analogy is interesting if the DIG in Irregulars shares a common

Table 3.2 The DIG in Different Types of Galaxies

Property	Milky Way	NGC 1569	NGC 4449	NGC 4214
He I λ 5876 / H α ^a	...	0.040	0.043	0.042
He I λ 5876 / H α ^b	$\lesssim 0.011$	0.032	0.039	0.040
$\chi(\text{He})/\chi(\text{H})$ ^c	$\lesssim 0.23$ < 0.13	~ 1	~ 1	~ 1
$\Sigma_{\text{H}\alpha}^{\text{DIG}}$ ^d (R)	1 - 10	100	50	50
$\Sigma_{\text{H}\alpha}^{\text{HII}}$ (R)	10 - 500	10,000	4,500	4,500
$\log U$ (DIG) ^e	$\lesssim -4.1$	-3.9	-4.3	-3.9
$\log U$ (HII)	...	-2.24	-3.2	-2.9
Distance ^f	≈ 1000	950 (400)	1900 (1000)	1200 (800)
Morphology ^g	Diffuse	Diffuse + Filaments + Wind	Diffuse + Filaments	Diffuse + Filaments
M_u ^h (M_\odot)	≤ 39	> 30	> 30	> 30

Notes – (a) Reddening corrected emission-line ratio. (b) Reddened line-ratio. Local value from Reynolds & Tufte (1995). (c) Relative ionization fraction. Galactic values from Reynolds & Tufte (1995) and Heiles et al. (1996). (d) The H α surface brightness of the DIG compared to that of HII regions in the Im’s and discrete sources in the Galactic plane (Reynolds 1983, 1984). One Rayleigh (R) is 10^6 photons $\text{s}^{-1} \text{cm}^{-2} \text{sr}^{-1}$. (e) Logarithm of ionization parameter, $U \equiv \frac{Q}{(4\pi R_S^2 n c)}$, (Martin 1996a; Domgörgen & Mathis 1994). (f) Projected distance from giant HII regions to the most extended H α emission in our images and, in parentheses, to the boundary of our He I measurements. Estimated scale height of Galactic diffuse, ionized gas (Reynolds 1991). (g) Morphology of extra-HII region ionized gas. (h) Upper-mass limits on present day mass function of stars contributing to the ionization of the DIG (this paper and Heiles et al. 1996).

morphology problem with the Reynolds Layer. Because the spectroscopic signature of gas photoionized by a distant association is nearly indistinguishable from that of a dilute HII region, we re-examine the possibility that the DIG in Im's is ionized locally. First, consider two nebulae surrounding identical stellar clusters which are located in different regions of a galaxy. Their ionization parameters would differ by the requisite factor of ten if the ambient gas densities differed by a factor of 10^3 . While a steep radial density gradient could, in principle, produce such a change in environment, the surface brightness of the low density nebula would be 10^4 times fainter – a much greater contrast than observed. An alternative scenario is that the DIG is ionized by individual, isolated O and B stars. In NGC 4449 and NGC 4214, this would require an abrupt jump, about a factor of 20, in the HII region luminosity function at the transition from HII regions ionized by clusters to single stars (cf. Kennicutt, Edgar, Hodge 1989). In NGC 1569, the contrast in morphology between the continuum and line emission and the violent kinematics of the line emission would be difficult to reconcile with local, stellar photoionization (cf. Figure 5a Waller 1991; Heckman et al. 1995). Hence, the photons ionizing the DIG are most likely leaking out of the giant HII regions. Additional support for this conclusion is provided by Leitherer et al. (1996) who resolved the central starburst in NGC 4214 and conclude that the HII region around it is density bounded.

Since a photon of energy 1 Rydberg will only travel a distance of $0.5(n_H/0.1 \text{ cm}^{-3})^{-1} \text{ pc}$ before ionizing a H atom, much attention has been devoted to describing the requisite geometry of the ISM from the vantage point of an OB association in the Milky Way (Dove & Shull 1994; Miller & Cox 1993). The scale height of the Galactic DIG is about 1 kpc (Reynolds 1991), and discrete Galactic O star HII regions are $\gtrsim 100$ times brighter (Reynolds & Tufte 1995). The situation in the Irregulars is quite similar. Although the region of the DIG

accessible spectroscopically in the Ims is brighter, it is still 100 times fainter than the giant HII regions in the same galaxies and extends at least as far as 1 kpc away from the nearest one. The evidence is not limited to morphology. Spectra of the low surface brightness gas in both environments indicate the relative density of photons to matter, described by the ionization parameter U , is low. In Table 2, U has been defined in terms of the Strömgren radius, R_S , such that $U \equiv \frac{Q}{4\pi R_S^2 n_c}$. In the Irregular galaxies the ionization parameter falls by a factor $\gtrsim 10$ over a decline in $H\alpha$ surface brightness of ~ 100 . Unless the DIG is ionized by an undetected population of isolated O stars, some of the ionizing photons produced near the giant HII regions must travel very large distances before being absorbed.

3.3.3. The Contribution of Shock-Excited Gas to He I $\lambda 5876$ Emission

Shocks contribute to the excitation of the DIG in these Im's. The shock velocities estimated from spectra of the DIG range from 60 km s^{-1} to 100 km s^{-1} (Martin 1996a), and high-resolution echelle spectra provide kinematic evidence for kiloparsec-scale, expanding shells with velocities toward the lower end of this range (Martin 1996b). The percentage of emission from shocked gas increases as the surface brightness decreases and typically reaches 20 – 30% in the lowest surface brightness regions represented in Figure 3.1, although as much as 50% of the emission may come from shocked gas in the low surface brightness regions of NGC 4449.

The He I $\lambda 5876$ / $H\alpha$ intensity is very sensitive to shock velocity. In the models of Shull & McKee (1979), the contribution to He I $\lambda 5876$ / $H\alpha$ is negligible until shock speeds reach 80 km s^{-1} , where He I $\lambda 5876$ / $H\alpha$ is still only 0.005. Yet, when the shock speed is increased just 20 km s^{-1} more ($v = 100 \text{ km s}^{-1}$), the He I $\lambda 5876$ / $H\alpha$ ratio has reached 0.047. Hence, shocks may contribute to the high values in Figure 3.1 but the current modeling is not sophisticated enough to make

a quantitative correction. The lack of any systematic variation in He I $\lambda 5876$ / $H\alpha$ with distance from the giant HII regions leads us to suspect the correction is not large.

3.4. Summary

We measure a mean He I $\lambda 5876$ / $H\alpha \approx 0.040$, 0.042 , and 0.043 across NGC 1569, NGC 4214, NGC 4449, respectively. We find no evidence for a systematic variation in He I $\lambda 5876$ / $H\alpha$ with either $H\alpha$ surface brightness or distance from the nearest giant HII region. For an abundance ratio $\text{He}/\text{H} = 0.085$, $\chi(\text{He})/\chi(\text{H}) \approx 1$. This high relative ionization fraction requires an ionizing continuum at least as hard as that supplied by a $30 M_{\odot}$ star. The young clusters in the HII regions of these galaxies are the most likely source of the ionizing photons. The transport of these photons over a kiloparsec to the DIG is not well-understood, but the situation is reminiscent of the “morphology problem” associated with the Galactic DIG and other spiral galaxies (Heiles et al. 1996; Dettmar 1992 and references therein). However, the contrast in the spectral energy distribution of the Lyman continuum powering the ionized gas in Im’s and the Galaxy indicates there are physical differences among the warm-ionized phase of the ISM in different types of galaxies. We speculate that the transport of ionizing radiation to the DIG may be sensitive to the luminosity of the largest star-forming complexes through their effect on the topology of the ISM.

CHAPTER 4

KINEMATIC EVIDENCE FOR SUPERBUBBLES IN I ZW 18

4.1. Introduction

The blue compact dwarf galaxy, I Zw 18, was first described as “a double system of compact galaxies” having an emission line spectrum with a fairly featureless continuum (Zwicky 1966). Its extremely blue colors and exceptionally low oxygen abundance indicate the present star formation rate exceeds the past average rate (Searle & Sargent 1972). Kunth & Sargent (1986) have argued that the metal abundance in I Zw 18 – $O/H \approx 0.02 (O/H)_{\odot}$ in the HII regions (Skillman & Kennicutt 1993 and references therein) – is close to the minimum observable in any self-enriched, HII region. The prospect that I Zw 18 may be forming stars for the first time out of primordial clouds of gas has drawn much attention (e.g. Sargent & Searle 1970; Lequeux & Viallefond 1980; Kunth, Lequeux, & Sargent 1994), and the galaxy has played a prominent role in determining the primordial He abundance (Lequeux et al. 1979; Davidson & Kinman 1985; Pagel et al. 1992).

The question of whether I Zw 18 formed stars prior to the current burst is not

settled, but several recent results support the young galaxy hypothesis. The colors extracted from UVB imaging studies of blue compact dwarfs typically uncover an older stellar population underlying the starburst. However, comparable efforts for I Zw 18 show no evidence for an old population (Sudarsky & Salzer 1995). Broadband HST images do resolve several spatially distinct populations within the main body of I Zw 18, but again show no evidence for an older population (Hunter & Thronson 1995). The three continuum patches strung out to the NW of the main body have progressively redder colors and are probably associated with the galaxy (Davidson, Kinman, & Friedman 1989; Dufour & Hester 1990). Dufour & Hester have speculated that the elements synthesized in these earlier, isolated star formation events escaped without significant mixing into the HI clouds. The C, N, and O abundances of the main HII regions are well described by a single burst that started about 10 Myr ago and restrict models with previous star formation to a short burst at least 10^9 years ago (Kunth, Matteucci, & Marconi 1995). Measurements of the metallicity of the HI gas (Kunth, Matteucci, & Marconi 1995; Pettini & Lipman 1995) should distinguish between these chemical evolution models, whose success relies on some primary production of N and a differential galactic wind (Marconi, Matteucci, & Tosi 1994).

Although the structure of the $H\alpha$ and 21-cm emission has been described previously (Dufour & Hester 1990; Viallefonde et al. 1987), several important questions about the gas dynamics remain. For example, Skillman & Kennicutt (1993) have questioned the assumption that the HI velocity field reflects a rotating disk. The implied total mass is 13 times larger than the HI mass (Viallefond et al. 1987) and causes I Zw 18 to deviate significantly from the mass-metallicity relation observed for dwarf irregular galaxies (Skillman et al. 1988). Examining the velocity field on finer scales will determine the contribution of non-virial motions to the

large-scale gas motions. Another outstanding question is the role of a galactic wind. Meurer (1991) has suggested that the $H\alpha$ emission extending roughly perpendicular to the main HI cloud is a minor axis outflow. It is important to substantiate this claim with supporting kinematic evidence.

We selected I Zw 18 for a case study within a broader program investigating the interplay between star formation and the ISM (Martin 1996). The feedback could have a particularly strong influence on the evolution of I Zw 18 since the low metallicity reduces radiative losses and the escape velocity is relatively low. This paper presents new imagery and longslit echelle spectra of the $H\alpha$ emission and previously unreported X-ray emission (§ 4.2). The objectives are to describe the kinematics of the ionized gas (§ 4.2), derive a consistent dynamical interpretation (§ 4.3), determine the implications for the star formation history of I Zw 18 (§ 4.3), and estimate what effect mass loss is likely to have on the galaxy's evolution (§ 4.4). Since the results suggest superbubbles mix the interstellar gas on kiloparsec scales, we examine new optical spectra in § 4.4.2 and place limits on the O/H abundance variations in the extended ionized gas. The results are summarized in § 4.5.

4.2. Observations and Analysis

4.2.1. Optical Imaging

Narrowband $H\alpha$ and red continuum images of I Zw 18 were obtained 1993 May 17 with the Steward Observatory 2.3 m telescope equipped with a Loral 800×1200 thinned CCD. The raw CCD frames were processed with standard techniques as described in Martin & Kennicutt (1995). Figures 4.1ab show the continuum subtracted $H\alpha$ image. The NW HII region is centered about $1''$ E of the brightest

continuum emission. A small, partial shell of diameter $3''.6$ (175 pc)¹ protrudes from the NW side of the NW HII region and wraps around the continuum emission (Davidson et al. 1989; Hunter & Thronson 1995). The SE HII region is coincident with the second brightest maximum in the continuum emission. The cores of both HII regions are offset NE of the two maxima in the HI map (Dufour & Hester 1990). The deeper reproduction in Figure 1a reveals additional features absent in the off-band image. For example, the ridge to the SW is thought to represent a radiation-bounded ionization front being driven into the main HI cloud (Dufour & Hester 1990). A prominent shell stretches $15''$ (740 pc) N-NE from the NW HII region, and bright $H\alpha$ emission extends symmetrically S-SW of the NW HII region. Faint, diffuse emission (emission measure $EM \approx 50 \text{ pc cm}^{-6}$ for $T_e = 1.9 \times 10^4 \text{ K}$) is detected along position angle of 42° in a band $21''$ (1 kpc) wide and extends $25''$ (1.2 kpc) and $31''$ (1.5 kpc) to the NE and SW, respectively. The 21-cm emission is less extended in this direction; the principal $30''$ by $60''$ HI cloud is elongated along the optical major axis, $PA \approx 328^\circ$ (Viallefond et al. 1987).

The $H\alpha$ image was flux calibrated using the absolute flux reported by Dufour & Hester (1990) through a $1' \times 1'$ square aperture centered on the NW HII region. Absolute fluxes were corrected for atmospheric extinction and foreground Galactic reddening ($A_V = 0.21 \text{ mag}$); the contribution of [NII] lines is negligible. The integrated $H\alpha$ flux within $30''$ of the NW HII region is $5 \pm 1 \times 10^{-13} \text{ ergs s}^{-1} \text{ cm}^{-2}$, where the 20% uncertainty is dominated by the flux calibration. Assuming the nebula is radiation-bounded, Case B conditions, and an electron temperature $T_e = 1.9 \times 10^4 \text{ K}$ (e.g. Skillman & Kennicutt 1993), the flux of hydrogen ionizing

¹A distance of 10 Mpc to I Zw 18 is adopted throughout this paper (Viallefond, Lequeux, & Comte 1987).

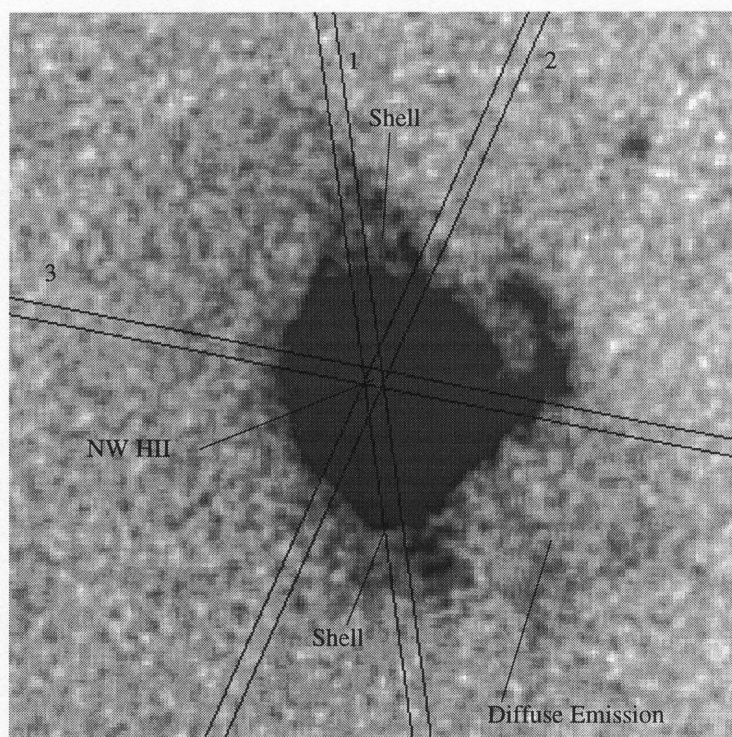


Figure 4.1 (a) $H\alpha$ image of I Zw 18 with echelle slit positions overlaid. (b) Same as (a) but the intensity is displayed on a logarithmic scale to show the structure of the inner nebula.

photons is $1.4 \pm 0.2 \times 10^{52} d_{10}^2 \text{ s}^{-1}$, where d_{10} is the distance to I Zw 18 in units of 10 Mpc (see Table 4.1). This ionizing luminosity is similar to that of 30 Doradus in the Large Magellanic Cloud (Kennicutt 1984). A spherical, homogeneous nebula of this size would have an rms electron density of $n_{\text{rms}} = 0.39 \pm 0.04 d_{10}^{-1/2} \text{ cm}^{-3}$. The ratio of the [SII] $\lambda\lambda 6717, 31$ line fluxes is near the low density limit, so the actual electron density in the emission line filaments is $n_e < 250 \text{ cm}^{-3}$. The volume filling factor of the ionized filaments must be at least $\epsilon > 1.0 \times 10^{-3}$, where $\epsilon \equiv n_{\text{rms}}^2 / n_e^2$. The estimated mass of ionized gas is then $M_{\text{HII}} = 1.0 \pm 0.1 \times 10^7 M_{\odot} \sqrt{\frac{\epsilon}{0.01}} d_{10}^{5/2}$. To estimate the radial density profile, the $\text{H}\alpha$ surface brightness was azimuthally averaged in annuli around the NW HII region. Assuming the nebula is spherical, inversion of the $\text{H}\alpha$ surface brightness integral implies $n_{\text{rms}} = n_e \sqrt{\epsilon} \propto r^{-1}$ within $7''$ (340 pc) of the NW HII region, and $n_{\text{rms}} = n_e \sqrt{\epsilon} \propto r^{-2}$ between $7''$ and $15''$ (730 pc).

Table 4.1 Properties of I Zw 18

Quantity	Value	Source
d	10 Mpc	1
B_T^0	15.8 mag	2
M_B	-14.2 mag	
$F_{H\alpha}$	$6.0 \pm 0.9 \times 10^{-13} \text{ ergs s}^{-1} \text{ cm}^{-2}$	
Q	$1.4 \pm 0.2 \times 10^{52} \text{ s}^{-1}$	
M_{HII}	$1.0 \pm 0.1 \times 10^7 M_{\odot} \sqrt{\frac{\epsilon}{0.01}}$	
M_{HI}	$6.63 \pm 1.06 \times 10^7 M_{\odot}$	1
$(U-B)_0^+$	-0.88 mag	3
$(B-V)_0^+$	-0.01 mag	3

1) Lequeux & Viallefond (1980)

2) Melisse & Israel (1994)

3) Colors corrected for emission lines but not nebular continuum; Sudarsky (1995).

Note: ϵ is the volume filling factor.

4.2.2. High-Resolution Spectroscopy

Longslit spectra of the H α line were obtained 1994 April 29 and 30 using the echelle spectrograph on the KPNO 4 m telescope. Three position angles were chosen based on the morphology of the H α emission (see Figure 4.1). An astrometric offset was used to center the slit on the NW HII region, and three 20 minute integrations were obtained at each position angle. The 1".5 slit produced a spectral resolution of $\sim 11 \text{ km s}^{-1}$ FWHM. The instrumental setup, calibration techniques, and data reduction are further described by Martin and Kennicutt (1995). The seeing varied from 1-2" FWHM, so spectra were extracted every 1".8 along the slit to maximize the spatial information. This binning provided sufficient S/N to measure the line center to an accuracy of 0.1 Å and fit two-component Gaussian line profiles down to the faintest intensities visible in Figure 4.1a.

The echellograms reveal the kinematic signatures of two expanding supergiant shells. Figure 4.2 shows the echellogram along slit 1, PA = 7.7°. Southwest of the NW HII region (continuum source), the line profile splits into two components forming a Doppler ellipse. Similar kinematic signatures have been observed in other starbursting, gas-rich dwarfs and almost certainly indicate the presence of an expanding shell of gas (Marlowe et al. 1995; Martin 1996). This Doppler ellipse extends 19" (930 pc) to the SW, and the maximum separation of the line-of-sight velocities reaches 59 km s^{-1} . Fits to the line profile northeast of the HII region are improved with a faint, secondary component redward of the main component, thereby providing some evidence for a second Doppler ellipse coincident with the NE shell in the H α image.

The asymmetry in the line profiles of these shells suggest the superbubbles form the two lobes of a bipolar bubble with polar axis inclined relative to our line-of-sight. In the NE Doppler ellipse the intensity of the blueshifted component

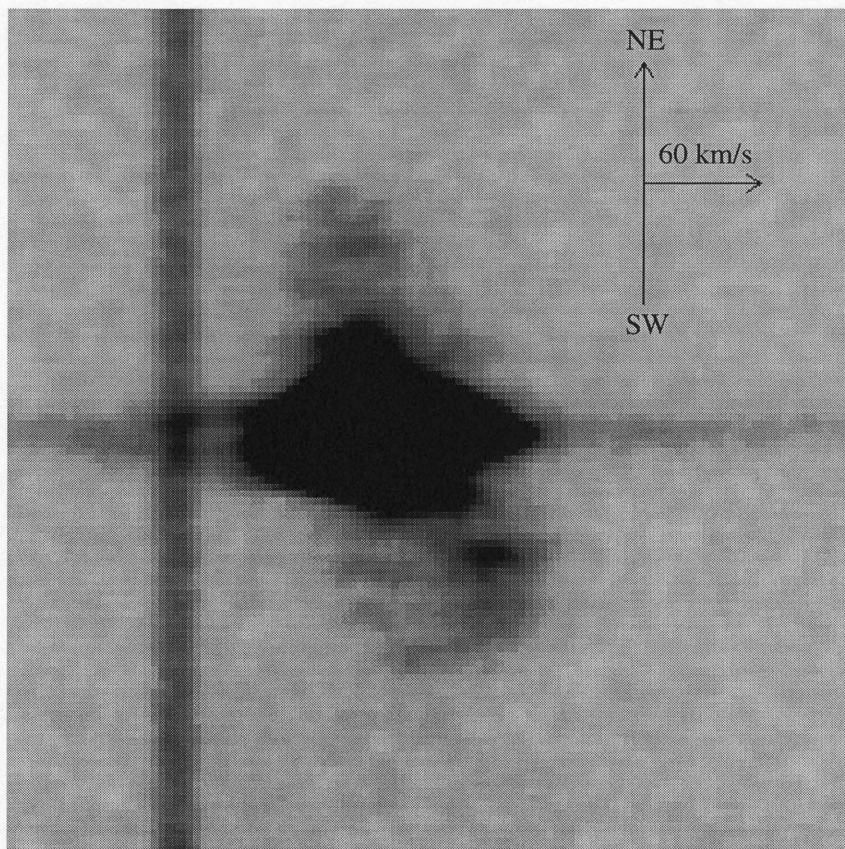


Figure 4.2 Echelle spectrum of $H\alpha$ emission line along slit 1. The horizontal line is the continuum of the NW HII region. A prominent Doppler ellipse is visible to the SW, and a second Doppler ellipse is discernible to the NE. Blue wings from high velocity gas near the HII region extend past the night-sky emission line (vertical line). The vertical arrow is approximately $20''$ long.

is several times higher than that of the redshifted component, but their relative intensities are reversed to the SW. This effect is illustrated in Figure 4.3, where the symbol “X” denotes the position of the weaker component in position-velocity space. The lack of line-splitting along the other slit positions lends credence to the bipolar bubble interpretation.

We also detect gas with velocities up to $\pm 230 \text{ km s}^{-1}$ from the systemic velocity and tentatively associate it with the small shell. These high-velocity wings are stronger on the blue side of the line profile and coincident with the small shell along all three slit positions. However, since this high-velocity component contributes only 5% of the line flux, the only other region with high enough signal-to-noise to reveal these wings is the SE HII region; and examination of the data along slit 2 shows a similar wing contributes 3% of the $\text{H}\alpha$ flux there. We hesitate to identify the high-velocity gas with an expanding shell because no Doppler ellipse is seen where slit 3 crosses the center of the small shell. A champagne flow (Yorke, Tenorio-Tagle, & Bodenheimer 1984) from the young HII regions and stellar winds might provide a better description of the gas kinematics.

The detection of large, expanding shells of gas reopens the question of whether galactic rotation produces all the velocity shear across the gas distribution. In Figure 4.3 the solid circles trace the velocity of the dominant component of the $\text{H}\alpha$ emission along each of the three slit positions. Along slit 1, the velocity is fairly constant to the NE but increases by $\sim 73 \text{ km s}^{-1}$ to the SW. At least part of this velocity shear is likely an artifact of the expansion of the superbubble. Along slit 2, $\text{PA} = 156.1^\circ$, the velocity gradient is steeper on the SE side of the nebula. Since this slit position is nearly parallel to the HI major axis, it might be expected to reveal the galactic rotation curve. However, the change in slope near the NW HII region and the similarity to the velocity gradient along slit 1 leave some ambiguity

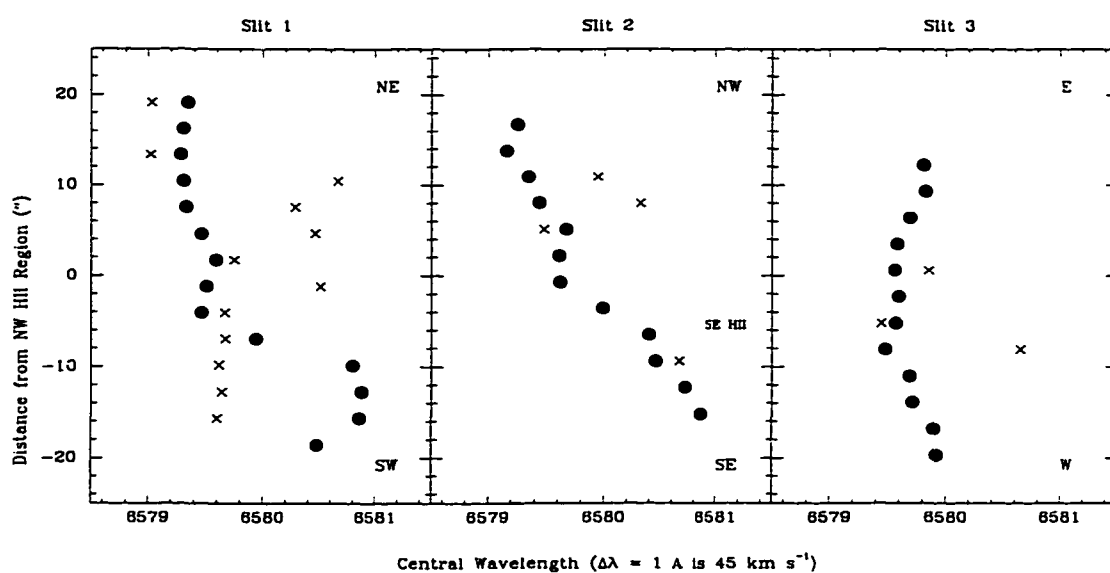


Figure 4.3 H α position-velocity diagrams. Circles mark the central wavelength of the brightest H α component, and X's denote the relative velocity of the second brightest component in the line profile. Slit positions are described in the text and shown in Figure 4.1a.

between the effects of galactic rotation and the expansion of the superbubble. The velocity is nearly constant along slit 3, $PA = 78.8^\circ$, which is 24° from the HI minor axis.

Along all three slit positions, the large-scale variations in the central velocity of the $H\alpha$ line appear to be shared by the HI velocity field (Viallefond et al. 1987). Given the better spatial coverage of the HI map and the strong suggestion of galactic rotation in it, we provisionally attribute the velocity gradient across echelle slit 2 to galactic rotation. Higher resolution HI observations are needed to determine whether the kinematic signatures of the bubbles are present in the HI and what affect they might have on the global HI velocity field. A significant perturbation on the local velocity field is already evident in the NE finger of HI, which is coincident with our large $H\alpha$ shell. The iso-velocity contours there depart from the overall pattern, and the HI radial velocity decreases by about 20 km s^{-1} across the $H\alpha$ shell.

4.2.3. X-Ray Detection

I Zw 18 was observed with the Position Sensitive Proportional Counter (PSPC) on the Röntgensatellit (ROSAT) for 16,964 sec during 1992 April 30 - 1992 May 11. We requested the data, originally obtained by Dr. C. Motch, from the ROSAT public archive. An unresolved X-ray source is located $2''.6$ W and $6''.6$ S of the peak red continuum emission. Pointing errors of this magnitude are typical for ROSAT observations, and we identify the X-ray source with I Zw 18. It is not clear whether a second, fainter source located $82''$ to the NNW is associated with I Zw 18. After background subtraction, the remaining ~ 130 net counts are insufficient to constrain a spectral fit. The X-ray colors, however, suggest a fraction of the X-ray flux is produced by hot, coronal gas in the ISM. The emission is slightly harder than the soft emission from the dwarf NGC 5253 (Martin &

Kennicutt 1995), but considerably softer than the hard sources, thought to be massive X-ray binaries, near the center of NGC 2403 (Martin 1996). To estimate the X-ray luminosity, L_x , in the ROSAT band (0.1 – 2.2 keV), a series of power law, bremsstrahlung, and Raymond-Smith spectral models were normalized to the total counts. For a Galactic absorbing column $N_{HI} \lesssim 2 \times 10^{20} \text{ cm}^{-2}$ (Heiles 1975; Stark et al. 1992), they all produced $L_x \approx 1 \times 10^{39} \text{ ergs s}^{-1}$ within a factor of two. For example, a Raymond-Smith model for a $5 \times 10^6 \text{ K}$ plasma of 10% solar abundance with a foreground absorbing column of $\log N_{HI} = 20.2$ implies $L_x = 1.1 \times 10^{39} \text{ ergs s}^{-1}$.

Until ROSAT HRI observations are obtained, the extent of the source will remain unknown. At 1 keV the FWHM of the ROSAT/PSPC point spread function is $24''$, about half the angle subtended by the $H\alpha$ emission along slit 1. However, the radius encircling 95% of the photons is substantially larger – about $45''$ (Hasinger et al. 1992) – so a diffuse halo should not be ruled out. If the X-ray source is found to reside deep within the galaxy, the intrinsic absorption column could be as high as $N_{HI} = 3.5 \times 10^{21} \text{ cm}^{-2}$ (Kunth et al. 1994); and the estimated X-ray luminosity would be increased by a factor < 7 , where the upper limit is derived for a column with solar abundances.

4.3. Modeling the Gas Dynamics

In this section, a simple model for a wind-blown bubble is used with the kinematic and morphological properties described in § 4.2 to constrain the dynamical age of the superbubble and the mechanical energy supplied to it. The luminous properties of a starburst which could drive the expansion are computed and compared to the integrated properties of the galaxy.

4.3.1. The Superbubble Model

The dynamical arguments presented in this paper are based on the standard model for a stellar wind bubble with a radiative shell (e.g. Castor, J., McCray, R., & Weaver, R. 1975; Weaver, McCray, & Castor 1977). The conceptual framework is illustrated schematically in Figure 4.4. Stellar winds and supernova explosions from hundreds of massive stars fuel a supergiant bubble over timescales $\gtrsim 10^7$ yr (zone 1). The kinetic energy in the ensemble's supersonic wind is thermalized by a stand-off shock, and the high pressure (zone 2) downstream drives a strong shock into the ambient ISM (zone 4). The swept-up gas condenses into a shell (zone 3) as a result of radiative cooling.

The solution for the shell's evolution as formulated by Ostriker & McKee (1988) provides a convenient power-law parameterization of a density gradient in the ambient medium,

$$\bar{\rho} = \bar{\rho}(1) \left[\frac{R_s}{R_s(1)} \right]^{-\kappa_\rho}, \quad (4.1)$$

and a time-dependent energy injection rate,

$$L_{in} = L_{in}(1) \left[\frac{t}{t(1)} \right]^{\eta_{in}-1}. \quad (4.2)$$

In this notation, $\bar{\rho}(1)$ is the average density of the ambient ISM within the fiducial radius $R_s(1)$, and supernovae and stellar winds supply a mechanical power $L_{in}(1)$ at time $t(1)$. The parameters $t(1)$ and $R_s(1)$ are not independent and must satisfy the relation $R_s/R_s(1) = (t/t(1))^\eta$, where $\eta \equiv (2 + \eta_{in})/(5 - k_\rho)$.

The radius of the spherical swept-up shell is

$$R_s(t, L_{in}(1)/\bar{\rho}(1)) = R_s(1) \left(\frac{\xi \Gamma L_{in}(1)}{\eta_{in} \bar{\rho}(1) R_s(1)^5} \right)^{\eta/3} t^\eta, \quad (4.3)$$

where ξ and Γ are numerical constants on the order of unity as defined by Ostriker & McKee (1988) and evaluated for a ratio of specific heats $\gamma = 5/3$. The shell

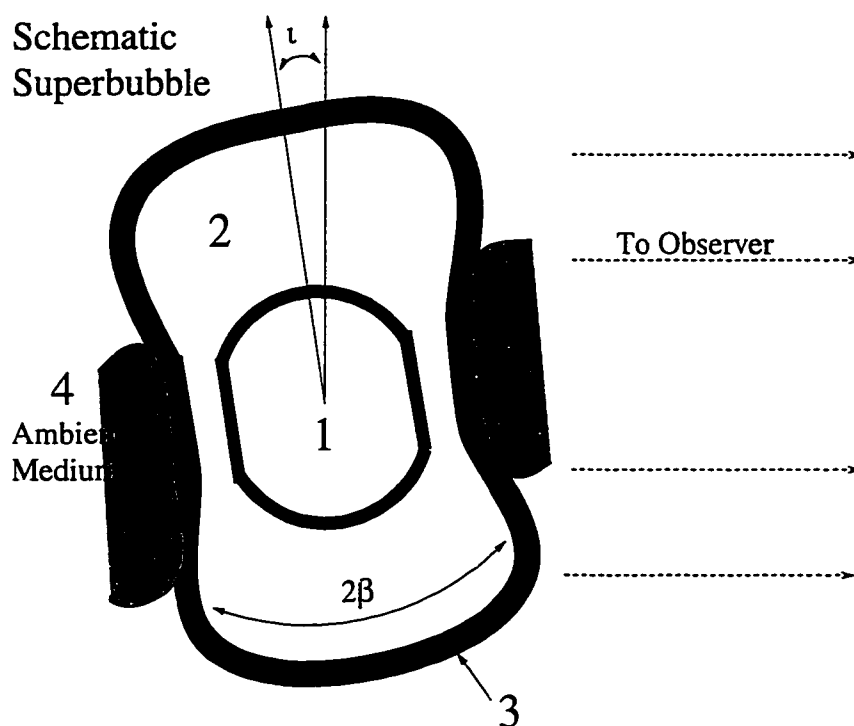


Figure 4.4 Cross section of favored bipolar bubble geometry. Heavy, solid lines represent the shocked shell (zone 3) of swept-up ambient medium (zone 4) and the stand-off shock separating the hot bubble (zone 2) and the starburst (zone 1). The polar axis is inclined $\iota \sim 10^\circ$ to our line-of-sight, and the angle subtended by a lobe from the central starburst is $\beta \sim 30^\circ$.

velocity is

$$v(t, L_{in}(1)/\bar{\rho}(1)) = \frac{dR_s}{dt} = \eta R_s(1) \left(\frac{\xi \Gamma L_{in}(1)}{\eta_{in} \bar{\rho}(1) R_s(1)^5} \right)^{\eta/3} t^{\eta-1}. \quad (4.4)$$

Solving equations 4.3 and 4.4 gives the dynamical age of the bubble,

$$t = \eta \frac{R_s}{v}, \quad (4.5)$$

and the ratio of the mechanical power to ambient density,

$$\frac{L_{in}(1)}{\bar{\rho}(1)} = \frac{\eta_{in}}{\xi \Gamma \eta^3} R_s(1)^{(5\eta-3)/\eta} v^3 R_s^{3(1-\eta)/\eta}. \quad (4.6)$$

The total mechanical energy injected into a bubble of age t is

$$E_{in}(t) = \frac{L_{in}(1)t(1)}{\eta_{in}} \frac{t^{\eta_{in}}}{t(1)^{\eta_{in}}}. \quad (4.7)$$

4.3.2. Application to I Zw 18

The Doppler ellipse discovered SW of the HII regions is not the signature of a spherical shell expanding radially. The measured radius and velocity would require a burst of star formation in the center of the bubble about 6 Myr ago which supplied $E_{in} = 1.8 \times 10^{53} \bar{n}(1)$ ergs of kinetic energy. The continuous emission from the fading population would easily be detected in our red continuum image.

We favor interpreting the data in the context of an expanding bipolar bubble. The bright $H\alpha$ emission coincident with the SW shell shares a common symmetry axis with the NE loop, which may form the second lobe. This polar axis intersects the brightest region of the galaxy – the obvious place for a power source. The reversal of the shape of the $H\alpha$ line profile between the two bubbles also supports this interpretation since it is easily explained by tilting the bubble with respect to our line-of-sight. Overall, the kinematic signature is reminiscent of that along the minor axis of M82, which exhibits the quintessential superwind (Heckman,

Armus, & Miley 1990; Martin 1996). However, while the outflow in M82 is clearly confined at its waist by the galactic disk, the collimating mechanism in I Zw 18 is not apparent. The polar axis presumably depicts the projection of the steepest pressure gradient, which we might expect to be perpendicular to the HI major axis. The proposed polar axis is 43° from the PA of the HI major axis in the map of Viallefond et al. (1987). We note that the major axis of the very diffuse, extended H α emission is perpendicular to the HI major axis.

To estimate the radius and expansion speed of the SW lobe from the data, we introduce two simplistic models for the shape and velocity field of the bipolar shell. A cone of half-opening angle β and inclination i , as illustrated in Figure 4.4, represents the thick shell behind the outer shock. We assume the density decreases as r^{-2} , where r is the distance from the starburst, which is consistent with the decline in surface brightness in our H α image. The inclination is not large because the shifts of the red and blue components of the SW Doppler ellipse with respect to the central velocity are similar. We estimate $\beta \sim 30^\circ$ from the width of the NE loop. An inclination of $i \sim 10^\circ$ then produces an intensity contrast of 2 – 3, similar to the data. The radial extent of the Doppler ellipse is essentially the length of the polar axis. In our “isobaric bubble” model, the shell velocity is normal to the conical surface, geometrical corrections are small, and we estimate an expansion speed $v \sim 35 \text{ km s}^{-1}$. (The variations in the magnitude of the velocity around the shell is thought to be considerably smaller.) In our “wind” model, the flow is radial, mimicking the boundary layer between a freely expanding supersonic wind and the halo, and the deprojected shell speed is $v = 61 \text{ km s}^{-1}$. Hence, the shell velocity is uncertain by a factor of 2. The uncertainty in the radius is dominated by the difference, about 20%, between the two lobes.

Despite the complex geometry, we apply the dynamical model of § 4.3 along

the polar axis. We expect to estimate the dynamical age to within a factor of two and $E_{in}/\bar{n}(1)$ to better than an order of magnitude based, primarily, on the uncertainties in radius, velocity, and density gradient (k_ρ) rather than the choice of dynamical model. The magnitude of the errors are believed to be similar. For example, the height of the polar lobe is larger than the radius of a spherical bubble supplied with the same energy, but a radial density gradient could also easily increase R by a factor of two relative to the constant density case. Our best estimate of the dynamical age from the isobaric bubble and wind geometries are 27 Myr and 15 Myr, respectively. The bubble requires $E_{in} = 7.5 \times 10^{54} \bar{n}(1)$ ergs of kinetic energy while the wind geometry increases the estimate to $E_{in} = 2.2 \times 10^{55} \bar{n}(1)$ ergs.

The mean density of the ambient ISM swept up by the shell is expected to be low. If all the HI gas were compressed into a uniform sphere the size of the bipolar bubble ($R_s \sim 900$ kpc), the average density would be $\bar{n}(1) = 0.63 \text{ cm}^{-3}$, where the number density $\bar{\rho}(1) = \bar{n}(1)m_H\mu$ and $\mu = 1.4$ amu is the average mass per H atom for a composition H:He = 10:1 by number. Adding the density of ionized H in the nebula (§ 4.2.1) yields an upper limit $\bar{n}(1) < 1 \text{ cm}^{-3}$ for the $k_\rho = 0$ models. Spreading the HI out uniformly over the HI clouds suggests a lower limit of $0.019 \text{ cm}^{-3} < \bar{n}(1)$. To explore the effect of a density gradient on galactic scales, we calculated models with $k_\rho = 1$ and 2 and $R_s(1) = 100$ pc. By an analogous argument, the acceptable ranges for the ambient density interior to $R_s(1)$ are $0.57 \lesssim \bar{n}(1) \lesssim 3.1 \text{ cm}^{-3}$ and $5.3 \lesssim \bar{n}(1) \lesssim 15 \text{ cm}^{-3}$, for $k_\rho = 1$ and 2 respectively. These central densities are similar to estimates of the HI density in the center of the main cloud ($\sim 10 \text{ cm}^{-3}$) and the rms electron density in the NW HII region.

4.3.3. The Star Formation History

Either a recent starburst or an IMF heavily biased towards massive stars can produce colors as blue as observed for I Zw 18. Searle & Sargent (1972) ruled out

the latter interpretation for I Zw 18 with a measurement of the gas phase O/H abundance ratio. Recently the stellar content of the starburst has been studied using very high spatial resolution. Stars down to O9.5 on the main sequence are resolved in broad-band, HST images (Hunter & Thronson 1995), and Hunter & Thronson identify three spatially distinct populations. First, the stars inside the small shell have ages from 1– 5 Myr. The second population in the southern component has no red supergiants (RSGs) and is probably younger. The third population is spread throughout the galaxy, comprises roughly half of the resolved stars, and is likely to be older than the shell population since it contains more red stars. In addition to this “general galaxy” population, an older, unresolved population with the colors of B or early A stars follows the main body of the galaxy and has an age $\gtrsim 10^7$ Myr.

Our detection of high velocity gas near the small shell confirms the observations of Davidson et al. (1989) and supports the conclusion of Hunter & Thronson (1995) that the shell population powers the small shell. As discussed in § 4.2.2, our data do not unambiguously determine the expansion velocity of the shell. So, it remains unclear whether a few massive stars that formed early created the shell, or whether a younger bubble is driven by many stars.

The supergiant bubble is clearly older than the shell cluster. Could its dynamical age indicate the duration of the starburst in I Zw 18 ? To check the consistency of this hypothesis, we use the evolutionary synthesis models of Leitherer & Heckman (1995) to describe the photometric properties of a stellar population which could power the bubble. We adopt their lowest metallicity models, $0.1Z_{\odot}$, and consider only an IMF of slope $\alpha = 2.35$, $M_{up} = 100 M_{\odot}$, and $M_{low} = 1 M_{\odot}$. Several integral properties of I Zw 18 are listed in Table 4.1 for comparison.

An instantaneous burst model is not a good description of the star formation

history of I Zw 18. A 15 Myr old population that produced hydrogen ionizing photons at the observed rate would generate 300 times more blue luminosity than observed. A continuous star formation rate over the 10 – 30 Myr lifetime of the bubble seems reasonable (cf. Meurer et al. 1995) and is consistent with the detection of stars only a few million years old (Hunter & Thronson 1995). Up to an age ~ 40 Myr, the mechanical power, $L_{in}(t)$, generated by this burst will grow with time as shown in Figure 56 (lower right) of Leitherer & Heckman (1995), and we incorporate this evolution in our dynamical model by setting $\eta_{in} = 3$ and $t(1) = 40$ Myr. The steep increase in the wind power keeps the shell moving at a constant velocity, which would also be obtained from a $k_p = 2$ density gradient.

The continuous star formation model produces a stellar population whose photometric properties resemble I Zw 18. As shown in Table 4.2, this result is not very sensitive to our choice of geometry as represented by the “isobaric bubble” and “wind” models. At dynamical ages of 15 Myr and 27 Myr, star formation rates of $0.021 \text{ M}_{\odot} \text{ yr}^{-1}$ (of 1 to 100 M_{\odot} stars) and $0.017 \text{ M}_{\odot} \text{ yr}^{-1}$, respectively, are required to generate the blue luminosity of I Zw 18. These model populations produce only half of the ionizing luminosity measured and are a bit redder than I Zw 18. This discrepancy is not bothersome as roughly 20% of the $H\alpha$ flux comes from the compact source on the eastern edge of the small shell. We could speculate that this star formation is an isolated, triggered event or that the global star formation rate is increasing. This population might be too young and hot to contribute substantially to the blue luminosity.

The continuous burst models easily produce enough supernovae and stellar winds to drive the superbubble. After 15 Myr and 27 Myr, the kinetic energy imparted to stellar ejecta is 6.6×10^{53} ergs and 2.7×10^{54} ergs, respectively. Since our echelle data constrain the ratio $E_{in}/\bar{n}(1)$ rather than E_{in} alone, we can choose the ambient

density, $\bar{n}(1)$, to make our dynamical model consistent with the starburst model of the same age. The inferred densities, 0.03 cm^{-3} and 0.36 cm^{-3} , are within the range estimated from the HI data in § 4.3.2.

4.3.4. Results

The aim of our modeling exercise was to describe the range of star formation histories that could easily explain the gas kinematics in I Zw 18. Uncertainties about the geometry of the superbubble and the distribution of the ambient gas limit the accuracy of our analysis. We stepped through the analysis for two models representing the likely range of shell velocities. We found that the star formation necessary to power the superbubble also produces most of the starburst's luminosity. This epoch of star formation probably started 15 – 27 Myr ago. We favor a higher age within this range because our “isobaric bubble” model is probably the closer analogy to the actual shell kinematics and also predicts a volume-averaged ambient density closer to expectations.

The evolutionary tracks for low metallicity, massive stars are controversial (e.g. Renzini et al. 1992) and could introduce errors in the models for the young starbursts. Near an age of 4 Myr, the blue luminosity of the $0.1 Z_{\odot}$ instantaneous burst brightens 65% more than the solar metallicity models (Figure 9 of Leitherer & Heckman 1995). Eliminating this jump would increase the ratio of ionizing luminosity to blue luminosity (Q/L_B). Since the error diminishes with age and an increase in Q/L_B would actually improve the agreement with the observations, a small error of this nature will not change our conclusions.

4.4. Discussion

In this section, we use our results from § 4.3 to explore the influence of the superbubble on the evolution of I Zw 18. A particularly interesting issue is the amount of global mass loss driven by the burst of star formation. It has been argued on a theoretical basis that a global wind created by the first burst of star formation may eject the interstellar gas from a dwarf galaxy (e.g. Larson 1974;

Saito 1979; Dekel & Silk 1986; Vader 1986). The transformation of gas-rich dwarfs to dwarf ellipticals by this mechanism is appealing but is not completely consistent with the systematic structural properties of dwarfs (Ferguson & Binggeli 1995, and references therein). It has also been emphasized that the escaping wind should be metal-enriched with elements recently dispersed in Type II supernovae (Vader 1987; DeYoung & Gallagher 1990). These differential galactic winds have been independently invoked to explain the locus of blue compact and dwarf irregular galaxies in the N/O - O/H and He/H - O/H planes (Marconi, Matteucci, & Tosi 1994). In § 4.4.1, we discuss the conditions necessary for the bipolar bubble to develop into a galactic wind, the escape of the hot gas from the galaxy's gravitational grip, and the mass of cooler gas permanently ejected. In § 4.4.2, we discuss the mass of metals produced by our starburst models and the role of the superbubble in mixing these elements into the interstellar gas. In § 4.4.3, measurements of O/H abundance variations are presented and discussed.

4.4.1. A Starburst-Driven Galactic Wind

Development of an Outflow

The power requirement for the superbubble to break free of the ISM is characterized by the minimum mechanical power, L_P , necessary for the bubble to grow as large as the gaseous extent of the galaxy. Following the derivation of Koo & McKee (1992), in which the effective scale height is defined by

$$H_{eff} \equiv \frac{1}{\rho_0} \int_0^\infty \rho(z) dz, \quad (4.8)$$

the critical rate of kinetic energy injection is

$$L_P = 17.9 \rho_0 H_{eff}^2 c_{s,0}^3 \text{ ergs s}^{-1}, \quad (4.9)$$

where $c_{s,0}$ and ρ_0 are the isothermal sound speed and midplane gas density in the ambient medium. Since $c_{s,0}$ is intended to serve as a measure of the pressure

in the ISM, we interpret $c_{s,0}$ as the effective one-dimensional velocity dispersion of the HI gas. The velocity dispersions measured in galactic disks typically fall in the narrow range from 3 – 10 km s⁻¹ (Kennicutt 1989), consistent with the estimate of 8 km s⁻¹ for the Galactic disk (McKee 1990). The HI linewidth provides an upper limit of $\sigma = 19$ km s⁻¹ (Kunth et al. 1994). From HI observations (Viallefond et al. 1987; Lequeux & Viallefond 1980), we estimate a scale height $360 \text{ pc} \lesssim H_{eff} < 720 \text{ pc}$. In units of $c_{s,0} = 13 \text{ km s}^{-1}$ and $H_{eff} = 360 \text{ pc}$, the “breakout” threshold is

$$\frac{L_P}{n_0} = (1.13 \times 10^{38}) \text{ ergs s}^{-1} \text{ cm}^3 H_{360}^2 c_{13}^3, \quad (4.10)$$

where $n_0 = \rho_0/(\mu m_H)$ is the midplane number density. The HI density in the core of the main cloud provides an upper limit of $n_0 \sim 9 \text{ cm}^{-3}$. Normalized to the blue luminosity of I Zw 18, our isobaric bubble and wind models in § 4.3 had average $\langle L_{in}(t) \rangle$ of $3.2 \times 10^{39} \text{ ergs s}^{-1}$ and $1.4 \times 10^{39} \text{ ergs s}^{-1}$ after 27 Myr and 15 Myr, respectively. We conclude that the bipolar bubble will likely break through the HI layer supersonically.

To open a channel for the hot gas inside the bubble to flow out of the galaxy, the shell must accelerate and break up from Rayleigh-Taylor instabilities. Mac Low & McCray (1988) and Mac Low, McCray, & Norman found that the wind luminosity required for this “blowout” to occur is larger than L_P . Their numerical simulations suggest that $L_{in}/L_P \gtrsim 5$ is a sufficient condition for blowout. Large $L_{in}/L_P \sim 1000$ produced blowout when the shell reached a height $\sim 3H_{eff}$; but, for smaller L_{in}/L_P , they suspect the bubble may grow larger in the z-direction before blowing out. For $n_0 = 1 \text{ cm}^{-3}$, the ratio of the superbubble’s mechanical power to the characteristic luminosity is $L_{in}/L_P = 12 - 28$, and we expect the superbubble to blowout.

Gravitational Potential

The mass of gas that will escape from the galaxy following blowout depends on the depth of the gravitational potential well. We assume the mass distribution is similar to an isothermal sphere and use the circular velocity, $v_c^2 = r d\phi/dr$, to estimate the depth of the potential well. For a halo that extends to r_{\max} , the escape velocity is given by

$$v_{\text{esc}} = \sqrt{2}v_c\sqrt{1 - \ln(r/r_{\max})}. \quad (4.11)$$

Using Bernoulli's theorem, we find the corresponding escape temperature,

$$T_{\text{esc}} = \frac{\gamma - 1}{2\gamma} \frac{\mu m_H}{k} v_{\text{esc}}^2, \quad (4.12)$$

which describes the specific thermal energy required to establish a smooth, supersonic outflow.

If the velocity gradient along the HI major axis of I Zw 18 is produced by a rotating disk, then the deprojected circular velocity is $v_c \sim 40 \text{ km s}^{-1}$. The dynamical mass is then $\sim 9 \times 10^8 M_\odot$ (Viallefond et al. 1987), and halos truncated at 1 kpc and 10 kpc, masses of $3.7 \times 10^8 M_\odot$ and $3.7 \times 10^9 M_\odot$ respectively, provide representative models. For reference, the escape velocity and escape temperature are tabulated in Table 4.3 as a function of radius.

Mass Loss

The predicted temperature for the bubble interior, $\sim 5 \times 10^6$ K (from Eqn. 4 of Martin & Kennicutt 1995), is considerably higher than the escape temperatures shown in column 4 of Table 4.3, so the hot bubble interior (zone 2) should easily escape following blowout. The ensuing question is how much mass resides in this hot phase of interstellar gas. In the canonical superbubble model, the hot interior is composed of shocked stellar ejecta and material conductively evaporated off the swept-up shell. From Eqn. 9 of Shull (1993), we estimate that the evaporated mass is $\sim (4 - 11) \times 10^5 M_\odot$, which is an order-of-magnitude more than the $\sim (2 - 5) \times 10^4 M_\odot$ of enriched gas returned to the ISM by the starburst models. Clouds that get run over by the shell and evaporate in the bubble's hot interior may further mass load the bubble (Martin & Kennicutt 1995).

Unfortunately, the X-ray observation provides only a rough upper limit on the mass of hot gas. If all the X-ray flux comes from hot gas of density n_x , the observed luminosity implies a mass of coronal gas $M_x \sim (1.1 \times 10^6 M_\odot)(0.05 \text{ cm}^{-3}/n_x)$ for a plasma with cosmic abundance. (Although the value of n_x is unknown, arguments about the gas pressure in the ISM suggest it is unlikely to exceed 0.05 cm^{-3} .) At a lower metallicity, the emissivity is expected to be lower, so the inferred mass would be even higher. This analysis merely demonstrates that thermal emission from hot gas could make a substantial contribution to the X-ray luminosity.

Although some of the gas in the shell may escape from the galaxy with the hot wind, the starburst will probably not eject the entire ISM of I Zw 18. For example, the escape velocity from the lower mass halo in Table 4.3 is $\sim 60 \text{ km s}^{-1}$ near the shell radius. Since the deprojected shell velocity is probably $30 - 60 \text{ km s}^{-1}$, only fragments of the ruptured shell could coast out of the galaxy. However, the starburst would have to transfer $\sim 7 \times 10^{54}$ ergs of kinetic energy to the interstellar

gas to accelerate all the HI to 100 km s^{-1} , a typical escape velocity in Table 4.3. In the spherical superbubble model, only 20% of the injected mechanical energy is converted into the shell's kinetic energy, so the starburst would have to generate at least 4×10^{55} ergs of mechanical energy to completely eject the ISM. In § 4.3.3 we estimated values of E_{in} over an order of magnitude smaller than this, so the complete ejection of the ISM is not energetically possible.

4.4.2. Chemical Enrichment of the ISM

Our dynamical interpretation of the gas kinematics has two interesting implications for the chemical enrichment of I Zw 18. First, elements synthesized and ejected by the starburst's massive stars may have been transported $\sim 900 \text{ pc}$ across the bubble interior in only 15 – 27 Myr. Second, most of the oxygen produced may not reside in the warm, ionized gas – a puzzle independently pointed out by others (e.g. Kunth & Sargent 1986). Using a fit to the oxygen yields calculated for 12 – 100 M_{\odot} stars (Prantzos 1994), we derive an oxygen yield $y = 0.01$ for an IMF with lower and upper mass limits of 0.1 M_{\odot} and 100 M_{\odot} and slope $\alpha = 2.35$, where y is the ratio of the net mass of oxygen produced to the total mass permanently locked up in remnants (e.g. Tinsley 1980). The starburst models in § 4.3.3 formed $(3 - 5) \times 10^5 M_{\odot}$ of 1 – 100 M_{\odot} stars, or about $(8 - 12) \times 10^5 M_{\odot}$ of 0.1 – 100 M_{\odot} stars, so $9 \pm 3 \times 10^3 M_{\odot}$ of oxygen are returned to the interstellar gas. If all this oxygen was mixed into the warm, ionized gas, the metallicity of the HII regions would be 5 – 6 times higher than measured.

The oxygen would have to be mixed throughout the entire mass of HI to produce a homogeneous oxygen abundance as low as 2% $(O/H)_{\odot}$. This unlikely scenario contradicts our hypothesis that the current burst is the first major star formation episode and that the size of the bubble is an indication of the mixing scale. We suggest that the extra oxygen may still be in the hot phase of the interstellar gas

– zone 2 in Figure 4.4. Assuming a remnant mass of $1.5 M_{\odot}$ for the stars in the $12 - 100 M_{\odot}$ range, we estimate that 10% of the mass turned into stars has been returned to the ISM. The oxygen mass fraction of this gas is then $X_O \approx 9 X_O^{\odot}$, where the solar value is $X_O^{\odot} = 9 \times 10^{-3}$ (Grevesse & Noels 1993). Gas evaporated from the cooler phases of the ISM will dilute the hot stellar ejecta (§ 4.4.1), and we expect oxygen to comprise $\lesssim 2\%$ of the mass of hot interstellar gas (i.e. $X_O \sim X_O^{\odot}$).

4.4.3. The O/H Abundance Ratio in the Ionized Gas

If the superbubble plays a prominent role in the dispersal of metals over large scales in I Zw 18, significant abundance inhomogeneities might be expected (cf. Kunth et al. 1994). We have examined deep longslit, optical spectra of I Zw 18, obtained for a related project (Martin 1996), to search for an abundance edge to the metal-enriched region and to constrain the chemical homogeneity of the ionized gas.

Optical Spectrophotometry

Longslit optical spectra of I Zw 18 were obtained in 1994 on the MMT using the Blue Channel Spectrograph equipped with a Loral $3k \times 1k$ CCD detector. A 500 gpm grating blazed at 5410 \AA in 1st order was used with a UV-36 blocking filter and a $1''$ slit. This configuration provides spectral coverage from approximately 3700 \AA to 6800 \AA at a moderate spectral resolution, about $\sim 5 \text{ \AA FWHM}$. Spectra were obtained at two slit positions, one centered on the NW HII region and rotated to PA 7.6° (slit A) and another positioned across the SE HII region at a PA of 131.0° (slit B); the total integration times were 12,000 s and 9,900 s, respectively. The spectrum of the night sky background was recorded on both ends of the slit. The seeing limited the resolution along the slit to $\sim 2''$. Care was taken to monitor

the effects of varying parallactic angle over the time sequence of frames (Filippenko 1982).

The data reduction followed standard techniques and employed the IRAF² software package. The raw CCD frames were bias subtracted, corrected for pixel-to-pixel sensitivity variations and slit illumination, transformed using exposures of an HeNeAr arc lamp, and extinction corrected. A new field flattener was being tested during the November run, and these data required an additional distortion correction. Cosmic rays were removed when the individual frames were combined. The spectra were flux calibrated using observations of standard stars (Massey et al. 1988).

Primordial Ionized Gas?

Figure 4.5 demonstrates that the ionized gas across the region where the superbubbles are detected is not primordial. The [OIII] $\lambda 5007$ emission extends along slit “A” as far (23” or 1100 pc) to the SW as the H β emission line which has comparable intensity. To the NE the intensity of [OIII] falls faster than the H β intensity but is clearly detected to 21” (1030 pc). A lower O abundance to the NE or a lower ionization state could explain the declining [OIII] $\lambda 5007$ / H β ratio. Along slit “B”, the emission lines [OIII] $\lambda 5007$ and H β are spatially coincident and detected over 35” . However, we find no evidence for an abrupt edge to the O-enriched gas within the ionized ISM in I Zw 18, as might be expected if the galaxy contains an ultra-low metallicity HI halo (Kunth et al. 1994).

²IRAF is distributed by the National Optical Astronomical Observatories, which are operated by the Association of Universities for Research in Astronomy, Inc. (AURA), under contract with the National Science Foundation.

Table 4.2 Starburst Models

Star Formation History	Instantaneous Burst	Continuous Rate	Continuous Rate
Age, τ (Myr)	15	15	27
Absolute Blue Magnitude, M_B	-20.4	-14.2	-14.2
Luminosity of H Ionizing Photons, Q (s^{-1})	1.2×10^{52}	6.6×10^{51}	5.4×10^{51}
Mass of $1 M_{\odot}$ – $100 M_{\odot}$ Stars, M_{\star} (M_{\odot})	1.4×10^8	3.2×10^5	4.6×10^5
U-B (mag)	- 0.53	-0.78	-0.70
B-V (mag)	0.04	-0.03	-0.02
Kinetic Energy, E_{in} (ergs)	8.8×10^{56}	6.6×10^{53}	2.7×10^{54}

Note – Population synthesis calculations from Leitherer & Heckman (1995).

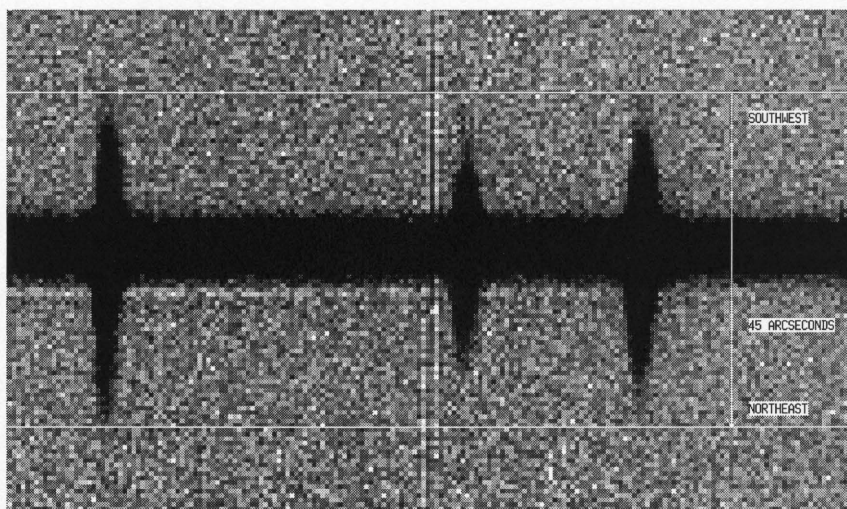


Figure 4.5 Longslit spectrum along the polar axis of the superbubble. The continuum, running horizontally, is centered on the NW HII region. The $H\beta$ emission line is on the left and $[OIII] \lambda\lambda 5007, 4959$ are on the right.

Table 4.3 Gravitational Potential Model

r_{max}	r	v_{esc}	T_{esc}
(kpc)	(pc)	(km s^{-1})	(K)
1	200	91	1.2e5
1	400	78	8.9e4
1	800	63	5.8e4
1	1000	57	4.8e4
10	200	125	2.3e5
10	400	116	2.0e5
10	800	106	1.7e5
10	1000	103	1.6e5

Column identifications:

- (1) – Truncation radius of isothermal sphere. The circular velocity is fixed at 40 km s^{-1} .
- (2) – Radius.
- (3) – Escape velocity at r .
- (4) – Escape temperature at r .

Abundance Variations

We use the data along slit A to place an upper limit on the variation of the O/H abundance ratio within the inner region of the nebula. The temperature-sensitive line [OIII] $\lambda 4363$ (e.g. Osterbrock 1989) is detected over $11''$ (530 pc). This region was divided into four $2''.9$ apertures (A1 to A4), whose positions relative to the NW HII region are shown in Figure 4.6. Table 4.4 lists the measured line fluxes. The logarithmic extinction at $H\beta$ was derived from the ratio of the $H\alpha$ and $H\beta$ fluxes assuming a stellar Balmer absorption equivalent width of 2 \AA (e.g. Shields & Searle 1978). The line ratio $R_t \equiv F([\text{OIII}]\lambda 5007 + \lambda 4959)/F([\text{OIII}]\lambda 4363)$ was corrected for reddening using the extinction curve of Miller & Matthews (1972). An external check of the line fluxes for the NW HII region yields excellent agreement with Skillman & Kennicutt (1993), and fluxes from slits A and B are consistent at their intersection.

Table 4.4 MMT Spectra and Derived Emission Line Ratios

Property	Region			
	A1	A2	A3	A4
$\lambda 3727$ [OII]	0.471 ± 0.017	0.268 ± 0.006	0.418 ± 0.010	0.497 ± 0.014
$H\beta$	1.000 ± 0.020	1.000 ± 0.020	1.000 ± 0.020	1.000 ± 0.020
$\lambda 4363$ [OIII]	0.061 ± 0.005	0.065 ± 0.002	0.053 ± 0.002	0.037 ± 0.003
$\lambda 4959$ [OIII]	0.615 ± 0.013	0.716 ± 0.014	0.678 ± 0.014	0.504 ± 0.010
$\lambda 5007$ [OIII]	1.805 ± 0.036	2.102 ± 0.042	1.998 ± 0.040	1.554 ± 0.031
$H\alpha$	3.457 ± 0.070	2.883 ± 0.058	2.906 ± 0.058	2.698 ± 0.054
$c(H\beta)^b$	0.29 ± 0.10	0.05 ± 0.10	0.05 ± 0.10	-0.04 ± 0.10
R_t^c	35.5 ± 3.1	42.6 ± 2.3	49.1 ± 3.1	56.4 ± 5.6

Note –Emission line fluxes relative to $H\beta$; no reddening corrections have been applied. Apertures A1 - A4 are described in the text.

^bLogarithmic extinction at $H\beta$.

^cDereddened flux ratio $R_t \equiv F([OIII]\lambda 5007 + \lambda 4959)/F([OIII]\lambda 4363)$

Along slit A, the line ratio R_i shows evidence for a significant temperature gradient from the SW to the NE side of the nebula, which is illustrated in the bottom panel of Figure 4.6. The photometric errors are dominated by the 2-3% uncertainty of our flux calibration for bright lines and by read noise and photon noise in the fainter lines. These uncertainties were combined in quadrature with the reddening uncertainty to derive the error bars denoted by “X” in Figure 4.6. The error bars denoted by “-” include an additional term for the maximum errors introduced by deviations from the parallactic angle.

The O/H abundance ratios shown in Figures 4.6bc were computed with the IRAF interface (Shaw & Dufour 1995) to the five-level atom program of De Robertis, Dufour, & Hunt (1987). The $T_e(O^+)$ temperature was calculated from $T_e(O^{++})$ and the parameterization of Pagel et al. (1992) which is based on model calculations by Stasinska (1990). The O^{+3}/H abundance was estimated from the HeII 4686 Å flux, and the contribution to the total O/H was found to be much less than the magnitude of our error bars.

Since our abundance analysis is quite sensitive to $T_e(O^{++})$, atmospheric dispersion shifting the nebular and auroral lines a few tenths of an arcsecond along the slit could cause a significant error in the measurements. To test for this effect, the frames with $d_{\perp} < 0''.1$ and the frames with $d_{\parallel} < 0''.1$ were separately combined and analyzed. The results from each set of spectra were similar. However, we decided to only use the frames taken at the parallactic angle, $d_{\perp} < 0''.1$, for the abundance analysis; and this selection criterion eliminated most of the frames along slit b. Unfortunately, the small aperture and steep surface brightness profile still make atmospheric dispersion along the slit (d_{\parallel}) a serious concern. For these observations, the atmospheric dispersion between 4000 Å and 5000 Å is $\lesssim 0''.3$ along the slit (Filippenko 1982). The resulting offset along the slit between the profiles

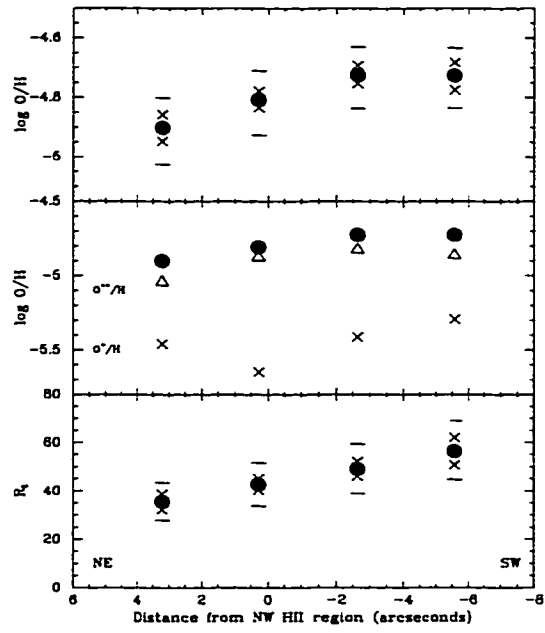


Figure 4.6 Abundance variations along slit a. (a) Temperature ratio, $R_t \equiv [\text{OIII}] \lambda\lambda 5007, 4959 / \lambda 4363$. (b) Ionic abundance ratios and their sum. (c) O/H abundance ratio with error estimates as described in the text.

of the [OIII] 4363 Å and [OIII] 5007 Å lines could introduce a systematic error in R_t as large as $\sim 20\%$ near the inflection point in the surface brightness profile. This effect could introduce an artificial gradient in the measured line ratio, but the slope would be in the opposite direction of the trend we measure. Hence, we believe the gradient in R_t is real but adopt the larger error bars to caution the reader about a potential systematic error. We conclude that the O/H abundance ratio in the central $11''$ (530 pc) is within 20% that of the NW HII region.

4.5. Summary

This paper reports new kinematic evidence for expanding, galactic-scale shells of ionized gas in I Zw 18 and determines their implications for the galaxy's evolution. We introduced a dynamical model to quantify the age and power requirements of these superbubbles and an evolutionary synthesis model to associate a stellar population with them. The mass of metals synthesized by this burst and the metallicity of the HII regions was used to discuss the mass of interstellar gas polluted by the starburst. The detection of oxygen emission lines from the diffuse gas demonstrates the large spatial extent of the metal-enriched, ionized gas. The following conclusions can be drawn.

1. A supergiant shell of ionized gas extends southwestward from the galaxy. The observed line splitting sets a firm lower limit of 30 km s^{-1} on the shell's expansion speed. The shell could be as old as 30 Myr.
2. On the opposite side of the NW HII region, an $H\alpha$ shell of comparable extent is seen, and the echellogram shows some evidence for a second supergiant shell in this region. These bubbles may constitute the lobes of a supergiant bubble driven by the starburst and constricted by the morphology of the ambient

medium to form a bipolar bubble. Geometrical considerations suggest the shell expands at a speed of $35 - 60 \text{ km s}^{-1}$.

3. The superbubble and starburst may be coeval. A star formation rate of $0.02 \text{ M}_{\odot}(\text{of } 1 \text{ M}_{\odot} \text{ to } 100 \text{ M}_{\odot} \text{ stars}) \text{ yr}^{-1}$ over the last $15 - 27 \text{ Myr}$ can accelerate the shell and produce the blue luminosity, the UV colors, and most of the ionizing luminosity of I Zw 18. Instantaneous burst models fail to produce enough hydrogen ionizing photons.
4. The superbubble will probably blow out of the galaxy, and the hot component of the ISM will escape from the galaxy in a galactic wind. Our analysis of the gas dynamics supports the general picture that galactic winds are an important process in the chemical evolution of dwarf galaxies (Matteucci & Chiosi 1983; Matteucci & Tosi 1985; Marconi et al. 1994).
5. The current starburst will probably eject only a small fraction of the galaxy's total gaseous mass. Catastrophic mass loss – proposed to transform gas-rich dwarfs into dwarf elliptical galaxies (Ferguson & Binggeli 1994 and references therein) – is unlikely from the current starburst, which may be the first in I Zw 18. Whether this is the common outcome of wind driven mass loss from dwarf galaxies is not yet clear (Heckman et al. 1995; Marlowe et al. 1995; Meurer et al. 1992).
6. The detection of the superbubble establishes a timescale ($\sim 15 - 27 \text{ Myr}$) and spatial scale ($\sim 900 \text{ pc}$) for dispersing the recently synthesized elements. Oxygen emission lines are detected in the diffuse gas over this spatial scale. A pilot study of the gas phase metal abundance suggests the SW side of the nebula has a lower $T(O^{++})$ and slightly higher oxygen abundance than the NE side.

7. The X-ray emission is slightly harder and brighter than that predicted from the superbubble. Higher resolution observations are needed to determine the fraction of X-ray luminosity produced by additional sources.

CHAPTER 5

THE FORMATION OF GALACTIC WINDS IN DWARF GALAXIES

5.1. Introduction

The interplay between massive stars and the interstellar medium (ISM) plays a fundamental role in the formation and evolution of galaxies. In addition to ionizing radiation and newly synthesized elements, massive stars deliver kinetic energy to the surrounding gas through stellar winds and supernovae. Supersonic shock waves driven by an ensemble of such stars may trigger additional star formation and/or sweep the interstellar gas out of the region actively forming stars (Tenorio-Tagle & Bodenheimer 1988). The gas flows create a turbulent pressure which helps support the weight of the ISM (e.g. McKee 1990), and the topology of the shells is apparently critical for the transport of the ionizing radiation (Dove & Shull 1994; Miller & Cox 1993).

This feedback is expected to have a profound influence on the evolution of low

mass galaxies. Superbubbles in dwarfs may live longer than in spiral galaxies due to the decreased radiative cooling rate of lower metallicity gas and the lack of shear forces from differential rotation. Although the total mass of stars formed in a dwarf galaxy is relatively small, the areal star formation rates in high surface brightness dwarfs are 10-100 times higher than the average rate across the disk of a late-type spiral. Based on energy requirements alone, the supernovae from a single episode of this intense star formation could unbind the entire interstellar medium from a low mass galaxy (e.g. Larson 1974). This idea was developed in a seminal paper by Dekel & Silk (1986) which demonstrated that supernova-driven ejection of the ISM could explain the observed mass-metallicity and mass-radius scaling relations if the dwarfs reside in dark matter halos. However, DeYoung & Heckman (1994) have recently drawn attention to the role the morphology of the surrounding ISM plays in channeling a superbubble to blow out along the minor axis. While their work suggests ejection of the ISM may not be as easy as previously thought, mass-loss from dwarfs continues to be frequently invoked to explain a number of issues ranging from abundance patterns (Marconi, Matteucci, & Tosi 1994) to the evolution of distant galaxies (Phillipps & Driver 1995; Babul & Rees 1992).

The observational evidence for galactic winds from dwarfs is encouraging but not compelling. The plethora of giant shells ($R < 300$ pc) and supergiant shells ($R \geq 300$ pc) in the Large Magellanic Cloud (LMC) testify to the propensity of irregulars toward this nascent stage in the formation of a wind (Davies, Elliot, & Meaburn 1976; Meaburn 1980). Among the nearby dwarfs, several potential examples of the wind stage, i.e. gas streaming out of the galaxy, have been proposed on the basis of $H\alpha$ morphology alone (Hodge 1974; Graham 1981; Dufour & Hester 1990). However, follow-up programs to study the gas kinematics have often lacked the sensitivity and/or spectral resolution required to measure the expansion

velocities of the partial shells and/or filaments that extend well above the galactic plane (e.g. de Vaucouleurs, de Vaucouleurs, & Pence 1974; Thuan, Williams, & Malumuth 1987). Of the prospects which have been studied in detail, NGC 1705 (Meurer et al. 1992) and I Zw 18 (Martin 1996a) were shown to be in the phase preceding blowout where the superbubble(s) are still breaking through the HI disk although NGC 1569 could be in a true wind stage (Heckman et al. 1995). Marlowe et al. (1995) present kinematic evidence for kiloparsec scale expanding, shells in 7 amorphous type dwarfs, but only one, NGC 3955, is a wind candidate. Messier 82 is the lowest mass galaxy that is unambiguously in a wind stage (Bland & Tully 1988). In both M82 and NGC 1569, the strongest arguments for actual mass loss are based on detections of X-ray emitting gas at temperatures well above the escape temperature extending high above the galactic plane (Bregman, Schulman, & Tomisaka 1995 ; Heckman et al. 1995). When blowout is achieved, the mass of gas escaping from the hot interior, while very significant for the chemical evolution of the galaxy, may be a negligible fraction of the interstellar gas mass (e.g. Heckman et al. 1995; Martin 1996a).

A more complete kinematic census is clearly required. Imaging surveys of irregulars show roughly 1/4 of them have at least one shell and nearly 1/2 have shells or extended filaments (Hunter, Hawley, & Gallagher 1993). However, Hunter & Gallagher (1990) have also shown that at least some supergiant filaments are kinematically quiescent (i.e. they are not expanding shells). This paper presents the results of a kinematic survey of the ionized gas in 15 dwarfs, whose properties were summarized in Table 1 of Chapter 2. Deep, high-resolution spectra of the H α emission were obtained with longslit, echelle observations. The excitation of the diffuse ionized gas in the same sample of galaxies was discussed in Chapter 2. The galaxies were selected from a volume of radius $d \leq 10$ Mpc, right ascension

$4h \leq \alpha \leq 14 h$, and declination $\delta \geq -35^\circ$, to cover a range in absolute luminosity from $M_B = -13.5$ to $M_B = -18.5$. The sample was reduced to 15 members on the basis of $H\alpha$ morphology and the propensity for violent gas kinematics.

The paper is organized as follows. The observations and data reduction are described in § 5.2. Section 5.3 describes the kinematics of the ionized gas, and § 5.4 discusses the dynamics of the expanding shells. The implications for the star formation history of these galaxies and the fate of the bubbles are also discussed in § 5.4. A preliminary look at the implications of these results for the evolutionary paths of dwarf galaxies is presented in § 5.5.

5.2. Observations and Analysis

Images of the galaxies were obtained with a Loral 800×1200 thinned CCD on the Steward Observatory 2.3m telescope through 70 Å FWHM filters centered at λ 6580 and λ 6450. After standard processing, the continuum image was subtracted from the on-band image to produce $H\alpha + [N II]$ emission-line images. Observations used in this paper were obtained under clear conditions on the nights of 1993 April 21 and 28, May 16 – 17, and 1994 January 3 and were flux calibrated using observations of standard stars. Comparison to other published values indicates the photometry is accurate to at least 20%. The images typically reveal structure on the scales of a few square arcseconds at the level of $\Sigma(H\alpha + [NII]) \geq 4 \times 10^{-17} \text{ ergs s}^{-1} \text{ cm}^{-2} \text{ arcsec}^{-2}$.

The structure of the ionized gas was used to select the slit positions for the spectroscopic observations. The number of observations and positioning strategy varied based on the size of the galaxy and was revised during the course of each observing run based on initial results. In general, most of the large complexes of extended emission were sampled and follow-up positions were used to determine

the spatial extent of the kinematically interesting features and provide continuous spatial coverage in the direction of the nearest giant HII region and/or super-star cluster. Table 5.1 lists the exact positions and provides a reference label for each. Note that M82 was observed as a comparison object.

Longslit spectra of the $H\alpha$ + [NII] emission lines were obtained using the echelle spectrograph on the KPNO 4 m telescope with the Tek $2k \times 2k$ CCD during the periods 1994 April 28 – May 2, 1995 December 10 – 11, and 1996 February 7–8. The instrumental setup, described in Martin & Kennicutt (1995), provided 11 km s^{-1} resolution (FWHM of the night sky lines) and a useable slit length of ~ 3.5 . Observing conditions were good on the first run and the last night of the third run. At these times, three 1200 sec exposures were sufficient to reveal the line profile of the faintest features detected in the images and to remove cosmic rays. Additional details concerning the reduction and calibration of the CCD frames can be found in Martin & Kennicutt (1995).

5.3. The Kinematic Atlas and Catalog

The results are presented as a kinematic atlas in Figure 5.1. A quick inspection immediately testifies to the variety and wealth of structure which would only broaden the profile of lower resolution spectra. In this section, I will use the echellograms, which are grouped by galaxy and arranged in a spatial sequence, to explore the large-scale kinematic structure of the ISM. In preparation for this tour, I begin the section by illustrating the kinematic signature of some structures seen at individual slit positions and emphasizing their relation to the $H\alpha$ morphology. I then introduce a notation of illustrating the location of the kinematic shells on the images, which is then used in subsequent sections to synthesize a picture of the large-scale gas kinematics.

Table 5.1 Slit Positions

Galaxy	Slit ID	Position Angle	Offset	
NGC 1569	4	110.0°	1.5'' W	4.2'' S from S
	6	110.0°	29.1'' E	61.5'' N from S
	7	110.0°	3.0'' E	26.7'' N from S
	10	46.0°	12.5'' W	2.1'' S from A
	11	-12.0°		
	12	36.0°	20.3'' E	28.8'' S from A (?)
	13	110.0°	11'' W	60'' S from A
NGC 1800	2	100.0°	1.9'' E	47.0'' N from S
II Zw 40	1	110.0°	6.3'' W	3.3'' S from nuc.
NGC 2363	6	75.0°	50.9'' W	39.2'' S from S
	1	75.0°	40.1'' W	47.3'' S from S
	4	178.1°	35.6'' W	60.4'' S from S
	5	75.0°	35.6'' W	55.3'' S from S
NGC 2537	3	74.0°	6.6'' E	11.6'' S from cont. knot
I Zw 18	1	7.67°	36.8'' W	9.8'' S from S
	2	156.1°	36.8'' W	9.8'' S from S
	3	78.8°	36.8'' W	9.8'' S from S
NGC 3034	2	151.0°	48.8'' E	44.6'' N from S
	4	64.0°	59.0'' E	148.3'' N from B
NGC 3077	5	107.3°	31.7'' E	59.7'' S from S
	2	174.1°	25.3'' E	56.8'' S from S
	3	66.0°	35.2'' E	44.5'' S from S
	4	25.8°	33.3'' E	66.2'' S from S
Sex A	1	180.0°	10.4'' E	16.9'' S from S
VII ZW 403	1	8.2°	26'' W	3'' N from S
NGC 3738	2	69.0°	23'' W	1'' S from S
	3	137.9°	23'' W	1'' S from S
NGC 4214	1	31.0°	24'' E	23'' S from S
	2	172.8°	24'' E	23'' S from S
	3	70.3°	24'' E	23'' S from S
	4	106.6°	16'' E	20'' S from S
NGC 4449	1	38.8°	47'' W	10'' N from S
	2	38.8°	52'' W	26'' N from S
	3	144.1°	55'' W	0'' from S
	8	106.0°	22'' W	42'' N
	9	90°	27'' W	75'' N from S
	11	-85.0°	12'' W	60'' N from S
	7	218.8°	39'' W	20'' S
	10	218.8°	8'' W	30'' S
	1	50.6°	2'' W	9'' N from nuc.
	2	50.6°	5'' E	-0'' S
	3	83.1°	1'' E	1'' S from K
NGC 5253	2	164.2°	56'' W	53'' S from S
	3	164.2°	56'' W	53'' S from S
	1	164.2°	56'' W	53'' S from S

5.3.1. Navigating the Echellograms

The most common kinematic structures are expanding shells of small angular diameter. The Doppler shift of the emission from the approaching and receding sides of the ionized shell leaves an elliptical ring of emission in the echellogram (e.g. Osterbrock 1989 Figure 6.6). Shell D near the west end of NGC 4449 - 9 is a classic example. Variations on this “Doppler ellipse” are observed frequently. The ellipse is often composed of several knots of emission as, for example, shell A in NGC 3738 - 3. Occasionally, the red-shifted and blue-shifted sides are offset spatially as seen near shell A in Sex A - 1. The small shell to the south of I Zw 18 is physically very large, ~ 1 kpc, and provides a good example of a “breakthrough bubble.” This type of structure is critical to the discussion in this paper and is characterized by (1) its extension far beyond the HII regions and (2) the intensity difference between the blue-shifted and red-shifted sides of the shell. The latter often results from projecting the emission from a bubble which protrudes out one side of the galaxy in a direction inclined to our line-of-sight (e.g. Martin 1996a; Heckman, Armus, & Miley 1990).

To study the large-scale gas dynamics, the radial velocity field measured from several slit positions must be combined and the mass of ionized gas estimated. Figure 5.2 introduces an efficient notation for illustrating the location of the expanding cavities with respect to the morphology of the $H\alpha$ emission, whose surface brightness constrains the column density of ionized gas. On the images of NGC 3738 and Sex A, for example, each Doppler ellipse identified on the echellograms is represented by an ellipse on the image. The axis aligned with the position of the slit represents the spatial locus where line-splitting is seen. The second axis, usually the minor axis, is scaled to the magnitude of the line splitting. Hence, the ellipticity of the symbol indicates the dynamical age derived from a

single slit position.

As a final aid to interpreting the atlas, I draw attention to the signature of the superwind emanating from M82. In Figure 5.1, echellogram M82 - 2 is oriented along the minor axis. The double-peaked line profile has a brighter redshifted component to the south while the blueshifted component dominates on the north side of the galaxy. The morphology of the velocity structure is very similar to I Zw 18 - 1, but the magnitude of the line splitting is about five times larger. An important difference, however, is that the Doppler ellipses in the M82 spectrum don't close (i.e. they are not ellipses). In Figure 5.2 I differentiate this structure from a closed Doppler ellipse on the image of M82. A line segment is drawn from the point nearest the center of the galaxy where the line splitting is seen to the farthest point where one side of the cavity is detected. A flag is drawn at the last position where both components of the double-peaked profile are detected, its length represents one-half the magnitude of their velocity separation on the same scale used for the Doppler ellipses, and its direction indicates the sign of the Doppler shift of the fainter component. The far side of the outflow was observed at a second slit position oriented perpendicular to the polar axis of the wind. Echellogram M82 - 4 reveals the width of the expanding cavity and Figure 5.2 shows its close correlation with the morphology of the extended filaments. The faint substructure interior to the big Doppler ellipse appears to form at least 3 and possibly 4 smaller ellipses, so the wind is apparently composed of several adjacent cells.

5.3.2. Highlights of the Tour

NGC 4861

Echellogram NGC 4861 - 1 traverses the complex of filaments to the NW of the giant HII region. A Doppler ellipse nearly $30''$ (about 1 kpc !) in diameter is plainly visible on the western half of the slit. The higher intensity of the blueshifted component immediately suggests that the outflow axis is directed away from our line-of-sight. A closer comparison to the $H\alpha$ image reveals the Doppler ellipse coincides with the relatively faint complex of filaments to the west of the giant HII region (bubble A). The Doppler ellipses detected at slit positions 2 and 3 confirm the presence of an oppositely directed polar bubble (bubble C) to the east of the HII complex. The position angles of the outflow axes are roughly 61° and 254° . The line profile across the two bright loops to the N of the HII complex does not reveal any large-scale structure. The eastern loop shows only a faint red wing. The emission is divided among at least two velocity components at the intersection with the two filaments connecting the western loop to the galaxy, although some of these seem to be associated with the eastern outskirts of bubble A.

NGC 3077

If absolute scales are set aside, NGC 3077 competes with its neighbor M82 in terms of dramatic feedback. At least four superbubbles, identified in Figure 5.2, are breaking out of the starburst region. Bubble A coincides with the bright shell extending $46''$ (~ 800 pc) to the east and leaves a clean Doppler ellipse on the eastern side of echellogram NGC 3077 - 5. Directly south of the starburst, a bright shell (J) extends $34''$ (590 pc) and a fainter loop protrudes further to $54''$ (940 pc). The southern ends of echelle slits 2 and 4 show Doppler ellipses coincident with

the inner loop; the blueshifted side is brighter. On the opposite side of the galaxy, echellogram NGC 3077 - 2 reveals a Doppler ellipse across the inner, bright region of complex G. The redshifted side of the Doppler ellipse is brighter consistent with a polar axis inclined toward our line-of-sight. Since the outflows associated with complex G and J point in opposite directions and have similar dynamical timescales ~ 10 Myr, they are likely a bipolar bubble created by the same star formation event. The unusual velocity field toward shell B just west of the galaxy makes its relation to the eastern shell (A) ambiguous. As seen in echellogram NGC 3077 - 5, the line splitting across the bright complex of filaments extends to $R \sim 33'' \sim 570$ pc and reaches a magnitude of 220 km s^{-1} ; however, the pattern in the echellogram is not well-described by a Doppler ellipse.

Closer to the starburst along slit 2, bubble D is projected against bubble G. Echellogram NGC 3077 - 3 confirms that it coincides exactly with the bright loop just north of the starburst. With a radius ~ 300 pc and expansion velocity $\sim 100 \text{ km s}^{-1}$, this is a bubble making the transition to the superbubble scale. Notice how spherical the shell is at this stage. To the west, a superposition of younger and older outflows is seen. Notice the extreme extent $\sim 80''$ (1400 pc) of the faint filaments. The inner region shows velocity splitting which extends over a substantial region and reaches values as high as 200 km s^{-1} but is not well-fit by the classic Doppler ellipse.

NGC 4214

Across the bright, ionized shell surrounding cluster NGC 4214 #1 of Leitherer et al., echellogram NGC 4214 - 1 shows the $\text{H}\alpha$ emission comes from two Doppler shifted components. The maximum line splitting is coincident with the peak continuum emission and offset $\sim 1.2''$ NE of the HII region. The surprise is that the

diameter of the Doppler ellipse is over twice that of the ring in the image. The Doppler ellipse in NGC 4214 - 3, which is aligned tangent to the ring, confirms that the bubble is larger than the ring. One explanation is that our line-of-sight is parallel to the polar axis of a wasp-waisted bipolar bubble. Southwest of complex A, NGC 4214 - 1 shows another Doppler ellipse out to $30''$ (530 pc) which I interpret as a polar outflow tilted toward our line-of-sight. We see high velocity wisps to NE and all along the main complex in NGC 4214 - 2 and NGC 4214 - 4. Many of these are unresolved in the spatial dimension ($\lesssim 26$ pc) and reach velocities $\sim 100 \text{ km s}^{-1}$. The physical interpretation is unclear; the velocities are typically recessional. By observing the overall tilt of each echellogram, notice the ionized gas rotates about the major axis of the galaxy !

Blowout in NGC 1569?

The nearby galaxy NGC 1569 provides a precious snapshot of wind formation. The galaxy is emerging from a burst of star formation which started about 10 Myr ago (Israel & deBruyn 1988); and the kinetic energy injection rate is expected to reach a maximum about this time. The galaxy is known to have at least two large bubbles protruding out along the minor axis (Heckman et al. 1995; de Vaucouleurs, de Vaucouleurs, & Pence 1974). I obtained extensive spatial coverage and higher spectral resolution to answer three primary questions: (1) Has the bubble ruptured? (i.e. Has it reached the blowout stage?) (2) How much mass will leave the galaxy? and (3) What is the covering angle of the outflow?

Echellograms NGC 1569 - 10 and NGC 1569 - 11 cover the outflow in an "X" pattern centered about $22''$ N-NE of super star cluster A. The continuum source in the center of ech - 11 is super star cluster A. Just to either side of it, the line profile has a broad blue wing extending $\sim 160 \text{ km s}^{-1}$ to lower velocity. A normal Doppler

ellipse is seen on the redward side; hence there appears to be blowout along our line-of-sight

The overall similarity of the large-scale ($30''$) features in these two echellograms show the gas kinematic features are coherent over kiloparsec spatial scales (so our results are not sensitive to the exact position of the slit). Consider ech - 11. To the S and to the N the emission comes from two Doppler shifted components. The redshifted component is brighter to the S while the blueshifted component is brighter to the N – an indication that the southern side is the closer side (Chapter 4). The velocity separation of the two components is still increasing when the fainter side fades below the detection limit (Ech - 10 which bisects the prominent bubble SW of the galaxy).

Echellograms - 6, 7, 4, and 13 form a sequence of steps parallel to the major axis of the galaxy. On the north side, ech - 6 shows line splitting coincident with the region strewn with radial filaments in the $H\alpha$ image. This region subtends about $\sim 140^\circ$ as seen from cluster A and has a projected height above the galactic plane of $29''$ (300 pc). The surprise is that there are three distinct Doppler ellipses, each of diameter ~ 600 pc. The other 3 positions were positioned approximately 140, 460, and 640 pc south of that plane and provide information on the (de)acceleration of the wind. In ech - 7 the bright arm leaves a signature of two pair of high velocity wisps extending to lower velocity which connects to the lower intensity blueshifted side of the shell. Similar features cover the $\sim 140^\circ$ angle subtended by the southern set of radial filaments. Higher above the disk (still to the south) one sees parts of three Doppler ellipses. The sensitivity of ech - 13 is higher than ech - 4. So even 650 pc above the plane, the radial expansion velocity is 40 km s^{-1} ! The radial velocity at 140 pc was about 90 km s^{-1} , so there seems to be some deceleration. A deep image of a larger field by Hunter et al. (1996) shows the filaments end a large

curved arc about 1.4 kpc above the plane (still on the S side).

NGC 4449

In Figure 5.2, the warm ionized medium in NGC 4449 is a particularly dramatic example of the disturbances involved in the star-gas feedback cycle. A remarkable aspect, not immediately obvious from the $H\alpha$ image, is that some of the faint, ionized gas is organized into several kiloparsec scale shells. Echellograms 1 and 2 are aligned parallel to the bar and offset to its NW side. On the southern half of these slits, the line profiles reveal partial Doppler ellipses whose Doppler shifted components are separated by as much as $120 - 160 \text{ km s}^{-1}$. The spatial extent of the line splitting increases from about $30''$ at a projected “height” above the bar of $10''$ to approximately $45''$ at a height of $24''$. This “complex A” is one of the most energetic features found in the whole sample. Slit 3 was positioned to intersect the regions of maximum line splitting found along slits 1 and 2 and demonstrates that the expanding cavity extends to a projected height of $\sim 40''$, where the Doppler ellipse ends. The intensity of the blueshifted side is stronger which suggests the polar axis is tipped away from our line-of-sight; however, the geometry is more complicated than the polar outflows discussed previously. Across the bar, echellogram-3 shows multiple high velocity wisps whose envelope has an elliptical shape but which do not form a clean Doppler ellipse. Most of the wisps extend to higher velocity and their interpretation is unclear – are they pieces of a fragmented shell on the far side of the galaxy or illuminated inflowing gas? Southeast of these wisps there is a hint of another Doppler ellipse coincident with the large hole in the $H\alpha$ emission to the east of the bar. Echellogram 7, which is parallel to slits 1 and 2, bisects the cavity along its major axis and confirms that it is expanding.

The kinematic activity in the ISM of NGC 4449 is not limited to the region driven by the star formation in the bar. Echellograms 9, 4, and 11 show Doppler ellipses at the NW end of the “t”, hereafter complex D. A larger region of line-splitting labeled “C” in Figure 5.2 shows several adjacent Doppler ellipses over $D \approx 25''$ region. Perhaps several bubbles are merging into a superbubble in this region. At the top of the “t”, bubble G extends from two HII complexes on the W to a faint arc on the E. In addition to these three superbubbles, the faint filaments about $45''$ east of the bar contain some smaller shells. Three Doppler ellipses are identified in ech - 10 and coincide with partial rings of emission in the $H\alpha$ image.

5.3.3. Summary: A Catalog of Superbubbles

Table 5.2 provides a catalog of all the shells identified in the sample. Each echellogram was examined on many spatial scales using a variety of intensity mappings to identify all the Doppler ellipses. Results from several slit positions were often used to define the shells or complexes listed in the table (cf. Figure 5.2). The radial velocities listed there are one-half the maximum line splitting found along any Doppler ellipse associated with the complex. The positions of these kinematic complexes are strongly correlated with locations of shells and filaments in the $H\alpha$ images, so the morphology of the $H\alpha$ emission was used to estimate the area of the bubble and compute the average $H\alpha + [\text{NII}]$ surface brightness (col. 5). The radius given in the table is the projected distance of the shell from the associated cluster(s) in the continuum image and/or a giant HII region. Figure 5.3 illustrates the distribution of bubbles in the radius – velocity plane.

Inspection of Figure 5.3 or Table 5.2 draws attention to the relatively large number of shells with $R \geq 800$ pc. Since my sampling technique is expected to be complete on large scales but certainly misses some smaller bubbles, one expects the distribution of detected shells to be strongly biased toward the larger

Table 5.2 Properties of Supershells

Complex	v (km s^{-1})	R ($''$)	R (pc)	$\Sigma(\text{H}\alpha + [\text{NII}])$ ($\text{ergs s}^{-1} \text{cm}^{-2} \text{arcsec}^{-2}$)	τ (Myr)	$L_{\text{H}}(1)/h(1)$ ($\text{cm}^2 \text{ergs s}^{-1}$)	$K.E. \sqrt{e/0.1}$ (ergs)
NGC4861-A	50	23.4	850	3.9e-16	10	3.6e40	7.1e52
C	30	26.4	960	3.8e-16	19	9.9e39	1.3e52
B	102	15.7	570	7.8e-16	3.3	1.4e41	1.4e53
NGC3077-D	106	17.7	310	2.00e-15	1.7	4.5e40	1.4e52
A	55	46.2	810	3.47e-16	8.6	4.3e40	4.2e52
J	67	53.8	940	1.94e-16	8.2	1.1e41	4.9e52
B	40	36.9	(1380)	(7.47e-16)	20	4.8e40	3.2e52
G	51	47.8	830	2.47e-16	10	3.6e40	1.6e52
NGC4214-A	45	8.33	150	1.27e-14	2	8.1e38	3.3e51
B	28	30.3	530	1.69e-15	11	2.4e39	1.0e52
C	(29)	30.7	540	1.11e-15	11	2.8e39	5.6e51
D	46	14.2	250	3.58e-15	3	2.4e39	4.5e51
NGC1569-C	79	8.07	85	1.45e-14	0.6	1.4e39	1.4e52
A	120	105	1120	4.69e-16	5.5	8.6e41	2.0e53
B	85	90.3	960	3.13e-16	6.6	2.2e41	8.6e52
D	54	98.4	1050	4.66e-16	11	6.9e40	2.4e52
E	44	76.6	820	2.48e-16	11	2.3e40	1.5e52
F	64	83.8	890	4.61e-16	8	8.2e40	8.2e52
G	47	99.5	1060	3.66e-16	13	4.6e40	2.2e52
NGC4449-A	79	34.5	600	3.00e-16	4.5	7.0e40	1.6e53
B	127	42.0	730	2.01e-15	3.4	4.3e41	(2.5e54)
E1	84	18.3	320	1.40e-15	2.2	2.4e40	2.8e52
E2	38	5.0	88	1.47e-15	1.4	1.7e38	2.5e49
E3	51	9.5	170	3.81e-16	2.0	1.5e39	1.2e51
F7	31	4.2	74	7.39e-16	1.4	6.5e37	4.5e50
D	33	13.6	240	6.11e-16	4.3	8.2e38	4.6e51
C	30	26.8	470	1.09e-15	9.2	2.4e39	4.0e52
G	25	8.1	250	2.43e-15	5.9	3.9e38	3.5e51
F10	27	3.4	60	5.04e-16	1.3	2.8e37	1.2e50
E11	40	4.5	80	3.49e-16	1.2	1.6e38	5.4e50
E13	146	7.7	134	1.22e-15	0.5	2.2e40	3.8e52
M82-N	176	85.4	1490	4.28e-16	5	4.8e42	2.4e55
S	146	126.7	2210	6.32e-16	8.9	6.0e42	8.7e54
NGC3738-A	35	8.9	173	1.58e-15	2.9	5.1e38	8.8e50
B	24	6.8	132	2.43e-16	3.2	9.6e37	9.2e49
C	22	7.1	138	1.32e-15	3.7	8.1e37	1.7e50
NGC2363-A	44	34	593	9.68e-17	8.5	9.62e39	1.4e52
B	69	38.4	670	3.66e-16	5.7	5.85e40	5.7e52
NGC2537-A	67	4.8	175	8.42e-17	1.5	3.7e39	4.9e51
NGC1800-N	27	34.3	1350	6.16e-17	29	1.4e40	2.5e52
SexA-A	62	13.9	88	2.38e-16	0.83	7.33e38	1.2e51
IZw18-S	34	19.9	970	1.98e-16	17	1.45e40	6.2e51

complexes relative to the true distribution. Without complete spatial coverage, it is therefore dangerous to interpret the bimodality of the size distribution physically. As a comparison, I examined all the shells/filaments identified in 51 Irregulars on morphological grounds by Hunter, Hawley, & Gallagher (1993). Using the features similar to my sample in their Table 3, I computed a histogram of shell sizes and found no evidence for a bimodal distribution. Nonetheless, the bimodal distribution of shells sizes in the Magellanic Clouds described by Meaburn (1980) has a minimum at nearly the same shell radius – about 750 pc. This result deserves further investigation elsewhere (e.g. Oey & Clarke 1996). The remainder of this paper will discuss the gas dynamics of these shells and their evolution.

Details about the gas kinematics in I Zw 18, Sex A, and NGC 1800 can be found in Appendix A, Hunter & Plummer (1996), and Hunter (1996). No kinematic evidence for expanding shells was found in II Zw 40, VII Zw 403, or NGC 5253. Although the first two may simply not have any large shells, NGC 5253 may have a shell that was simply missed by my selection of slit positions (cf. Marlowe et al. 1995).

5.4. Dynamical Interpretation

5.4.1. Timescales and Energies

The dynamical age and power requirements of the structures in § 5.3 were estimated using the conventional solution for the motion of a wind-driven shell (Castor, McCray, & Weaver 1975; Weaver, McCray, & Castor 1977; Ostriker & McKee 1988; Koo & McKee 1992). The model assumes kinetic energy is continuously injected at a fixed location in a homogeneous medium. A shock wave propagates outward and sweeps the ambient medium into a thin, radiating shell. A second shock travels back into the wind leaving an adiabatic cavity (i.e. low density) of hot, shocked

stellar ejecta. The pressure of the hot bubble then drives the expansion of the shell. A grid of energy injection rates and dynamical ages computed from this model (cf. Chapter 4 equations 5 and 6) is overlaid on the observed $R - v$ distribution in Figure 5.4, and the location of each complex in these coordinates is tabulated for reference in Table 5.2.

The power requirements of a shell of a given size and expansion velocity are proportional to the density of the ambient ISM (cf. eqn. 6 of Martin 1996a). The mean ambient density encountered by supershells in the LMC is typically about 1 cm^{-3} (Meaburn 1980). In Figure 5.4, I have parameterized the mechanical power, L_{in} , in terms of $n_0 = 1 \text{ cm}^{-3}$. Comparison of the data and the grid of models indicates that the energy injection rates range from $L_{in}/n_0 = 10^{38} \text{ cm}^3 \text{ ergs s}^{-1}$ to $\gtrsim 10^{42} \text{ cm}^3 \text{ ergs s}^{-1}$. Since the winds from normal O stars supply $L_{in} \sim \text{few} \times 10^{36} \text{ ergs s}^{-1}$ (e.g. Chiosi & Maeder 1986) – which is similar to the contribution from an average supernovae (i.e. $10^{51} \text{ ergs} / 10 \text{ Myr}$), many thousands of stars contribute to the formation of the bubbles discussed in this paper.

The one-dimensional model predicts a wind-blown shell carries a kinetic energy, $T = 0.5 M_s v_s^2$ or $1.44 \times 10^{52} n_0 R_{100}^3 v_{100}^2 \text{ ergs}$, which is 19% of the total kinetic energy supplied by stellar winds and supernovae. Since the kinematic shells show a close correlation with the $\text{H}\alpha$ morphology, the ionized mass in a shell can be estimated directly from its $\text{H}\alpha$ surface brightness. In terms of the volume filling factor of the warm ionized gas, ϵ , the column density of ionized gas, $\Upsilon \equiv N_e \mu_e m_H$, may be expressed as,

$$\Upsilon = 0.294 (\Sigma_{\text{H}\alpha} \epsilon \Delta s)^{1/2} d_{\text{Mpc}}^2 \text{ M}_{\odot} \text{ arcsec}^{-2},$$

where d is the distance to the galaxy in Mpc, the electron temperature is 10^4 K , and the mass per electron is $\mu_e = \frac{14}{11} \text{ amu}$. Estimating Δs , the depth of the emitting

region along the line-of-sight, from one of the projected, angular dimensions, the mass per angular area is conveniently expressed as

$$\Upsilon = 0.36 \left(\frac{\Sigma}{10^{-18} \text{ergs sec}^{-1} \text{ cm}^{-2} \text{ arcsec}^{-2}} \frac{\epsilon}{0.1} \frac{\Delta s}{''} \right)^{1/2} d_{\text{Mpc}}^{5/2} M_{\odot} \text{ arcsec}^{-2}.$$

Using this expression, I estimated the mass of ionized gas in the filaments/arcs associated with the expanding complexes from surface photometry of the $\text{H}\alpha$ + [NII] images. Requiring the associated kinetic energy, $T = 1/2 M_s v_R^2$, to be consistent with the one-dimensional dynamical model constrains the two parameters n_0 and ϵ .

The measured kinetic energy of each shell is compared to the prediction of the one-dimensional, shell model in Figure 5.5. For $n_0 = 0.1 \text{ cm}^{-3}$ and $\epsilon = 0.1$, the predicted kinetic energy of the large shells is systematically high. This behaviour may be easily explained by the average density seen by the expanding shells becoming smaller as the shells get larger.

The parameters derived from the idealized, wind-blown bubble model are probably accurate to a factor of a few. The largest systematic errors are introduced by the geometry of many of the large bubbles, which is better described as polar than spherical. As a bubble outgrows the surrounding environment of ambient HI, the shell will expand most rapidly in the direction of the steepest density gradient. The HI velocity field has been coarsely mapped in many of the galaxies in my sample and typically reveals orderly rotation on a large scale; hence, a disk of HI may collimate the direction in which the bubble breaks through. However, the rotation axis of the HI is not necessarily aligned with the optical minor axis of the galaxy (e.g. Kobulnicky et al. 1995). Estimates of disk inclination and scale height are typically poorly constrained. Besides the added hydrodynamic complexity, the polar geometry means the measured radial shell velocity and shell radius will be systematically lower than their true values.

5.4.2. Implications for the Star Formation History

Age estimates for several of the supergiant bubbles exceed the lifetime of the ionizing radiation from a single generation of massive stars. The lifetime of a B2 V star, roughly the coolest stars contributing significantly to the ionizing flux, is about 10 Myr (e.g. Martin & Arnett 1995). In Figure 5.4, eight bubbles from six galaxies have inferred dynamical ages > 10 Myr. It is likely that the ambient density encountered by the shell decreases over the large scale of these shells and that the wind luminosity increases for a time period of about 40 Myr at which time the lower mass ($8-10 M_{\odot}$) stars explode as supernovae. Either correction to the isochrones would decrease the shell's deceleration, thereby increasing the age estimate. If corrections to the shell radius and velocity for projection effects are negligible, then the isochrones shown in Figure 5.4 denote a lower limit for the age.

The distribution of bubbles found in a galaxy in the τ vs L_{in}/n_0 plane can provide a new perspective on the recent star formation history. For example, in Figure 5.4 shells B and C in NGC 4214 lie close together, which supports the prediction based on the line profile shape and filament morphology that they are related to the same star formation event. Shell A requires the same L_{in}/n_0 but is only about one-third as old. Hence, shell A would look like bubbles B and C if mechanical power continues to be supplied at the current rate. A similar situation is found in NGC 3077, where bubbles J, A, and G are clustered near $\tau \approx 10$ Myr, $L_{in}/n_0 \approx 5 \times 10^{40} \text{ cm}^3 \text{ ergs s}^{-1}$. The power requirements of the younger shell D are comparable. An interesting observation is that while the average L_{in}/n_0 appears to be roughly constant over 10 – 15 Myr, something about the location of the star formation or the distribution of the collimating ambient gas has changed during this period. Otherwise, the current winds and supernovae would not be forming a separate bubble.

The rather old dynamical age (10 – 15 Myr) of the bubbles in NGC 1569 is not surprising since the high frequency cutoff in the nonthermal radio spectrum and photometry of the super star clusters indicate the galaxy is in a postburst phase. In § 5.3, I presented evidence for three pairs of polar bubbles breaking through the HI disk. In Figure 5.4, bubbles D and G lie close together at $\tau \approx 12$ Myr and $L/n \approx 5 \times 10^{40} \text{ cm}^3 \text{ ergs s}^{-1}$, and bubbles F and E are very nearby. Bubbles A and B, on the other hand, may be somewhat younger and require a larger power input. (More detailed modeling accounting for the geometry is required to confirm this suggestion.) In addition to the famous super star clusters A and B (Ables 1971), the galaxy contains another cluster (hereafter called C) located $\sim 7''$ NW of cluster A whose visible luminosity is about 8 times fainter than cluster A. This opens the question of whether each star cluster can be associated with a bipolar breakthrough. Spectra (Arp & Sandage 1985) and HST photometry (O’Connell, Gallagher, & Hunter 1994) indicate cluster B is slightly older than cluster A whose core age is ~ 15 Myr. An instantaneous burst of star formation 15 Myr ago normalized to the V band luminosity of cluster A would have produced an average mechanical power of $4 \times 10^{39} \text{ ergs s}^{-1}$ (Leitherer & Heckman 1995). Hence the average ambient density would have to be fairly low, $n \sim 0.1 \text{ cm}^{-3}$, for cluster A to drive one of the outflows by itself. Cluster C is probably younger (Rieke 1995); however, it is not luminous enough to drive one of the outflows by itself. When cluster A was 5 Myr old, its visual luminosity would have been nearly a magnitude brighter whereas cluster C is one magnitude fainter. Hence, while it appears to be energetically feasible for the combined clusters to power the outflow, I find no clear correspondence between individual super star clusters and the cells comprising the outflow.

NGC 4449 is the largest galaxy in the sample, and its global star formation rate

over timescales from 10^6 yr to 10^9 yr is thought to be much more uniform (Hill et al. 1994). The age – power distribution of catalogued bubbles, Figure 5.4, does not follow the constant L/n evolutionary path found in some of the other galaxies. The power is supplied on scales ranging from $\lesssim 10^{38} \text{cm}^3 \text{ ergs s}^{-1}$ to $\gtrsim 10^{41} \text{cm}^3 \text{ ergs s}^{-1}$. However, the bubbles have a relatively narrow age range – most have dynamical ages of 1 – 5 Myr. Using far ultraviolet and Balmer-line imagery of the large OB complexes in NGC 4449, Hill et al. conclude that massive star formation terminated in the bar 5 – 6 Myr ago and continues in association with the large HI cloud along the northern rim of the $\text{H}\alpha$ image. These ages can be interpreted as the age of an instantaneous burst or the time since the end of an epoch of continuous star formation. Hill et al. adopted the latter interpretation because of the concentration of light at many wavelengths along this ridge suggests it is a longstanding site of star formation. However, the young upper limit on the superbubble dynamical age suggests the bar experienced a burst of enhanced star formation ~ 5 Myr ago.

5.4.3. The Fate of the ISM

Since superbubbles have grown to galactic dimensions, their fate is expected to depend critically on the large-scale distribution of HI and the galactic gravitational potential. By analogy to the HI holes surrounding the ionized supershells in the LMC (1980), some of the neutral ISM in these galaxies may participate in the starburst-driven gas motions. Consequently, estimates of the dynamical mass require two-dimensional mapping of the HI velocity field. Although this requires a large amount of telescope time, many of these nearby, gas-rich galaxies have been mapped with the VLA or Westerbork Synthesis Radio Telescope. Table 5.3 summarizes the HI observations which will be used to constrain the environment of the superbubbles.

The HI rotation curves generally show solid body rotation across the optical

Table 5.3 Superbubble Environment

Galaxy	M_{HI} (M_{\odot})	v_{circ} (km s^{-1})	$R(v_{circ})$ (kpc)	i ($^{\circ}$)	v_{circ} (km s^{-1})	$v_{esc}(R_{25})$ (km s^{-1})	HI Extent (kpc \times kpc)	Ref.
NGC4449	2.2e9	75	31.4	51	97	248	43 \times 70	1,2
NGC4214	2.4e9	55	2.5	88	14.6 \times 12.9	2,3,4
NGC1569	8.4e7	45	1.1	64	3.07 \times 1.92	2,5,6
NGC4861	5.4e8	80	16.5	67	87	188	11.9 \times 15.7	2,7
NGC3077	1.2e9	40	12.3	76	12.7 \times 8.0	2,8,9
M82	8.8e8	112	6.48		113	160	...	8
NGC1800	1.6e8	30	6.5	60	35	70	13.9 \times 8.08	10, 11
II Zw40	4.5e8	53	5.2	75	15.2 \times 2.4	13, 12
SexA	1.1e8	40	1.43	63	2.9 \times 2.9	14, 15
IZw18	7e7	40	0.87	110	2.9 \times 1.5	16, 17
NGC5253	1.4e8	28	1.49	40	4.3 \times 4.3	18, 19
NGC2363	9.9e8	53	5.5	58	63	100	7.67 \times 16.7	12, 22
NGC2537	2.8e8	12
VI Zw403	4.9e7	20
NGC3738	1.6e8	21

NOTES: (col 2) Atomic hydrogen mass. (col 3) Projected rotation speed at the radius in column 4. (col 5, 6) Inclination of the galaxy and corrected rotation speed. (col 7) Example of a typical escape velocity at the radius where the continuum emission is 25 B mag / (arcsec)². (col 8) Spatial dimensions of the neutral hydrogen.

REFERENCES: (1) Bajaja, E., Huchtmeier, W. K., & Klein, U. 1994, A&A, 285, 385. (2) deVaucouleurs 1991 RC3 (3) Kobulnicky, H. A., & Skillman, E. D. 1996, (preprint). (4) Kobulnicky, H. A. 1996, pvt. comm. (5) Israel, F. P., & van Driel, W. 1990, A&A, 236, 323. (6) Reakes, M. 1980, MNRAS, 192, 297. (7) Wilcots, E. M., Lehman, C., & Miller, B. 1996, AJ, 111, 1575. (8) Appleton, P. N., Davies, R. D., & Stephenson, R. J. 1981, MNRAS, 195, 327. (9) van der Hulst, J. M. 1979, A&A, 75, 97. (10) Hunter, D. A., van Woerden, H., Gallagher, J. S. III 1994, ApJS, 91, 79. (11) Gallagher, J. S., Knapp, G. R., & Hunter, D. A. 1981, AJ, 86, 344. (12) Thuan, T. X., & Martin, G. E. 1981, ApJ, 247, 823 (TM). (13) Brinks, E. & Klein, U. 1988, MNRAS, 231, 63P. (14) Skillman, E. D., Terlevich, R., Teuben, P. J., & van Woerden, H. 1988, A&A, 198, 33. (15) Huchtmeier, W. K., Sciradakis, J. H., Materne, J. 1981, A&A102, 134. (16) Viallefonde, F., Lequeux, J., and Comte, G. 1987, in Starbursts and Galaxy Evolution, ed. T. X. Thuan, T. Montmerle, and J. Tran Than Van (Editions Frontière: Gif sur Yvette), p. 139. (17) Lequeux, J., & Viallefond, F. 1980, A&A, 91, 269. (18) Kobulnicky, H. A., & Skillman, E. D. 1995, ApJ, 454, L121. (19) Reif, K., Mobold, U., Goss, W. M., vanWoerden, H., & Siegman, B. 1982, A&AS, 40, 451. (20) Tully, R. B., Boesgaard, A. M., Dyck, H. M., & Schempp, W. V. 1981, ApJ, 246, 38. (21) Hunter, D., Gallagher, J., & Rautenkranz, D. 1982, ApJS, 49, 53. (22) Braun, R. 1995, A&AS, 114, 409.

galaxy and several begin to flatten out at larger distances. The potential far above the plane is probably dominated by a dark halo, so the circular velocities measured from these rotation curves provide a lower limit on the escape velocity, $v_{\text{esc}} = \sqrt{2}v_{\text{circ}}$. To provide an indication of how much higher the escape velocity at the location of the shells might be, Table 5.3 also lists a rough estimate of v_{esc} at the radius of the 25 B-mag / arcsec² isophote. This value was computed assuming a spherical, isothermal halo which extends as far as the detected HI, so that $v_{\text{esc}}(r) = \sqrt{2}v_{\text{circ}}\sqrt{1 - \ln \frac{r}{r_{\text{max}}}}$. In all but a few cases, no inclination correction has been applied, so the estimates of v_{esc} are systematically low. Inclination determinations are often not straightforward. The rotation axis of the HI “disk” is not necessarily aligned with the optical minor axis (e.g. Kobulnicky et al. NGC 5253), and some of the disks may not be circular (e.g. Skillman et al. Sex A). Huchtmeier et al. (1981) suggest the scale height of these gaseous “disks” is larger than that of typical late-type spirals.

Breakthrough and Blowout

Once the massive stars die off, a supershell would in principle continue to coast outward conserving its momentum. The bubble’s environment, however, will dictate which of several possible fates it meets. Shear forces are negligible in these disks due to the solid-body rotation. I will consider in turn the role of radiative losses, the pressure of the ambient medium, and the distribution of the HI.

The simple solution for the shell’s motion assumes the pressure from the adiabatic bubble of shocked wind pushes the radiating shell of swept-up ISM outward. Should radiative losses from the bubble’s interior become significant, the shell’s growth rate would slow down to that of the momentum-conserving solution. The cooling time depends on the amount of mass residing in the cavity through

its effect on the cooling rate. In the self-similar solution for the shell's motion, the thermal energy in the bubble is 5/11 of the kinetic energy supplied by the stars, so in terms of the cooling function $\Lambda(T)$ the time t_c for the bubble to radiate all its thermal energy can be estimated from

$$t_c = \frac{5/11 L_w t}{4/3\pi R_c^3 \Lambda n_H n_e}.$$

This mass is probably much higher than the mass of shocked wind due to “mass loading” by conductive evaporation off the shell and possibly entrained clouds. Here, I adopt the conventional solution for the maximum temperature and density inside a bubble whose structure is determined by classical conductivity (e.g. Shull 1993). The classical conductivity can be multiplied by a dimensionless scaling factor κ_0 to account for either magnetic suppression ($\kappa_0 < 1$) or the enhanced surface area of clouds ($\kappa_0 > 1$). The cooling rate is fit reasonably well by a power law, $\Lambda = \Lambda_0 T^{-0.5}$, at temperatures between 10^5 K and $10^{7.5}$ K. At cosmic abundance $\Lambda_0 \approx 1.6 \times 10^{-19}$ ergs s⁻¹ cm³ (Koo & McKee 1992). Any decrease in the cooling rate in the dwarfs will serve to make the cooling time longer than the estimate. The cooling time is then

$$t_c = (2.46 \times 10^8 \text{ yr}) v_{100}^{1/7} R_{100}^{5/7} n_0^{-2/7}.$$

The critical velocity at which the cooling time drops below the age of the bubble is

$$v \gtrsim (0.51 \text{ km s}^{-1}) R_{100}^{1/4} n_0^{1/4} \kappa_0^{5/8}.$$

A glance at Figure 5.3 indicates radiative losses from the bubble interior are not a concern.

The lower-bound around 20 km s^{-1} is a consequence of two related effects. On a microscopic scale, the net effect of thermal and turbulent motions broadens the H α line and limits our spectral resolution such that $\delta\lambda/\lambda = v_{mp}/c$ where

$v_{mp} = \sqrt{\frac{2kT}{m_H}} = \sqrt{2}c_0$. On a macroscopic scale the pressure of the ISM stops the growth of the bubble when the ram pressure of the shell, which is comparable to the interior pressure of the bubble, drops to that of the ambient medium. This happens when $v_s \approx c_0$, the isothermal sound speed. The wind power from an aging starburst is nearly constant in time, so a supershell will evolve along a loci of constant L_{in}/n in Figure 5.3 until it reaches the horizontal pressure confinement line at $v \approx 13 - 20 \text{ km s}^{-1}$. Most of the shells are not near this termination line.

The most common evolutionary route for the large bubbles is breakthrough. This scenario could be postulated based on the morphology of the $H\alpha$ emission alone. However, a stronger statement can be made based on the gas dynamics. In order for a shell to break through the HI disk, it must be traveling faster than the sound speed in the ambient medium when it reaches the scale-height of the disk. For a midplane gas density ρ_0 , effective scale height H_{eff} , and sound speed c_0 , the critical energy injection rate which meets this criterion is

$$L_{crit}/n \geq 2.2 \times 10^{38} H_{500}^2 c_{13}^3$$

ergs $\text{s}^{-1} \text{ cm}^3$. In Figure 5.3, most of the shells lie well above this line.

5.5. Summary: Some Comments on the Role of Gas Dynamical Feedback in the Evolution of Dwarf Galaxies

Inspection of Table 5.2 or Figure 5.3 leads one to conclude that expanding supergiant shells with radii exceeding 300 pc are the “norm” in this sample of 14 galaxies. Since roughly one out of every four high-surface-brightness dwarfs exhibit emission-line shells and/or filaments that would meet the criteria for membership in my sample (e.g. Hunter et al. 1993), such large-scale gas flows are evidently

relatively common in dwarfs in general. The enormity of this spatial scale is quite important in two respects. First, since the impact of individual massive stars occurs on spatial scales that are unresolved in the data, the observation of large, coherent structures attests to the hierarchical nature of the feedback. It was also shown that the range of sizes can often be interpreted as evidence for the growth of supergiant shells. Secondly, the scale of the largest shells is comparable to and probably determined by the scale height of a thick, ambient HI disk.

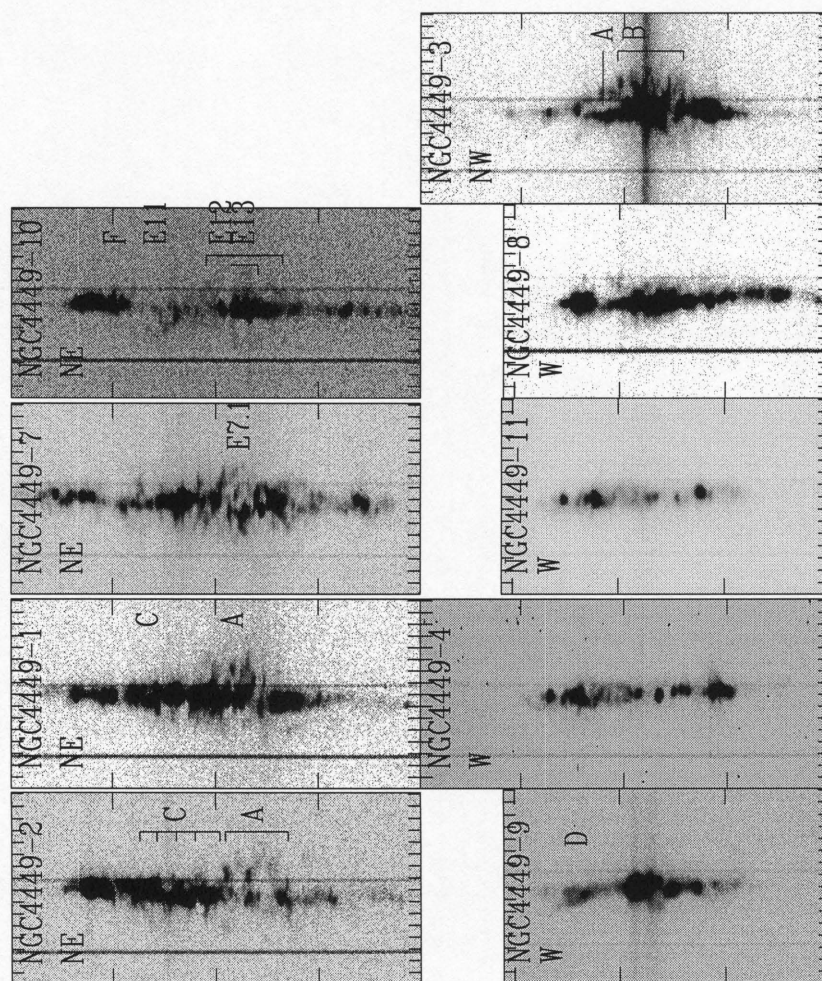
The fate of the larger shells, and the ISM in general, remains a challenging question. While it was shown that many of the bubbles are energetic enough to break through the HI disk, their estimated kinetic energy typically falls significantly short of the minimum kinetic energy required to unbind all the ISM from the galaxy. Although most of these “dwarfs” are considerably more massive than the local stellar systems referred to as dwarf spheroidal galaxies, their rotation velocity (columns 3 and 6 of Table 5.3) still lie slightly below the critical virial velocity, 100 km s^{-1} , that Dekel & Silk (1986) arrived at for supernova-driven galactic gas loss.

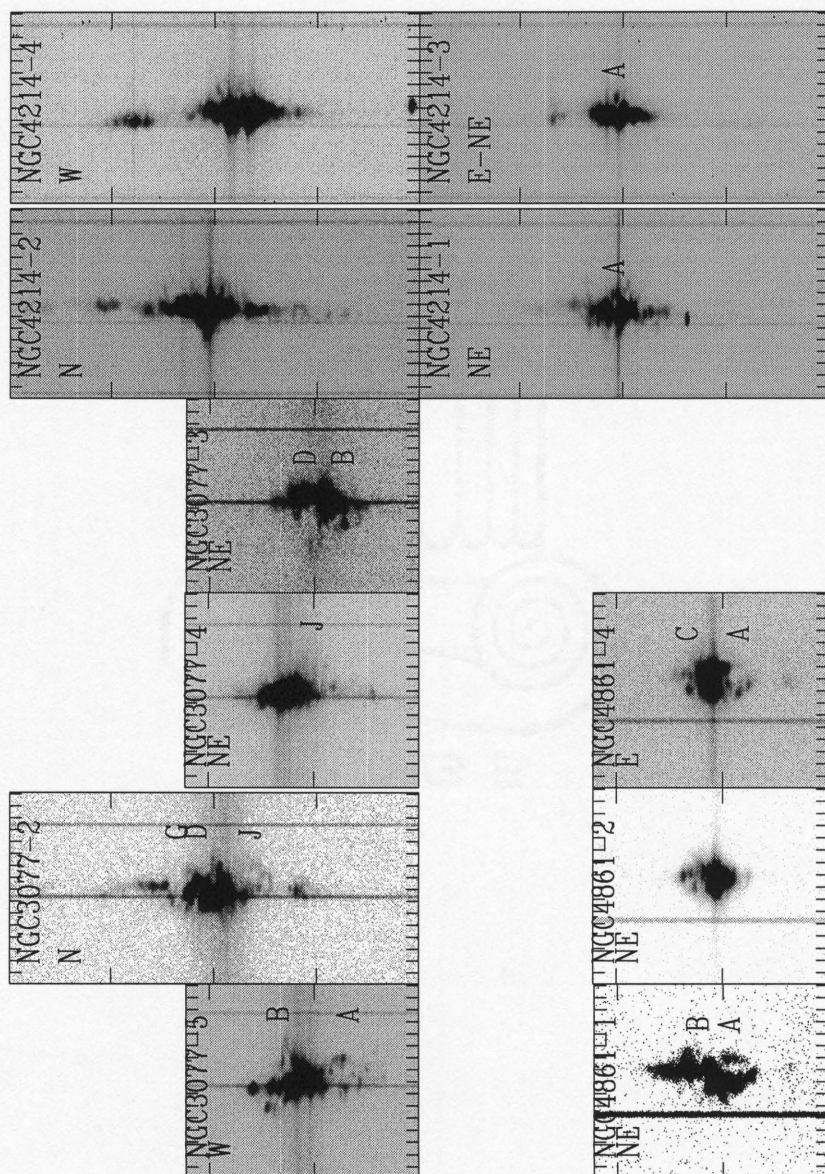
So why is it that we do not find many galaxies in the “wind” stage? Part of the answer may be connected to the multi-dimensional nature of the global hydrodynamics (DeYoung & Heckman 1994). The location of kinematic shells relative to the $\text{H}\alpha$ shells and filaments and to the continuum emission provides strong evidence that at least several of the larger bubbles have a polar rather than a spherical geometry. From an empirical standpoint, projection effects could introduce errors amounting to a factor of two in the inferred shell radius or velocity which would propagate into the estimated energy nonlinearly ($E_{\text{in}} \propto v^2 R^3$). The error introduced by a spherical dynamical model is harder to quantify. A well-planned grid of multi-dimensional numerical simulations may improve our understanding, although the lack of observational constraints on the three-dimensional distribution

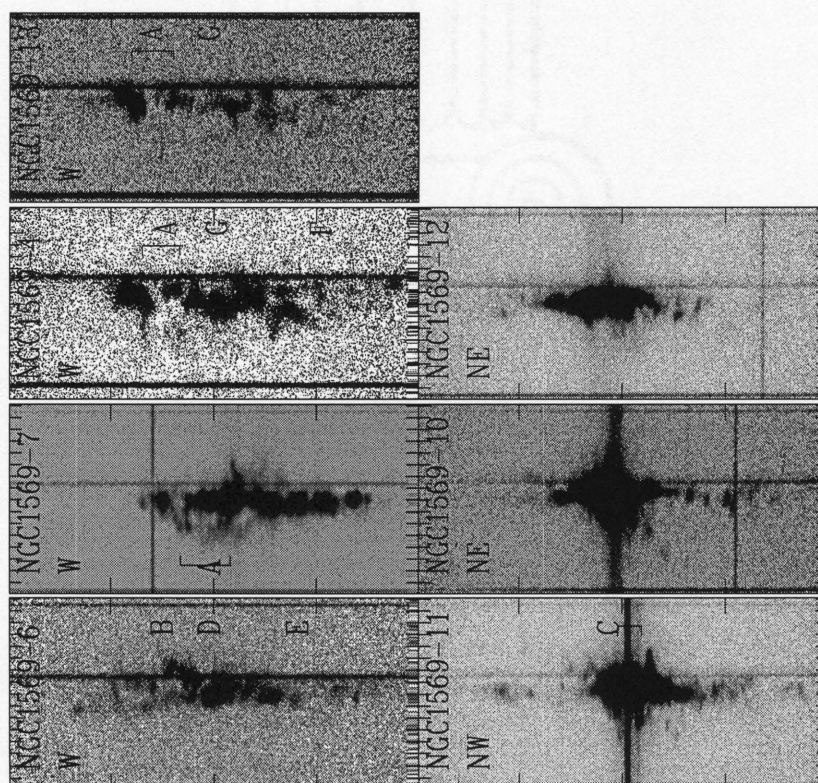
of the HI disk and halo would appear to impose some limitations on the accuracy of such modeling. The large number of shells that seem to be in the breakthrough stage may be an indication that the shells are trapped in this state for a long time. Further numerical simulations could help us understand the transition from breakthrough to blowout, and a comparison with the data might constrain the HI disk-halo geometry.

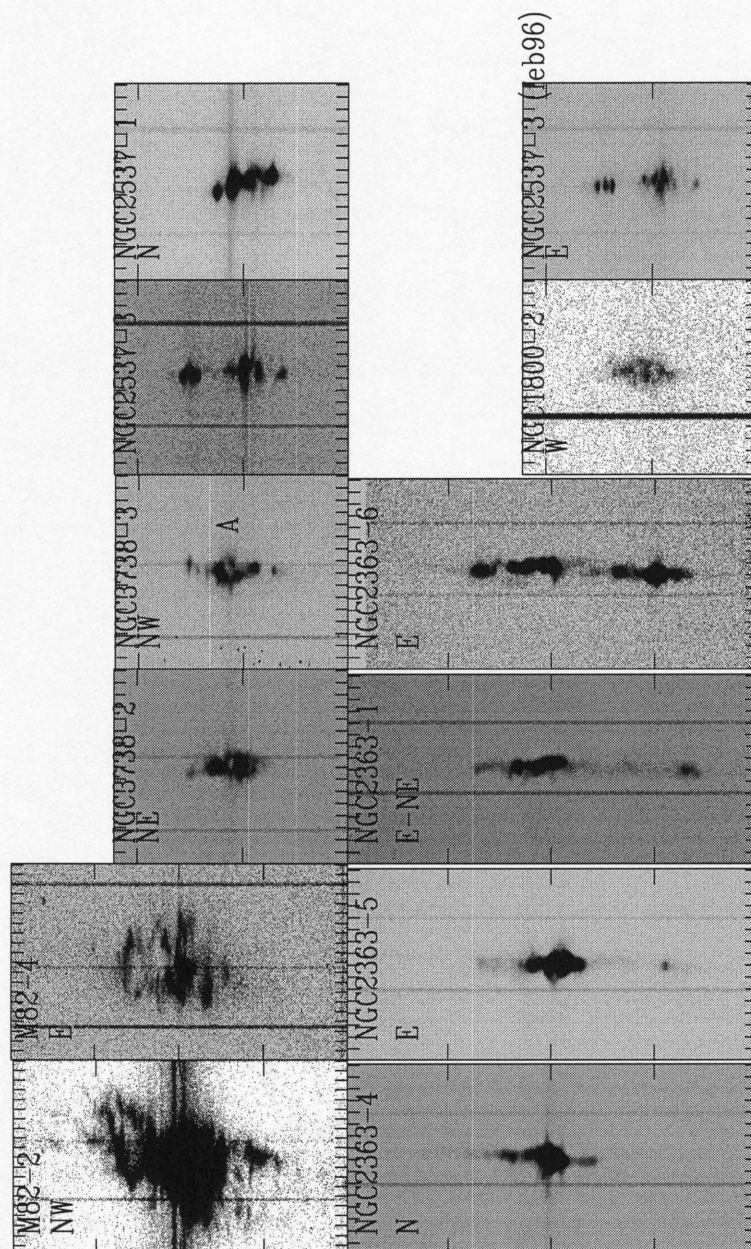
The break with spherical geometry may allow for the inflow of gas to the starburst region. This circulation might affect how many star formation events contribute to a particular supergiant bubble. The resulting duration of the mechanical input from the burst is critical to the mass ejection issue. For example, if star formation continues at the present rate for another 100 Myr in NGC 3077, then the kinetic energy in the shells becomes comparable to the binding energy of the interstellar gas. While the color gradients across these galaxies generally provide evidence for an older, underlying population of stars, the star formation history on 10^8 yr timescales is generally not well constrained.

Figure 5.1 H α echellograms. The ticks mark increments of 46 km s⁻¹ in the horizontal direction and 60 " in the vertical direction. Wavelength increases to the right. The name of the galaxy and label identifying the position in Table 5.1 are printed at the top of each slit.









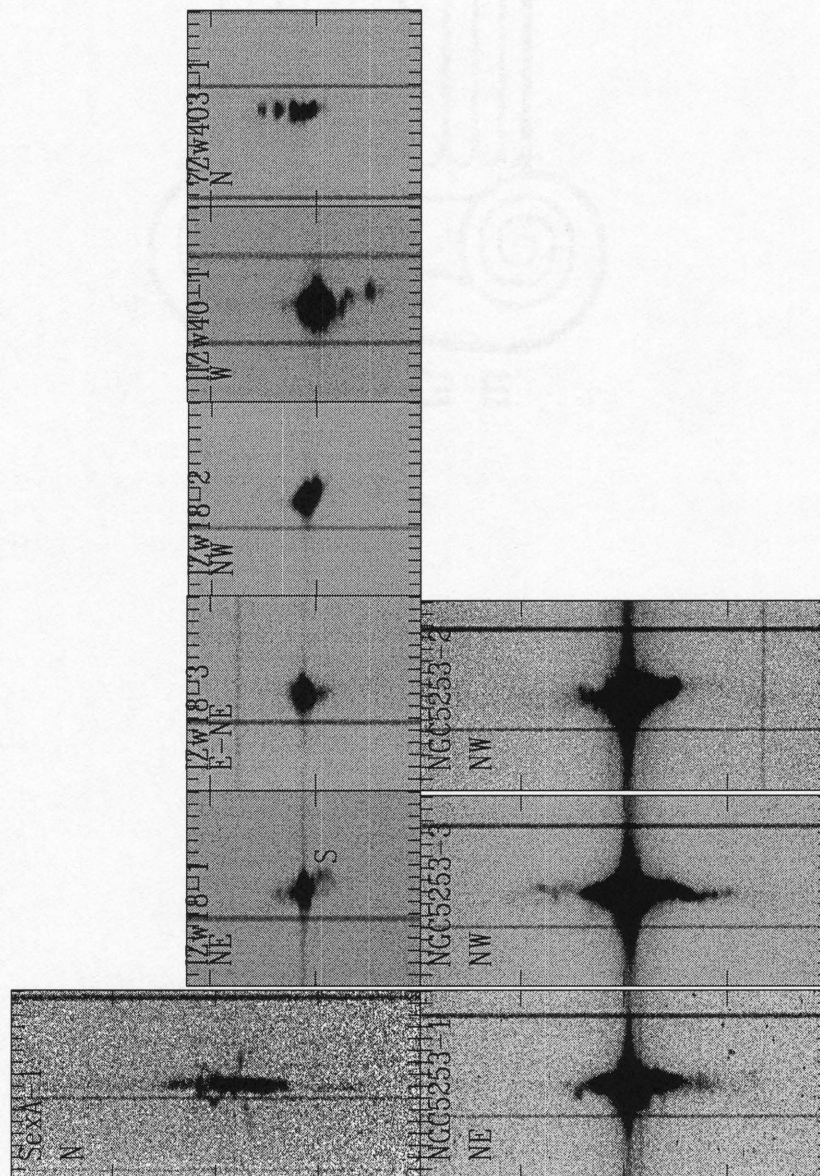
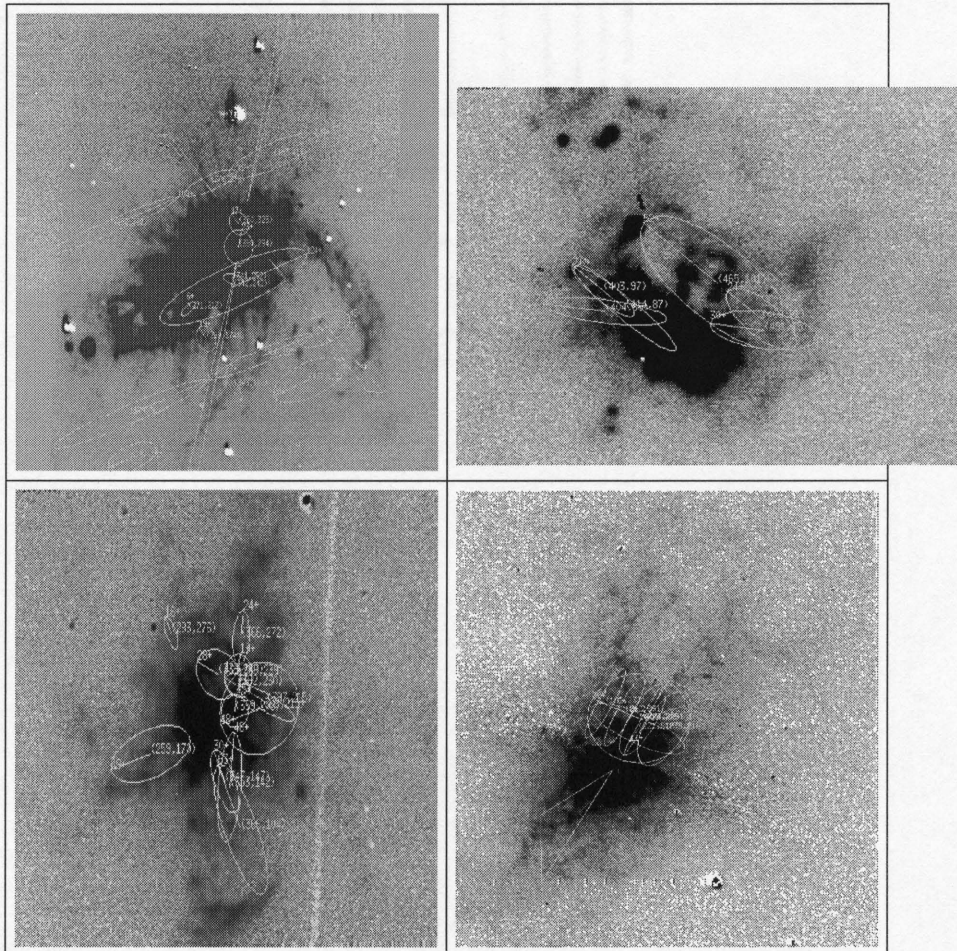
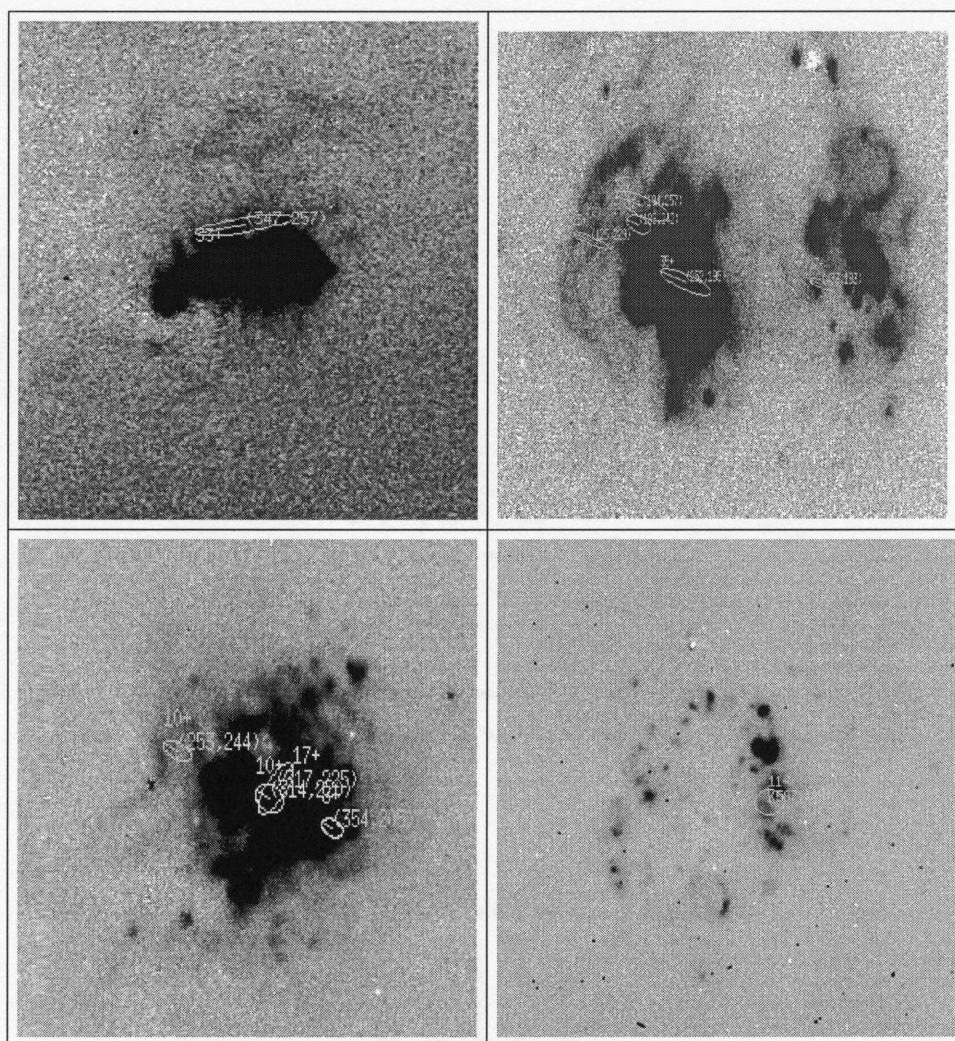
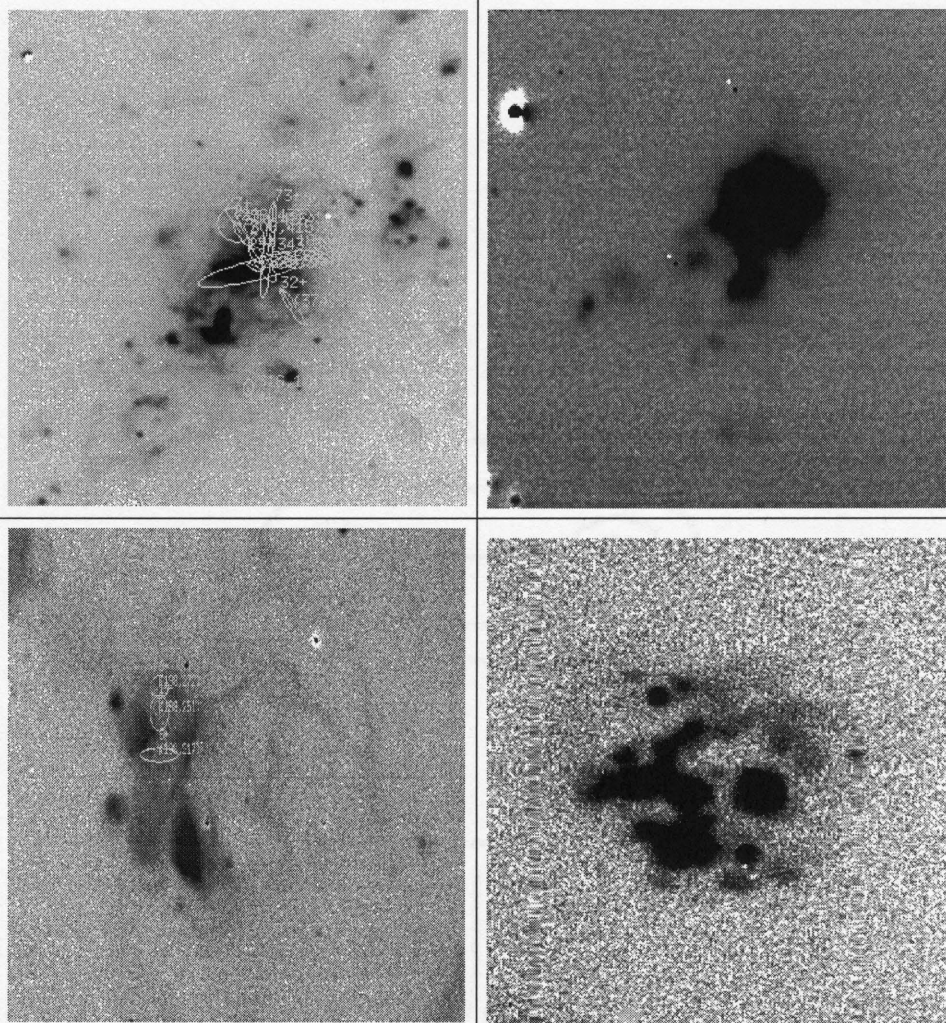


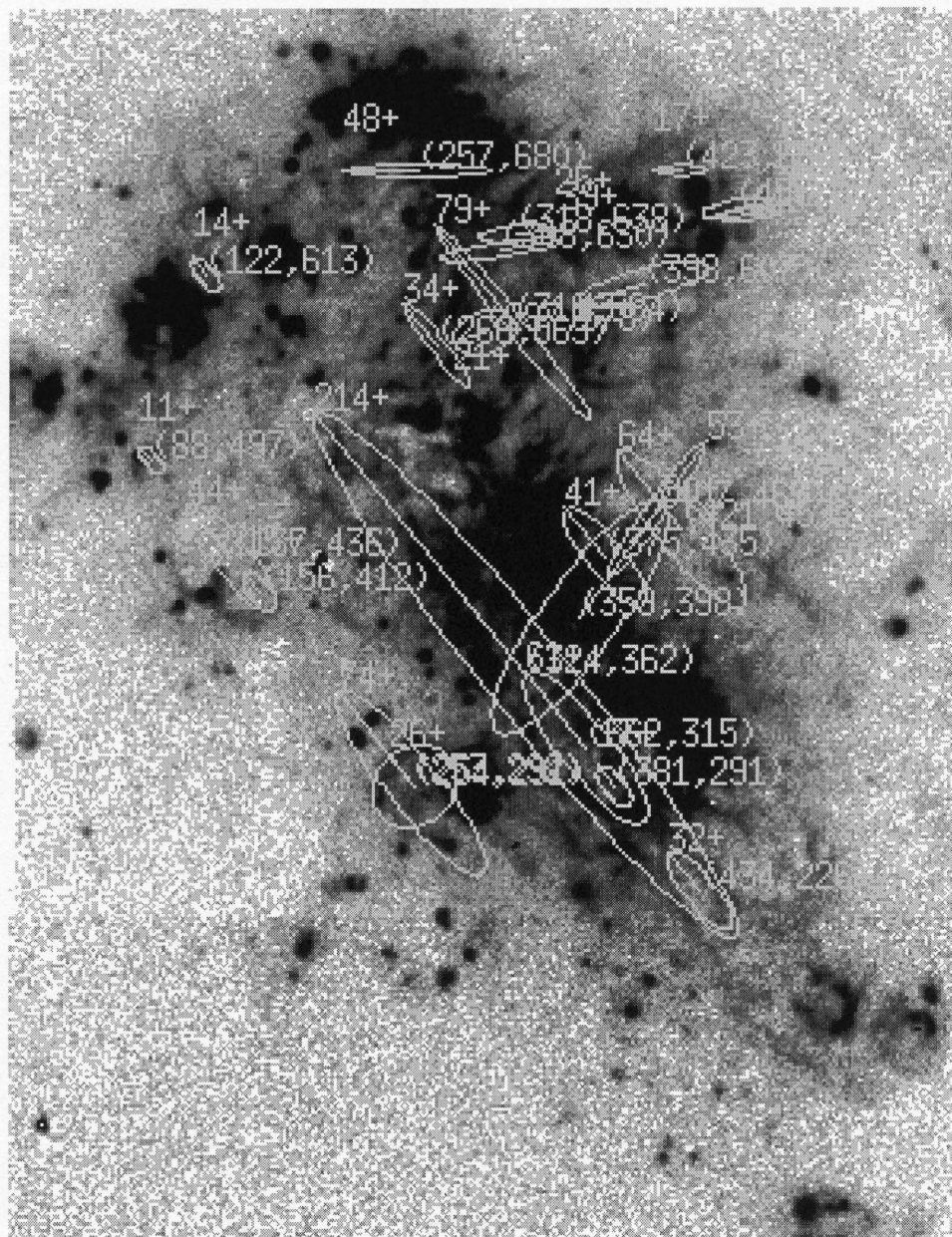
Figure 5.2 Positions of expanding shells relative to the $H\alpha$ morphology. The axis of the ellipse colinear with the position angle of the slit represents the spatial dimension of the Doppler ellipse, and the second axis (usually the minor axis) is scaled such that 1 pixel is approximately 0.73 km s^{-1} of velocity splitting.







ACID FREE



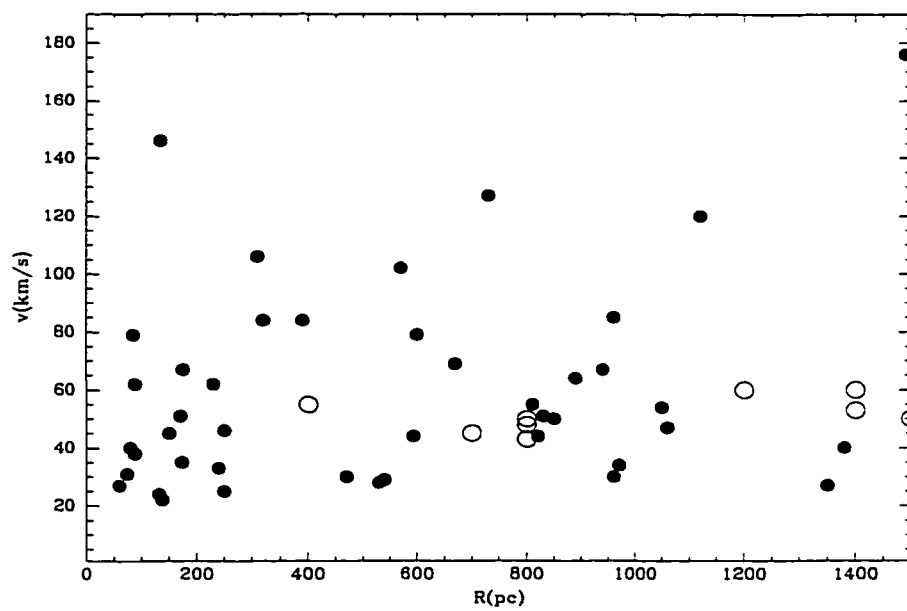


Figure 5.3 Measured radii and radial velocities of kinematic shells. Open symbols show the kinematic shells found by Marlowe et al. (1995) in 7 amorphous dwarfs.

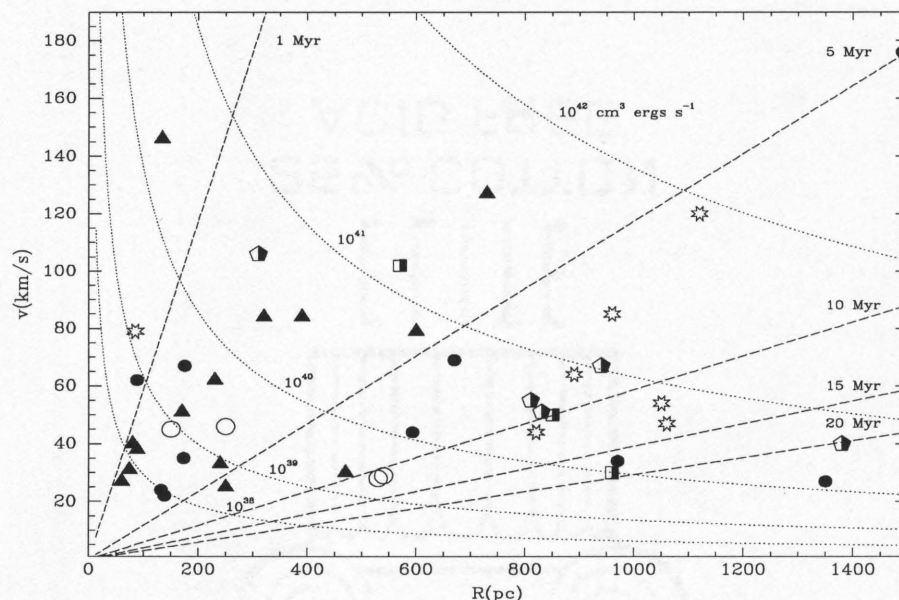


Figure 5.4 (a) The ages of wind-blown bubbles and their power requirements. Data are the same as in Figure 5.3. Shell isochrones are denoted by dashed lines. The dotted lines follow the trajectories of shells powered by a constant rate of kinetic energy injection and are normalized to an ambient hydrogen number density of $n(\bar{1}) = 1 \text{ cm}^{-3}$. The units for these curves are $(n(\bar{1})/1 \text{ cm}^{-3}) \text{ ergs s}^{-1}$. Modifications for a density gradient or time-dependent energy injection follow directly from equations (5) and (6) of Martin (1996) which were derived from the general solutions discussed in Ostriker and McKee (1988).

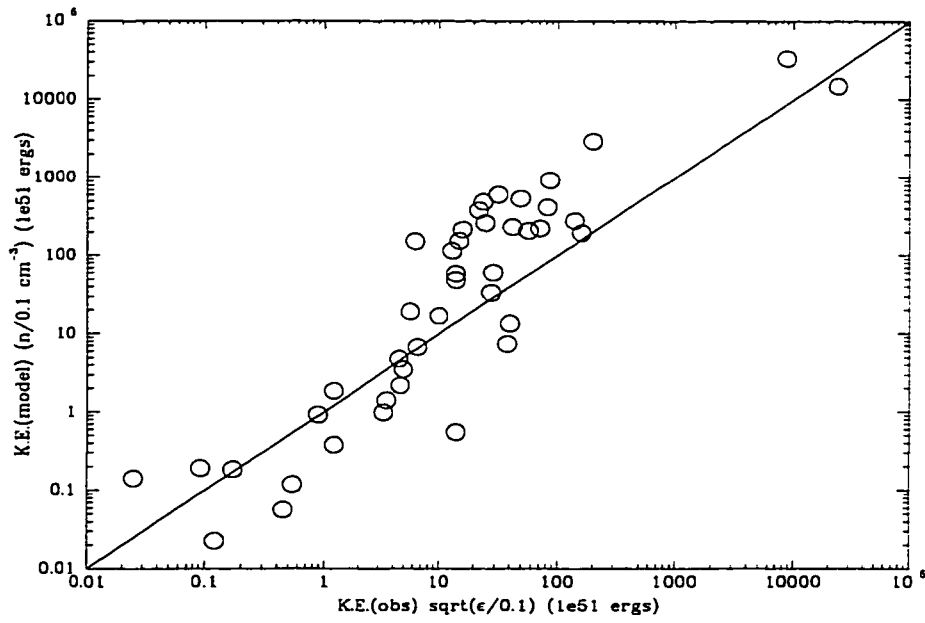


Figure 5.5 Constraints on the average ambient H density. The kinetic energy of the shell derived from the shell radius and velocity using the simplest one-dimensional model is compared to that estimated from the total mass of ionized hydrogen in the complex and the expansion velocity.

CHAPTER 6

SUMMARY

6.1. Main Results

The main results from the analysis of the emission line spectra in Chapter 2 and Chapter 3 are summarized here.

- Relative to HII regions, the spectrum of the DIG is characterized by high $[\text{O I}] / \text{H}\alpha$ in addition to the high $[\text{O II}] / [\text{O III}]$, $[\text{S II}] / \text{H}\alpha$, $[\text{N II}] / \text{H}\alpha$ and low $[\text{O III}] / \text{H}\beta$ reported previously by others.
- The spectral change is gradual and continuous, so a boundary between HII regions and the DIG is difficult to define spectroscopically. The value of any particular line ratio in the DIG is coupled to the metallicity, ionization parameter, and effective stellar temperature of the nearby giant HII regions.
- The spectral transition advances along a narrow sequence in the diagnostic-line-ratio diagrams commonly used to distinguish nebular excitation mechanisms. The distance of the aperture from a giant HII region or the average $\text{H}\alpha$ surface brightness within the aperture serve equally well as the sequencing parameter.

- In contrast to the HII region excitation sequence for the same set of galaxies, spectral modeling demonstrates that the HII-DIG sequence is driven primarily by a decrease in ionization parameter – the relative density of ionizing photons to atoms. This result confirms earlier suggestions that the dominant excitation mechanism of the extended, ionized gas is photoionization by distant (~ 1 kpc) clusters.
- An excitation mechanism in addition to photoionization is required to explain the spectral signature of the lowest surface brightness gas. Shocks with speeds from $60 - 100 \text{ km s}^{-1}$ are shown to be the most likely mechanism. The evidence for shocks is particularly strong in NGC 4449, for example, where neither the moderately high $[\text{OIII}]\lambda 5007 / \text{H}\beta$ at very high $[\text{SII}]\lambda\lambda 6717, 31 / \text{H}\alpha$ nor the sharp increase in $[\text{OI}]\lambda 6300 / \text{H}\alpha$ with a moderate increase in $[\text{OII}]\lambda\lambda 3727 / [\text{OIII}]\lambda 5007$ is easily produced by dilute photoionization models. The contribution from shocks is harder to distinguish in galaxies where the HII regions have low metallicity and/or high ionization parameters. At metallicities near solar a contribution to the spectrum from 100 km s^{-1} shocks can actually change the sign of the gradient in $[\text{OIII}]\lambda 5007 / \text{H}\beta$ along the transition sequence. Typically, shocks excite no more than 30% of the emission from the extended, low surface brightness ($\sim 100 \text{ R}$) regions, although their contribution probably reaches 50% in NGC 4449.
- In the three high surface brightness Magellanic irregular galaxies studied, the mean reddening-corrected ratio of $\text{He I } \lambda 5876 / \text{H}\alpha$ is ≈ 0.041 independent of spatial location. This value is much higher than the value measured in the diffuse, warm ionized interstellar medium of the Milky Way (Reynolds

& Tufte 1995) and implies the He^+ ionization fraction, $\chi(\text{H}) \equiv \frac{n(\text{He}^+)}{n(\text{He})}$, is approximately equal to the H^+ ionization fraction, $\chi(\text{He}) \equiv \frac{n(\text{H}^+)}{n(\text{H})}$, in the diffuse ionized gas (DIG). If the DIG is powered by young stars as suspected, then stars of mass $\geq 35 M_{\odot}$ must contribute to the Lyman continuum radiation reaching the DIG.

- The contrast with the low $\chi(\text{He})/\chi(\text{H})$ in the Galactic DIG, however, is intriguing and provides the first strong evidence that the DIG's physical state, not just its presence, varies among galaxies.

The case study of I Zw 18 (Chapter 4) and the preliminary analysis of 14 other dwarf galaxies in chapter 5 lead to the following results.

- Large, i.e. kpc scale, expanding shells of ionized gas are detected in many of the galaxies. Even smaller galaxies, i.e. I Zw 18, sometimes contain kinematic structures on this scale.
- The geometry of most of these supergiant bubbles is not spherical. Generally, there is no evidence for the remains of a star cluster near their center. However, one end of the shell is typically located near a giant HII region and/or star cluster in the main body of the galaxy. The diameter of the bubbles is often \gtrsim the estimated scale height of the ambient HI. Hence, the geometry of these bubbles can be described as “polar.”
- The mechanism collimating these bubbles is not as simple as one might have hoped. The bipolar outflows in M82, NGC 1569, and NGC 1800 are clearly directed along the minor axis of the HI. However, although the distributions of HI in NGC 4861, I Zw 18, NGC 2363, and NGC 3077 are

best described as rotating disks, the polar axes of the breakthrough bubbles are not perpendicular to the plane of the disks.

- The true expansion velocity and spatial dimensions of the bubble are related to the measured radial velocity and projected dimensions of the bubble. However, this relationship depends on the inclination of the polar axis with respect to our line-of-sight and the hydrodynamic interaction of the bubble with the density gradient in the ambient medium. Assuming a simple density gradient with scale height in the shell, the inclination and opening angle of a bipolar bubble can be constrained from the line profiles across the two lobes.
- Spherical, dynamical models are useful for obtaining a rough estimate of the ages and power requirements of the bubbles. Ages estimated this way range from a few Myr to ~ 20 Myr; power requirements are equivalent to $10 - \sim 10,000$ massive stars. This suggests that more than one generation of stars may supply energy to some bubbles. However, the accuracy of the simple models is no better than a factor of a few, so dynamical models incorporating the non-sphericity of the problem will be necessary to put such statements on firmer ground.
- The likelihood of a $0.002 L^* - 0.2 L^*$ galaxy ejecting its entire ISM remains an open issue. My sample is drawn from the population of nearby, gas-rich dwarfs containing ionized shells or filaments. Such galaxies are thought to comprise about $1/4$ of the local population of high-surface-brightness dwarfs. The shells in roughly $1/2$ of my galaxies are powerful enough to breakthrough the ambient HI disk. However, the total kinetic energy in these shells at the current epoch is insufficient to remove the entire ISM. The fate of such galaxies is inherently a multi-dimensional problem. For example, removal

would become feasible if the bubble is fed at the current rate for another 10 – 100 Myr. Also, blowout in the direction of least resistance may vent much of the energy out of the galaxy without disturbing much of the ISM.

- Some gas will inevitably escape from several of these galaxies. Once a shell ruptures, the coronal gas inside the bubbles will not be bound to the galaxy. The mass of this material is, however, only a few percent of the interstellar gas mass. In some galaxies, in particular NGC 1569, some of the warm ionized gas will probably also be entrained in the outflow. The expansion velocity of the filaments far above the galactic plane is of the same order as the estimated escape velocity from the galaxy there.
- If the breakthrough bubbles rupture and blowout occurs, the subsequent escape of the hot ISM may have profound consequences for the galactic chemical evolution even if only a very small fraction of the interstellar gas escapes from the galaxy.

APPENDIX A

SOFT X-RAY EMISSION FROM NGC 5253

THE ASTROPHYSICAL JOURNAL

Founded in 1895 by George E. Hale and James E. Keeler

CENTENNIAL YEAR

HELMUT A. ABT
Managing Editor
Kitt Peak National Observatory

YERVANT TERZIAN
Associate Editor
Cornell University

VIRGINIA TRIMBLE
Associate Editor
University of Maryland and
University of California, Irvine

ANNE P. COWLEY
Associate Editor
Arizona State University

BERNHARD M. HAISCH
Associate Editor
Lockheed Palo Alto Research
Laboratory

THEODORE SIMON
Associate Editor
Institute for Astronomy
University of Hawaii

JOHN H. THOMAS
Associate Editor
University of Rochester

EDWARD L. WRIGHT
Associate Editor
University of California
Los Angeles

A. DALGARNO
Letters Editor
Center for Astrophysics

EUGENE H. AVRETT
Deputy Letters Editor
Center for Astrophysics

AAS PUBLICATIONS BOARD

JAMES W. LIEBERT (1994-1996), *Chairperson*
University of Arizona

JAMES J. CONDON (1994-1997)
NRAO, Charlottesville, Virginia

JOHN A. NOUSEK (1994-1997)
Pennsylvania State University

HUGH M. VAN HORN (1995-1998)
National Science Foundation

MOSHE ELITZUR (1995-1998)
University of Kentucky

Production Manager: TULIE O'CONNOR

Chief Manuscript Editor: GERALDINE BRADY

Manuscript Editors: WALTER G. GLASCOFF III, BETE GARRISON, KAREN LESLIE BOYD, DEAD A. DONIA, IVAN BRUNETTI,
DIANA GILLOOLY, AND JONATHAN R. BERNIERE

Production Staff: KIM LANGFORD, CINDY GARRETT, RICK SCHORN, CAROLYN CEMIEL, AND KELLY PATRICK CROWDY
Tucson Editorial Office: BLAKE WITTEN, JANICE SEXTON, ALICE PROCIENOW, AND CANDACE M. HAUZER

VOLUME 447, PART 1
1995 JULY 1 AND JULY 10

University of Arizona
Steward
Parker Road
Tucson, AZ 85724-5001

PUBLISHED BY THE UNIVERSITY OF CHICAGO PRESS FOR
THE AMERICAN ASTRONOMICAL SOCIETY

Under the copyright agreement with the Astrophysical Journal authors retain permission to reprint articles, and I grant myself permission.

SOFT X-RAY EMISSION FROM NGC 5253 AND THE IONIZED INTERSTELLAR MEDIUM

CRYSTAL L. MARTIN¹ AND ROBERT C. KENNICUTT, JR.¹

Steward Observatory, University of Arizona, Tucson, AZ 85721

Received 1994 October 3; accepted 1995 January 17

ABSTRACT

A new *ROSAT* PSPC observation of the gas-rich dwarf galaxy NGC 5253 reveals an extended, soft X-ray source near the center of the galaxy. The pulse-height spectrum is well fit with a Raymond-Smith model for a thermal plasma at a temperature of $(4.0 \pm 1.3) \times 10^6$ K for a foreground absorbing column of $\log N_H = 21.4$ cm⁻². The X-ray luminosity between 0.1 and 2.4 keV is $L_X = (6.5^{+1.4}_{-1.4}) \times 10^{39}$ ergs s⁻¹. Higher resolution X-ray imaging is needed to determine the contribution to L_X from point sources. However, we argue that hot interstellar gas produces most of the X-ray emission and investigate whether stellar winds and supernovae in the central starburst can heat the required mass of X-ray-emitting gas. We find the simplest superbubble model underpredicts L_X by a factor of 16 but show that a superbubble evolving in a clumpy ambient medium can easily reproduce the observed X-ray properties. Our model suggests the most recent burst is young ($\sim 5 \times 10^6$ yr) and requires evaporating clouds or filaments to fill a small fraction of the nebula.

To provide additional insight into the dynamics of the interstellar medium (ISM) in NGC 5253, we present results from H α imaging and follow-up high-resolution spectroscopy of the H α emission line. The spectacular filaments extending from the galaxy in the H α image do not show unusually high velocities; in the outer part of the nebula, the velocity of the gas producing the H α emission shifts randomly by ± 10 –30 km s⁻¹ over scales of ~ 100 –200 pc. The complex velocity field in the core can be interpreted as a slow, global expansion of the warm ionized medium coincident with the region of X-ray emission. We discuss the relation of the hot and warm phases of the ISM in NGC 5253 and draw analogies to giant H II regions and superwind galaxies.

Subject headings: galaxies: individual (NGC 5253) — galaxies: ISM — galaxies: kinematics and dynamics — X-rays: galaxies

1. INTRODUCTION

This paper is the first in a series on the ionized components of the interstellar medium (ISM) in dwarf galaxies. Our study aims to quantify the impact of violent star formation on the dynamical and physical properties of the ISM. This type of feedback is common in late-type galaxies and occurs over scales ranging from isolated supernova remnants (SNRs) to galactic-scale superwinds. Heckman, Armus, & Miley (1990) demonstrated that superwinds may significantly influence the evolution of far-infrared galaxies and the intergalactic medium. We are obtaining new data on a sample of blue compact dwarfs and Magellanic irregulars. They were selected as likely candidates to reveal violent ISM dynamics and are characterized by shallow gravitational potential wells, low metallicities (reduced cooling rates), extended emission-line filaments, and giant H II regions.

NGC 5253 is a low-luminosity, amorphous galaxy (Sandage & Brucato 1979). Its spectrum shows early-type absorption features and emission lines from low-density, photoionized gas. Caldwell & Phillips (1989) identified a young halo population and estimated its age and the age of the star clusters outside of the nucleus to be 10^8 – 10^9 yr. They measured a low stellar rotation rate (≤ 7 km s⁻¹) and high stellar velocity dispersion (50 km s⁻¹) and suggested the galaxy was a dwarf elliptical before the current starburst began. The galaxy's distance as determined from 11 Cepheid variables is 4.1 ± 0.1 Mpc (Sandage et al. 1994). The galaxy is a member of the NGC 5128 Centaurus group (e.g., van Woerden et al. 1993), and its closest

neighbor is M83 (NGC 5236) at a projected distance of 120 kpc.

The present epoch of star formation is concentrated in the central region. The ultraviolet spectrum of the region shows features from Wolf-Rayet stars and complex absorption (Kinney et al. 1993). Walsh & Roy (1989) have spectroscopically mapped the central $16'' \times 48''$ and find that one of the central knots is distinguished by a particularly blue continuum and a broad He II $\lambda 4686$ emission line. The inferred presence of Wolf-Rayet stars in the nucleus of NGC 5253 indicates the burst is at least 3×10^6 yr old, and the enhanced N/O in this region suggests the age is not much more than 5×10^6 yr (Walsh & Roy 1989; Leitherer, Robert, & Drissen 1992). Campbell & Terlevich (1984) have constrained the number of red supergiants in the nucleus (their knot A) and also reach the conclusion that the nucleus is quite young. Although prominent dust lanes are seen in NGC 5253 (see Fig. 1a [PL 5]) and infrared spectrophotometry suggests some regions are totally obscured at optical wavelengths (Aitken et al. 1982), the highest visual extinction derived from the Balmer decrement is $A_V = 1.8$ mag, and 0.84 mag is typical of the central region (Walsh & Roy 1989). The galaxy's spectral energy distribution peaks at 60 μ m, where thermal emission from dust probably dominates.

The morphology of the galaxy's gaseous component is strikingly different from that of the starlight (see Fig. 1b [PL 6]). The surface brightness contours of the H α emission and H I emission (Brinks 1994) are roughly circular. Deep optical images reveal a spectacular network of emission-line filaments (see Fig. 1b; also Hodge 1966), and Marlow et al. (1994) have recently identified an expanding bubble within this halo. The mass of H I scaled to the assumed distance of 4.1 Mpc is

¹ Visiting Astronomers, Kitt Peak National Observatory, NOAO, operated by AURA, Inc., under contract with the NSF.

$1.4 \times 10^6 M_{\odot}$ (Reif et al. 1982; Lewis & Davies 1973), about 10 times the estimated mass of the optically emitting ionized gas. The galaxy's radio continuum is unusual because the emission is almost entirely thermal (Beck 1994).

NGC 5253 was detected in X-rays with the *Einstein Observatory*. Based on its blue luminosity, NGC 5253's X-ray luminosity conforms to the trend established for more luminous spiral and irregular galaxies in the *Einstein* Normal Galaxy Sample (Fabbiano & Trinchieri 1985; Fabbiano, Gioia, & Trinchieri 1988). At an absolute blue magnitude of $M_B = -17.60$, however, the low number of counts in the *Einstein* observation precluded an analysis of its X-ray morphology or spectrum. We requested a deep *ROSAT* PSPC observation to determine whether NGC 5253 has diffuse, hot interstellar gas.

In this paper we discuss the hot and warm components of ionized interstellar gas in NGC 5253. Section 2 presents the results from the new *ROSAT* observation, and § 3 discusses the source of the X-ray emission. In § 4 we introduce H α imagery and high-resolution spectroscopy to describe the distribution and kinematics of the warm ionized medium (WIM). Section 5 summarizes the results obtained in §§ 2, 3, and 4, compares the ISM in NGC 5253 to other star-forming regions, and discusses the energetics and dynamics of the ionized ISM in NGC 5253.

2. X-RAY OBSERVATIONS AND RESULTS

NGC 5253 was observed with the Position Sensitive Proportional Counter (PSPC) on the *Röntgensatellit* (*ROSAT*) during 1993 July 16–20. The net exposure time after eliminating periods of enhanced background was 35,093 s. The galaxy is at the center of the 2° field of view, well inside the inner ring of the PSPC window support structure. The X-ray Mirror Assembly (XMA) + PSPC combination is sensitive over the energy range 0.1–2.4 keV. The spatial resolution and spectral resolution on-axis at 0.93 keV are $\sim 25''$ and $E/\Delta E = 2.3$, respectively. The X-ray emission from the galaxy shows no time variability in the Kolmogorov-Smirnov test

performed in the standard processing (Standard Analysis Software System, Rev. 1). Most of the data analysis was done with the IRAF and PROs software packages; exposure maps were generated with IDL routines (Reichert 1994) using the method described in Snowden et al. (1994).

2.1. Spatial Analysis

To detect diffuse emission, we extracted $15' \times 15'$ images with $4''$ pixels, divided by the exposure map for the energy band, and smoothed the images with a Gaussian function of standard deviation $\sigma = 12''$. The low pulse height bins (pulse-invariant [PI] channels 11–19 at low gain) were excluded to avoid confusion from electronic ghost images. Figures 1b and 2 show contour maps of images in the 0.14–2.04 and 0.44–2.04 keV bands, respectively. About 95% of the X-ray flux comes from the central source; a faint second source shows up $100''$ to the southwest in the hard image. The lowest contours around the central source show slight additional deviations from circular symmetry.

The centroid of the X-ray emission coincides with the position of maximum H α surface brightness (Fig. 1b). The optical positions are accurate to better than $2''$, but the positional accuracy of the X-ray image is uncertain. We searched the *Hubble Space Telescope* (HST) Guide Star Catalog for stars within $45''$ of any X-ray source in the field and found only 13 coincidences, comparable to the expected number of chance alignments. Histograms of the right ascension and declination offsets between the stars and X-ray sources verify that the offsets are random. The faint source to the southwest is $43''$ north and $22''$ west of the position of SN 1972E.

Comparison of the radial X-ray surface brightness profile and XMA + PSPC point-spread function (PSF) suggests that the X-ray emission from the central source is extended. To verify this, we performed a χ^2 test on the observed event distribution. We confined the analysis to a circular region of radius $37.5''$ centered on the peak X-ray emission to avoid any

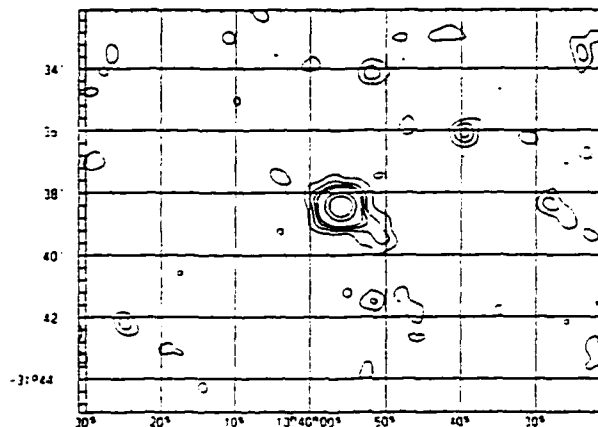


FIG. 2.—Surface brightness contours of hard X-rays (0.44–2.04 keV). The lowest contour represents a surface brightness twice the standard deviation of the background level. The contours are incremented linearly by 1 standard deviation until confusion becomes a problem, then only the contours at 20, 30, and 50 counts $s^{-1} \text{ deg}^{-2}$ are shown.

influence from the secondary source to the southwest. The parent event distribution was estimated from the weighted average of the on-axis XMA + PSPC PSF at 19 energies. We find a significant disagreement between the PSF and observed radial distribution of counts and reject the central source being a point source at the 95% confidence level. We cannot exclude the possibility that two or more point sources produce the X-ray emission; however, we favor an extended source interpretation (see § 3).

We estimated the spatial extent of the X-ray source from the ratio of counts in circular apertures of radius $50''$ and $25''$. The surface brightness of the source was modeled with a two-dimensional Gaussian function whose standard deviation represents the radial extent of the emission region. A series of these Gaussian sources with increasing standard deviation were convolved with the PSF, and the count ratio was measured for each of the resulting models. Figure 3 shows that the expected count ratio rises by $\sim 50\%$ as the source size increases from $1''$ to $15''$. The measured ratio for NGC 5253, plotted as an open circle, implies that the X-ray emission comes from a region of radius of $10'' \pm 2''$, or 200 ± 40 pc.

2.2. Spectral Analysis

Our spectral modeling includes ~ 350 events detected within $75''$ of the centroid of the X-ray emission. The raw and background subtracted spectra are shown in Figure 4. The background region extends from a radius of $75''$ to $1126''$ and excludes all detected X-ray sources. The background counts dominate the raw spectrum at energies less than 0.87 keV, and the net spectrum is very noisy in the lower channels. Using the Morrison & McCammon (1983) absorption model, we fit the

pulse-height spectrum with blackbody, power-law, bremsstrahlung, and Raymond-Smith emission models. We cannot distinguish the Raymond-Smith, bremsstrahlung, and blackbody models based on goodness of fit. However, the best fit to the power-law model is not as good and can be rejected based on its extremely large energy index and absorbing column. The Raymond-Smith model, which includes optically thin continuum radiation and metallic lines from a cosmic abundance plasma in ionization equilibrium (Raymond & Smith 1977), provides the best single-component fit (Fig. 4). We favor it over the bremsstrahlung and blackbody models because the latter require extremely large absorbing columns ($\log N_H \approx 22.0$) and intrinsic X-ray luminosities ($L_x \approx 10^{41} - 10^{43}$ ergs s $^{-1}$). Adding a harder, more heavily extinguished component to the Raymond-Smith model improves the fit only slightly, and the second component is poorly constrained. Given the low S/N of the pulse-height spectrum, we did not pursue multiple-component fits further and adopted the simple, single-component Raymond-Smith model.

The success of the Raymond-Smith model at describing the spectrum suggests NGC 5253's X-ray emission is dominated by thermal emission from hot plasma. We use this model to constrain the physical properties of the plasma. Figure 5 presents the confidence contours derived by minimizing χ^2 for a grid of models in the kT - N_H plane. At the 90% confidence level the temperature of the plasma is $(4.6^{+1.4}_{-1.7}) \times 10^6$ K. The X-ray absorption in terms of hydrogen column density is $\log N_H = 20.6^{+0.4}_{-0.7}$ at the 90% confidence level. The fit is not sensitive to the metal abundance of the plasma, but the X-ray temperature and luminosity are very sensitive to the absorbing column. The galactic H I column is $\log N_H = 20.7$ (Heiles 1975), and the H II

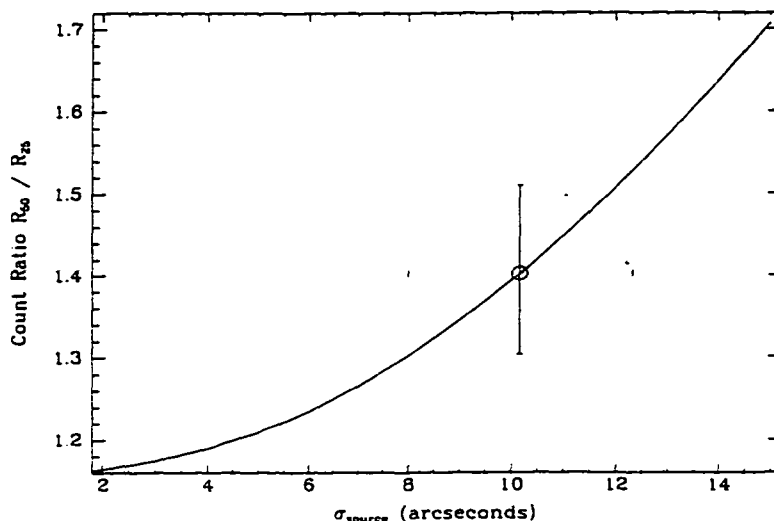


FIG. 3.—Spatial extent of X-ray source. The expected dependence of the count ratio between circular apertures of radius $50''$ and $25''$ on the source size is shown by the solid line. The measured count ratio for NGC 5253 is plotted with an open circle and vertical error bar. The estimated extent of the X-ray emission is shown by the horizontal error bar. See text for details.

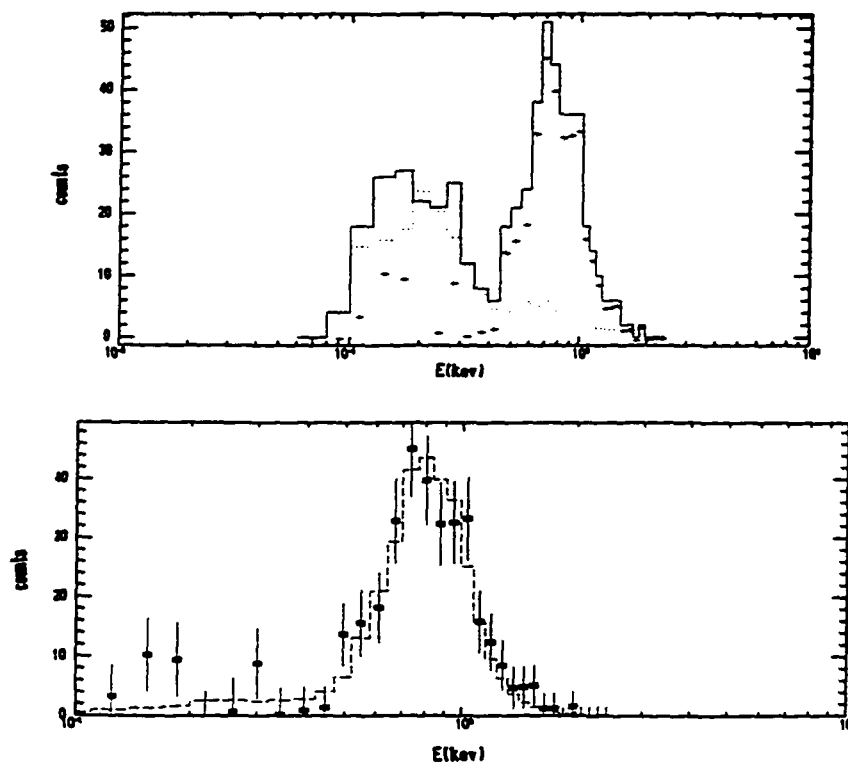


FIG. 4.—Top: Pulse-height spectrum of NGC 5253. Raw counts, background counts, and background-subtracted counts are shown with a solid line, dotted line, and plus signs, respectively. Bottom: Raymond-Smith model fit to pulse-height spectrum. Boxes are the data, and the dotted line is the fit.

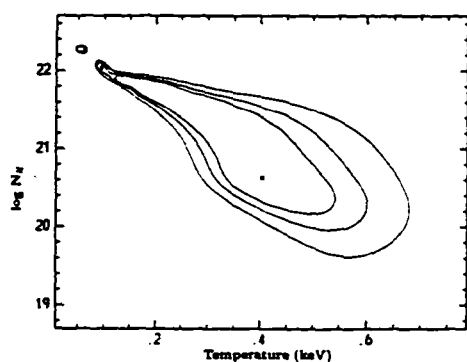


FIG. 5.— χ^2 grid for the temperature and absorbing column parameters in the X-ray spectral fit for NGC 5253. The three contours correspond to 68%, 90%, and 99% confidence levels.

column should be roughly $\frac{1}{2}$ of this (Bregman & Pildis 1994). The intrinsic absorption in NGC 5253 is less certain since the relative geometry of the dust and gaseous phase is unknown. We estimate $\log N_{\text{H}} \approx 21.0$ based on the H α emission measure in the central $10''$ of NGC 5253. Examination of an H I map, kindly lent to us by Elias Brinks, suggests the core of the nebula is deficient in H I and $\log N_{\text{H I}} \approx 20.9$ is typical of the surrounding region. Assuming the gas-to-dust ratio in NGC 5253 is similar to the Galactic value, the visual extinction in the core implies a total H column density of $\log N_{\text{H}} \approx 21.2$ – 21.5 , which is consistent with the sum of estimated H II and H I column densities.

Adopting a total column density of $\log N_{\text{H}} = 21.4$, the best-fit plasma temperature and emission measure are 4.0×10^6 K and $1.24 \times 10^{10} \text{ cm}^{-3}$. The temperature is constrained to lie in the range $(2.7$ – $5.3) \times 10^6$ K at the 90% confidence level, and the normalizations at the limits are 2.39×10^{10} and $7.78 \times 10^9 \text{ cm}^{-3}$, respectively. The corresponding X-ray luminosity in the 0.1–2.4 keV band is $L_{\text{x}} = (6.5^{+1.5}_{-1.0}) \times 10^{28} \text{ ergs s}^{-1}$. The χ^2 grid shown in Figure 5 reveals a second minimum at $\log N_{\text{H}} = 22.05$ and $T = 1.0 \times 10^6$ K. We regard this solution

as unlikely. If the source of the X-ray emission were embedded in this much material, its X-ray luminosity would be $L_x = 6 \times 10^{42}$ ergs s^{-1} , which is higher than the far-infrared luminosity of the galaxy!

3. THE PHYSICAL NATURE OF THE X-RAY EMISSION

The luminosity, spatial extent, and temperature of the X-ray emission from NGC 5253 are summarized in Table 1, and we use them to constrain the dominant source of the X-ray emission in this section. We show that the contribution to L_x from normal stars is small and X-ray binaries are unlikely to dominate the X-ray emission (§ 3.1). The gas is too hot to be heated by galactic accretion (§ 3.2), and models for individual supernovae (§ 3.3) or a simple superbubble (§ 3.4) contradict the observations. However, a combination of stellar winds and supernovae in a clumpy ambient medium can produce the observed X-ray properties (§ 3.5). The latter model makes useful predictions for the starburst's mechanical luminosity and age.

3.1. X-Rays from Normal Stars and X-Ray Binaries

The contribution to L_x from normal stars can be estimated from the galaxy's far-infrared (FIR) luminosity and typical L_x/L_{FIR} ratios for normal stars. Using the galaxy's 60 and 100 μ m flux densities, we find $L_{\text{FIR}} \sim 1 \times 10^9 L_\odot$ (Vader et al. 1993; Hoffer et al. 1986; Helou et al. 1989). The contribution to L_x from massive stars should be $\sim 10^2 L_\odot$ since $L_x/L_{\text{FIR}} = 1.4 \times 10^{-7}$ for type O-A5 stars (Pallavicini et al. 1981). The lower mass stars emit a much larger fraction of their energy in X-rays, $L_x/L_{\text{FIR}} \sim 10^{-3}$ (Stoeckel et al. 1991). For a Salpeter initial mass function (IMF) with $m_\odot = 120$ and $m_\odot = 1$, we expect the $1-2 M_\odot$ stars to emit $\sim 10^3 L_\odot$ in X-rays. So the expected stellar contribution to the X-ray luminosity is over 100 times lower than our measured value.

X-ray binaries are expected to contribute to the X-ray luminosity of NGC 5253, but they are unlikely to dominate the emission. The spectra of massive X-ray binaries are too hard (Griffiths & Padovani 1990; Trümper et al. 1991). Low-mass X-ray binaries (LMXBs) have soft spectra but exhibit a wide range of X-ray luminosities making an estimate of the necessary number of these stars uncertain. Extremely luminous LMXBs, like CAL 83 (Smale et al. 1988), could produce the observed L_x and T_x . However, we regard this as unlikely for three reasons: (1) the Raymond-Smith model for a hot, diffuse gas gives a better fit to the pulse-height spectrum than a power law, (2) no X-ray variability is detected, and (3) the X-ray region is spatially coincident with the core of the H α nebula (i.e., the young stars).

3.2. Spherical Accretion

Gas flowing into the galaxy from an extended H I halo would heat up as it fell deeper into the galaxy's gravitational potential well. For a steady, subsonic inflow in a spherically symmetric mass distribution, we can estimate the gas tem-

perature at any radial distance, r , by equating the specific enthalpy and specific gravitational potential energy in the flow. Expressed in convenient units, the temperature of accreted gas would be

$$T \approx 5.2 \times 10^5 \text{ K} \left[\frac{M(r)}{10^9 M_\odot} \right] \left(\frac{200 \text{ pc}}{r} \right). \quad (1)$$

where $M(r)$ is the galactic mass interior to r . To reproduce the observed $T \approx 4 \times 10^6$ K, roughly $10^{10} M_\odot$ would have to reside in the central 200 pc of the galaxy. The virial mass estimated for the entire galaxy, assumed to be at a distance of 4.1 Mpc, is only $(0.8-4.1) \times 10^9 M_\odot$ (Reif et al. 1982; Lewis & Davies 1973).

3.3. Supernova Remnants

Supernova remnants in ordinary environments are not likely to dominate the X-ray emission from NGC 5253. The source extends over too large an area, $R \sim 200$ pc, for a single SNR to explain all the X-ray emission. Several unresolved SNRs could generate the X-ray emission. However, the two recorded Type Ia supernovae were located in the halo beyond the central X-ray source (Caldwell & Phillips 1989). Also, NGC 5253 lacks significant nonthermal radio emission, and the [S II] $\lambda\lambda 6717, 6731/\text{H}\alpha$ emission line ratio in the region of X-ray emission is significantly lower than the typical value in SNRs. Although the superposition of a bright H II region might hide these signatures, their absence makes it difficult to argue that SNRs generate most of NGC 5253's X-ray luminosity. The X-ray temperature derived from the pulse-height spectrum does lie within the range typically fit to the soft-component of SNRs (Shull 1982, and references therein).

The remnants of supernovae that explode inside a hot, low-density superbubble may not be detected in traditional surveys, and we can ask whether this type of SNR produces the X-ray emission in NGC 5253. These remnants will emit X-rays when they collide with the shell of the superbubble. The resulting X-ray luminosity depends strongly on the distance between the supernova and the shell wall, the age of the remnant, and the density of the shell. Numerical simulations of the N51D shell in the LMC indicate that a supernova occurring at 0.85 of the radius of the dense shell will generate a peak X-ray luminosity of $\sim 8 \times 10^{43}$ ergs s^{-1} (Chu & Mac Low 1990, Fig. 10). It would take a rather large number, about 800, of these SNRs colliding with a similar shell wall to produce the observed X-ray luminosity of NGC 5253. However, the hot gas in a superbubble is itself a source of X-ray emission, and we propose that the collective effect of supernovae and stellar winds in the central region of NGC 5253 might generate a superbubble large enough to account for the X-ray emission.

3.4. Standard Superbubble

In the standard superbubble model (Shull 1993, and references therein) stellar winds and supernovae from hundreds of clustered, massive stars inject energy, mass, and momentum into a homogeneous medium at a constant rate. Three physically distinct regions develop behind the shock which propagates outward from the source region: (a) outermost, a dense shell of swept-up ambient material, (b) a hot cavity of shocked stellar wind and evaporated shell material, and (c) innermost, a freely flowing, supersonic wind outside the region of energy injection. The high pressure in region b drives the shell outward. The equations of energy and momentum conserva-

TABLE 1
MEASURED PROPERTIES OF THE X-RAY-EMITTING GAS

Parameter	Measured Value
Source radius, R	$10'' \pm 2''$
Gas temperature, T	$(4.0 \pm 1.3) \times 10^6$ K
Luminosity in ROSAT band, L_x	$(6.5^{+1.5}_{-1.0}) \times 10^{41}$ ergs s^{-1}

tion for an adiabatic bubble yield a self-similar solution for the shell radius and velocity (Castor, McCray, & Weaver 1975; Weaver et al. 1977). Expressed in terms of the H number density, n_0 , of the ambient ISM in units of cm^{-3} , the mechanical luminosity, L_{38} , of the starburst in units of $10^{38} \text{ ergs s}^{-1}$, and the bubble's age, t_0 , in units of 10^6 yr , the radius and velocity of the superbubble shell are

$$R = (65.9 \text{ pc}) L_{38}^{1/5} n_0^{-1/5} t_0^{2/5} \quad (2)$$

and

$$v = (38.6 \text{ km s}^{-1}) L_{38}^{1/5} n_0^{-1/5} t_0^{-2/5} \quad (3)$$

Equating the conductive flux and the mechanical flux between the bubble interior and the shell yields an approximate similarity solution for the temperature in the bubble. Its radial profile is nearly flat and characterized by a temperature

$$T = (5.3 \times 10^6 \text{ K}) L_{38}^{2/5} n_0^{2/5} t_0^{-4/5} \kappa_0^{-2/7} \quad (4)$$

where $\kappa_0 \leq 1$ is a dimensionless scaling factor for the classical conductivity.

The X-ray luminosity of the bubble is the integral of the volume emissivity over the bubble interior,

$$L_x = \int_0^R \Lambda_e(T) n_e n_H dV \quad (5)$$

where n_H is the hydrogen number density, n_e is the electron density, Λ_e is the X-ray emissivity, and $R \approx (11/12)R$ is the radius of the contact discontinuity between the bubble interior and the shell. Suchkov et al. (1994) derived emissivities in the 0.1–2.2 keV *ROSAT* band from the cooling models of Raymond, Cox, & Smith (1976) for hot, optically thin plasma with cosmic abundance in ionization equilibrium. From Figure 1 of Suchkov et al. (1994), we estimate $\Lambda_e \approx 10^{-22.65} \text{ ergs cm}^3 \text{ s}^{-1}$, which should be accurate to $\pm 30\%$ for gas temperatures between 2.7×10^6 and $5.3 \times 10^6 \text{ K}$. Substituting the density profile of the superbubble interior (Shull 1993, eq. [11]) in equation (5), the integral yields an X-ray luminosity

$$L_x = (2.12 \times 10^{36} \text{ ergs s}^{-1}) L_{38}^{3/5} n_0^{17/55} t_0^{19/55} \kappa_0^{4/7} \quad (6)$$

This standard superbubble model underpredicts the X-ray luminosity of NGC 5253. Solving equations (2), (4), and (6) with $R = 200 \text{ pc}$, $T = 4.0 \times 10^6 \text{ K}$, and $n_0 = 12 \text{ cm}^{-3}$ yields $L_x \approx 4 \times 10^{37} \text{ ergs s}^{-1}$, or 6% of the observed value. Although increasing n_0 to 170 cm^{-3} would appear to raise L_x to $6.0 \times 10^{38} \text{ ergs s}^{-1}$, the pressure of the ambient medium stalls the bubble long before it reaches the observed radius. To make the model work, the X-ray temperature would have to be $T \geq 1.0 \times 10^7 \text{ K}$, which is much higher than the temperature fit to the pulse-height spectrum.

After the contribution from point sources is subtracted, the X-ray luminosity of the diffuse emission will probably still exceed the prediction of the simple superbubble model. We estimate about one-half of NGC 5253's X-ray luminosity is likely to come from point sources (e.g., X-ray binaries and SNRs) based on spatially resolved studies of NGC 1569 and NGC 5471. Both of these starburst regions have X-ray luminosities similar to NGC 5253. In the gas-rich dwarf galaxy NGC 1569 more than half of the total X-ray flux comes from a diffuse component (Heckman 1994). NGC 5471 is a giant H II region in M101 about 5 times less luminous in X-rays than NGC 5253, and Williams & Chu (1994) estimate that a point source is responsible for 40% of its X-ray flux.

3.5. Superbubble in a Cloudy Medium

The traditional superbubble model fails because there is not enough mass in the bubble to produce the observed combination of a relatively high X-ray luminosity and low temperature. In that model, shell material conductively evaporated into the hot interior dominates the X-ray-emitting mass, $\sim 4 \times 10^4 M_\odot$ for $R = 200 \text{ pc}$, $T = 4 \times 10^6 \text{ K}$, and $n_0 = 12 \text{ cm}^{-3}$ (Shull 1993, eq. [9]). Loading more material into the bubble would decrease T , because the bubble's thermal energy would be distributed over more mass. The X-ray luminosity would also increase as the square of the density of hot gas.

We can estimate the actual mass of X-ray-emitting gas from the volume emission measure and spatial extent of the X-ray emission. The fit to the pulse-height spectrum is normalized by $EM_\nu/4\pi d^2 = 10^{10.09} \text{ cm}^{-5}$, where EM_ν is the volume emission measure and d is the distance to NGC 5253. We assume the emission region is spherical, substitute $R = 200 \text{ pc}$ and $d = 4.1 \text{ Mpc}$ in the normalization expression, and solve for the rms electron density of the emitting gas, $n_e = 0.16 \text{ cm}^{-3}$. Propagating the error estimates for the temperature and radius, we estimate n_e lies between 0.1 and 0.3 cm^{-3} . The mass of X-ray-emitting gas is then

$$M_b = (1.5 \times 10^5 M_\odot) f^{1/2} \quad (7)$$

where the volume filling factor of hot gas f would be close to unity in the interior of a bubble.

A superbubble model can generate the extra mass of hot gas if the ambient medium is clumpy. Suppose the ambient medium contains clouds or filaments of density n_c in an otherwise homogeneous, lower density medium. The superbubble shell sweeps up most of the ambient medium as before. The clouds, however, will survive being run over by the outer shock if their column density is much larger than the column density of the shell. The cloud will then evaporate in the hot interior of the bubble. This additional mass flux into the bubble will change the density and temperature structure of region b, but the overall dynamics of the bubble's evolution will not change much if cooling losses from the bubble interior remain small. For example, if the ISM is composed of clouds of density $n_c \sim 180 \text{ cm}^{-3}$ and radius $r_c \sim 3 \text{ pc}$ which fill a fraction $\epsilon \sim 0.001$ of the intercloud medium ($n_0 = 12 \text{ cm}^{-3}$), then the mass of clouds penetrating the shell will be similar to what is required to account for the X-rays ($M_b \sim 1.5 \times 10^5 M_\odot$). An overrun cloud evaporates on a timescale ($\sim 7 \times 10^4 \text{ yr}$) which is less than the age of the bubble and the cooling timescale of the hot gas ($\sim 2 \times 10^6 \text{ yr}$). A wide range of cloud properties can supply the necessary evaporating mass. We illustrate only one set of parameters since a full development of the model is beyond the scope of this paper. Numerical simulations of cloud ablation and evaporation following the passage of a shock are becoming feasible; see the work by Klein, McKee, & Colella (1994) for a discussion of numerical results.

This model predicts an age and mechanical luminosity for the starburst as well as the expansion velocity of the shell. In the self-similar solution (eqs. [2] and [3]), the internal energy of the bubble is 5/11 of the wind's mechanical energy. Estimating the internal energy from measurements of the bubble's temperature ($T = 4.0 \times 10^6 \text{ K}$), density ($n_0 = 0.16 \text{ cm}^{-3}$), and radius ($R = 200 \text{ pc}$), the product of the wind luminosity and bubble age becomes

$$L_{38} t_0 \approx 5.49 \times 10^{53} \text{ ergs} \quad (8)$$

Solving this equation for t_0 and substituting in equation (2), the mechanical luminosity of the wind becomes $L_w \approx 3.3 \times 10^{39}$

ergs s^{-1} , and the age of the superbubble is $\tau \approx 5.3 \times 10^4$ yr. Using equation (3), the predicted shell velocity is $v \approx 24$ km s^{-1} . Examining the uncertainties in the superbubble radius, interior temperature, and interior density, we estimate τ could be as young as 2.6×10^4 yr or as old as 9.7×10^4 yr. Similarly, the wind luminosity should lie within the range 1.3×10^{39} ergs s^{-1} , and the shell velocity would be between 16 km s^{-1} and 39 km s^{-1} .

Although the structure of the ISM in NGC 5253 is probably much more complex than a single expanding bubble, we find this model is useful for forming a quantitative picture of the ISM in NGC 5253. We will come back to the connection between the hot gas in NGC 5253 and the bubble model in § 5. First, we present optical observations that allow us to constrain the mechanical luminosity and age of the starburst in NGC 5253 and establish the distribution of the WIM and its kinematics.

4. STRUCTURE OF THE WIM

When the mechanical energy supplied by supernovae and stellar winds in a stellar system shock-heats an extended component of hot, interstellar gas, distinctive kinematic signatures are generally detectable in the optically emitting ionized gas. For example, in M82 the optical emission line filaments extending along the galaxy's minor axis show the kinematics of an outflow and are thought to lie on the surface of a cone encasing the extended X-ray-emitting gas. On much smaller spatial scales in 30 Doradus, Chu & Kennicutt (1994) find the diffuse X-ray emission correlates well with fast-expanding shells. We obtained an H α image of NGC 5253 and high-resolution spectra of the H α line to determine whether similar kinematic processes occur in NGC 5253. In this section we present results for the spatial distribution of the WIM, its ionization requirements, and kinematics.

4.1. Optical Imaging

4.1.1. Observations

Narrowband H α and red continuum images of NGC 5253 were obtained on 1993 April 28 with the Steward Observatory 2.3 m telescope (see Fig. 1). The detector was a Loral 800 \times 1200 thinned CCD which was binned 2×2 to yield 0.730 pixels and a field coverage of $2' \times 3'$. The matched interference filters (69 Å FWHM) have central wavelengths of 6580 and 6450 Å, and the exposure time through each filter was 1200 s. The galaxy covered most of the field, and the radial intensity profile of the foreground stars had FWHM ≈ 2.0 . Observations of the spectrophotometric standard Feige 34 provided an absolute flux calibration (Massey et al. 1988). The raw images were processed using standard techniques. The 6450 image was iteratively scaled by a constant value and subtracted from the 6580 image until the foreground stars disappeared in the resulting H α image. The absolute H α flux was corrected for atmosphere extinction, foreground Galactic extinction ($A_V = 0.08$ mag), and [N II] $\lambda\lambda 6548, 6583$ line emission in the bandpass ([N II]/H $\alpha = 0.05$). Fluctuations in the background level and [N II] $\lambda\lambda 6548, 6583$ /H α flux ratio dominate the errors in the H α photometry. Comparison of our photometry of other H II regions observed that night with Kennicutt (1988) indicates our absolute fluxes are accurate to better than $\pm 20\%$.

4.1.2. Morphology of the WIM

The H α emission displays strong circular symmetry and extends ~ 1 kpc in diameter. The radial surface brightness

profile steepens within $10''$ (200 pc) of the nucleus. We define the nucleus as the star cluster coincident with the prominent centroid of the H α emission. We will refer to the region within $10''$ of the nucleus as the "core" and to the region outside $10''$ as the "halo." A spectacular network of filaments winds through the halo and has led to speculation that material is flowing out of the galaxy (Meurer 1991). These filaments extend furthest along the minor axis of the galaxy's elliptical, continuum isophotes and are most easily traced in an image of the H α equivalent width as shown in Figure 6. The most prominent radial filaments have dimensions ~ 800 pc \times 90 pc. Two giant loops with diameter ~ 600 pc are visible to the northwest and southwest of the brighter halo. The emission measure in the faint, outer arcs is ~ 50 cm $^{-6}$ pc.

We mapped the radial surface brightness profile of the H α emission into the radial rms electron density distribution shown in Figure 7. We assumed the WIM is spherically symmetric and adopted case B recombination rates at 10^4 K (Brocklehurst 1971) and a H:He ratio of 10:1 by number. No correction was made for internal extinction. The rms electron density falls off as $\sim r^{-1}$ in the core and $\sim r^{-2}$ in the halo. However, the interpretation of the decrease in n_{rms} with radius is not straightforward because radial gradients in the actual electron density and/or the volume filling factor of the emitting gas could produce it (e.g., O'Dell & Castañeda 1984). We assume the WIM is clumpy on small scales as is the case for H II regions in general (Kennicutt 1984) and work with a simple model in which warm filaments of electron density n_f fill a fraction ϵ of the ISM. The rms electron density will be less than the actual electron density of the filaments, $n_{\text{rms}}^2 = \epsilon n_f^2$. In principle, radial variations of the electron density in the filaments can be derived from the ratios of the [S II] $\lambda 6717$ and [S II] $\lambda 6731$ emission lines. Unfortunately, the density of the filaments is too low for this technique to be effective in most of the region mapped spectroscopically by Walsh & Roy (1989).

To estimate the mass of the WIM, we assume the volume filling factor, ϵ , is constant throughout the nebula. Walsh & Roy (1989) arrived at an electron density of $n_e = 290 \pm 40$ cm $^{-3}$ in the nucleus (their region 1), where we find $n_{\text{rms}} \approx 20$ cm $^{-3}$, or $\epsilon \sim 5 \times 10^{-3}$. If this filling factor is characteristic of the nebula, then the mass of the WIM is

$$M_{\text{WIM}} = 3.24 \times 10^6 M_{\odot} \left(\frac{\epsilon}{5 \times 10^{-3}} \right)^{1/2}.$$

4.1.3. Energy Input from Massive Stars

The H α luminosity of the WIM is $(3.0 \pm 0.6) \times 10^{40}$ erg s^{-1} , which requires an impressive ionizing flux. For case B recombination rates at 10^4 K and a radiation-bounded volume, the ionizing photon flux is $Q_{\text{Ly}} \approx 2.3 \times 10^{52}$ s $^{-1}$. The infrared data indicate that portions of the core are dusty and optically invisible, so this ionizing flux should be treated as a lower limit. The typical extinction in the core region is $A_{\text{H}\alpha} = 1.0$ mag (Walsh & Roy 1989), which corresponds to $A_{\text{H}\alpha} = 0.66$ mag for a standard Galactic reddening curve (Whitford 1958) as parameterized by Miller & Mathews (1972). Hence, the extinction-corrected ionizing photon flux is $Q_{\text{Ly}} \approx 4 \times 10^{52}$ s $^{-1}$, the equivalent of 980 O5 V stars (Leitherer 1990) or nearly four 30 Doradus H II regions (Kennicutt 1984). If a substantial portion of the exciting stars reside in the dusty, compact infrared nebula (e.g., Aitken et al. 1982), then the ionizing flux could be much higher.

On a galaxywide scale we can estimate an upper limit to the extinction by comparing the 1.49 GHz radio continuum flux density to the H α flux. The electrons emitting the free-free

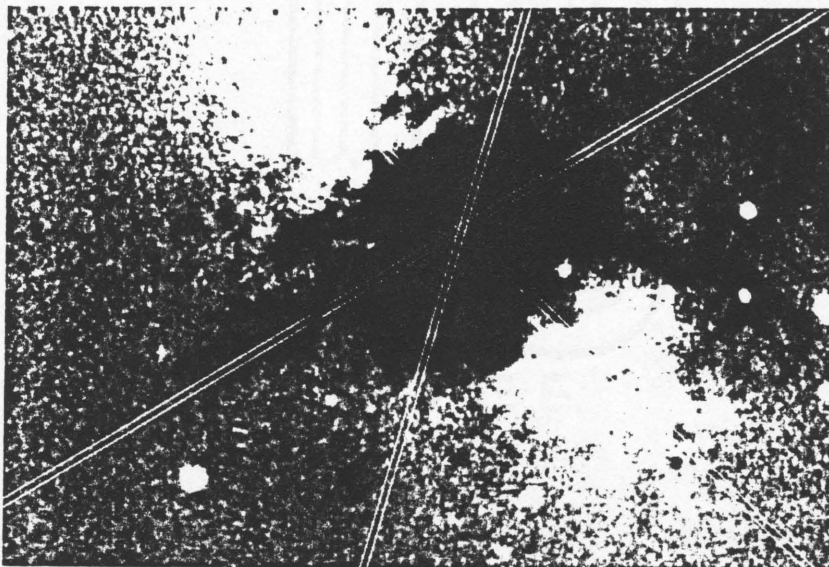


FIG. 6.—Image of equivalent width of $H\alpha + [N II]$ emission. The dark regions trace the WIM where the equivalent width is high. The white region (low equivalent width) follows the contrasting morphology of the stellar component where there is little emission from gas.

radiation are the same ones recombining with H ions. Following Caplan & Deharveng (1986), recombination theory yields

$$A_{H\alpha} = -2.5 \log \left[(1.23 \times 10^{12} \text{ mJy erg}^{-1} \text{ s}^{-1} \text{ cm}^{-2}) \frac{F_{H\alpha}}{S_{1.49}} \right] \quad (9)$$

at 1.0×10^4 K. Substituting the 1.49 GHz measurement of

Condon (1987) and our $H\alpha$ flux in equation (9) implies $A_{H\alpha} \lesssim 1.6$. The upper limit is only appropriate if all the radio emission is thermal and would imply $\dot{Q}_{Ly} \approx 1 \times 10^{53} \text{ s}^{-1}$. Caution should be used here since the $H\alpha$ flux was measured from a smaller aperture than the radio continuum, but we believe both are representative of the integrated values for the galaxy.

Measurements of the Lyman continuum flux constrain the number of massive ($> 10 M_{\odot}$) stars, which can be used to

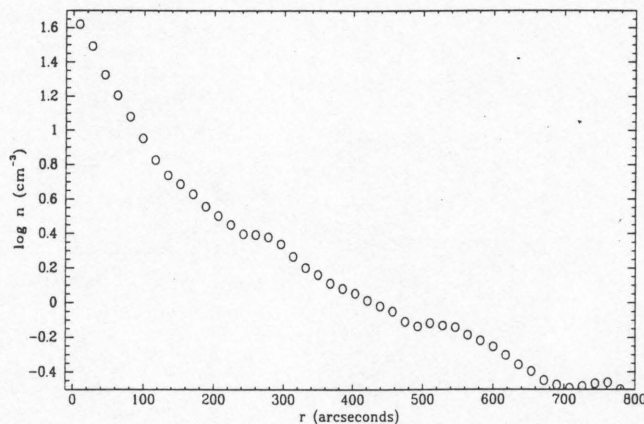


FIG. 7.—Radial profile of rms electron density in the WIM

estimate the rate of mechanical energy injection into the ISM. We consider two limiting cases for the star formation law—continuous star formation at a constant rate and an instantaneous burst. Normalizing the solar metallicity starburst models of Leitherer & Heckman (1994) to an ionizing flux of $Q_{\text{Ly}} = 4 \times 10^{52} \text{ s}^{-1}$ at an age of $5 \times 10^6 \text{ yr}$, gas is turned into stars at a rate of $0.16 M_{\odot} \text{ yr}^{-1}$ in the continuous star formation rate (SFR) model; and the instantaneous burst model converts $2.5 \times 10^6 M_{\odot}$ of gas into stars. The corresponding mechanical luminosities are 2.4×10^{40} and $1.3 \times 10^{41} \text{ ergs s}^{-1}$, respectively. These values assume a Salpeter IMF with lower and upper mass cutoffs of 1 and $100 M_{\odot}$. Although the total SFR is sensitive to the lower mass cutoff, the conversion from ionizing flux to mechanical luminosity is determined by the formation rate of massive stars, which is reasonably well constrained. To ascertain the effect of biasing the IMF against massive stars, we can examine the starburst models for two other IMFs discussed by Leitherer & Heckman (1994). Their steeper ($\alpha = 3.3$) IMF model produces $L_{\text{mech}} = 1.6 \times 10^{39} \text{ ergs s}^{-1}$ in the continuous star formation case and $1.8 \times 10^{39} \text{ ergs s}^{-1}$ for the instantaneous burst model. Retaining the $\alpha = 2.35$ slope but reducing the upper mass cutoff to $30 M_{\odot}$ yields mechanical luminosities of 1.4×10^{40} and $6.3 \times 10^{40} \text{ ergs s}^{-1}$ for the continuous and instantaneous star formation laws, respectively. Compared to the rather large change with IMF slope and upper mass cutoff, the variation of the inferred L_{mech} across our age range (2.6×10^6 to $1.0 \times 10^7 \text{ yr}$) is small. The effect of the galaxy's low metallicity is not negligible, however. The strength of the stellar winds depends strongly on metallicity, and stellar winds, rather than supernovae, dominate the total mechanical luminosity in bursts as young as NGC 5253. For $Z = 0.25 Z_{\odot}$, the models yield L_{mech} between 6.4×10^{37} and $1.0 \times 10^{40} \text{ ergs s}^{-1}$ for continuous star formation; the mechanical luminosity falls between 2.5×10^{38} and $7.9 \times 10^{40} \text{ ergs s}^{-1}$ in their instantaneous burst model. The rough agreement, between these mechanical luminosities and the value [$L_{\text{mech}} = (1-9) \times 10^{39} \text{ ergs s}^{-1}$] inferred from the dynamical model of the X-ray emission in § 3.5, strengthens our argument that stellar winds and supernovae in the starburst could shock-heat enough interstellar gas to produce the observed X-ray emission.

4.2. Kinematic Structure of the WIM

4.2.1. High-Resolution Spectroscopy

We obtained high-resolution spectra of the H α and [N II] $\lambda\lambda 6548, 6583$ emission lines in NGC 5253 during 1994 April 29–May 3 using the echelle spectrograph on the 4 m telescope at Kitt Peak National Observatory. The 79–63° echelle grating was used with a 1.75 slit, which provided a resolution of 11 km s^{-1} FWHM. The cross-dispersing grating was replaced with a flat mirror, and an interference filter (central wavelength [CWL] = 6568 Å , FWHM = 75 Å) was used to isolate a single order around H α . The spectrum was imaged over the entire 3.9 slit with the red long-focus camera and the T2KB 2048 × 2048 CCD detector. The detector was binned to produce a pixel scale of 0.52 along the slit by 0.08 Å along the dispersion. The echellograms were reduced using standard techniques, and the absolute intensity scale was derived by comparing the velocity-integrated H α profile with the flux-calibrated H α image. The deeper exposures reach an H α surface brightness of $1.5 \times 10^{-16} \text{ ergs s}^{-1} \text{ cm}^{-2} \text{ arcsec}^{-2}$. The unvignetted coverage along the slit was about 2.5. Comparison of the night-sky lines in the three frames shows the calibration is accurate to 0.1 Å .

Spectra were taken at the three slit positions illustrated in Figure 6. The slits all intersect the prominent peak in the H α surface brightness near the center of the galaxy, which we call the nucleus. Position 1 (P.A. = 45.5°) follows the galaxy's major axis. Slits 2 and 3 are offset to opposite sides of the galaxy's minor axis at position angles of 164.2° and 121.4° , respectively. Slit 3 runs along Graham's Fork (Graham 1981), the prominent filament extending to the southeast, and slit 2 crosses the arc 25° southeast of the nucleus which appears to be part of a shell of ionized gas. Figure 8 shows an example of the reduced data to illustrate the structure in the emission lines.

4.2.2. Large-Scale Velocity Structure

Figure 9 shows the variation in central velocity of the H α line along each of the three slits. The line center was determined by fitting a Gaussian profile of width 1.0 Å FWHM to the narrow component of the H α profile (see § 4.2.3). Along each slit the radial velocity across the core region increases with increasing radius, but the velocity does not converge to a common systemic velocity in the halo. Within the halo the velocity of the WIM randomly shifts ± 10 – 20 km s^{-1} over scales ~ 100 – 200 pc . About half of these bumps and depressions in the halo's velocity profile are coincident with loops or arcs in the H α image, although their physical relationship is not clear.

Galactic rotation makes only a minor contribution to the global velocity structure. It is probably not responsible for the steepest gradients seen in the core along slits 2 and 3 since the rotation axis would have to run roughly parallel to the optical major axis and miss the optical center of the galaxy by $\sim 150 \text{ pc}$. Rotation can, however, explain the overall velocity gradient of $\sim 17 \text{ km s}^{-1}$ along slit 1, which runs along the major axis of the outer optical isophotes. The stellar rotation curve measured from the Ca II triplet lines along the major axis is strikingly similar (Caldwell & Phillips 1989, Fig. 10).

We have compared the observed large-scale velocity patterns to those expected from spherical accretion, spherical expansion, and bipolar winds. Emission from clumps of gas falling in radially would show a maximum redshift at the center of the nebula and fall to the systemic velocity in the outermost portions of the halo (assuming dust obscures the far side of the nebula). The data contradict this model. The lowest velocity gas is found at the nucleus along all three slits, and the velocities in the halo are typically 15 – 30 km s^{-1} higher than the nucleus. The steady increase in velocity from the nucleus across the core ($r \lesssim 10''$) resembles the position-velocity profile expected from spherical expansion at $\sim 10 \text{ km s}^{-1}$. The double-peaked emission-line profiles which characterize superwinds in FIR galaxies (Heckman et al. 1990) are absent in our data for NGC 5253. However, Marlowe et al. (1994) have recently found double-peaked emission-line profiles northeast of the galaxy center which they interpret as emission from the shell of an expanding superbubble. We conclude that spherical inflow or a galactic wind cannot readily explain the global kinematics, a slow expansion of the core is consistent with the data, and a few coherent superbubble shells evidently reside in the chaotic halo.

4.2.3. Line Profiles

At most positions the H α line profile is quite smooth, but the residuals from a Gaussian fit reveal asymmetric wings. We will refer to these broad wings (FWHM $\sim 130 \text{ km s}^{-1}$) as the broad component and to the stronger component as the narrow component. The width of the narrow component gen-

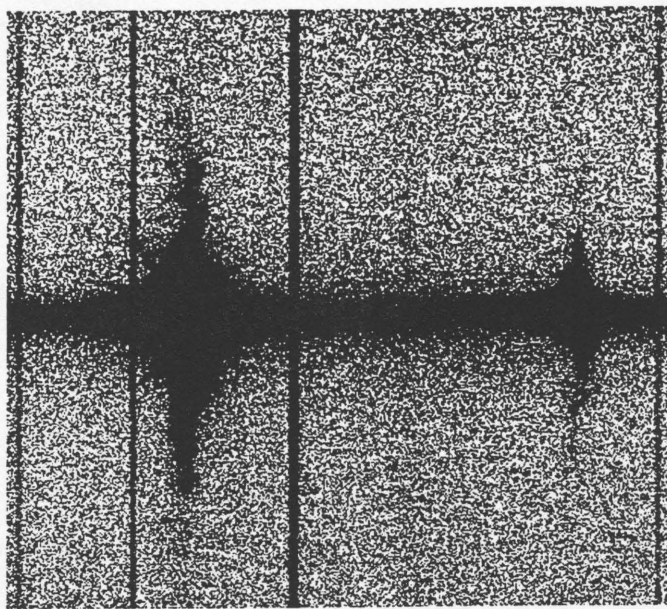


FIG. 8.—Echellogram 3, displayed with logarithmic scaling, reveals complex kinematic structure of the WIM. The north-northwest end of the 3'9 slit is at the top. The emission line on the left is H₂. The [N II] 6583 emission line on the right illustrates the dynamic range of the data. The narrow lines are telluric OH and H₂. The strong continuum source near the center is the nucleus. The shift of the line center along the slit is immediately obvious, and closer inspection reveals the asymmetry in the line profile.

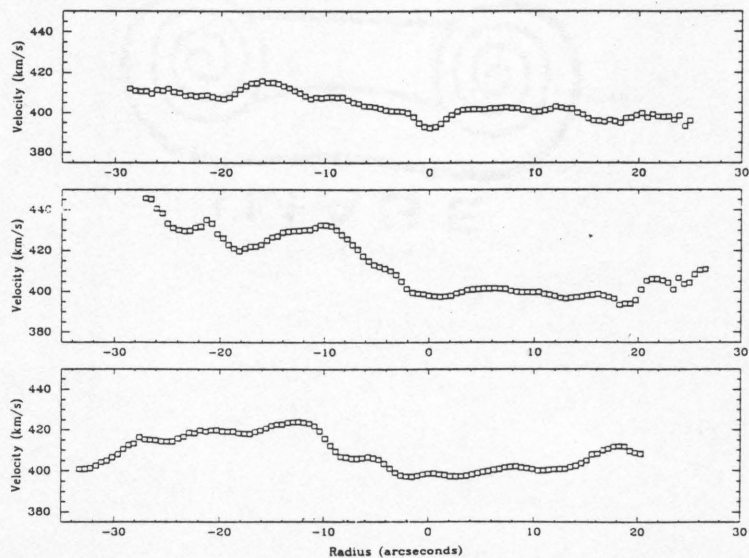


FIG. 9.—Position-velocity diagram along slits 1 (*top*), 2 (*middle*), and 3 (*bottom*). The northernmost position along each slit lies the furthest to the right. Only the rows with S/N sufficient to measure the central wavelength to 0.1 Å are plotted.

SOFT X-RAY EMISSION FROM NGC 5253

181

erally exceeds the expected thermal width of 33 km s^{-1} , which our setup would resolve. (The symmetric instrumental profile has a width of 11 km s^{-1} FWHM.) The broad component is often offset in velocity with respect to the narrow component by as much as $\pm 35 \text{ km s}^{-1}$. The relative structure of these two components tends to persist over distances $\sim 50 \text{ pc}$ and is similar in the H α and [N II] $\lambda 6584$ line profiles. The broad component is most prominent in the nucleus, where it contributes $\sim 50\%$ of the line flux. Multiple Gaussian fits to the nuclear [N II] $\lambda 6583$ and H α lines are shown in Figure 10. The [N II] $\lambda 6583$ line is well fit with two Gaussian profiles of width 36 and 100 km s^{-1} FWHM having a peak intensity ratio of 1.9:1.0, respectively. The broad component is blueshifted by 32 km s^{-1} relative to the narrow component. The best two-component fit to the H α line is similar: peak intensity ratio of 1.7:1.0 between components of width 45 and 96 km s^{-1} FWHM. The residuals to the H α fit suggest a weak, third component spread over $300\text{--}400 \text{ km s}^{-1}$ is also present.

This unique line profile persists over a substantial region of the nebula's core. The broad, blue component is easily followed

from the nucleus toward the southeast along slit 2 for 5.7". A kinematically similar line profile is observed along slit 3 from the nucleus to a position $4''\text{--}5''$ to the southeast. Along slit 1 this line shape persists from the nucleus to the southwest for $\sim 4''$, and a fainter (relative to the narrow component) broad, blue component extends an additional $8''$ to the position of knot B. This kinematically disturbed region is spatially coincident with the region of knots in the red continuum image and covers $\approx 110 \text{ pc}$.

Macroscopic kinematics are probably the dominant line-broadening mechanism throughout the nebula. Turbulence, as defined by Roy, Arsenault, & Joncas (1986), cannot be the sole broadening process because it does not explain the offset between the broad and narrow components and the spatial gradients in the narrow component's velocity. Since the widths of the H α and [N II] $\lambda 6584$ profiles are similar, thermal motion cannot be the dominant broadening mechanism. We suggest energetic mass transport from stars into the ISM may explain the shape of the line profile in the core. Chu & Kennicutt (1994) have demonstrated that expanding structures in giant H II

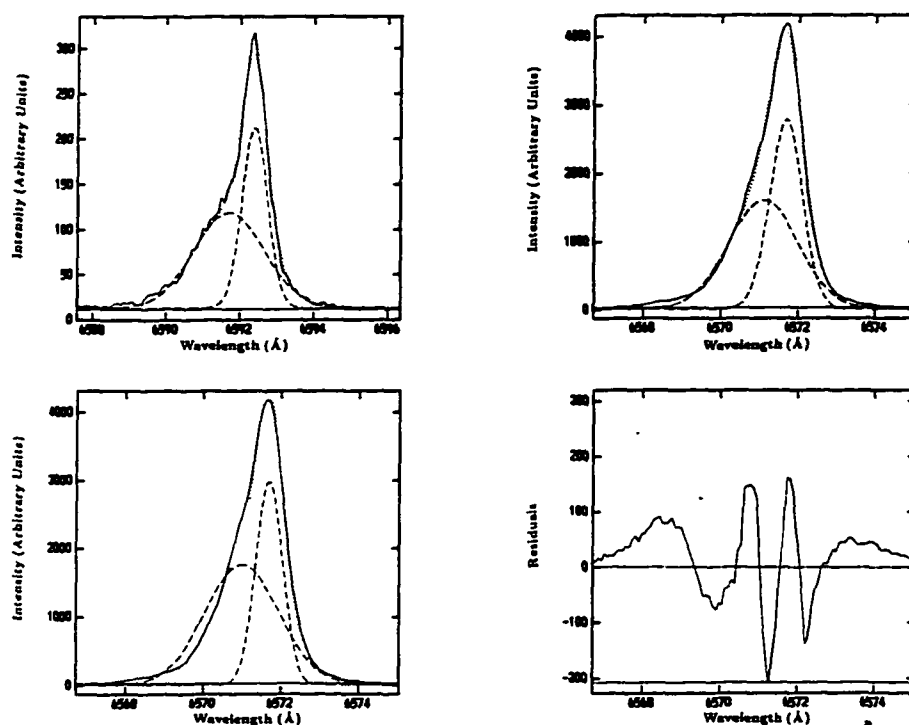


FIG. 10.—Gaussian decomposition of unique emission-line profile in core. The spectrum (solid line) was extracted from one row of echellogram 2, $1''.6$ southeast of the nucleus. The dashed lines show the fitted Gaussian components, and the dotted line is their sum. Upper left, Fit to [N II] $\lambda 6583$ emission line requires a broad component Doppler-shifted 32 km s^{-1} blueward of the narrow component. Lower left, Same fit applied to H α line. The separation and FWHM of the two components are fixed at their values in the upper-left panel but their peak intensities are allowed to vary freely. The fit is close but can be improved as shown in the upper-right panel. Upper right, Best fit to the H α line. Lower right, Residuals of the best fit to H α line show a third component at high velocity. (See text for a complete description.)

regions create velocity substructure on spatial scales smaller than we can resolve in NGC 5253, where we expect similar dynamical processes. Additionally, the self-gravity of the star/gas complex may begin to contribute substantially to the velocity dispersion as the size and total mass of an H II region grow from giant H II region proportions to those of the WIM in NGC 5253 (Hippelstein 1986; Roy et al. 1986). The total kinetic energy of the WIM, defined as $(3/2)M_{\text{WIM}}\sigma_v^2$, is $(5.1_{-1.6}^{+2.4}) \times 10^{52} [e/(5 \times 10^{-3})]^{1/2}$ ergs. We used the total mass of the WIM and the corrected standard deviation of the integrated H α line profile.

5. SUMMARY AND DISCUSSION

The results from the *ROSAT* PSPC observation of NGC 5253 and our interpretation can be summarized as follows. The central source is spatially extended. We provisionally attribute the emission to hot gas while we await higher resolution X-ray images to confirm our estimate of the source size ($R = 200 \pm 40$ pc) and constrain the contribution from point sources. Assuming an absorbing column of $\log N_H = 21.4$, the hot gas (volume filling factor f) has a mass $\sim 1.5 \times 10^5 M_\odot f^{1/2}$, an rms electron density of $n_e = (0.2 \pm 0.1)f^{-1/2} \text{ cm}^{-3}$, a temperature of $T = (4.0 \pm 1.3) \times 10^6 \text{ K}$, and an X-ray luminosity in the *ROSAT* band of $L_x = (6.5_{-1.2}^{+1.5}) \times 10^{48} \text{ ergs s}^{-1}$. We suggest that shocks driven by supernovae and stellar winds in the central starburst heat the hot gas and that the subsequent evaporation of clouds/filaments is important for generating the total mass of X-ray-emitting gas.

The data presented in § 4 lead to the following characteristics for the WIM in NGC 5253. The maximum surface brightness of the diffuse H α emission is coincident with the centroid of the X-ray emission. The H α emission profile indicates the radial structure of the WIM changes around $r = 200$ pc. Beyond this radius, the halo is "stirred-up"; we measure random velocity gradients of $\sim 10\text{--}30 \text{ km s}^{-1}$ over $\sim 100\text{--}200$ pc in the halo, consistent with the Fabry-Perot data of Atherton et al. (1982). The halo WIM has a substantial kinetic energy, although the spectacular emission-line filaments extending from the halo show rather unremarkable kinematics. The kinematics are most structured in the core. For example, the H α echellograms reveal: (1) the central wavelength of the emission is blueshifted $\sim 10 \text{ km s}^{-1}$ throughout much of the core, (2) the broader component of the line profile is offset $\sim 32 \text{ km s}^{-1}$ to the blue in part of the core, and (3) the velocity width of this broad component is $\sim 40 \text{ km s}^{-1}$ in the core. A SFR $\sim 0.5 M_\odot \text{ yr}^{-1}$ is required to ionize the $3.24 \times 10^6 M_\odot [e/(5 \times 10^{-3})]^{1/2}$ of warm gas. In the remainder of this paper we relate NGC 5253 to other objects and discuss the energetics and dynamics of its ISM.

5.1. Comparison with Other Starburst Regions

NGC 5253's exotic network of H α filaments is reminiscent of the more luminous superwind galaxy M82 and less luminous giant H II regions such as 30 Doradus. Both of those systems have extended X-ray emission which is coincident with distinctive kinematics in the warm ionized filaments. In spite of the ambiguity in the interpretation of the WIM kinematics in NGC 5253, we can say that the X-ray emission is coincident with the core of the H α nebula and the kinematics show the most structure within this region. The pressure of the optical emission line gas and hot X-ray-emitting gas in M82 is much higher than typical interstellar pressures. Heckman et al. (1990) showed this high pressure is regulated by the starburst (see also

Heckman, Lehnert, & Armus 1994). We estimate the pressures of the WIM and hot ionized medium (HIM) in NGC 5253 are $\sim (3.9 \times 10^6 \text{ K cm}^{-3})[(5 \times 10^{-3}/e)]^{1/2}$ and $\sim (1.2 \times 10^6 \text{ K cm}^{-3})(1.0/f)^{1/2}$, respectively, near the lower limit for the central pressure in M82 (Bregman & Schulman 1995). Although the poor constraints on the filling factors (e and f) introduce a significant uncertainty in these values, the estimated pressures exceed the local interstellar pressure in the Milky Way by almost three orders of magnitude (McKee & Ostriker 1977), which suggests global processes related to the starburst govern the structure of the ISM. In both M82 and 30 Doradus, the energetics of the gas kinematics are consistent with the expected mechanical energy injection from stellar winds and supernovae.

In § 3.4 we found that the simple superbubble model underpredicts the X-ray luminosity of NGC 5253. This model faces similar shortcomings when applied to X-ray-bright superbubbles in the LMC. For example, the diffuse X-ray emission from N51D and the two largest shells in N44 is an order of magnitude larger than the simple superbubble model predicts (Chu et al. 1993; Chu & Mac Low 1990). Although the standard explanation for the enhanced emission in this case is transient SNRs hitting the shell of a superbubble rather than evaporating clouds (Wang & Helfand 1991; Chu & Mac Low 1990), the analogy demonstrates that higher than expected L_x can be generated from the mechanical luminosity of a starburst.

The agreement between observation and theory is better for the diffuse X-ray emission from the shocked shell of a superbubble (region a in § 3.4). However, the bubble interior emits hard X-rays, and its predicted luminosity is much less than the observational estimates (Suchkov et al. 1994). In addition, *ROSAT* images show structure in the diffuse X-ray emission of superwind galaxies—an indication that most of the soft X-ray emission comes from ambient clouds that are shock-heated or evaporated (Heckman et al. 1994). This picture is very similar to the cloudy superbubble model we introduced in § 3.5 to explain the X-ray emission from NGC 5253. We will begin our discussion of the energetics in NGC 5253 with this model and then conclude that a more realistic picture of the ISM in NGC 5253 would be similar to the McKee & Ostriker (1977) multiphase ISM.

5.2. Energetics and Dynamics of the Ionized ISM in NGC 5253

We described the X-ray properties of NGC 5253 in terms of a superbubble in a cloudy medium. The key physical difference from the standard superbubble model is a higher mass flux of warm/cold gas evaporating into the hot gas. Although a serious test of this model would require numerical simulations, our estimates of the required starburst mechanical luminosity and age are consistent with the observational estimates for the age of the nucleus and L_x associated with the ionizing luminosity of the nebula. The model is oversimplified, but it provides a means to discuss the energetics and dynamics of the ISM in NGC 5253. The model suggests the starburst efficiently heats the hot ISM, $L_x/L_{\text{WIM}} \sim 0.2$, and accelerates the shell of WIM, $KE/L_{\text{WIM}} \leq 0.19$, where the upper limit is for an adiabatic bubble. Our estimate of the WIM's kinetic energy, $KE/L_{\text{WIM}} \geq 0.10$, from the broad integrated H α emission line is a lower limit on the kinetic energy of the ISM since it samples the velocity dispersion over a small fraction of the nebula and does not include the kinetic energy of the neutral gas; it is, however, consistent with the model $KE/L_{\text{WIM}} \geq 0.10$. The

model predicts the HIM will extend as far as the filaments of warm ionized gas in $\sim (2-7) \times 10^7$ yr. If the H I is distributed similarly to the WIM, then our estimated value of L_{H} suggests a fraction of the hot gas could escape from the galaxy in a wind (Mac Low & McCray 1988).

The model is clearly inadequate for discussing the WIM, since it makes no quantitative prediction of the H α surface brightness as a function of radius. Detailed work on a similar problem, the evolution of a SNR in a cloudy medium, indicates that the H α emission from evaporating clouds in the bubble interior can dominate the emission from the shell (White & Long 1991). This effect could explain why we do not see a shell in the WIM's radial density profile. A more realistic picture might involve several merging supershells. Their interaction would generate a network of filaments which would become indistinguishable from our clouds as they broke up. The blue-shift of the broad-line component in the nucleus might represent the overall expansion of the near-side filaments with respect to the systemic velocity, and its large velocity dispersion could be caused by the superposition of many filaments along the line of sight. The global dynamics might be similar to a single bubble if the filling factor of the hot gas is large, and the energetics could be described with the multiphase ISM model of McKee & Ostriker (1977).

Further study will clear up some of the weaknesses in our interpretation. A pending *ROSAT* HRI observation will resolve the spatial distribution of the X-ray emission. Analysis of our echelle data for several other dwarf galaxies may clarify the interpretation of the broad-line profiles. Infrared spectroscopy of the central knots would allow a better estimate of L_{H} , which affects the evolution of the superbubble (Koo & McKee 1992; Shull & McKee 1992; Shull & Saken 1995). Mapping the distribution of the extended H I gas would constrain the arguments about a wind developing.

We thank Mike Shull, You-Hua Chu, and Rene Walterbos for their comments on an early version of this paper. Our analysis also benefited from the kindness of Elias Brinks, who shared his unpublished H I map with us. We also thank Sara Beck, Tom Fleming, Tim Heckman, Mordecai-Mark Mac Low, and Jon Saken for valuable discussions. We gratefully acknowledge support from an NSF Graduate Fellowship and NASA grant 345550. This research was also supported in part by the NSF through grant AST 90-19150. We acknowledge the use of the NASA/IPAC Extragalactic Data Base (NED) which identified many references to NGC 5253.

REFERENCES

- Aitken, D., Roche, P., Allen, M., & Phillips, M. M. 1982, *MNRAS*, 199, 3p.
 Atherton, P., Taylor, K., Pike, C. D., Harmer, C. F. W., Parker, N. M., & Hook, R. N. 1982, *MNRAS*, 201, 661.
 Beck, S. 1994, private communication.
 Bregman, J. N., & Pildis, R. A. 1994, *ApJ*, 420, 570.
 Bregman, J. N., Schulman, E., & Tomsaka, K. 1995, *ApJ*, 439, 155.
 Brinks, E. 1994, private communication.
 Brocklehurst, M. 1971, *MNRAS*, 153, 471.
 Caldwell, N., & Phillips, M. M. 1989, *ApJ*, 338, 789.
 Campbell, A. W., & Terlevich, R. 1984, *MNRAS*, 211, 15.
 Caplan, J., & Deharveng, L. 1986, *A&A*, 155, 297.
 Castor, J., McCray, R., & Weaver, R. 1975, *ApJ*, 200, L107.
 Chu, Y.-H., & Kennicutt, R. C. 1994, *ApJ*, 425, 720.
 Chu, Y.-H., & Mac Low, M.-M. 1990, *ApJ*, 365, 510.
 Chu, Y.-H., Mac Low, M.-M., Garcia-Segura, G., Wakker, B., & Kennicutt, R. C. 1993, *ApJ*, 414, 213.
 Condon, J. J. 1987, *ApJS*, 65, 485.
 Fabbiano, G., Gioia, I. M., & Trinchieri, G. 1988, *ApJ*, 324, 749.
 Fabbiano, G., & Trinchieri, G. 1985, *ApJ*, 296, 430.
 Graham, J. A. 1981, *PASP*, 93, 552.
 Griffiths, R. E., & Padovani, P. 1990, *ApJ*, 360, 483.
 Heckman, T. M. 1994, private communication.
 Heckman, T. M., Armus, L., & Miley, G. K. 1990, *ApJS*, 74, 833.
 Heckman, T. M., Lehnert, M. D., & Armus, L. 1994, in *The Environment and Evolution of Galaxies*, ed. J. M. Shull & H. A. Thronson (Dordrecht: Kluwer), 455.
 Heiles, C. 1975, *A&AS*, 20, 37.
 Helou, G., Khan, I. R., Malek, L., & Boehmer, L. 1989, *ApJS*, 68, 151.
 Hippenheiler, H. H. 1986, *A&A*, 160, 374.
 Hodge, P. 1966, *ApJ*, 146, 593.
 Kennicutt, R. C. 1988, *ApJ*, 334, 144.
 ——— 1984, *ApJ*, 287, 116.
 Kinney, A. L., Bohlin, R. C., Calzetti, D., Panagia, N., & Wyse, R. F. G. 1993, *ApJS*, 86, 5.
 Klein, R. L., McKee, C. F., & Colella, P. 1994, *ApJ*, 420, 213.
 Koo, B.-C., & McKee, C. F. 1992, *ApJ*, 388, 103.
 Leitherer, C. 1990, *ApJS*, 73, 1.
 Leitherer, C., & Heckman, T. M. 1994, preprint.
 Leitherer, C., Robert, C., & Drissen, L. 1992, *ApJ*, 401, 596.
 Lewis, B. M., & Davies, R. D. 1973, *MNRAS*, 165, 213.
 Mac Low, M.-M., & McCray, R. 1988, *ApJ*, 324, 776.
 Marlowe, A. T., Heckman, T. M., Wyse, R. F. G., & Schommer, R. 1994, preprint.
 Massey, P., Strobel, K., Barnes, J. V., & Anderson, E. 1988, *ApJ*, 328, 315.
 McKee, C. F., & Ostriker, J. P. 1977, *ApJ*, 218, 148.
 Meurer, G. 1991, *Proc. ASA*, 9, 98.
 Miller, J. S., & Mathews, W. G. 1972, *ApJ*, 172, 593.
 Morrison, R., & McCammon, D. 1983, *ApJ*, 278, 119.
 O'Dell, C. R., & Castañeda, H. O. 1984, *ApJ*, 283, 158.
 Pallavicini, R., Golub, L., Rosner, R., Vaisna, G. S., Ayres, T., & Linsky, J. L. 1981, *ApJ*, 248, 279.
 Raymond, J. C., Cox, D. P., & Smith, B. W. 1976, *ApJ*, 204, 290.
 Raymond, J. C., & Smith, B. W. 1977, *ApJS*, 35, 419.
 Reichert, G. 1994, private communication.
 Ref. K., Mebold, U., Goss, W. M., van Woerden, H., & Siegmund, B. 1982, *A&AS*, 50, 451.
 Roy, J.-R., Arsenault, R., & Joncas, G. 1986, *ApJ*, 300, 624.
 Sandage, A., & Bruester, R. 1979, *AJ*, 84, 472.
 Sandage, A., Saha, A., Tammann, G. A., Labhardt, L., Schwengel, H., Panagia, N., & Macchetto, F. D. 1994, *ApJ*, 423, L13.
 Shull, J. M. 1982, *ApJ*, 262, 308.
 ——— 1993, in *Massive Stars: Their Lives in the Interstellar Medium*, ed. J. P. Cassinelli & E. B. Churchwell (San Francisco: ASP), 327.
 Shull, J. M., & Saken, J. M. 1995, *ApJ*, 444, 663.
 Smale, A. P. et al. 1988, *MNRAS*, 233, 51.
 Snowden, S. L., McCammon, D., Burrows, D. N., & Mendenhall, J. A. 1994, *ApJ*, 424, 714.
 Soifer, B. T., Sanders, D. B., Neugebauer, G., Demelson, G. E., Lonsdale, C. J., Madore, B. F., & Persson, S. E. 1986, *ApJ*, 303, L41.
 Stocke, J. T., Morris, S. L., Gioia, I. M., Maccaruro, T., Schild, R., Wolter, A., Fleming, T. A., & Henry, J. P. 1991, *ApJS*, 76, 813.
 Sothkov, A. A., Balsara, D. S., Heckman, T. M., & Leitherer, C. 1994, *ApJ*, 430, 511.
 Trümper, J. et al. 1991, *Nature*, 349, 579.
 Vader, J. P., Frogel, J. A., Terndrup, D. M., & Hesser, C. A. 1993, *AJ*, 106, 1743.
 van Woerden, H., van Driel, W., Braun, R., & Rots, A. H. 1993, *A&A*, 269, 15.
 Walsh, J. R., & Roy, J.-R. 1989, *MNRAS*, 239, 297.
 Wang, Q., & Helfand, D. J. 1991, *ApJ*, 373, 497.
 Weaver, R., McCray, R., Castor, J., Shapiro, P., & Moore, R. 1977, *ApJ*, 218, 377.
 White, R. L., & Long, K. S. 1991, *ApJ*, 373, 543.
 Whitford, A. E. 1958, *AJ*, 63, 201.
 Williams, R., & Chu, Y.-H. 1994, preprint.

PLATE 6

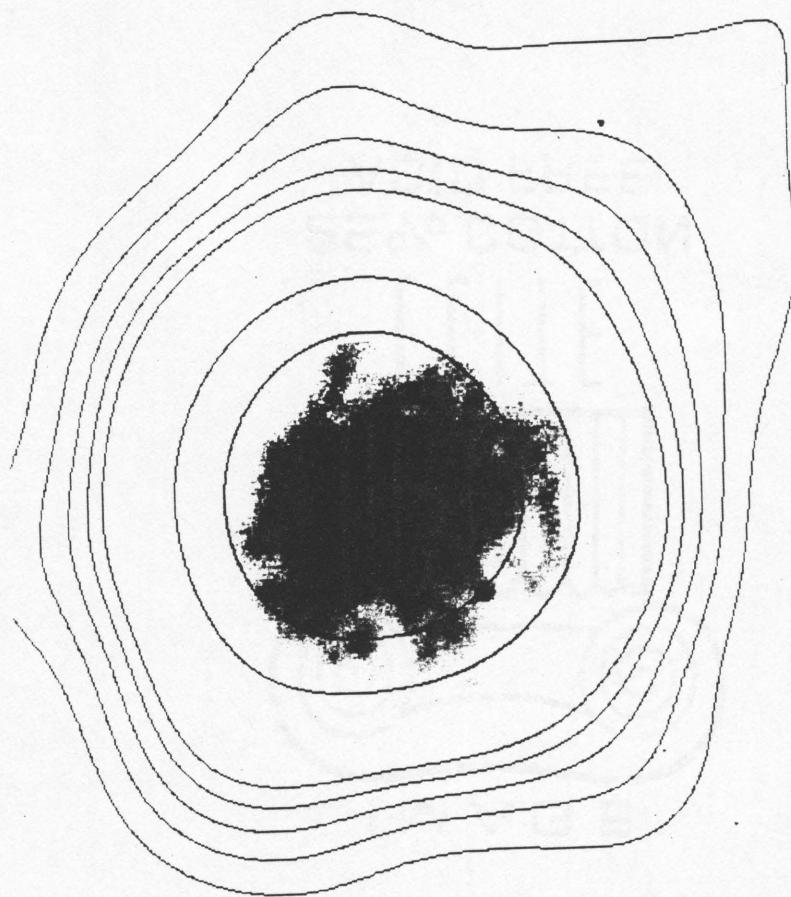


FIG. 1b

MARTIN & KENNICUTT (see 447, 171)

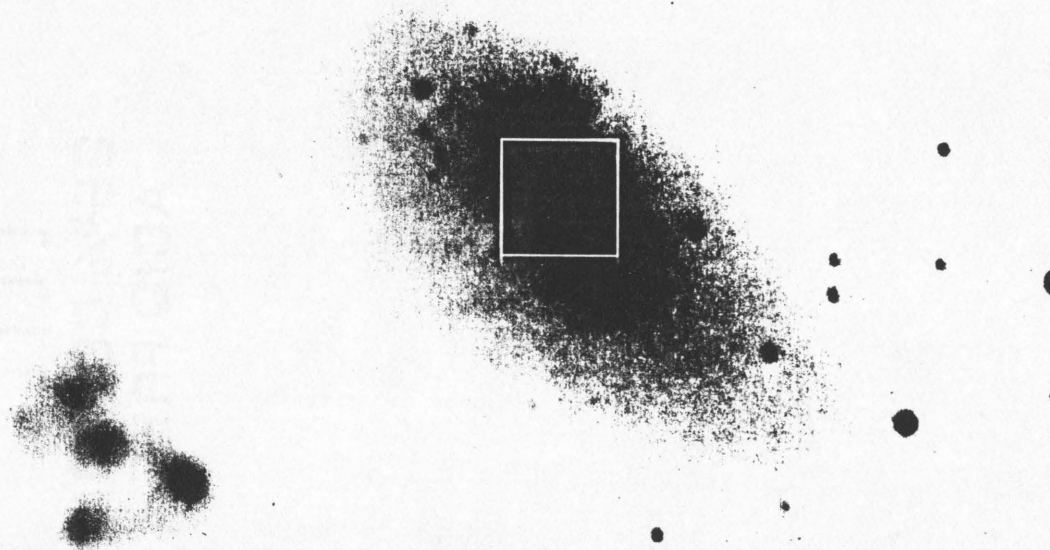


FIG. 1a

FIG. 1.—(a) Red continuum image of NGC 5253. North is up, and east is to the left. The region inside the white square ($18'' \times 18''$) is shown enlarged and rescaled in the lower left corner. (b) H α image of NGC 5253 overlain with contours of constant X-ray surface brightness in the 0.11–2.04 keV band. The spatial scale and orientation are identical to those in (a). The lowest contour represents a surface brightness twice the standard deviation of the X-ray background. The next four contours are linearly incremented by 1 standard deviation, and the highest contours have intensity values of 20, 30, and 50 counts $s^{-1} \text{ deg}^{-2}$.

MARTIN & KENNICUTT (see 447, 171)

REFERENCES

- Armus, L., Heckman, T. M., & Miley, G. K. 1989, *ApJ*, 347, 727.
- Armus, L., Heckman, T. M., & Miley, G. K. 1990, *ApJ*, 364, 471.
- Arp, H., & Sandage, A. 1985, *AJ*, 90, 1163.
- ASP Conference Series. 1992, *Astronomical CCD Observing and Reduction Techniques*, ed. S. B. Howell, (PASP: San Francisco).
- Babul, A., & Rees, M. J. 1992, *MNRAS*, 255, 346.
- Baldwin, J. A., Phillips, M. M., & Terlevich, R. 1981, *PASP*, 93, 5.
- Bland, J., & Tully, B. 1988, *Nature*, 334, 43.
- Bregman, J. N., Schulman, E., & Tomisaka, K. 1995, *ApJ*, 439, 155.
- Brocklehurst, M. 1972, *MNRAS*, 157, 211.
- Burrows, D. N., & Mendenhall, J. A. 1994, in *The Soft X-Ray Cosmos*, ed. E. M. Schlegel, R. Petre, AIP: New York.
- Campbell, A., Terlevich, R., & Melnick, J. 1986, *MNRAS*, 223, 811.
- Castor, J., McCray, R., & Weaver, R. 1975, *ApJ*, 200, L107.
- Chiosi, C., & Maeder, A. 1986, *ARA&R*, 24, 329.
- Conti, P. S. 1991, *ApJ*, 377, 115.
- Conti, P. S., Garmany, C. D., de Lore, C., Vanbeveren, D. 1983, *ApJ*, 274, 302.
- Davidson, K., Kinman, T. D. 1985, *ApJS*, 58, 321.
- Davidson, K., Kinman, T. D., & Friedman, S. D. 1989, *AJ*, 97, 1591.
- Davies, R. D., Elliot, K. H., & Meaburn, J. 1976, *MNRAS*, 81, 89.
- Dekel, A., & Silk, J. 1986, *ApJ*, 303, 39.

- De Robertis, M., Dufour, R., & Hunt, R. 1987, JRASC, Vol, 81, No. 6, 1 95.
- Dettmar, R. J. 1992, in *Fundamentals of Cosmic Physics*, Vol 15, (Gordon and Breach Science Publishers: USA).
- de Vaucouleurs, G., de Vaucouleurs, A., & Pence, W. 1974, ApJ, 194, L119.
- DeYoung, D. S., & Gallagher, J. S. III 1990 ApJ, 356, L15.
- DeYoung, D. S., & Heckman, T. M. 1994, ApJ, 431, 598.
- Dekel, A., & Silk, J. 1986, ApJ, 303, 39.
- Diaz, 1988, MNRAS, 231, 57.
- Dinerstein, H. L. & Shields, G. A. 1983, ApJ, 311, 45.
- Domgörgen, H., & Mathis, J. S. 1994, ApJ, 428, 647.
- Dopita, M. A. 1985, ApJ, 295, L5.
- Dove, J. B. & Shull, J. M. 1994, ApJ, 430, 222.
- Drissen, L., Roy, J., & Moffat, A. F. J. 1993, AJ, 106, 1460.
- Dufour, R. J., & Hester, J. J. 1990, ApJ, 350, 149.
- Ferguson, H. C., & Binggeli, B. 1994, A&AR, 6, 67.
- Ferland, G. J. 1993, University of Kentucky Department of Physics and Astronomy Internal Report.
- Field, G. B., Goldsmith, D. W., & Habing, H. J. 1969, ApJ, 155, L149.
- Filippenko, A. V. 1982, PASP, 94, 715.
- Garnett, D. R. 1990, ApJ, 363, 142.
- Garnett, D. R., Skillman, E. D., Dufour, R. J., Peimbert, M., Torres-Peimbert, S., Terlevich, R., Terlevich, E., & Shields, G. A. 1995, ApJ, 443, 64.

- Golla, G., Dettmar, R.-J., & Domgörgen, H. 1996, A&A, preprint.
- Graham, J. A. 1981, PASP, 93, 552.
- Grevesse, N., & Anders, E. 1989, in *Cosmic Abundances of Matter*, AIP Conference Proceedings 183, ed. C. J. Waddington, (New York: AIP).
- Grevesse, N. & Noels, A., 1993, in *Origin and Evolution of the Elements*, ed. N. Prantzos, E. Vanigioni-Flam, & M. Cassé, (Cambridge University Press), p 14.
- Hasinger, T., Turner, T. J., George, I. M., & Boese, G. 1992, OGIP Calibration Memo CAL/ROS/91-001, (NASA: GSFC).
- Heckman, T. M., Armus, L., & Miley, G. K. 1990, ApJS, 74, 833.
- Heckman, T. M., Dahlem, M., Lehnert, M. D., Fabbiano, G., Gilmore, D., & Waller, W. H. 1995, ApJ, 448, 98.
- Heiles, C. 1975, A&AS, 20, 37.
- Heiles, C., Koo, B.-C., Levenson, N. A., & Reach, W. T. 1996, ApJ, 462, 326.
- Hill, R. S., Home, A. T., Smith, A. M., Bruhweiler, F. C., Cheng, K. P., Hintzen, P. M. N., & Oliverson, R. J. 1994, ApJ430, 569.
- Hodge, P. W. 1974, ApJ, 191, L21.
- Huchtmeier, W. K., Seiradakis, J. H., & Materne, J., 1981, A&A, 102, 134.
- Hummer, D. G., & Storey, P. J. 1987, MNRAS, 224, 801.
- Humphreys, R. M., Nichols, M., & Massey, P. 1985, AJ, 90, 101.
- Hunter, D. A. 1982, ApJ, 260, 81. g irregulars
- Hunter, D. A. 1996, ApJ, 457, 671.
- Hunter, D. A., & Gallagher, J. S. III 1990, ApJ, 362, 480.

- Hunter, D. A., Gallagher, J. S., & Rautenkranz, D. 1982, *ApJS*, 49, 53.
- Hunter, D. A., Hawley, W. N., & Gallagher, J. S. 1993, *AJ*, 106, 1797.
- Hunter, D. A., & Plummer, J. D. 1996, *ApJ* 461, 202.
- Hunter, D. A., & Thronson, H. A. 1995, *ApJ*, in press.
- Israel, F. P., & deBruyn 1988, *A&A* 198, 109.
- Kennicutt, R. C. 1983, *ApJ*, 272, 54.
- Kennicutt, R. C. 1984, *ApJ*, 287, 116.
- Kennicutt, R. C. 1988, *ApJ*, 334, 144.
- Kennicutt, R. C. 1989, *ApJ*, 344, 685.
- Kennicutt, R. C., Edgar, B. K., & Hodge, P. W. 1989, *ApJ*, 337, 761.
- Kennicutt, R. C., & Garnett, D. R. 1996, *ApJ*, 456, 504 (RG96).
- Kennicutt, R. C. & Kent, S. M. 1983, *AJ*, 88, 1094.
- Kennicutt, R. C., Tamblyn, P., & Congdon, C. W. 1994, *ApJ* 435, 22.
- Kobulnicky, H. A., & Skillman, E. D. 1996, to appear in *ApJ*.
- Koo, B.-C., & McKee, C. F. 1992, *ApJ*, 388, 93.
- Kulkarni, S. R., & Heiles, C. 1987, in *Interstellar processes*, D. J. Hollenbach & H. A. Thronson (Dordrecht: Reidel Publishing Co.).
- Kunth, D., Lequeux, J., Sargent, W. L. W., & Viallefond, F. 1994, *A&A*, 282, 709.
- Kurucz, R. L. 1979, *ApJS*, 40, 1.
- Larson, R. B. 1974, *MNRAS*, 169, 229.
- Lehnert, M. L., & Heckman, T. M. 1996, *ApJ*, 462, 651.
- Leitherer, C., & Heckman, T. M. 1995, *ApJS*, 96, 9L.

- Leitherer, C., Vacca, W. D., Conti, P. S., Filippenko, A. V., Robert, C., Sargent, W. L. W. 1996, (preprint).
- Lequeux, J., Peimbert, M., Rayo, J. F., Serrano, A., & Torres-Peimbert, S. 1979, A&A, 80, 155.
- Lequeux, J., & Viallefond, F. 1980, A&A, 91, 269.
- Mac Low, M-M, & McCray, R. 1988, ApJ, 324, 776.
- Mac Low, M-M, & McCray, R., Norman, M. L. 1989, ApJ, 337, 141.
- Marconi, G., Matteucci, F., & Tosi, M. 1994, MNRAS, 270, 35.
- Marlowe, A. T., Heckman, T. M., Wyse, R. F. G., & Schommer, R. 1995, ApJ, 438, 563.
- Martin, C. L. 1996a, ApJ, 465, 680.
- Martin, C. L. 1996b, ApJ, (in preparation).
- Martin, C. L. 1996c, ApJ, (in preparation).
- Martin, C. L., & Kennicutt, 1995, ApJ, 447, 171.
- Martin, C. L., & Arnett, D. A. 1995, ApJ, 447, 378.
- Massey, P., Strobel, K., Barnes, J. V., & Anderson, E. 1988.
- Mathis, J. S. 1986, ApJ, 301, 423.
- Matteucci, F. & Chiosi, C. 1983, A&A, 123, 121.
- Matteucci, F. & Tosi, M. 1985, MNRAS, 217, 391.
- Massey, P., Strobel, K., Barnes, J. V., & Anderson, E. 1988, ApJ, 328, 315.
- McCall, M. L., Rybski, P. M., & Shields, G. A. 1985, ApJS, 57, 1 (MRS).
- McCray, M., & Kafatos, M. 1987, ApJ, 317, 190.

- McCray, R., & Snow, T. P. 1979, *ARA&R*, 17, 213.
- McGaugh, S. S. 1991, *ApJ*, 380, 140.
- McKee, C. F. 1990, in *The Evolution of the Interstellar Medium*, ed. Leo Blitz, (ASP: San Francisco), p 3.
- Meaburn, J. 1980, *MNRAS*, 192, 365.
- Melisse, J. P. M., & Israel, F. P. 1994, *A&AS*, 103, 391.
- Meurer, G. R. 1991, *Proc. ASA*, 9, 98.
- Meurer, G. R., Freeman, K. C., Dopita, M. A., & Cacciari, C. 1992, *AJ*, 103, 60.
- Miller, W. W., Cox, D. P. 1993, *ApJ*, 417, 579.
- Miller, J. S., & Mathews, W. G. 1972, *ApJ*, 172, 593.
- O'Connell, R. W., Gallagher, J. S., Hunter, D. A. 1994, *ApJ*, 433, 650.
- Oey, S. & Clarke, 1996, *BAAS*.
- Olofsson, K. 1995, *A&AS*, 111, 570.
- Osterbrock, D. E. 1989, *Astrophysics of Gaseous Nebulae and Active Galactic Nuclei* (University Science Books: Mill Valley, CA).
- Osterbrock, D. E., Tran, H. D., & Veilleux, S. 1992, *ApJ*, 389, 196.
- Ostriker, J., & Cowie, L. 1981, *ApJ*, 243, L127.
- Ostriker, J. P., & McKee, C. F. 1988, *Reviews of Modern Physics*, 60, 1.
- Pagel, B. E. J., Simonson, E. A., Terlevich, R. J., & Edmunds, M. G. 1992, *MNRAS*, 255, 325.
- Pettini, M., & Lipman, K. 1995, *A&A*, 297, 63.
- Phillipps, S., & Driver, S. 1995, *MNRAS*, 274, 832.

- Prantzos, N. 1994, A&A, 284, 477.
- Rand, R. J. 1996, ApJ, 462, 712.
- Reakes, M. 1980, MNRAS, 192, 297.
- Renzini, A, Greggio, L., Ritossa, C. & Ferrario, L. 1992, ApJ, 400, 280.
- Rieke, G. 1995, *pvt. commun.*
- Reynolds, R. J. 1984, ApJ, 282, 191.
- Reynolds, R. J. 1985a, ApJ, 294, 256.
- Reynolds, R. J. 1985b, ApJ, 288, L27.
- Reynolds, R. J. 1985c, ApJ, 298, L27.
- Reynolds, R. J. 1989, ApJ, 345, 811.
- Reynolds, R. J. 1991, ApJ, 372, 17.
- Reynolds, R. J. & Tufte, S. L. 1995, ApJ, 439, L17.
- Saito, M. 1979, PASJ, 31, 193.
- Sargent, W. L. W., & Filippenko, A. V. 1991, AJ, 102, 107.
- Sargent, W. L. W., & Searle, L. 1970, ApJ, 162, L155.
- Schechter, P. 1976, ApJ, 203, 297.
- Searle, L. & Sargent, W. L. W. 1972, ApJ, 173, 25.
- Shaw, R. A., & Dufour, R. J. 1995, PASP, (in press).
- Shields, G. A., & Searle, L. 1978, ApJ, 222, 821.
- Shelton, R. L., & Cox, D. P. 1994, ApJ, 434, 599.
- Shull, J. M. 1993, in Massive Stars: Their Lives in the Interstellar Medium, ed. J. P. Cassinelli & E. B. Churchwell (San Francisco: ASP), 327.

- Shull, J. M., & McKee, C. F. 1979, ApJ, 227, 131.
- Skillman, E. D. & Kennicutt, R. C. 1993, ApJ, 411, 655.
- Skillman, E. D., Kennicutt, R. C., & Hodge, P. W. 1989, ApJ, 347, 875.
- Skillman, E. D., Melnick, J., Terlevich, R., & Moles, M. 1988, A&A, 196, 31.
- Slavin, J. D., & Cox, D. P. 1993, ApJ, 417, 187.
- Slavin, J. D., Shull, J. M., & Begelman, M. C. 1993, ApJ, 407, 83.
- Smits, D. P. 1996, MNRAS, 278, 683.
- Stark, A. A., Gammie, C. F., Wilson, R. W., Bally, J., Linke, R. A., Heiles, C., & Hurwitz, M. 1992, ApJS, 79, 77.
- Stasinska, G. 1982, A&AS, 48, 299.
- Stasinska, G. 1990, A&AS, 48, 299.
- Sudarsky, D. L. & Salzer, J. J., 1995, baas 186, 3904.
- Sudarsky, D. L. 1995, private communication.
- Talent, D. L. 1980, Ph.D. thesis, Rice University.
- Tenorio-Tagle, G., & Bodenheimer, P. 1988, ARA&R, 26, 145.
- Thuan, T. X., & Martin, G. E. 1981, ApJ, 247, 823.
- Thuan, T. X., Williams, T. B., & Malumuth, E. 1987, in *Starbursts and Galaxy Evolution*, ed. Thuan, Montmerle, Tran Thanh Van (Editions Frontieres: Gif-sur-Yvette, France).
- Tinsley, B. 1980, Fund. Cosm. Phys., 5, 287.
- Tully, R. B., Boesgaard, A. M., Dyck, H. M., & Schempp, W. V. 1981, ApJ, 246, 38.
- Vader, J. P. 1986, ApJ, 305, 669.

- Vader, J. P. 1987, *ApJ*, 317, 128.
- Veilleux, S., & Osterbrock, D. E. 1987, *ApJS*, 63, 295.
- Viallefonde, F., Lequeux, J., and Comte, G. 1987, in *Starbursts and Galaxy Evolution*, ed. T. X. Thuan, T. Montmerle, and J. Tran Than Van (Editions Frontière: Gif sur Yvette), p. 139 (VLC87).
- Waller, W. H. 1991, *ApJ*, 370, 144.
- Walsh, J. R. & Roy, J. 1989, *MNRAS*, 239, 297.
- Walsh, J. R. & Roy, J. 1993, *MNRAS*, 262, 27.
- Walterbos, R. A., & Braun, R. 1994, *ApJ*, 431, 156.
- Weaver, R., McCray, R., & Castor, J. 1977, *ApJ*, 218, 377.
- Yorke, H. W., Tenorio-Tagle, G., & Bodenheimer, P. 1984, *A&A*, 138, 325.
- Zwicky, F. 1966, *ApJ*, 143, 192.